Numerical Modeling and Experimental Characterization of the Asymmetric Creep Behavior of Refractory Materials

Lucas Breder Teixeira

UNIVERSITÉ D'ORLÉANS

Energie, Matériaux, Sciences de la Terre et de l'Univers – EMSTU

Laboratoire de Mécanique Gabriel Lamé (LaMé)

THESIS presented by:

Lucas BREDER TEIXEIRA

Defense date: **9 December 2022**

Thesis submitted for the degree of:

Doctor of Philosophy

Discipline/Specialty: **Mechanical Engineering**

Numerical Modeling and Experimental Characterization of the Asymmetric Creep Behavior of Refractory Materials

(In the framework of the EU Horizon 2020 Marie Skłodowska–Curie ATHOR project)

THESIS SUPERVISORS:

Mr. BLOND Eric	Professor, University of Orléans
Mr. SAYET Thomas	Associate Professor, University of Orléans
Mr. GILLIBERT Jean	Associate Professor, University of Orléans

REVIEWERS:

Mr. SCHMITT Nicolas	Professor, Paris-Est Créteil University
Mr. CUTARD Thierry	Professor, IMT Mines Albi

JURY:

Mr. LOURENCO Paulo	Professor, University of Minho, President of the jury
Mr. SCHMITT Nicolas	Professor, Paris-Est Créteil University
Mr. CUTARD Thierry	Professor, IMT Mines Albi
Mr. FRANCOIS Marc	Professor, Nantes University
Mr. LEPLAY Paul	Doctor, Saint-Gobain Research Provence
Mr. HUGER Marc	Professor, University of Limoges
Mr. BLOND Eric	Professor, University of Orléans
Mr. SAYET Thomas	Associate Professor, University of Orléans
Mr. GILLIBERT Jean	Associate Professor, University of Orléans

UNIVERSITÉ D'ORLÉANS

Energie, Matériaux, Sciences de la Terre et de l'Univers – EMSTU

Laboratoire de Mécanique Gabriel Lamé (LaMé)

THÈSE présentée par:

Lucas BREDER TEIXEIRA

soutenue le: **9 décembre 2022**

pour obtenir le grade de:

Docteur de l'Université d'Orléans

Discipline/ Spécialité : **Génie mécanique**

Modélisation Numérique et Caractérisation Expérimentale du Comportement de Fluage Asymétrique des Matériaux Réfractaires

(Dans le cadre du projet EU Horizon 2020 Marie Skłodowska–Curie ATHOR)

THÈSE DIRIGÉE PAR :

M. BLOND Eric	Professeur, Université d'Orléans
M. SAYET Thomas	Maître de conférences, Université d'Orléans
M. GILLIBERT Jean	Maître de conférences, Université d'Orléans

RAPPORTEURS :

M. SCHMITT Nicolas	Professeur, Université Paris-Est Créteil
M. CUTARD Thierry	Professeur, IMT Mines Albi

JURY :

M. LOURENCO Paulo	Professeur, Université du Minho, Président du jury
M. SCHMITT Nicolas	Professeur, Paris-Est Créteil University
M. CUTARD Thierry	Professeur, IMT Mines Albi
M. FRANCOIS Marc	Professeur, Université de Nantes
M. LEPLAY Paul	Doctor, Saint-Gobain Research Provence
M. HUGER Marc	Professeur, Université de Limoges
M. BLOND Eric	Professeur, Université d'Orléans
M. SAYET Thomas	Maître de conférences, Université d'Orléans
M. GILLIBERT Jean	Maître de conférences, Université d'Orléans

Lucas BREDER TEIXEIRA

Modélisation Numérique et Caractérisation Expérimentale du Comportement de Fluage Asymétrique des Matériaux Réfractaires

Résumé:
Les matériaux réfractaires sont conçus pour fonctionner à des températures élevées et sous des charges chimiques, thermiques et mécaniques sévères. En général, ces matériaux présentent un comportement de fluage asymétrique prononcé, c'est-à-dire des vitesses de déformation de fluage différentes en traction et en compression. Dans ce travail, deux modèles de fluage asymétrique sont proposés pour représenter numériquement le comportement d'un réfractaire alumine-spinelle utilisé dans des poches de coulée d'acier. Le premier modèle introduit la possibilité de considérer les effets primaires de fluage sous traction et compression, et l'effet de chaque signe de contrainte est calculé en utilisant une stratégie de pondération basée sur la division du tenseur de contrainte en parties positives et négatives. Le deuxième modèle étend le comportement en compression, permettant de prendre en compte le fluage transitoire, c'est-à-dire un passage progressif de la phase primaire à la phase secondaire en fonction d'un critère basé sur l'état actuel des variables internes. Le travail expérimental est divisé en deux parties : premièrement, les paramètres des lois de fluage sont identifiés à l'aide d'essais de traction et de compression uniaxiaux, considérés comme des techniques expérimentales traditionnelles ; Dans un deuxième temps, une procédure de caractérisation basée sur le test brésilien et sur la technique de corrélation d'images numériques (DIC) est proposée. Étant donné que la distribution des contraintes dans un échantillon de test brésilien est caractérisée par des valeurs positives et négatives simultanées, c'est un choix approprié pour étudier les effets asymétriques. Les résultats obtenus à l'aide de chacune des techniques sont comparés, et des essais de flexion à quatre points sont utilisés comme étape de validation supplémentaire. Il est conclu que les modèles de fluage proposés sont adéquats pour la simulation du matériau alumine-spinelle, et que les protocoles expérimentaux nouveaux et traditionnels peuvent être utilisés de manière complémentaire pour caractériser et valider les paramètres du modèle.

Mots clés : Fluage asymétrique, Réfractaires, Méthode des éléments finis, Corrélation d'Images Numériques, Haute Température, Caractérisation Expérimentale

Laboratoire de Mécanique Gabriel Lamé (LaMé)
8 Rue Léonard de Vinci
45072 Orléans

Numerical Modeling and Experimental Characterization of the Asymmetric Creep Behavior of Refractory Materials

Abstract:
Refractory materials are designed to work at high temperatures and under severe chemical, thermal and mechanical loads. In general, these materials present a pronounced asymmetric creep behavior, i.e., different creep strain rates under tension and compression. In this work, two asymmetric creep models are proposed to numerically represent the behavior of an alumina-spinel refractory used in steel ladles. The first model introduces the possibility to consider primary creep effects under tension and compression, and the effect of each stress sign is calculated using a weighting strategy based on the split of the stress tensor into positive and negative parts. The second model extends the compression behavior, allowing for the consideration of transient creep, i.e., a progressive change from the primary to the secondary phase depending on a criterion based on the current state of the internal variables. The experimental work is divided in two parts: first, the parameters of the creep laws are identified using uniaxial tensile and compressive tests, considered traditional experimental techniques; Second, a characterization procedure based on the Brazilian test and on the Digital Image Correlation (DIC) technique is proposed. Since the stress distribution in a Brazilian test sample is characterized by simultaneous positive and negative values, it is an appropriate choice to study asymmetric effects. The results obtained using each of the techniques are compared, and four-point bending tests are used as an extra validation step. It is concluded that the proposed creep models are adequate for the simulation of the alumina-spinel material, and that the novel and traditional experimental protocols can be used in a complementary way to characterize and validate the model parameters.

Keywords : Asymmetric Creep, Refractories, Finite Element Method, Digital Image Correlation, High Temperature, Experimental Characterization

Laboratoire de Mécanique Gabriel Lamé (LaMé)
8 Rue Léonard de Vinci
45072 Orléans

Acknowledgments

During my work as a PhD candidate I was helped by many people, without whom I wouldn't be able to succeed. There are no words able to express all of my gratitude, therefore I will limit myself to mention a few of the ones that were closer to me during this journey.

First, I would like to thank my thesis supervisors Prof. Eric Blond, Dr. Thomas Sayet and Dr. Jean Gillibert, for giving me the opportunity to develop this work and for their very appreciated help along the way. I was also very fortunate to work with the great staff from the LaMé laboratory at Orléans, and I give special thanks to Toum Cam and Christelle Chanteloup in this regard.

I thank Dr. Dietmar Gruber and Dr. Paul Leplay for their supervision during my internships at the University of Leoben and at Saint-Gobain Research Provence, respectively. I also thank the members of the jury for my thesis defense, that kindly accepted to be part of this important moment in my career.

Nothing of this would have been possible without the framework of the ATHOR, and I specially thank Prof. Marc Huger for all his efforts in making it work. All the industrial and academic partners are also very much appreciated, and I consider myself very lucky to have had the change to work with all these highly qualified people. I also express my deepest gratitude to all ESRs, that became friends and not only colleagues.

Finally, I want to thank my beloved wife Nicole and my son Arthur, they are the reason why all this was worth it. Many thanks to my parents Edson and Terezinha, and to my sister Larissa, which supported me from Brazil while I came to live this adventure.

Table of Contents

Table of Contents ii

List of Figures v

List of Tables x

Introduction 1

I State of the Art 5

I.1 Refractories and the steel ladle . . . 7

I.1.1 The steel ladle . . . 7

I.1.2 Thermo-mechanical properties of refractory materials . . . 10

I.1.3 The alumina-spinel material . . . 12

I.2 Mechanical tests – Applications to refractories . . . 13

I.2.1 Traditional tests applied to refractories . . . 13

I.2.2 Brazilian test . . . 15

I.2.3 Four-point bending test . . . 16

I.3 Inverse analysis applied to parameters identification . . . 19

I.3.1 Problem well-posedness . . . 20

I.3.2 General steps of an inverse analysis . . . 22

I.3.3 Optimization algorithms . . . 26

I.4 Creep of refractories . . . 32

I.4.1 Viscoplasticity models for primary and secondary creep . . . 33

I.4.2 Asymmetric Creep Models . . . 37

I.5 Conclusion . . . 44

II Traditional Approach for the Identification of Creep Parameters 45

II.1 Experimental protocol . . . 47

II.1.1 Compression tests . . . 47

II.1.2 Tensile tests . . . 48

II.1.3 Choice of the imposed temperatures and loads . . . 48

II.2 Tension and compression raw curves . . . 50

II.3 Inverse identification using one-dimensional creep laws . . . 53

II.3.1 Primary and secondary creep laws . . . 53

II.3.2 Transient creep law . . . 54

II.3.3 Statistical analysis . . . 55
II.4 Identification of the creep parameters for the alumina-spinel brick . . . 56
II.4.1 Compression – Primary creep . . . 56
II.4.2 Compression – Transient creep . . . 63
II.4.3 Tension – Secondary creep . . . 67
II.5 Conclusion . . . 73

III Proposed Approach for the Modeling and Identification of Creep Parameters – Theory 75
III.1 Proposition of new creep models . . . 77
III.1.1 Asymmetric creep model considering primary and secondary creep . . . 77
III.1.2 Asymmetric creep model considering transient creep under compression and secondary creep under tension . . . 81
III.2 Numerical simulations using the proposed asymmetric creep models . . . 82
III.2.1 Isotropic creep model . . . 82
III.2.2 Kinematic creep model . . . 96
III.2.3 Application of the proposed models to simulate two bricks of a steel ladle 99
III.3 Digital Image Correlation technique . . . 109
III.3.1 DIC fundamentals . . . 109
III.3.2 Inverse identification of material parameters using DIC techniques . . . 112
III.3.3 Experimental aspects related to mechanical tests and image acquisition . 113
III.3.4 DIC at high temperatures . . . 115
III.3.5 Proposition of an identification procedure using an I-DIC technique combined with Brazilian tests . . . 117
III.4 Analysis of the error function using virtual experiments . . . 124
III.4.1 Influence of images quality . . . 126
III.4.2 Influence of images encoding . . . 128
III.4.3 Influence of the residual function under unstable lightening conditions . 130
III.5 Conclusion . . . 131

IV Proposed Approach for the Identification of Creep Parameters – Practice 135
IV.1 Identification of material parameters using the Brazilian test . . . 137
IV.1.1 Experimental methodology . . . 137
IV.1.2 First identification approach – DIC and numerical simulations . . . 145
IV.1.3 Second identification approach – Integrated Digital Image Correlation . 152
IV.2 Validation of the results using four-point bending tests at 1300 °C . . . 158
IV.2.1 Experimental methodology . . . 158
IV.2.2 Validation results . . . 162
IV.3 Comparison between the proposed and traditional identification approaches . . 166
IV.3.1 Test design . . . 166
IV.3.2 Sample preparation . . . 167
IV.3.3 Experimental data post-processing and amount of retrieved information 167
IV.3.4 Availability of testing equipment and test's robustness . . . 168
IV.3.5 Time and budget constraints . . . 168
IV.4 Conclusion . . . 169

Conclusions and Perspectives 171

Bibliography **175**

List of Figures

I.1 Steel production process (NSC, 2017). 8
I.2 Example of a steel ladle. (a) Cutaway view showing the refractory linings. (b) Schematic representation of a lining ring. 8
I.3 Factors influencing the behavior of refractories 10
I.4 Typical refractory stress-strain curves in (a) compression and in (b) tension. 11
I.5 Stress distribution in a refractory brick. (a) Thermo-elastic approach. (b) Multi-physics, non-linear approach. Adapted from Blond (2017). 12
I.6 Brazilian test geometry. (a) Classic. (b) Flattened 15
I.7 Four-point bending test - Schematic representation. 17
I.8 Four-point bending. (a) σ_x in the symmetry line. (b) Distribution of σ_x in the sample. 18
I.9 Direct vs Inverse problems. Adapted from Groetsch (1999) 19
I.10 Representation of different inverse problems regarding their stability. Adapted from Mahnken (2017). 21
I.11 Overview of search techniques. Adapted from Sivanandam and Deepa (2007) . . . 27
I.12 Generic evolutionary algorithm. Adapted from Sivanandam and Deepa (2007) . . . 30
I.13 Three stages of creep. 32
I.14 Drucker-Prager Creep model yield surface. Adapted from Abaqus (2018) 38
I.15 Yield surface of Blond's model. 43

II.1 Compression creep experimental setup. 47
II.2 Tensile creep experimental setup: Gluing device 48
II.3 Tensile creep experimental setup: Testing machine 49
II.4 Compressive creep curves. (a) 1300 °C. (b) 1400 °C. (c) 1500 °C. 51
II.5 Tensile creep curves. (a) 1200 °C. (b) 1300 °C. (c) 1400 °C. 52
II.6 Compression at T = 1300 °C. (a) σ = 8 MPa. (b) σ = 9 MPa. (c) σ = 10 MPa. . . 58
II.7 Compression at T = 1400 °C. (a) σ = 4 MPa. (b) σ = 4.5 MPa. (c) σ = 5 MPa. . . 58
II.8 Compression at T = 1500 °C. (a) σ = 3.5 MPa. (b) σ = 4.0 MPa. (c) σ = 4.5 MPa. 60

II.9 Compression at $T = 1300$ °C – Reduced number of samples. (a) $\sigma = 8$ MPa. (b) $\sigma = 9$ MPa. (c) $\sigma = 10$ MPa. 60
II.10 Compression at $T = 1400$ °C – Reduced number of samples. (a) $\sigma = 4$ MPa. (b) $\sigma = 4.5$ MPa. (c) $\sigma = 5$ MPa. 61
II.11 Compression at $T = 1500$ °C – Reduced number of samples. (a) $\sigma = 3.5$ MPa (b) $\sigma = 4$ MPa (c) $\sigma = 4.5$ MPa 61
II.12 Variation of the compression parameters. (a) $\log_{10}^{A}$. (b) n. (c) m. 62
II.13 Transient creep identification at $T = 1300$ °C. (a) $\sigma = 8$ MPa. (b) $\sigma = 9$ MPa. (c) $\sigma = 10$ MPa. (d) Evolution of H 63
II.14 Transient creep identification at $T = 1400$ °C. (a) $\sigma = 4$ MPa. (b) $\sigma = 4.5$ MPa. (c) $\sigma = 5$ MPa. (d) Evolution of H 64
II.15 Transient creep identification at $T = 1500$ °C. (a) $\sigma = 3.5$ MPa. (b) $\sigma = 4$ MPa. (c) $\sigma = 4.5$ MPa. (d) Evolution of H 65
II.16 Variation of material parameters – Transient creep. (a) n. (b) $\log_{10} a$. (c) $\log_{10} b$. (d) $\log_{10} c$. 66
II.17 Tension creep curves – Extensometer front, extensometer rear and average. (a) 1200 °C, sample 2. (b) 1300 °C, sample 6. (c) 1300 °C, sample 9. (e) 1400 °C, sample 4. 68
II.18 Tension at $T = 1200$ °C. (a) $\sigma = 0.25$ MPa. (b) $\sigma = 0.35$ MPa. (c) $\sigma = 0.45$ MPa . 69
II.19 Tension at $T = 1300$ °C. (a)$\sigma = 0.20$ MPa. (b)$\sigma = 0.25$ MPa 69
II.20 Tension at $T = 1400$ °C. (a) $\sigma = 0.15$ MPa. (b) $\sigma = 0.18$ MPa 70
II.21 Tension at $T = 1200$ °C – Reduced number of samples. (a) $\sigma = 0.25$ MPa. (b) $\sigma = 0.35$ MPa. (c) $\sigma = 0.45$ MPa 71
II.22 Tension at $T = 1300$ °C – Reduced number of samples. (a) $\sigma = 0.20$ MPa. (b) $\sigma = 0.25$ MPa 72
II.23 Tension at $T = 1400$ °C – Reduced number of samples. (a) $\sigma = 0.15$ MPa. (b) $\sigma = 0.18$ MPa 72
II.24 Variation of the tension parameters. (a) $\log_{10} A$. (b) n. 73

III.1 Asymmetric creep model algorithms. Blond et al. (2005) (full lines) and the proposition of this work (dashed lines) 79
III.2 Stress distribution – Normal loads. (a) Simulation model. (b) Stress path. (c) σ_x vs Time. (d) σ_y vs Time. 84
III.3 Accumulated viscoplastic strain – Normal loads. 85
III.4 Brazilian test – Geometry, mesh and boundary conditions. 86
III.5 (a) Vertical and (b) horizontal displacements in the Brazilian test sample. 86

III.6 Maximum principal stress distribution on a Brazilian test sample. (a) compression (b) tension and (c) asymmetric material properties. 87
III.7 Minimum principal stress distribution on a Brazilian test sample. (a) compression (b) tension and (c) asymmetric material properties. 87
III.8 Variation of the total strain in direction x with time – Symmetric and asymmetric models. 88
III.9 Variation of the total strain in direction y with time – Symmetric and asymmetric models. 88
III.10 Accumulated viscoplastic strain distribution on a Brazilian test sample. (a) compression (b) tension and (c) asymmetric material properties. 89
III.11 Change on the asymmetric creep model response due to variations of the material parameters – Brazilian test. 90
III.12 Four-point bending test – Geometry, mesh and boundary conditions. 91
III.13 (a) Vertical displacement on the lower center point of the four-point bending sample. (b) Detail of the first 15 min. 92
III.14 Distribution of axial stresses on the four-point bending test sample. (a) Symmetric – Compression. (b) Symmetric – Tension. (c) Asymmetric. 93
III.15 Distribution of accumulated viscoplastic strain on the four-point bending test sample. (a) Symmetric – Compression. (b) Symmetric – Tension. (c) Asymmetric. 93
III.16 Variation of the neutral line's position on the four-point bending sample over time. . 94
III.17 Change on the asymmetric creep model response due to variations of the material parameters – Four-point bending test. 95
III.18 Change on the kinematic asymmetric creep model response due to variations of the material parameters – Brazilian test. 97
III.19 Change on the kinematic asymmetric creep model response due to variations of the material parameters – Bending test. 98
III.20 Bending test: Maximum principal stress in direction I at $t = 2h$ using the kinematic creep model. (a) Nominal material parameters. (b) $a^- - 20\%$. (c) $A^+ - 20\%$. . . . 99
III.21 Brazilian test: Maximum principal stress in direction I at $t = 2h$ using the kinematic creep model. (a) Nominal material parameters. (b) $a^- - 20\%$. (c) $A^+ - 20\%$. . . . 100
III.22 Mesh and boundary conditions for the simulations of the steel ladle. 100
III.23 Compression tests for the identification of the elastic properties. 102
III.24 Temperature distribution over time at the brick's hot face, cold face and center position. 103
III.25 Spatial temperature distribution over time – 5^{th} cycle. 103
III.26 Equivalent creep strain in the integration point 1 of element A. The zoomed area shows the detail of the first cycle. 104

III.27Minimum principal stress in the integration point 1 of element A. The zoomed area shows the details of the first cycle. . . . 105
III.28(a) Maximum principal stress in the integration point 1 of element A – Isotropic and kinematic models. (b) Detail of the fifth cycle. . . . 105
III.29Equivalent creep strain at the end of treatment – Isotropic model. . . . 106
III.30Equivalent creep strain at the end of treatment – Kinematic model. . . . 106
III.31Evolution of the positive values of minimum principal stress on the brick after the thermal shock. . . . 107
III.32Contact force distribution in the brick's length over time. . . . 108
III.33Subset-based Digital Image Correlation. . . . 111
III.34FEMU – Schematic representation. Adapted from (Mathieu et al., 2015) . . . 113
III.35I-DIC – Schematic representation. Adapted from (Mathieu et al., 2015) . . . 114
III.36Brazilian tests: Vertical displacement in mm at 1300 °C. (a) $t \approx 0.6$ h. (b) $t \approx 1$ h. (c) $t \approx 1.5$ h. . . . 117
III.37Proposed identification procedure – Modeling strategy . . . 119
III.38Proposed identification procedure – Application of the forces and predefined time steps. . . . 120
III.39Interpolation of an image's pixel values. (a) 1 pixel rigid body displacement. (b) 0.1 pixel rigid body displacement. . . . 121
III.40I-DIC – Proposed algorithm. . . . 123
III.41Images with different qualities. (a) Room temperature image. (b) Image at 1300 °C – Higher quality. (c) Image at 1300 °C – Lower quality . . . 127
III.42Variation of the error function with the material parameters. . . . 129
III.43Variation of the error function with the material parameters – Comparison between 8-bits and 12-bits images. . . . 130
III.44Variation of the error function with the material parameters – Comparison between SSD and ZNSSD residual functions. . . . 132

IV.1 Experimental setup for the Brazilian tests at high temperature . . . 137
IV.2 Blue band pass filter – Transmission variation according to the wavelength (Source: manufacturer's website) . . . 139
IV.3 Brazilian tests: heating curve and evolution of machine displacements prior to the test. . . . 141
IV.4 Influence of the blue light and the blue band pass filter in the quality of the image. (a) Image at room temperature. (b) No blue light and no filter. (c) No filter. (d) Use of blue light and blue band pass filter. . . . 142
IV.5 Histograms of the images at room and high temperature. . . . 143

IV.6 Distribution of stresses in a Brazilian test considering linear elastic material properties - Distribution according to the area percentage. (a) Maximum principal stresses. (b) Minimum principal stresses. 144
IV.7 Brazilian tests time vs displacement curves obtained by DIC – 1300 °C. 146
IV.8 Brazilian tests time x displacement curves and parameters envelope. 147
IV.9 Brazilian tests time vs displacement curves and inverse identification. 148
IV.10 Brazilian tests: Vertical displacement in mm at 1300 °C – DIC sample 6. (a) Point A. (b) Point B. (c) Point C. 149
IV.11 Brazilian tests: Vertical displacement in mm at 1300 °C – Simulation. (a) Point A. (b) Point B. (c) Point C. 149
IV.12 Brazilian tests: Vertical displacement in the central line of the sample. 150
IV.13 Validation of the identified kinematic creep parameters – Vertical displacement at the load application point in a Brazilian test. 151
IV.14 Proposed modified genetic algorithm. 155
IV.15 First generation of the I-DIC identification 156
IV.16 Experimental setup for four-point bending tests at high temperature. 158
IV.17 Four-point bending: Internal view of the furnace. 159
IV.18 Four-point bending: Sample and testing setup geometries. 160
IV.19 Four-point bending: Sample before (below) and after (above) a test that took three days. 160
IV.20 Four-point bending: Example of speckle pattern at 1300 °C. 161
IV.21 Bending tests: Vertical displacements at 1300 °C and 59.3 N. 163
IV.22 Bending tests: Vertical displacements at 1300 °C and 59.3 N – Detail of the first 4 hours. 164
IV.23 Bending tests: Vertical displacements of the samples at 1300 °C. (a) Displacements at the vertical center line of sample 1, (b) DIC results for sample 1 at t =10 h. (c) Displacements at the vertical center line of sample 2, (b) DIC results for sample 2 at t =10 h. 164
IV.24 Bending tests: Vertical displacements at 1300 °C and 59.3 N – Validation range. . . 165
IV.25 Bending tests: Vertical displacements at 1300 °C and 40.2 N. 165

List of Tables

II.1 Identification results – Compression creep 57
II.2 Identification results – Compression creep with reduced number of samples 59
II.3 Identification results – Transient creep 66
II.4 Identification results – Tensile creep 68
II.5 Identification results – Tensile creep with reduced number of samples 71

III.1 Material parameters used in the numerical simulation tests – Isotropic creep model 82
III.2 Variation of the material parameters – Isotropic creep model 89
III.3 Material parameters used in the numerical simulation tests – Kinematic creep model 96
III.4 Variation of the material parameters – Kinematic creep model 96
III.5 Convection coefficients and sink temperatures for each phase of the thermal cycle . 101
III.6 Thermo-elastic material properties used in the numerical simulations. 102
III.7 Isotropic compressive creep and tensile creep parameters 102
III.8 Material parameters used in the virtual tests – Isotropic creep model 125
III.9 Variation of the material parameters for the virtual tests 125

IV.1 Isotropic creep parameters – Identification using Brazilian creep tests 146
IV.2 Kinematic creep parameters – Identification using Brazilian creep tests 150
IV.3 Range of variation for the parameters used in the I-DIC identifications. 152
IV.4 Parameters identified using the I-DIC method – first generation 157

Introduction

Refractory materials are of primary importance in several production processes involving the manipulation of high temperature molten material, such as steel, cement, glass, copper, among others. These materials are fundamental to guarantee a safe and energy efficient process, and, as such, receive considerable attention from academic and industrial research groups from different countries.

Refractory producers strive to optimize the material's performance from different aspects, be it chemical, thermal or mechanical. Besides, the behavior of refractory linings greatly influences the stresses and strain in the steel shell of equipments as the steel ladle, the BOF and the RH-degasser, that are used in the production of steel and need to be kept under controled conditions.

To avoid the failure of refractory materials during operation, their stability need to be guaranteed, otherwise considerable economical losses can be faced and, more importantly, the lives of those working around the equipments where they are used can be put at risk. Therefore, it is interesting to be able to design and predict the life cycle of refractory linings as accurately as possible, and phenomena such as irreversible creep strains and stress relaxation due to the high temperatures need to be considered on structural analysis.

As it is shown in this work, creep and relaxation are two major phenomena related to the application of refractories at high temperatures. The characterization and modeling of these time-dependent behaviors is crucial to predict accurately the thermo-mechanical stresses and strains in refractory linings under operating conditions, as well as in the steel shells that surround them. In particular, refractories present an asymmetric creep behavior, i.e., different material properties under tension and compression, what makes their study even more challenging.

Currently, there are no creep constitutive models available in commercial software that can be used to accurately simulate the asymmetric creep behavior of refractories under complex thermo-mechanical loads. Also, the characterization of these materials at high temperatures is expensive and time consuming, therefore innovative experimental methods that can generate more information per sample are constantly required by the industry.

The application of optical instrumentation coupled with Digital Image Correlation (DIC) tech-

niques is an interesting option to obtain more data from high temperature tests, since it can measure the full displacements field in the sample, therefore allowing for more complex loading paths to be applied. Naturally, these techniques require a more sophisticated testing setup and post-treatment of the data, involving the application of inverse identification techniques and advanced optimization algorithms.

The use of DIC techniques to study the thermo-mechanical behavior of refractories at high temperatures is a relatively recent practice, with a limited number of published research works. This thesis aims to contribute to the move towards a faster, cheaper and more robust modeling and characterization of refractories, that is the first step into a deeper understanding of the effects of the heterogeneous nature of these materials into equipments operating at high temperatures.

Project ATHOR

The project ATHOR (Advanced THermomechanical multiscale mOdelling of Refractory linings)[1] is composed of a network of industrial and academic partners in the field of refractories, that cooperate with the goal of better understanding the thermo-mechanical behavior of such materials. The project is directly linked to the Federation for International Refractory Research and Education (FIRE) [2].

The project ATHOR applies a multiscale approach to fully understand the thermo-mechanical behavior of refractories, from the effects of the microstructure design to the application of refractory linings composed of thousands of bricks. Important aspects for the design and selection of refractories are addressed, such as corrosion resistance, creep behavior, fracture initiation and propagation, interaction of bricks in large assemblies, among others. This work is focused on the mesoscale of the problem, i.e., the scale of the refractory bricks, as it contributes to the characterization and modeling of the individual building blocks of refractory linings.

The project ATHOR was supported by the funding scheme of the European Commission, Marie Skłodowska-Curie Actions Innovative Training Networks, Grant 764987.

Thesis goals

The main goals of this thesis are:

- Explore the traditional approach currently used to characterize and model the creep behavior of refractories, using one-dimensional tension and compression tests.

[1] https://www.etn-athor.eu/
[2] http://fire-refractory.org/

- Based on the experimental behavior observed from the traditional characterization techniques, propose new creep constitutive models that are able to represent the asymmetry of refractories, i.e., different thermo-mechanical behavior under tension and compression.

- Implement the proposed creep constitutive models in a commercial finite element software, allowing to perform computations under complex loads paths and geometries Demonstrate the capabilities of the proposed model using suitable numerical simulations.

- Implement an experimental setup using the Brazilian test and optical devices to allow the acquisition of high quality images of the test at temperatures up to 1300 °C. These images should be post-processed using a Digital Image Correlation (DIC) based algorithm, to identify the mechanical properties of the material with a reduced number of experiments in comparison to traditional techniques.

- Validate the results obtained by the Brazilian test and the DIC technique, using four-point bending tests. Compare them to the results obtained using the traditional characterization approach.

Thesis structure:

This thesis is divided into four chapters:

Chapter I begins with an introduction about the thermo-mechanical properties of refractory materials, and also an explanation about the main characteristics of a steel ladle used in steel plants, where the material studied in this work is applied. In this chapter, the state of the art of the high temperature mechanical tests applied to refractories is described, as well as the fundamentals of Brazilian tests and four-point bending tests, that are used in this work to propose a new characterization procedure.

Chapter I also discusses the general framework of inverse identification methods, that is one of the central parts of this thesis. In this discussion, the objective is to highlight the key points that need to be addressed during an inverse analysis to increase the chance of success, including regularization techniques, the choice of suitable residuals and error functions and possible numerical instabilities.

Finally, Chapter I provides an in-depth discussion about viscoplastic material models, both from a theoretical and a numerical point of view, based on a thermodynamic framework. The main symmetric and asymmetric creep models available in the literature are presented, and their possible use to model the time-dependent behavior of refractories is discussed.

In Chapter II, the details about the traditional high temperature tension and compression creep tests are presented, together with the creep strain-time curves obtained for the alumina-spinel material. The parameters of the material under compression are inversely identified for an isotropic and a kinematic primary creep laws, described in Chapter I. The parameters of the material under tensile loads are identified using a secondary creep law.

The first part of Chapter III proposes two novel asymmetric creep model. The first model is able to represent the primary or secondary creep behavior of materials under tension and compression, while the second one represents a transient creep behavior under compression (i.e., transition from primary to secondary creep) and secondary creep under tension. Numerical simulations of increasing order of magnitude are performed to test the capabilities of the new models.

The second part of Chapter III starts with a review of the DIC techniques available in the literature, with special emphasis on the inverse identification procedures that use these techniques, such as the Finite Element Model Update (FEMU) and the I-DIC. Later, the details of the specific I-DIC algorithm used in this work are described, and its capabilities are tested using virtual experiments.

Chapter IV describes the experimental setup used to obtain high quality pictures of Brazilian tests at temperatures up to 1300 °C, as well as the results of inversely identified creep properties of the alumina-spinel material. The setup of four-point bending tests used for the validation of the experimental results is also presented.

This work is concluded with a comparison between the traditional and proposed creep models and identification procedures, showing the advantages and disadvantages of each. Based on the results obtained, possible new research topics are suggested, both in the fields of numerical modeling and materials characterization.

CHAPTER I

State of the Art

The goal of this chapter is to present the current state of the technology used to characterize and predict the behavior of refractories and other non-linear materials, as well as to stablish the theoretical basis to support the developments made during this work.

Section I.1 presents the main thermo-mechanical characteristics of refractory materials. The alumina-spinel brick studied in this work is introduced, in the context of its application on steel ladles used on steel plants.

Section I.2 describes traditional mechanical tests applied to the characterization of refractories and ceramics, and the fundamentals of Brazilian and four-point bending tests that were used to identify and validate the parameters of the creep models developed in this work.

Section I.3 presents the main steps to perform an inverse identification of material properties, the methods available to conduct a sensitivity analysis of the testing protocol and an overview of optimization methods that can be used to minimize the functional relating the experimental results to the model computations.

Section I.4 discusses the fundamentals of constitutive modeling using a thermodynamics framework, with special emphasis on symmetric and asymmetric creep (viscoplastic) models available in the literature, and their application to refractories.

Chapter Contents

I.1 Refractories and the steel ladle 7
I.1.1 The steel ladle 7
I.1.2 Thermo-mechanical properties of refractory materials 10
I.1.3 The alumina-spinel material 12
I.2 Mechanical tests – Applications to refractories 13
I.2.1 Traditional tests applied to refractories 13
I.2.2 Brazilian test 15
I.2.3 Four-point bending test 16
I.3 Inverse analysis applied to parameters identification 19
I.3.1 Problem well-posedness 20
I.3.2 General steps of an inverse analysis 22
I.3.3 Optimization algorithms 26
I.4 Creep of refractories 32
I.4.1 Viscoplasticity models for primary and secondary creep 33
I.4.2 Asymmetric Creep Models 37
I.5 Conclusion 44

I.1 Refractories and the steel ladle

Refractory ceramics are materials designed to work at highly aggressive environments, and need to resist to thermo-mechanical stresses and strains, corrosion and erosion at temperatures that can reach over 2000 °C (Banerjee, 2004). In the production of steel, cement, glass, copper, among other materials processed at high temperatures, the goal of refractory linings is to protect the vessels used in the production, normally made of steel, from overheating and consequent mechanical failure, as well as to control the heat losses from the process (Schacht, 2004).

Refractory materials are available in many chemical compositions, and can be classified as basic, high-alumina, silica, fireclay and insulating, also including silicon carbide, graphite, zircon, zirconia and other raw materials. These materials are also classified according to their shape, that can be preformed (bricks, sliding gate plates, ladle shrouds, etc) or delivered in the form of clays, mortars, castables, ramming mixes, and others (Harbison-Walker, 2005).

This work is dedicated to the study of the creep behavior of an alumina-spinel material shaped in the form of bricks, that is commonly applied to ladles used in steel plants. The following sections discuss the operational cycle of this vessel, such as the fundamental mechanical properties of refractories.

I.1.1 The steel ladle

The transformation of raw materials into finished steel products involve high temperature processes, and different vessels lined with refractories are used to contain the molten metals, such as blast furnaces, basic oxygen furnaces (BOFs), electric arc furnaces (EAFs), ladles and tundishes. Figure I.1 shows the steps in steel production.

Among those vessels, the steel ladle has a considerable importance, since it is used in the secondary metallurgy and is responsible for a non-negligible consumption of refractories (Dutta & Chokshi, 2020). The integrity of the ladle is also important regarding the safety of the production site, since it transits between other equipments and workers, carrying molten steel, and a failure can lead to serious consequences.

Figure I.2a shows a cutaway view of a steel ladle, where it is possible to see the refractories and the steel shell. Usually, different refractory grades are used depending on the region of the lining, and more than one lining is used on the thickness, to ensure the safety of the operation and the appropriated thermal insulation (Maupin, 2004). The choice of the refractories to be applied in each layer of the lining greatly influences the temperature distribution on the ladle, therefore playing also a crucial role in the thermo-mechanical behavior (Volkova & Janke, 2005) and on the energy consumption.

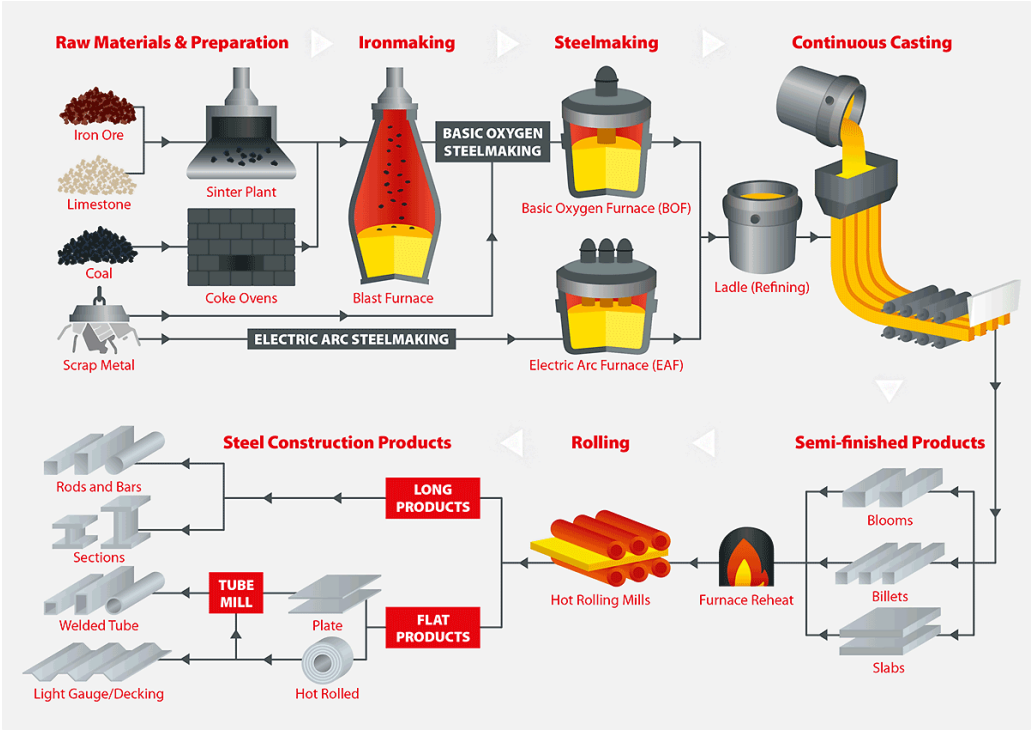

Figure I.1: Steel production process (NSC, 2017).

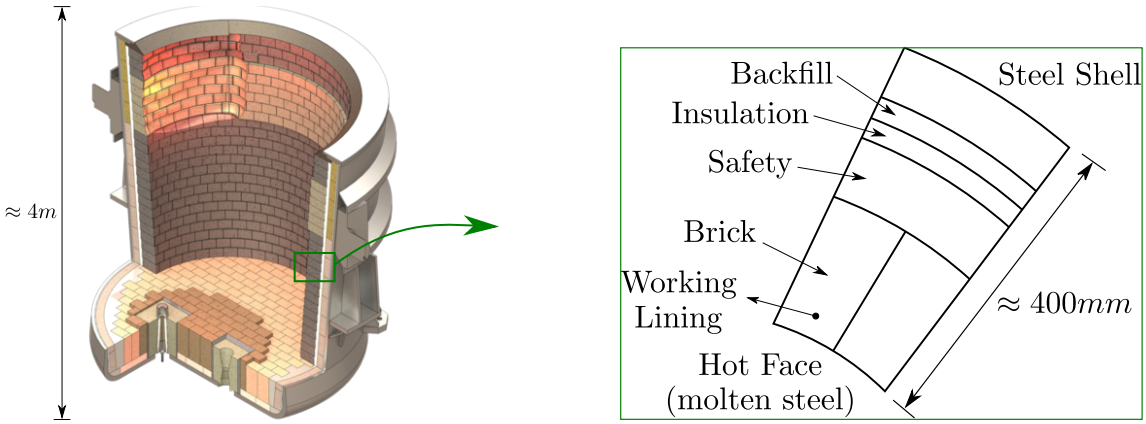

(a) (b)

Figure I.2: Example of a steel ladle. (a) Cutaway view showing the refractory linings. (b) Schematic representation of a lining ring.

A schematic representation of one ring of a ladle lining is given in Figure I.2b, showing the different layers that can be used. The layer in contact with the steel is called working lining, and is responsible to withstand most of the corrosion and thermo-mechanical loads, being replaced with a certain frequency defined by the refractory specialists, depending on its wear rate.

The permanent or safety lining, as the name implies, guarantees there is enough time to take actions in case of the failure of the working lining, avoiding that molten steel reaches the metallic

shell and causes an accident. This layer is replaced less frequently than the working lining.

It is also a common practice to use insulating materials to reduce heat losses, what greatly decreases energy costs and the risk of a drop in the temperature of the molten steel below acceptable values. Finally, a backfill can be used between the shell and the insulation to fill the empty spaces caused by irregularities on the metallic vessel, acting also as an expansion allowance in the radial direction.

According to Gasser et al. (2000), steel ladle's refractories can be subjected to the following thermo-mechanical loads:

- Thermal gradient in the direction of the lining thickness, due to the difference between the temperatures of the refractory in contact with the molten steel (hot face) and the steel shell in contact with the plant's environment.
- Difference in the thermal expansion coefficient of the different refractories used in the lining and that of the steel shell. This difference results in complex loading conditions, and the equipment needs to be carefully designed to avoid a loose lining during cooling, as well as a overstressed lining during operation (Schacht, 2004).
- Thermal cycling of the ladle, alternating between situations of operation, heat treatment and maintenance.

Apart from the material's resistance to the thermo-mechanical loads, the refractory lining needs to be structurally and chemically stable during the entire operational cycle of the ladle. Since the refractories are assembled in a cylindrical pattern while the ladle is at ambient temperature, expansion joints need to be predicted during the calculation of bricks dimension and the material's selection. When the ladle is filled with molten steel, it is important that the joints are not excessively compressed, to avoid premature compressive failure of the refractory, but are closed enough to restrict the infiltration of the molten steel.

An important phenomena to be considered in the design of the steel ladle is the creep and stress relaxation of the working lining bricks. The absence of a non-linear viscoplastic behavior can lead to an increase of the stresses that can't be supported by the material, causing a mechanical failure. Nevertheless, if the material presents excessive creep, it will have a considerable reduction on its size caused by the compression stresses at the hot face, and joints may open during the cooling of the ladle, making the lining loose and allowing for steel infiltration in posterior cycles.

Given the complex loads to which the steel ladle is exposed, a deep understanding of the thermo-mechanical behavior of the refractories and their interaction with the steel shell is of primary importance to design a safe and efficient equipment.

I.1.2 Thermo-mechanical properties of refractory materials

Modeling the behavior of refractory materials under working conditions is intrinsically a multiphysics and multiscale problem (Blond, 2017). Figure I.3 shows the four main factors that influence the performance of a refractory. All these factors influence each other, and the following interactions can be expected:

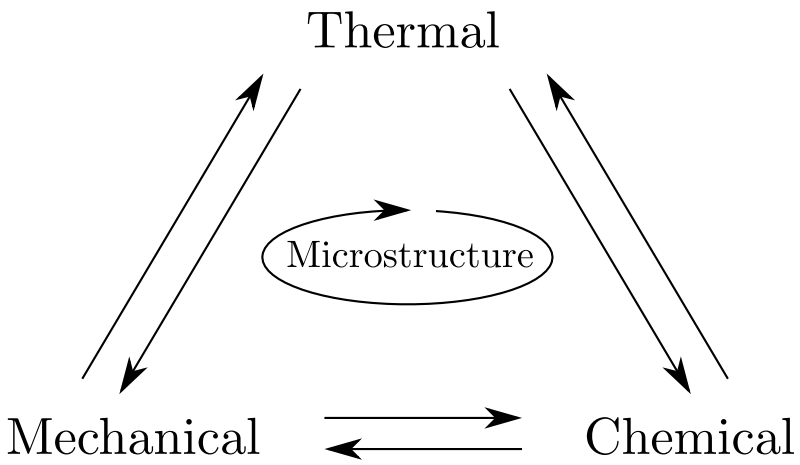

Figure I.3: Factors influencing the behavior of refractories

1. The mechanical properties of refractories vary significantly with the temperature, going from a mostly brittle material at room temperature to viscoplastic (creep) damageable at high temperatures. On the other hand, the thermo-mechanical wear decreases the thickness of the refractories in the working lining, which changes the temperature distribution.

2. Similarly, the material is more easily corroded at certain temperatures, depending on its composition, and the corrosion leads to a change on the microstructure and, consequently, on the thermal and the mechanical properties.

3. Mechanical loads can change the structural integrity of the material, leading to accelerated corrosion.

4. The material's microstructure plays a central role on the thermo-chemo-mechanical properties of refractories, so that it influences all the stages of its working life.

Due to the variety of refractory materials available in the market, the selection of the most suitable ones for a given application is a non-trivial task. Regarding the need to resist thermo-mechanical stresses and strains, it is import to predict if the lining will be more exposed to stress-controlled or strain-controlled loads. Figure I.4a shows the example of a compression stress-strain curves of two different materials under the same temperature. Material 1 has a high value of stress strength (σ_1^{max}), but a relatively low maximum strain before failure (ε_1^{max}), and therefore is more suitable to resist to stress-controlled loads. Material 2 presents a lower stress strength, but can resist to larger strains, therefore being applicable in case where thermal loads are dominant (Schacht, 2004).

Similarly, Figure I.4b shows an example of tension stress-strain curves for two materials. Material 1 presents a brittle behavior, with a linear curve until σ_1^{max}, then a sudden failure. Material 2 has a post-peak behavior, allowing the material to resist to strain loads even after the maximum stress was reached, and follows a softening curve with exponential shape. In general, material 2 is preferred for the applications on refractory linings, since thermal strains are dominant and it is unlike that the initiation of a fracture can be avoided. Therefore, the strategy employed to guarantee the integrity of the structure is to delay the crack propagation, increasing the level of non-linearity on the stress-strain curve (Harmuth & Bradt, 2010; Tschegg et al., 2009). Case the maximum couple stress-strain predicted in a given application corresponds to zone A in Figure I.4, both materials can be used. Case zone B is anticipated, only material 2 is suitable, and for zone C only material 1 can be applied. If the stress-strain is expected to reach zone D, none of the materials would resist properly.

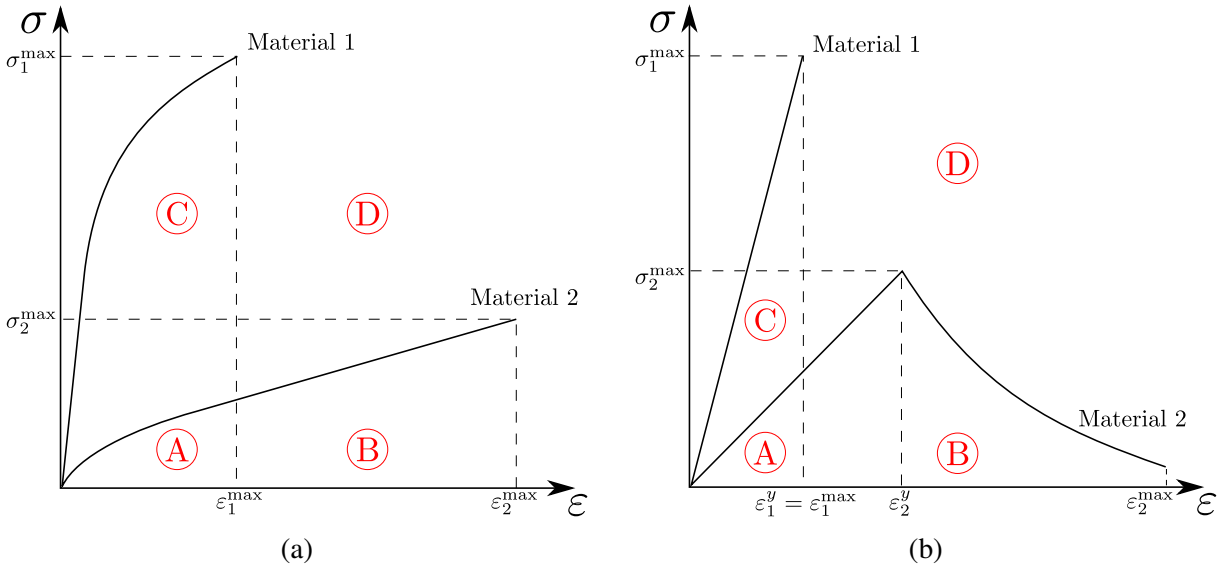

Figure I.4: Typical refractory stress-strain curves in (a) compression and in (b) tension.

Figure I.5a represents the stress distribution on a refractory brick used at the working lining of a

steel ladle in the circumferential direction. At the hot face, the brick is subjected to compression stresses, due to its thermal expansion and consequent closure of the joints. At point A, located at a given distance from the hot face, the temperature is not high enough to cause sufficient thermal expansion to close the joints, so they remain open from this point until the brick's cold face. This causes the bending of the brick around point A, resulting in tension stresses.

In a real application case, the effects of joints opening and closing still exist, but are superposed to the effects of corrosion, creep, damage and microstructural changes during operation, making the stress distribution considerably more complex, as in the example of Figure I.5b. Besides, the stress and strain distribution also changes over time, since the steel ladle is frequently operating under transient thermal conditions, due to the thermal cycling explained in Section I.1.1.

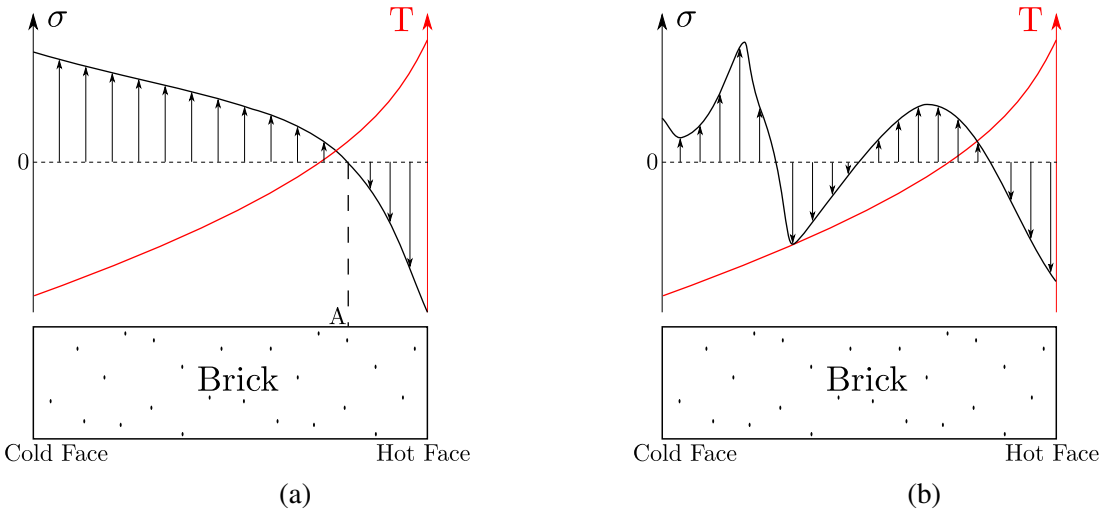

Figure I.5: Stress distribution in a refractory brick. (a) Thermo-elastic approach. (b) Multi-physics, non-linear approach. Adapted from Blond (2017).

Since this work is mainly focused in the development of creep models for refractories and their characterization, this topic is explored in more details in Sections I.2 and I.4.

I.1.3 The alumina-spinel material

The Alumina-Spinel brick studied in this work has a maximum grain size of 3 mm, and it's used in the working lining of steel ladles in steel plants. According to the material's technical data sheet, it is mainly composed of 94% Al_2O_3, 5% MgO, 0.3% SiO_2 and 0.1% Fe_2O_3, with a bulk density of 3.13 g/cm^3 and apparent porosity of 19 vol%.

I.2 Mechanical tests – Applications to refractories

The refractories field has been made extensive use of experimental methods to design and characterize its materials. Since these materials have to resist high thermo-chemo-mechanical loads, it is mandatory to understand their behavior under operational conditions, to avoid safety problems and to obtain the maximum performance for the concerned applications.

In what follows, the mechanical tests that have been traditionally applied to refractories are discussed in Section I.2.1, with a special focus on creep. In Sections I.2.2 and I.2.3 the Brazilian test and the four-point bending test are explained, since they are used in this work to identify the parameters of the alumina-spinel brick.

I.2.1 Traditional tests applied to refractories

Baxendale (2004) divides the tests applied to refractories into three categories:

1. Characterization / data sheet tests: describe the fundamental properties of refractories, and should not be used to specify a material for a given application, but to measure quality control variables.

2. Service related properties: are more representative of the behavior of refractories under real working conditions, and include modulus of rupture at high temperatures, refractoriness under load and thermal shock resistance.

3. Design properties: represent more in-dept investigations, allowing the use of numerical methods to predict the thermo-mechanical behavior of refractory parts or linings. Those tests include thermal conductivity, heat capacity, emissivity, thermal expansion, creep in tension and compression, Poisson's ratio and stress-strain tests at high temperatures.

From a thermo-mechanical point of view, high temperature testing procedures are still to be more developed and validated, since the real conditions under which refractories operate need to be better represented. Next sections focus on the special case of creep tests applied to refractories, showing their applications and limitations.

I.2.1.1 Refractoriness under Load and Creep in Compression tests

The Refractoriness under Load (RuL) is a standardized test (ISO-1893, 2007), that intends to provide a qualitative ranking of different refractory materials according to their capacity to withstand thermo-mechanical loads over time. This test determines the deformation of a dense or insulating shaped refractory when subjected to a constant load and progressive temperature

increase. Therefore, effects of creep and relaxation are combined in the final response, and the identification of creep parameters using this test is made difficult, since the temperature is not constant.

Another disadvantage of this test is the low value of stress applied on the sample, that equals 0.2 MPa. This value is considerably lower than the compression stresses imposed over refractory bricks at the hot face of linings, and therefore is not representative for the estimation of strains and failure time.

The Creep in Compression (CiC) test (ISO-3187, 1989) uses the same device and load magnitude as the RuL test, but it requires the load to be applied at the moment when the furnace is switched on, or after the sample has been maintained at the test temperature from 1 h to 4 h. The CiC test complements the RuL as an easy-to-do qualitative mechanical characterization test, and presents the same disadvantages of it.

In general, the results of these tests are not used to calculate the lifetime of refractory linings, but to compare the results obtained from two different materials, allowing an approximated ranking of the lining composition.

I.2.1.2 Direct tension and compression creep tests

In recent years, direct tension and compression creep tests have been developed and applied to characterize refractories under more theoretically explorable loads (Jin et al., 2014; Samadi et al., 2020; Schachner et al., 2019; Sidi Mammar et al., 2016; Teixeira et al., 2020).

One important advantage of direct tension and compression tests is that, due to the simple stress distribution over the sample, the transition between the different creep stages can be clearly defined, and the identification of the material parameters is straightforward.

Although this experimental procedure is well established in the refractories field, they present two disadvantages: the need for a large number of tests to identify the parameters of creep laws and the accuracy of the alignment between the load application and the sample's axis, specially in the case of tension creep, since bending moments can lead to premature failure and provide inaccurate results. Since refractories are highly sensitive to tension loads, this test is more difficult to control.

More details about tension and compression creep tests are given in Chapter II, that is dedicated to their application to the alumina-spinel material.

I.2.2 Brazilian test

Traditionally, the Brazilian test has been applied to study the tensile strength of concretes and geomaterials, as a replacement to direct tensile tests. As pointed by several studies, the results of a Brazilian test to calculate the tensile strength of a given material is only valid if the crack initiation is at the center of the sample, and not at the stress concentrations present at the contact points (Darvell, 1990; Fairhurst, 1964; García et al., 2017). Nevertheless, those studies have shown this is not always the case.

One alternative to the classical Brazilian test consists in the use of flattened disks or cylinders, where the parts of the sample in contact with the jaws form two planes, instead of two lines (H. Lin et al., 2015; H. Lin et al., 2016; Q.-Z. Wang & Xing, 1999; Q. Wang et al., 2004). Figure I.6 shows a comparison between the traditional and the flattened samples.

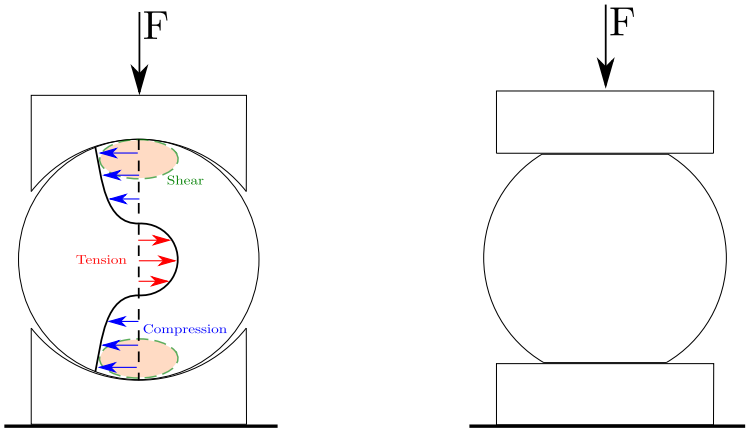

Figure I.6: Brazilian test geometry. (a) Classic. (b) Flattened

For the applications in the current work, the position of the initiation of the crack is not important, since no fracture is expected during the test. However, to guarantee an easier convergence on the finite element calculations during the identifications procedure, smooth boundary conditions are beneficial.

The problem of determining the stress distribution in the simplest case, where a concentrated load F is assumed to be applied at a sample of diameter D and thickness e, and the sample is considered to remain linear elastic until the failure, has been solved many years ago (Muskhelishvili, 1977; Timoshenko & Goodier, 1951), and the equations are summarized by Fahad (1996) as:

$$\sigma_x = \frac{2F}{\pi F e} - \frac{2P}{\pi e}\left\{\frac{x^2(R-y)}{[x^2+(R-y)^2]^2} + \frac{x^2(R+y)}{[x^2+(R+y)^2]^2}\right\} \tag{I.1}$$

$$\sigma_y = \frac{-2F}{\pi De} - \frac{2F}{\pi e}\left\{\frac{(R-y)^3}{[x^2+(R-y)^2]^2} + \frac{x^2(R+y)^3}{[x^2+(R+y)^2]^2}\right\} \tag{I.2}$$

$$\tau_{xy} = \frac{2F}{\pi e}\left\{\frac{x(R-y)^2}{[x^2+(R-y)^2]^2} - \frac{x(R+y)^2}{[x^2+(R+y)^2]^2}\right\} \tag{I.3}$$

Although these equations can't be accurately applied to predict the tensile strength of materials presenting irreversible deformations (Procopio et al., 2003), such as refractories at high temperatures, they can be used as a reference to predict the maximum load that can be applied to the sample for a creep test.

Hild and Roux (2006) used a Digital Image Correlation (DIC) technique to obtain the full strain field of a polycarbonate material under Brazilian testing conditions. Stirling et al. (2013) used a 3D DIC technique to compare the strain fields generated in a Brazilian test sample when using the standards proposed by ASTM (American Society for Testing and Materials), ISRM (International Society for Rock Mechanics and Rock Engineering) and the flattened Brazilian test according to Q.-Z. Wang and Xing (1999) on a sandstone material. The authors concluded that the flattened sample provided more homogeneous strain distributions, with the crack initiating at the center position in most of the tests. It should be added that sample's preparation for the flattened test is more complex, and requires specialized machinery to guarantee the parallelism between the surfaces, as well as that they are diametrically opposed.

The application of Brazilian tests to refractory materials is still limited, specially regarding the characterization of creep behavior. Belrhiti et al. (2017) used this test in association to a DIC technique to characterize the mechanical behavior of magnesia hercynite refractories used in cement rotary kilns, estimating the elastic modulus, Poisson's ratio and fracture energy at room temperature. (Gazeau et al., 2015) used the Brazilian test associated with the integrated DIC technique to identify the Young's modulus and the tensile strength of plane membranes at temperatures up to 900 °C. These two applications demonstrate the potential of this method to provide various information using a single experimental setup, what can result in the reduction of the required number of tests to characterize a material. This is specially important considering the cost and time demand of high temperature tests.

I.2.3 Four-point bending test

Four-point bending is a classical mechanical test used in several different types of applications, and is widely used to replace tension tests for brittle and quasi-brittle materials. As highlighted by Baxendale (2004), in the refractories field, ambient temperature bending strength is used as

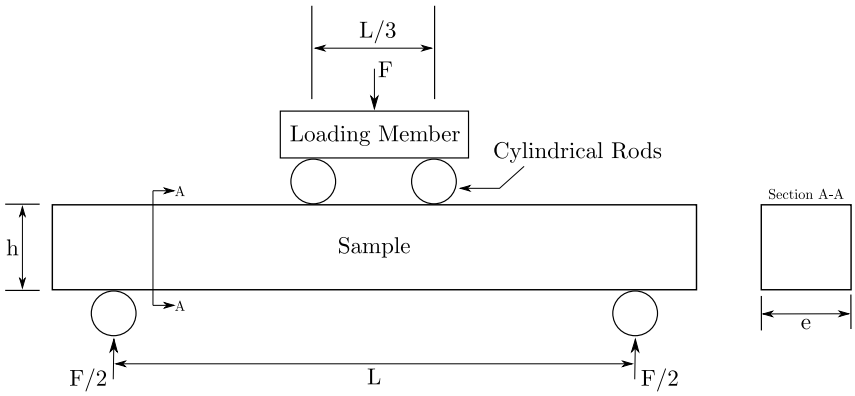

Figure I.7: Four-point bending test - Schematic representation.

a quality control parameter, while high temperature bending strength is used qualitatively to determine the suitability of a material to a given application.

Such as the Brazilian test, standards also exist for bending tests (ASTM-C1161, 2013), considering elastic behavior, although there is no specific standard for the use of four-point bending in the determination of creep parameters of refractories.

In this test, when the upper cylindrical rods are separated by a distance $L/3$, the maximum stress is located at the symmetry line at the center of the sample (Figure I.7), and is calculated as:

$$\sigma = \frac{FL}{eh^2} \tag{I.4}$$

where F is the applied force, L is the distance between the two lower supports, e is the thickness and h is the height of the sample. As in the Brazilian test, Equation I.4 can't be used to accurately predict the maximum stress in the sample for a refractory at high temperature, since the material is asymmetric, but it provides a reasonable initial estimation of the maximum force to be applied to avoid the premature cracking of the material.

Figure I.8a shows the stress distribution in direction x at the center line of a sample with $L = 120$ mm, $t = h = 30$ mm and $F = 60$ N. In this case, Equation I.4 predicts a maximum value of $\sigma_x = 0.266$ MPa, that corresponds exactly with the simulated value. Figure I.8b shows the full field distribution of σ_x.

The interest to use bending tests to study the creep behavior of ceramic materials dates from many years. In a simplified empirical study, (Rosenfield et al., 1985) used this kind of tests to show the importance of the consideration of tension-compression asymmetry in the analysis of ceramic structures. Abbé et al. (1989) used bending tests to calculate tension and compression creep parameters of $SiC - SiC$ composites. Lee (1996) used four-point bending tests to estimate the tensile creep rate of ceramics, with the simplification assumption that the sample only creeps

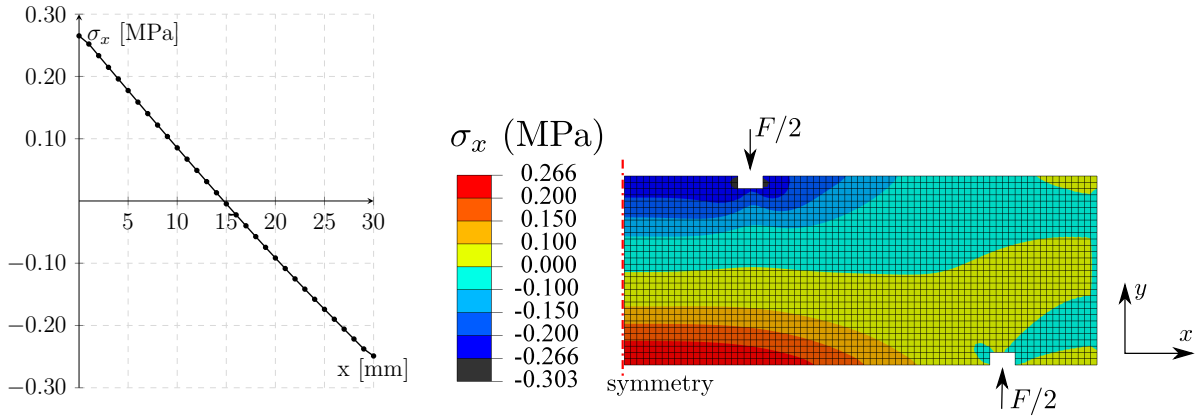

(a) (b)

Figure I.8: Four-point bending. (a) σ_x in the symmetry line. (b) Distribution of σ_x in the sample.

in tension, which allows the formulation of an analytical expression. Lim et al. (1997) simulated four-points bending test using the finite element method to validate an asymmetric creep model applied to ceramics.

Full field measurements, especially DIC techniques, have more recently been applied to analyze the stress and strain fields of four-points bending tests. Leplay et al. (2010) identified the position of the neutral line in an asymmetric ceramic material using DIC at room temperature, while Leplay et al. (2012) studied the same material for temperatures up to 900 °C. Leplay et al. (2015) analysed the asymmetric creep of an industrial zircon ceramics at 1350 °C using a similar methodology.

Nazaret et al. (2006) compared the values of Young's modules calculated using tensile, compressive and bending tests for refractory castables. Dusserre et al. (2013) evaluated the asymmetry ratio of fiber reinforced refractory castables at 1200 °C using four-point bending and analyzing the residual inelastic strain field, and Dusserre et al. (2016) calibrated a Drucker-Prager creep law using the same experiments.

Compared to Brazilian tests, one disadvantage of the four points bending test is the restricted range of stresses to which the sample is exposed, since the maximum force that can be applied is governed by the tensile strength of the material. As shown in Figure I.8, the order of magnitude of the tension and compression stresses is the same in this test, which does not correspond to the situation observed on real applications of refractories.

I.3 Inverse analysis applied to parameters identification

Groetsch (1999) defines three basic types of problems. In the direct problems (Figure I.9a), also known as forward problems (Tarantola, 2005), the input parameters x and the process K are known. In other words, the cause and the model that describes a given phenomena are known, but not the effect.

The inverse problems can be defined as the ones where the effect and the model are known, but not the cause (Figure I.9b) or the ones where the cause and the effect are known, but not the model (Figure I.9c).

Another type of problem, not mentioned by Groetsch (1999), can still be defined, where neither the cause nor the model are known, but only the effect (Figure I.9d). This is the type of problem studied in this work, in the context of parameters identification using DIC techniques, since a model is initially supposed to represent the behavior of the material, but needs to be validated.

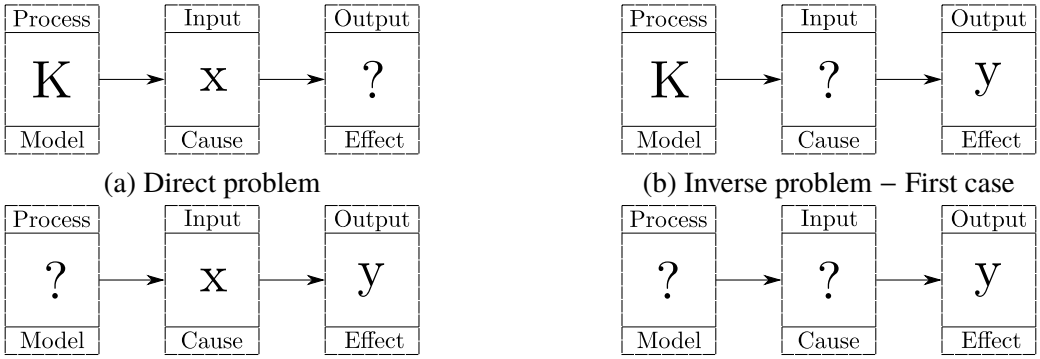

(a) Direct problem

(b) Inverse problem – First case

(c) Inverse problem – Second case

(d) Inverse problem – Third case

Figure I.9: Direct vs Inverse problems. Adapted from Groetsch (1999)

Inverse identification techniques are interesting in the context of refractories testing, since they allow for the characterization of thermo-mechanical behavior that would otherwise be more difficult or more time consuming using traditional techniques. This is due to the fact that, when inverse techniques are used, more complex loading conditions can be applied to the sample, consequently allowing for the verification of more convoluted theoretical assumptions, such as the laws governing the asymmetric creep of the material under multi-dimensional stress conditions.

Formally, direct and inverse problems are defined as (Kirsch, 2011; Mahnken, 2017):

Definition (Direct Problem)**.** Find $y(x, \theta) \in \Upsilon$ such that $K(x, \theta) = y$ for given $x \in \chi$ and $\theta \in \Theta$

Definition (Inverse Problem)**.** Find $\theta^* = \theta(\overline{d}) \in \Theta$ such that $D(y(\theta)) = \overline{d}$ and $K(x, \theta) = y(\theta)$ for given $x \in \chi$ and $\overline{d} \in D$

where χ is the space of the control (input) variables x, Υ is the space of the state (output) variables y, $\Theta \subset \mathbb{R}^{n_p}$ is the space of the admissible parameters θ, being n_p the number of material parameters, $D \subset \mathbb{R}^{n_d}$ is the space of experimental data $\overline{d}$, being n_d the number of experimental data. Generally, to enforce the uniqueness of the solution, it is required that $n_d \geq n_p$.

The solution of inverse problems can be obtained following a systematic mechanistic approach, that involves (Mahnken & Stein, 1996a):

1. Execution of standard, normally uniaxial, ideal tests.
2. Distinguish each of the physical effects separately on the experimental data.
3. Make some *ad hoc* assumptions to simplify the identification.
4. Evaluate the parameters sequentially, i.e., for a given test, fix some of the parameters and identify the remaining, mostly using simplified curve fitting techniques; later, fix the previously identified ones and identify others; proceed until all parameters are identified.

One example of application of this approach to identify the parameters of viscoplastic constitutive models can be seen at Senseny and Fossum (1995). The main disadvantages of this approach are that ideal test conditions can be difficult to reproduce in the laboratory, the *ad hoc* assumptions may oversimplify the problem and, mainly, the parameters values obtained can be dependent on the order which they are evaluated (Mahnken & Stein, 1996a).

A more robust approach consists in treating the identification as a mathematical optimization problem, evaluating all parameters at the same time, as explained in the next sections.

I.3.1 Problem well-posedness

One important aspect in the solution of mathematical problems, specially in the case of inverse problems, is that of *well-posedness*. Kirsch (2011), Moura Neto and da Silva Neto (2013) describe the conditions for a problem to be properly posed, also known as Hadamard conditions, after the French mathematician Jacques Hadamard:

1. *Existence*: For every $y \in \Upsilon$, there is (at least one) $x \in \chi$ such that $K(x, \theta) = y$
2. *Uniqueness*: For every $y \in \Upsilon$ there, is at most one $x \in \chi$ with $K(x, \theta) = y$
3. *Stability*: The solution of the problem depends continuously on the data and on the model

Due to the intrinsic error of experimental measures, condition 1 can never be satisfied for inverse problems, unless the notion of "solution" is extended to take into account approximations that better fit the data.

To satisfy condition 2, the problem needs to be framed correctly, in the sense that information about the control variables and boundary conditions need to be included in the data set. For example, Mahnken (2017) explains that, to determine the Young's modulus of a material from tensile tests, it is not possible to use only the displacement data obtained from the measurement device, but also the force boundary condition should be used, otherwise the differential equation describing the relation between the variables has an infinite number of solutions.

Condition 3 is a fundamental part of the study of inverse problems, and it requires the solution to present reasonable levels of stability regarding the input data, i.e., small variations in the input, that can be caused by measurement errors, should not cause large deviations on the output (in this case, the material parameters being estimated). To mitigate situations of low stability and render the problem "less ill-posed", regularization techniques are often used (Moura Neto & da Silva Neto, 2013).

Figure I.10 illustrates the issue of lack of stability for a one-dimensional case. In the ideal case, the model's output $f(\theta)$ has a reasonably sharp dependency regarding the input θ, being considered stable, i.e., variations $\delta\theta$ around the solution θ^* lead to considerable variations of the error ($\delta f_s = f_s(\theta') - f_s(\theta^*) > 0$).

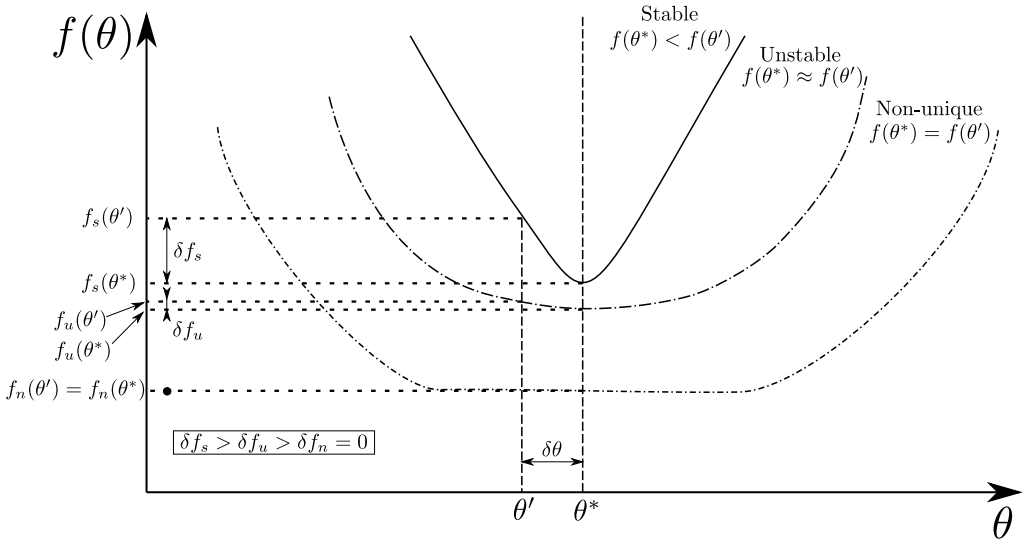

Figure I.10: Representation of different inverse problems regarding their stability. Adapted from Mahnken (2017).

The problem is considered unstable if the same variation $\delta\theta$ generates a small variation $\delta f_u \approx 0$ of the error, that is due to a more flat curve for the output parameter. It should be emphasized

that what is considered a "small variation" depends on the accuracy and on the resolution of the identification procedure.

Finally, when $f(\theta)$ presents a completely flat curve near the minimum, the solution of the problem is non-unique, leading to a situation where several values of θ generate the same error, making it impossible for the optimization algorithm to find the correct value.

Mahnken (2017) explains that the main reasons for instabilities and/or non-uniqueness are the excess of model parameters, that can become linear dependent (*overparametrization*), or the fact that the experiments used in the identification are not adequate, in the sense they do not activate all parameters of the model. This evidences the importance of pre-studies on the model before actual identification runs are tried, which involves a deep understanding of the mathematical constitutive model and a sensitivity analysis to study the influence of each of the parameters that need to be identified.

I.3.2 General steps of an inverse analysis

The inverse analysis applied to parameters identification is a complex task, and therefore should always follow a systematically defined procedure. Considering the material's constitutive model is already defined, the following general steps can be used as a base (Buljak, 2012):

1. Selection of an experimental procedure that is capable to reproduce the type of loading expected to be imposed over the material during its working life (Section I.3.2.1).
2. Definition of an analytic or numerical model that can represent the experimental procedure (for example, a finite element's model), called by Buljak (2012) the "numerical counterpart" of the experimental system (Section I.3.2.2).
3. Definition of a residual or discrepancy function that measures the difference between the experimental observation and the calculations using the numerical counterpart (Section I.3.2.3).
4. Definition of the cost function, that provides a scalar measure of the overall error based on the residuals (Section I.3.2.4).
5. Sensitivity analysis of the experimental procedure and of the error function regarding the material parameters (Section I.3.2.5).
6. Minimization of the error function using an optimization algorithm (Section I.3.3).

The next sections explain each of these steps. Due to their importance to this work, optimization algorithms are discussed in more details in Section I.3.3.

I.3.2.1 Selection of the experimental procedure

While in direct parameters' identification the goal is to perform experiments with simple, preferably uniform, load paths, such as one-dimensional tension and compression, inverse analysis can benefit from more complex stress distributions over the sample to activate various physical effects at the same time, or to extract more information from otherwise under-explored traditional tests, avoiding large experimental campaigns. Examples of experiments already used for this end include bi-dimensional loading of cruciform shaped samples (Bertin, Hild, Roux, et al., 2016; Prates et al., 2014; Réthoré, 2010), one-dimensional traction of a perforated plate (Denys et al., 2016; Zhang et al., 2018), tensile bar with two circular notches (A. P. Ruybalid et al., 2016), compact tension specimen with a notch (Mahnken & Stein, 1996b), thermal loading (Archer et al., 2020), Brazilian disk tests (Gazeau et al., 2015; Hild & Roux, 2006), bending tests (Belrhiti et al., 2012; Leplay et al., 2010, 2012), tension-torsion cyclic test (Maier et al., 2005), wedge-splitting tests (Vargas et al., 2016, 2018), among others. For more examples of heterogeneous stress fields already used in inverse identifications, see Pagnacco et al. (2013).

It is considered to be a good practice, prior to the experimental phase, to search for the optimal configuration for the specimen's shape and for the experimental setup as a role, in order to extract as much information as possible from the often expensive and time consuming tests. This is important to mimic the actual load paths that arise during the material's lifetime in operation and to increase the signal-to-noise ratio of the output variable (Bertin, Hild, & Roux, 2016; Prates et al., 2014).

This practice is intimately connected with the sensitivity analyzes described in Section I.3.2.5, as they work as a mean to quantify the influence of each model parameter, including the geometry, the boundary conditions and the constitutive law, in the final output. To this end, forward and inverse analysis of the experimental setup using virtual tests, where the goal is to evaluate how the model behaves under controlled conditions created in a digital environment, are a common practice (see, for example, Gazeau et al. (2015), Mahnken and Stein (1996b), Mathieu et al. (2015), Mathieu et al. (2013), A. P. Ruybalid et al. (2016), A. Ruybalid et al. (2019)).

I.3.2.2 Model counterpart

The model counterpart is the mathematical representation of the physical test, that is used to estimate the values of the control variable given a set of input parameters. Ideally, it needs to be fast, accurate and robust.

Although in the context of structural analysis the finite element method is by far the most used one (see, for example, Pagnacco et al. (2013), Springmann and Kuna (2005)), applications can also be found using the eXtended Finite Element Method (X-FEM) (Roux et al., 2009), the Boundary

Element Method (Ferreira, 2010; Stavroulakis et al., 2005), the Discrete Element Method (Chen et al., 2020) and analytical closed form solutions, when they are available (Gazeau et al., 2015; Hamam et al., 2007; Mathieu et al., 2013). Other analytical or computational models are used depending on the physics of the problem to be solved (Anderssen, 1999; Hohage et al., 2007).

The main difficulty regarding the model definition is the correct application of boundary conditions, since it was already demonstrated that, even for the most simple loading conditions, such as uniaxial tension or compression, the experiment can rarely, if ever, be set to correspond to the idealized assumptions of load alignment and contact homogeneity between the sample and the testing machine (de Melo et al., 2020; Réthoré, 2010)

I.3.2.3 Residuals function

The next step in the optimization procedure is related to the definition of the residuals, i.e., the calculation of the difference between the experimental and the numerical values of the output variables. Considering an output variable $\mathbf{y} = f(K, \underline{\theta})$ that depends on model K and on the material properties $\underline{\theta}$, the absolute residual of the i^{th} experiment and the j^{th} experimental point is calculated as (Prates et al., 2016):

$$r_{ij}(\underline{\theta}) = \mathbf{y}_{ij}^{Num} - \mathbf{y}_{ij}^{Exp} \tag{I.5}$$

where Num and Exp denote the numerical and experimental values, respectively. It should be noticed that the output variable $\mathbf{y}$ can be chosen according to the availability of testing procedures and to the needs of the model. It can take values of force, stress, strain, displacements, pixel values in a picture, etc. The bold symbol $\mathbf{y}$ indicates this is a tensor of any given order. For example, $\mathbf{y}_{ij}$ will take a scalar value if it is a point in a force-displacement curve, and Equation I.5 will correspond to a simple arithmetic operation. On the other hand, if the output of the model is a set of pixel values distributed in a matrix form to represent an image, or a two-dimensional full displacements field, the residual needs to be summed over the two dimensions after the subtraction represented in Equation I.5, so that r_{ij} assumes a scalar value.

When values with different orders of magnitude and/or measurement units need to be used in the same cost function, relative residuals are more suitable to represent the differences between experiments and simulations (Prates et al., 2016), and Equation I.5 becomes:

$$r_{ij}(\underline{\theta}) = \frac{\mathbf{y}_{ij}^{Num} - \mathbf{y}_{ij}^{Exp}}{\mathbf{y}_{ij}^{Exp}} \tag{I.6}$$

I.3.2.4 Cost function

The cost function, also known as the error or objective function, is at the core of the inverse analysis procedure, since it transforms the residuals vector into a scalar value that will ultimately be used to describe the fitness of a numerical calculation regarding the experimental data. Therefore, the choice of this function can be crucial to guarantee the stability of the problem, and even the success of the identification.

Cao and Lin (2008) define the properties of an ideal cost function as:

- For a single curve, all experimental data points should be considered in the optimization and have an equal opportunity to be optimized, considering that errors in the experimental data have been eliminated.
- If multiple experimental curves are available, all of them should have the same opportunity to be optimized.
- Different sub-objectives should have an equal opportunity to be optimized, independently of their units and/or number of experimental curves.
- Weighting factors shouldn't be chosen manually.

Among the many representations of the cost function available (Bard, 1970), the least-squares technique is one of the most used ones. Combining the definitions provided by Bard (1970), Mahnken and Stein (1996a), Prates et al. (2016), it is possible to define the following general form for the least-squares approximation:

$$\phi(\underline{\theta}) = \frac{1}{m}\sum_{i=1}^{m}\psi_i\left(\frac{1}{2n_i}\sum_{j=1}^{n_i}\omega_{ij}[r_{ij}(\underline{\theta})]^2\right) \rightarrow \min_{\underline{\theta}\in\mathbb{R}^p} \tag{I.7}$$

where the superscripts n_i and m represent the number of experimental points for a given experiment and the number of experiments, respectively, and p is the number of material parameters. The parameters ψ_i are the weights applied to each experiment and ω_{ij} are the weights applied to each point of each experiment. The division by m and n_i normalizes the expression for the error, contributing to enforce points 1 to 3 defined above. Equation I.7 can be written in terms of a weighted euclidean norm as:

$$\phi(\underline{\theta}) = \frac{1}{m}\sum_{i=1}^{m}\psi_i\left(\frac{1}{2n_i}\|\underline{r}_i(\underline{\theta})\|^2_{\Omega_2}\right) \rightarrow \min_{\underline{\theta}\in\mathbb{R}^p} \tag{I.8}$$

being

$$\|\underline{r}_i(\underline{\theta})\|^2_{\Omega_2} = \underline{r}_i^T \, \underline{\underline{\Omega}} \, \underline{r}_i \tag{I.9}$$

where $\underline{\underline{\Omega}} \in \mathbb{R}^p \times \mathbb{R}^p$ can be a diagonal matrix of the weights or the inverse of the covariance matrix when each experimental data has a standard deviation associated to it (Buljak, 2012).

The use of a least-squares functional with an optimization strategy can already contribute to turn the originally ill-posed problem into a well-posed one, since the discretization is a form of regularization (Kirsch, 2011). But, to avoid instabilities during the solution, the cost function can be regularized more, taking the following form in the most general case:

$$\phi(\underline{\theta}) = \frac{1}{m} \sum_{i=1}^{m} \psi_i \left(\frac{1}{2n_i} \left\| \underline{\underline{B_\delta}} \, \underline{r}_i(\underline{\theta}) \right\|^2_{\Omega_2} + \frac{\gamma}{2} \left\| \underline{\underline{B_\mu}} (\underline{\theta} - \overline{\underline{\theta}}) \right\|^2_2 \right) \rightarrow \min_{\underline{\theta} \in \mathbb{R}^p} \tag{I.10}$$

where $\underline{\underline{B_\delta}} \in \mathbb{R}^n \times \mathbb{R}^n$, $\underline{\underline{B_\mu}} \in \mathbb{R}^p \times \mathbb{R}^p$, $\gamma \in \mathbb{R}^+$ and $\overline{\theta} \in \mathbb{R}^p$ are regularization parameters.

I.3.2.5 Sensitivity analysis

Saltelli et al. (2019) make a distinction between Uncertainty Analysis (UA) and Sensitivity Analysis (SA), UA being the characterization of the uncertainty in a model prediction, and SA being the definition of how much each of the input parameters contribute to this uncertainty. In this work this distinction won't be made, and SA will be assumed as the study of how much the variation of a given input parameter (and not necessarily its uncertainty) affects the output of the model. It should be noticed that everything that can change during the analysis is considered to be an input, including the mathematical model (Saltelli, 2008).

Before an inverse identification analysis, it is important to perform a sensitivity analysis to evaluate if the experimental procedure is sensitive to all variables to be identified. From another point of view, this allows for the elimination of unimportant variables, that have no effect on the final outcome of the calculations, and that can increase the run time of the optimization algorithm.

I.3.3 Optimization algorithms

The most fundamental part of an inverse identification software is the choice of the optimization algorithm, since it defines how well the mathematical model will fit the data and how long this is going to take. There are many different classification frameworks for optimization algo-

rithms, depending on the context, and Figure I.11 shows a general overview of such algorithms (Sivanandam & Deepa, 2007). The models described in this work are highlighted in blue.

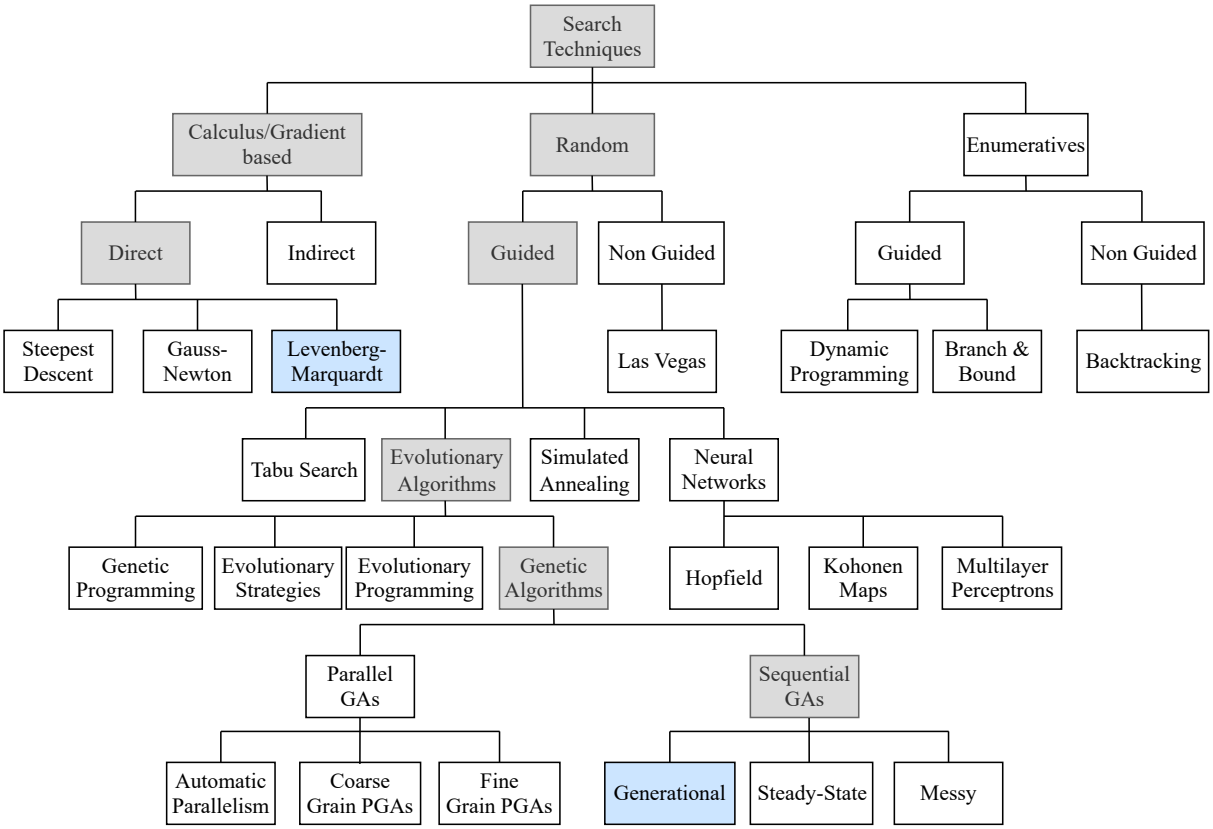

Figure I.11: Overview of search techniques. Adapted from Sivanandam and Deepa (2007)

Chaparro et al. (2008) divides the algorithms used in inverse identification procedures in three groups, being derivative-free search algorithms, gradient-based algorithms and evolutionary algorithms.

Derivative-free algorithms, as their name implies, do not require the calculation of derivatives, what make them simpler. However, these methods can't avoid converging to local minima, and are dependent on the user inputs. Besides, their convergence takes a considerable amount of time, since many evaluations of the underlying model need to be done.

Gradient-based algorithms (Section I.3.3.1), also called calculus based (Sivanandam & Deepa, 2007), make use of the derivatives of the model function to improve convergence time, by looking for the direction of faster decrease. Nevertheless, when second derivatives need to be calculated, the time gains are not expressive. These methods are extensively used in inverse identification procedures, but are also prone to local minima, specially in the case where the error function do not vary smoothly with the input parameters or is unstable (Section I.3.1). This problem can be mitigated by having a good intuitive first guess for the material parameters given by a specialist,

and by initializing the computations under different points on the variable's domain (Mahnken et al., 1998), but it still requires considerable previous knowledge about problem being solved.

Evolutionary algorithms are population-based, and make use of "genetic" operators, such as reproduction, mutation, cross-over, etc, to improve the quality of the population over the generations. These methods are generally more robust, in the sense they have a better chance to converge to the global minima, since at every generation points outside the zone of influence of the current best solution are also simulated. As a disadvantage, evolutionary algorithms are sub-optimal, i.e., they do not necessarily converge to the absolute minimum; also there is no clear stopping criteria, and the run time can be large. The most popular type of genetic algorithms are the so called Genetic Algorithms (Section I.3.3.2). Genetic algorithms are also classified, together with neural networks and filtering techniques, as a soft-computing method (Stavroulakis, 2001).

I.3.3.1 Gradient based optimization methods

Gradient based methods are iterative in nature, and they are so called because they require the calculation of the gradient $\underline{q}$, which is the direction of highest variation of the function. This is represented mathematically by

$$\underline{\theta}^{i+1} = \underline{\theta}^{i} + \alpha^{i} \underline{\underline{R}}^{i} \underline{q}^{i} \tag{I.11}$$

where $\underline{\theta}$ is the vector containing the unknowns, $\underline{q}$ is the gradient vector of the error function at the point $\underline{\theta} = \underline{\theta}^{i}$, i is the step number, α is the step size and $\underline{\underline{R}}$ is a matrix. What differs one method from the others is the choice of α and $\underline{\underline{R}}$.

Three conditions should be observed when choosing α and $\underline{\underline{R}}$ (Bard, 1970):

- $\dfrac{\underline{\underline{R}}^{i}}{\alpha^{i}}$ should be positive definite, which guarantees that, if $\underline{q} \neq 0$, then for a sufficiently small

$$\phi(\underline{\theta}^{i+1}) > \phi(\underline{\theta}^{i}) \tag{I.12}$$

- $\underline{\underline{R}}^{i}$ should be some approximation of $(-\underline{\underline{H}}^{-1})^{i}$, where $\underline{\underline{H}}^{i}$ is the hessian matrix of ϕ at $\underline{\theta} = \underline{\theta}^{i}$. The hessian is a square matrix of second order partial derivatives.
- α^{i} should be chosen so that Equation I.12 holds.

Some of the most popular gradient-based methods in the literature are the Steepest Descent method, the Newton-Raphson method, the Gauss-Newton method and the Levenberg-Marquardt

method. The method proposed by Marquardt (1963) is based on the fact that, if a matrix $\underline{\underline{P}}$ is a positive definite matrix, then $\underline{\underline{A}} + \lambda \underline{\underline{P}}$ also is positive definite for sufficiently large λ for all $\underline{\underline{A}}$. The variation δ of the parameters to be optimized is given by the equation:

$$(\underline{\underline{J}}^{T^i} \underline{\underline{J}}^i + \lambda^i \underline{\underline{I}}) \underline{\delta}^{i+1} = -\underline{\underline{J}}^{T^i} \underline{r}^i \tag{I.13}$$

where $\underline{\underline{J}}$ is the jacobian matrix and $\underline{r}$ is the residuals vector. The identity matrix $\underline{\underline{I}}$ was chosen to be the reference positive definite matrix.

This method has the advantage to be an interpolation between the Steepest Descent (SD) method and the Gauss-Newton (GN) method. The SD method is not efficient close to the minimum, since it has a zig-zag fashion convergence, while the GN method is not reliable far from the minimum, since a simplification of the hessian matrix has been made considering the residuals to be sufficiently small. Therefore, an interesting strategy is to use the first far from the minimum and the later close to the minimum, which is achieved with the Levenberg-Marquardt method (Marquardt, 1963).

I.3.3.2 Genetic algorithms

Genetic algorithms (GAs) are a family of optimization methods inspired by the biological evolution. Those methods aim to mimic nature's phenomena to select the individuals that better fit a determined criteria, defined by a cost function (Mitchell, 1999).

Due to their specific nature, GAs have a particular terminology. Some of the most common terms that need to be known to understand GAs are (Sivanandam & Deepa, 2007):

- **Individual**: A point in the variables' space. For example, for a problem where the value of a function $f = f(x, y)$ needs to be minimized, a point $p = (x, y)$ in the problem domain is a individual.
- **Genes**: The individual parts, or representation of the variables, that form an individual.
- **Population**: A collection of individuals. The population evolves over time to improve the fitness of the solution.

Genetic algorithms are different from gradient-based algorithms in the sense that they (Toropov & Yoshida, 2005):

1. Work with a population of points instead of a single point, increasing the chance to find the global minimum.

2. Don't depend on the derivative of the cost function.

3. Are probabilistic, not deterministic, what make them highly explorative.

Another advantage of genetic algorithms over gradient based algorithms is the fact they can largely benefit from parallelized computational structures. Since the members of a given population are completely independent from each other, they can all be evaluated at the same time, while for gradient methods each new iteration depends on the previous ones, so they need to be computed sequentially (Sivanandam & Deepa, 2007).

Genetic algorithms are fundamentally simple, what normally results in computational implementations easy to understand and modify. Figure I.12 shows a basic GA algorithm.

The first step consists in the initialization of the population, i.e., the definition of the first individuals' variables. Several methods are available to perform this step, such as a random initialization, a latin hypercube sampling or a custom initialization, where initial values are pre-defined by the user based on a specific criterion.

Once the population is initialized, the values of the fitness functions are evaluated for each individual. For example, to identify the mechanical properties of a material, an analytical or numerical computations can be compared to experimental results, where the maximum fit would be obtained when both results are identical.

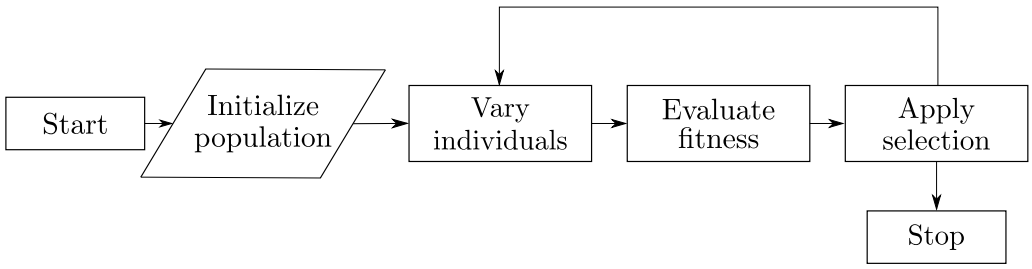

Figure I.12: Generic evolutionary algorithm. Adapted from Sivanandam and Deepa (2007)

Next step consists of the selection, that is one of the three basic operators of genetic algorithms (Coley, 1999) and defined that, at each generation, some individuals of the population are excluded, to allow new ones to be generated, given that the population size is constant. Two of the most popular selection methods are the roulette wheel, where the probability of selection of an individual is proportional to its fitness value, and the tournament selection, where the best individuals are selected (Poloni & Pediroda, 2000).

If the stopping criteria was not yet fulfilled, the algorithm varies the individuals according to two operators:

- **Crossover (recombination)**: is the analogous to the reproduction on biological systems, i.e., individuals exchange genetic information to form new ones.
- **Mutation**: random change in the values of genes of certain individuals to continue the exploration of the variables' space.

One important operator in GAs is selection elitism, where a defined number of best individuals is kept unchanged to the following generations. The goal of elitism is to avoid to loose good fitting individuals through mutation or selection. Although elitism has been shown to be an efficient way to improve the algorithm's robustness, a limited percentage of the population should come from it, since it restricts the exploration capabilities of the algorithm, potentially leading to the convergence to a local minimum (Guariso & Sangiorgio, 2020).

I.4 Creep of refractories

As discussed in Section I.1, the thermo-mechanical behavior of refractory materials is highly dependent of their creep properties. Nevertheless, only in recent years this became a research topic in the refractories community, since the use of structural analysis methods themselves is a relatively new topic, although other mechanical aspects such as fracture (Gruber et al., 2007; Ribeiro & Rodrigues, 2010; Tschegg et al., 2009), thermal shock (Hein & Kuna, 2012; Tomba Martinez et al., 2008; Volkov-Husović et al., 1999) and thermochemical coupling (Merzouki et al., 2016) have received more attention. In other cases, simpler linear elastic models were used to build intuition about the in-field behavior of refractories (Jin et al., 2011), often associated with linear homogenization techniques to model large masonries (Gasser et al., 2000; Nguyen et al., 2009; Teixeira et al., 2017).

The creep behavior of ceramic materials can be split in three stages, as shown in Figure I.13. The first stage, called primary creep, presents a time-dependent strain rate which decreases with time. In the secondary creep stage, the strain rate is considered to be constant, and an approximate equilibrium between hardening and softening processes can be assumed (Naumenko & Altenbach, 2007). Finally, in the third creep stage, the strain rate increases with time until the failure of the material (Jin et al., 2014).

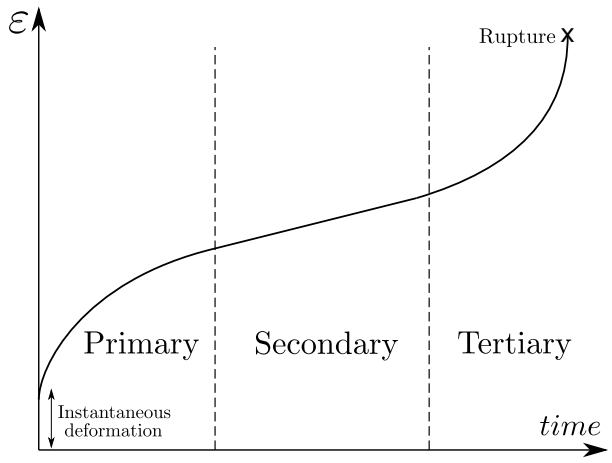

Figure I.13: Three stages of creep.

The creep models available in the literature are categorized into micro-mechanical and phenomenological models. Micro-mechanical models are used to evaluate what are the creep mechanisms taking place at a given material. The most common mechanisms that contribute for the creep of ceramics are grain boundary sliding, diffusion and dislocation motion (Hynes & Doremus, 2006). This methodology was applied to refractory materials by Martinez et al. (2012). The one-dimensional form of the most frequently used model for secondary creep strain rate equation in the context of micro-mechanical models is (Cannon & Langdon, 1988):

$$\dot{\varepsilon} = \frac{KDGb}{kT}\left(\frac{b}{d}\right)^{p}\left(\frac{\sigma}{G}\right)^{n} \tag{I.14}$$

where σ is the applied stress, K, p and n are material's constants, G is the shear modulus, b is the Burger's vector, k is the Boltzmann's constant, T is the temperature, D is the diffusion coefficient and d is the grain size.

Conversely, phenomenological models attempt to evaluate the effects of creep in a given material regardless of the possible mechanisms that could cause them. This normally results in simpler models with less parameters, at the cost of being less general. The most used phenomenological creep strain rate model is the Norton-Bailey's creep law. Its one-dimensional form is shown in Equation I.15:

$$\dot{\varepsilon}^{cr} = A\sigma^{n}(\varepsilon^{cr})^{m} \tag{I.15}$$

where ε^{cr} is the accumulated creep strain and A, n and m are temperature dependent material parameters. In this work, all the studied models are phenomenological and are described in details in Section I.4.1, using the thermodynamics framework as the theoretical base (Lemaître & Chaboche, 1990). For the sake of brevity, this framework will not be described in details.

I.4.1 Viscoplasticity models for primary and secondary creep

In the literature regarding the description of creep models, it is a common practice to begin the discussion by the secondary creep behavior, since it is simpler and has less material parameters. The same strategy is used in this work, in the following sections.

I.4.1.1 Secondary creep models

As explained in Section I.4, secondary creep, also known as perfect viscoplasticity, corresponds to the case where there is mutual exclusion between hardening and softening effects taking place at the material. Therefore, no internal variable is used in the description of the phenomenon, and the thermodynamic potential associated with the model can be written as (Lemaître & Chaboche, 1990):

$$\varphi^{*} = \Omega(\underline{\underline{\sigma}}) \tag{I.16}$$

Von Mises type creep model The Norton-Bailey's creep law have been extensively used to characterize refractory materials, due to its simplicity and good fitness to experimental results

(Jin et al., 2014; Samadi et al., 2020; Schachner et al., 2019; Sidi Mammar et al., 2016; Teixeira et al., 2020). To generalize Equation I.15 to three-dimensional description of creep, two changes are required. First, the uniaxial stress should be replaced by an equivalent stress; therefore, Equation I.16 becomes:

$$\Omega = \Omega(\sigma_{eq}) \tag{I.17}$$

Considering a von Mises equivalent stress:

$$\sigma_{eq} = \sqrt{3J_2} = \sqrt{\frac{3}{2}\underline{\underline{s}} : \underline{\underline{s}}} \tag{I.18}$$

where $\underline{\underline{s}}$ is the deviatoric component of the stress tensor. Second, a flow tensor should be defined. Again, considering the von Mises flow potential:

$$\underline{\underline{N}} = \frac{3}{2}\frac{\underline{\underline{s}}}{\sigma_{eq}} \tag{I.19}$$

Therefore, the three dimensional creep strain rate, known as Odqvist's law, is given by:

$$\underline{\underline{\dot{\varepsilon}}}^{cr} = \frac{3}{2}\frac{\underline{\underline{s}}}{\sigma_{eq}} A\sigma_{eq}^{n} \tag{I.20}$$

This model, sometimes referred to as classic creep law (Altenbach, 1999; Jin et al., 2015), is totally defined by the parameters A and n, i.e., by the definition of the one-dimensional creep law.

If an elastic region needs to be considered in the model, a simple modification in Equation I.20 can be done to take it into consideration:

$$\underline{\underline{\dot{\varepsilon}}}^{cr} = \frac{3}{2}\frac{\underline{\underline{s}}}{\sigma_{eq}} A \left\langle \sigma_{eq} - \sigma_y \right\rangle^{n} \tag{I.21}$$

where σ_y is the yield stress and $\langle \quad \rangle$ are the Macaulay brackets, used to denote that a function $f(x)$ equals zero if $x < 0$, and $f(x) = x$ otherwise.

It should be note that the same idea described in this section can be applied to other uniaxial laws other than the Norton's law. The choice of which law and that of the equivalent stress should be used depends on how accurately it fits the mechanical tests.

As can be seen in the equations, this model is not capable to describe the asymmetry between tensile and compressive creep. Section I.4.2 will provide different strategies to overcome this difficulty.

I.4.1.2 Primary Creep Model with Isotropic Hardening

As remarked by Esposito and Bonora (2011), in many applications the primary creep of materials can't be neglected, since a considerable part of the allowable design strain occurs in this stage. This is the case of the alumina-spinel material studied in this work, as it is evident by the creep curves presented in Section II.4.1.

To include primary creep effects in the calculations, hardening needs to be considered in the viscoplastic strain rate equation. In the case of isotropic hardening, the accumulated plastic strain, also called equivalent creep strain (Abaqus, 2018), is considered to be an internal variable (Lemaître & Chaboche, 1990). In general, the accumulated plastic strain rate is an invariant of the plastic strain rate tensor, and is calculated as:

$$\dot{p} = \sqrt{\frac{2}{3}\underline{\underline{\dot{\varepsilon}}}^{cr} : \underline{\underline{\dot{\varepsilon}}}^{cr}} \tag{I.22}$$

For the case of the von Mises type creep model previously described, the evolution law for the accumulated plastic strain becomes:

$$\dot{p} = A \left\langle \sigma_{eq} - \sigma_y \right\rangle^n \tag{I.23}$$

Equation I.21 can then be modified, resulting in:

$$\underline{\underline{\dot{\varepsilon}}}^{cr} = \frac{3}{2}\frac{\underline{\underline{s}}}{\sigma_{eq}} A \left\langle \sigma_{eq} - \sigma_y \right\rangle^n p^m \tag{I.24}$$

where m is a temperature dependent material property.

I.4.1.3 Primary creep model with kinematic hardening – Creep transients

The kinematic creep model was introduced by Malinin and Khadjinsky (1972) and is described in details by Naumenko and Altenbach (2007). The stress tensor can be divided into an active part $\underline{\underline{\overline{\sigma}}}$ and a translation part $\underline{\underline{\alpha}}$, also called back stress tensor, resulting in the equation:

$$\underline{\underline{\sigma}} = \underline{\underline{\overline{\sigma}}} + \underline{\underline{\alpha}} \tag{I.25}$$

As explained by Chaboche (2008), this allows the yielding surface to translate in the principal stresses space, as opposed to the increase of its radius promoted by isotropic hardening rules. As usual, the new stress tensors defined in Equation I.25 can be decomposed into hydrostatic and deviatoric parts, resulting in:

$$\begin{aligned}
\overline{\underline{\underline{\sigma}}} &= \frac{1}{3} tr\overline{\underline{\underline{\sigma}}}.\underline{\underline{I}} + \overline{\underline{\underline{s}}} \\
\underline{\underline{\alpha}} &= \frac{1}{3} tr\overline{\underline{\underline{\alpha}}}\underline{\underline{I}} + \underline{\underline{\beta}} \\
\underline{\underline{\sigma}} &= \frac{1}{3}(tr\overline{\underline{\underline{\sigma}}} + tr\overline{\underline{\underline{\alpha}}})\underline{\underline{I}} + \underline{\underline{s}} \\
\underline{\underline{s}} &= \overline{\underline{\underline{s}}} + \underline{\underline{\beta}}
\end{aligned} \tag{I.26}$$

The fundamental idea of this model is that the inelastic strain rate is calculated considering only the active part of the stress tensor. This makes the creep potential a function of the back stress, that is treated as an internal variable. The von Mises equivalent stress is therefore calculated as:

$$\overline{\sigma}_{eq} \equiv \sqrt{\frac{3}{2}(\underline{\underline{s}} - \underline{\underline{\beta}}) : (\underline{\underline{s}} - \underline{\underline{\beta}})} \tag{I.27}$$

To calculate the creep strain rate, the following set of equations needs to be integrated simultaneously:

$$\begin{aligned}
\dot{\underline{\underline{\varepsilon}}}^{cr} &= \frac{3}{2}\frac{\overline{\underline{\underline{s}}}}{\overline{\sigma}_{eq}} a\overline{\sigma}_{eq}^{n} \\
\dot{\underline{\underline{\beta}}} &= \frac{2}{3} b\dot{\underline{\underline{\varepsilon}}}^{cr} - c\alpha_{eq}^{n-1}\underline{\underline{\beta}} \\
\alpha_{eq} &\equiv \sqrt{\frac{3}{2}\underline{\underline{\beta}} : \underline{\underline{\beta}}}
\end{aligned} \tag{I.28}$$

where a, b and c are material properties.

Esposito and Bonora (2011) developed a transient creep model to be applied to Class M alloys, such as high chromium steel and nickel based super alloys. Their model is based in Orowan's equation, that relates the creep strain rate to the dislocations density ρ_m and the average dislocations velocity $\overline{v}_m$ during creep, represented by Equation I.29:

$$\dot{\varepsilon} = b\rho_m\overline{v}_m \tag{I.29}$$

where b is a material parameter. Their basic assumption is that during transient creep both parameters will vary with time, reaching a constant value at the steady state where the structural dynamic equilibrium is obtained, leading to

$$\dot{\varepsilon}_{ss} = b\rho_{ss}\overline{v}_{ss} \tag{I.30}$$

where ss stands for steady-state. The proposed creep strain rate is given by:

$$\frac{\dot{\varepsilon}}{\dot{\varepsilon}_{ss}} = \exp\left[\frac{\beta+1}{RT}\Omega\overline{\sigma}_{iss}\exp\left(-\frac{\varepsilon}{\varepsilon_0}\right)\right] \tag{I.31}$$

where β, $\dot{\varepsilon}_{ss}$, $\overline{\sigma}_{iss}$, Ω and ε_0 are material parameters. Although this model shows to be accurate for the applications described in the original paper, its elevated number of parameters and its close connection with the creep mechanisms of metals and alloys make it non-applicable to refractories, since the two types of materials have different microstructures and creep mechanisms.

I.4.1.4 Applications to refractory materials

Apart from a few exceptions that will be reported in later sections, the study of the creep behavior of refractories have been mainly based on symmetric models (Boussuge, 2001). This is probably due to the fact that commercial finite element codes don't present a large variety of asymmetric models, and until recently the characterization of the creep parameters under tension remained mostly unexplored, being addressed in more details by Sidi Mammar et al. (2016), although it continues to be a challenging task.

Only a few application of creep models to refractories are found in the literature, since most part of the publications in this area are focused on the identification of material parameters, without proceeding to the simulation of complex geometries and loading conditions. As an example, Jin et al. (2020) modeled the spalling of torpedo cars bricks using a simplified bidimensional model, considering the Norton-Bailey's law at the working lining of the equipment.

I.4.2 Asymmetric Creep Models

I.4.2.1 Model 1 – Abaqus (2018) Drucker-Prager Creep model

The software Abaqus (2018) provides a model to describe the asymmetric creep behavior using an equivalent stress calculation based on the traditional pressure-dependent Drucker-Prager model. This model can also be used to simulate the primary creep of materials.

In this model, the material's parameters A and n of Equation I.15 (or the equivalent parameters of other uniaxial creep laws that may be used) should be defined based on compression, tension or shear test, and the asymmetry is defined by an extra parameter β, equivalent to the angle of internal friction in the Drucker-Prager model (de Souza Neto et al., 2008).

For example, suppose that compression tests' results are available and the parameters of the creep law are identified, following the same identification procedure as in the case of classic creep. The Drucker-Prager Creep equivalent stress will then be:

$$\sigma^{cr} = \frac{\sigma_{eq} - p \tan\beta}{1 - \frac{1}{3}\tan\beta} \tag{I.32}$$

where p is the hydrostatic stress. As demonstrated by Dusserre et al. (2016), for a uniaxial compression stress, Equation I.32 reduces to:

$$\sigma^{cr} = -\sigma \tag{I.33}$$

while for a tensile uniaxial stress with the same absolute value it leads to:

$$\sigma^{cr} = \sigma \frac{1 + \frac{1}{3}\tan\beta}{1 - \frac{1}{3}\tan\beta} \tag{I.34}$$

Therefore, the equivalent stress is higher in tension than in compression, giving the asymmetric characteristic to the model. A direct consequence of this equivalent stress calculation is the difficulty to fit the material data from experiments.

Figure I.14 shows a representation of Drucker-Prager Creep yield surface on the p-q plane. The equivalent creep surface is defined to always have the same slope as the yield surface. Since it makes no physical sense to have negative equivalent stresses in the model, a "no creep" zone is created, where the stresses don't produce creep. This is considered to be a disadvantage, since, again, it gives less flexibility to the model.

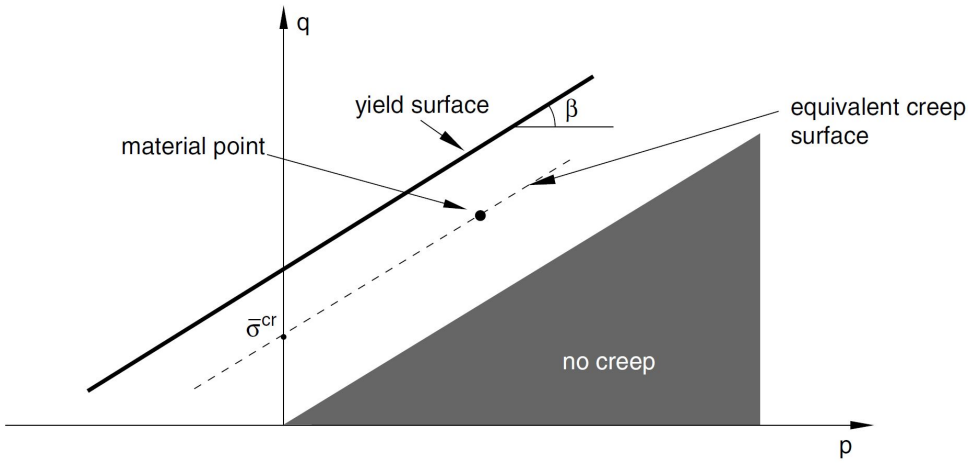

Figure I.14: Drucker-Prager Creep model yield surface. Adapted from Abaqus (2018)

Pressure-dependent models intrinsically generate volume expansion, since the derivative of the flow potential leads to a non-zero volumetric component, contrary to pressure-independent models that only present a deviatoric component (de Souza Neto et al., 2008). For the case of Drucker-Prager Creep model, the flow potential is hyperbolic and given by:

$$G = \sqrt{(\epsilon\sigma|_0 \tan\Psi)^2 + \sigma_{eq}^2} - p\tan\Psi \tag{I.35}$$

where ϵ is the eccentricity parameter, $\sigma|_0$ is the initial yield stress defined using the hardening properties of the model and Ψ is the dilatation angle. When $\Psi = \beta$, the flow is associated, but this often produces unrealistic volume expansion, so normally $\Psi < \beta$. For the case when $\Psi = 0$, the model doesn't present any dilatancy, and the flow potential is reduced to a von Mises type, therefore leading to a flow vector equivalent to the one presented in Equation I.19.

Jin et al. (2015) used the Drucker-Prager creep model to simulate the thermo-mechanical behavior of RH-snorkel refractories used in steel plants. The authors compared this model with a symmetric creep model in terms of the axial stresses and the joints opening due to excessive creep strain on the edge of the bricks, and concluded that new creep laws should be determined to describe the behavior of such materials.

Dusserre et al. (2016) studied the asymmetric primary creep behavior of a fiber reinforced refractory concrete using the Drucker-Prager creep model, identifying the material parameters by a bending test and an inverse analysis. The authors showed how the neutral line of the bending sample changes over time after creep strains are developed.

I.4.2.2 Model 2 (Altenbach, 2001)

The asymmetry in the material's response was approached by Altenbach (2001) using a creep strain rate formulation that depends on three linear independent invariants of the stress tensor, being:

$$\begin{aligned} I_1\left(\underline{\underline{\sigma}}\right) &= \underline{\underline{\sigma}} : \underline{\underline{I}} \\ I_2\left(\underline{\underline{\sigma}}\right) &= \underline{\underline{\sigma}} : \underline{\underline{\sigma}} \\ I_3\left(\underline{\underline{\sigma}}\right) &= \left(\underline{\underline{\sigma}} \cdot \underline{\underline{\sigma}}\right) : \underline{\underline{\sigma}} \end{aligned} \tag{I.36}$$

where $\underline{\underline{I}}$ denotes the unit tensor. One can easily see that a model depending on I_1 and I_3 is intrinsically dependent of the stress sign. These invariants can be combined to result in an equivalent stress of the form:

$$\sigma_{eq} = \tilde{\alpha}\sigma_1 + \tilde{\beta}\sigma_2 + \tilde{\gamma}\sigma_3 \tag{I.37}$$

with $\tilde{\alpha}$, $\tilde{\beta}$ and $\tilde{\gamma}$ being weights for the invariants and

$$\begin{aligned} \sigma_1 &= \mu_1 I_1 \\ \sigma_2^2 &= \mu_2 I_1^2 + \mu_3 I_2 \\ \sigma_3^3 &= \mu_4 I_1^3 + \mu_5 I_1 I_2 + \mu_6 I_3 \end{aligned} \tag{I.38}$$

where μ_1 to μ_6 are material parameters. Therefore, nine parameters need to be identified, unless the weights are considered to be equal to one, in which case six parameters are necessary.

The creep rate equation for this model is therefore given by:

$$\underline{\underline{\dot{\varepsilon}}}_{cr} = \dot{\varepsilon}_{eq}^{cr} \left[\mu_1 \underline{\underline{I}} + \frac{\mu_2 I_1 \underline{\underline{I}} + \mu_3 \underline{\underline{\sigma}}}{\sigma_2} + \frac{\left(\mu_4 I_1^2 + \frac{\mu_5}{3} I_2\right) \underline{\underline{I}} + \frac{2}{3}\mu_5 I_1 \underline{\underline{\sigma}} + \mu_6 \underline{\underline{\sigma}} \cdot \underline{\underline{\sigma}}}{\sigma_3^2} \right] \tag{I.39}$$

being $\dot{\varepsilon}_{eq}^{cr} = \dot{\varepsilon}_{eq}^{cr}\left(\sigma_{eq}\right)$ the uniaxial creep strain rate obtained from experiments. In the particular case where $\tilde{\alpha} = \tilde{\gamma} = 0$, Equation I.39 reduces to the classic creep equation.

Although this model is mathematically consistent, it presents the inconvenient to require a considerable number of experiments to determine the creep parameters, since tension and compression behaviors are coupled.

Altenbach (2001) suggests that, assuming a Norton-type creep law with a constant creep exponent with respect to the kind of loading, a possible experimental protocol would involve uniaxial tension, uniaxial compression, simple shear and hydrostatic pressure tests. Also, the weights need to be adjusted accordingly. For the case of refractories, that need to be characterized for several values of high temperature, this is a difficult task. As was explained in Section I.3, an inverse identification procedure can be more suitable to identify the material parameters, but the elevated number of unknown variables makes the optimization algorithm more difficult to converge.

I.4.2.3 Model 3 (Mahnken, 2003)

Mahnken (2003) proposed an asymmetric creep model that uses a scalar variable expressed in terms of the ratio of the second and third invariants of the deviatoric stress tensor, called stress

mode angle in the octahedral plane in the deviatoric stress space. In this work, the inelastic (creep) strain rate is decomposed into different parts, according to the following equation:

$$\underline{\underline{\dot{\varepsilon}}}^{cr} = \sum_{i=1}^{M} w_i \dot{\lambda}_i \underline{\underline{N}}_i \tag{I.40}$$

where $\dot{\lambda}_i$ and $\underline{\underline{N}}_i$ are the flow factor and flow tensor direction associated with each mode M, respectively, and $w_i = w_i(\underline{\underline{\sigma}})$ is a weighting function dependent on the stress and associated to each mode angle θ, which is calculated as:

$$\begin{aligned} \theta &= \frac{1}{3}\arccos(\xi) \\ \xi &= \frac{\sqrt{27}}{2}\frac{J_3}{J_2^{3/2}} \\ J_i &= \frac{1}{i}\underline{\underline{I}} : \underline{\underline{s}}^i, i = 2, 3 \end{aligned} \tag{I.41}$$

Equations for $\dot{\lambda}_i$ and $\underline{\underline{N}}_i$ are also provided by the author, but won't be reproduced here for the sake of brevity.

For the case where tension and compression tests are available, the author proposes the following weighting functions:

$$\begin{aligned} w_1(\theta) &= \frac{1}{2} + \frac{1}{2}\cos(3\theta) \\ w_2(\theta) &= \frac{1}{2} + \frac{1}{2}\cos(3\theta - \pi) \end{aligned} \tag{I.42}$$

In order to increase the accuracy of the model, more stress modes can be included in the calculation of the weights and consequently of the creep strain rate, but this requires other loading cases, such as a shear test, for example.

Mahnken (2003) proposes an identification procedure where the results of the different tests are used in a semi-independent way, together with an optimization algorithm, to make the identification of the material parameters.

I.4.2.4 Model 4 (Blond et al., 2005)

To account for the well-known asymmetric creep of refractories, Blond et al. (2005) extended the model proposed in Section I.4.1.1 using the split of the principal stress vectors into a positive and a negative parts to propose a secondary creep model, resulting in:

$$\underline{\underline{\sigma}} = \left\langle \underline{\underline{\sigma}} \right\rangle - \left\langle -\underline{\underline{\sigma}} \right\rangle \tag{I.43}$$

This split results in the definition of the model in terms of independent tension and compression parameters. In this sense, the two parts of the deviatoric stress tensor are given by:

$$\underline{\underline{s}}^{\pm} = \left\langle \pm\underline{\underline{\sigma}} \right\rangle - \frac{1}{3} Tr(\left\langle \pm\underline{\underline{\sigma}} \right\rangle) \underline{\underline{I}} \tag{I.44}$$

where the indexes ± indicate the positive and negative parts of the variables, respectively. The equivalent von Mises stresses are, then:

$$\sigma_{eq}^{\pm} = \sqrt{\frac{3}{2} \underline{\underline{s}}^{\pm} : \underline{\underline{s}}^{\pm}} \tag{I.45}$$

Resulting in a viscoplastic strain rate of the form:

$$\underline{\underline{\dot{\varepsilon}}}^{cr} = \frac{3}{2} \frac{\underline{\underline{s}}^{+}}{\sigma_{eq}} A^{+} \left\langle \sigma_{eq}^{+} - \sigma_{y}^{+} \right\rangle^{n^{+}} - \frac{3}{2} \frac{\underline{\underline{s}}^{-}}{\sigma_{eq}} A^{-} \left\langle \sigma_{eq}^{-} - \sigma_{y}^{-} \right\rangle^{n^{-}} \tag{I.46}$$

where $A^{\pm}$ and $n^{\pm}$ are material's constants in tension (+) and compression (−). As in the case of classic creep, Blond's model can also present a yield surface, but this isn't mandatory.

Figure I.15 shows a representation of Blond's model in the 2D principal stresses domain. In this case, the tensile yield stress is $\sigma_y^+ = 2$ MPa and the compressive yield stress is $\sigma_y^- = -8$ MPa. In the figure, the two stress states D and E marked as green triangles are inside the elastic region, therefore no creep is observed.

Point A in the figure shows a stress state in the second quadrant, with a compressive component in direction 1 and a tensile component in direction 2. Therefore, the stress split described by Equation I.43 results in other two stress states, shown as circular markers. As can be seen, the point (-5, 0) is in the elastic region, so no creep is expected for the compressive component. On the other hand, the point (0, 3) lays outside the elastic region, so the first term of the right hand side of Equation I.46 is activated, and creep in tension is observed.

Point B in the figure corresponds to the opposite situation, i.e., creep is activated in compression but not in tension. The stress state represented by Point C results in creep in both tension and compression.

From Figure I.15 is also evident that Blond's yield surface presents singularities in the points where it crosses axis 1 and 2, as well as in the corners present in the second and fourth quadrants.

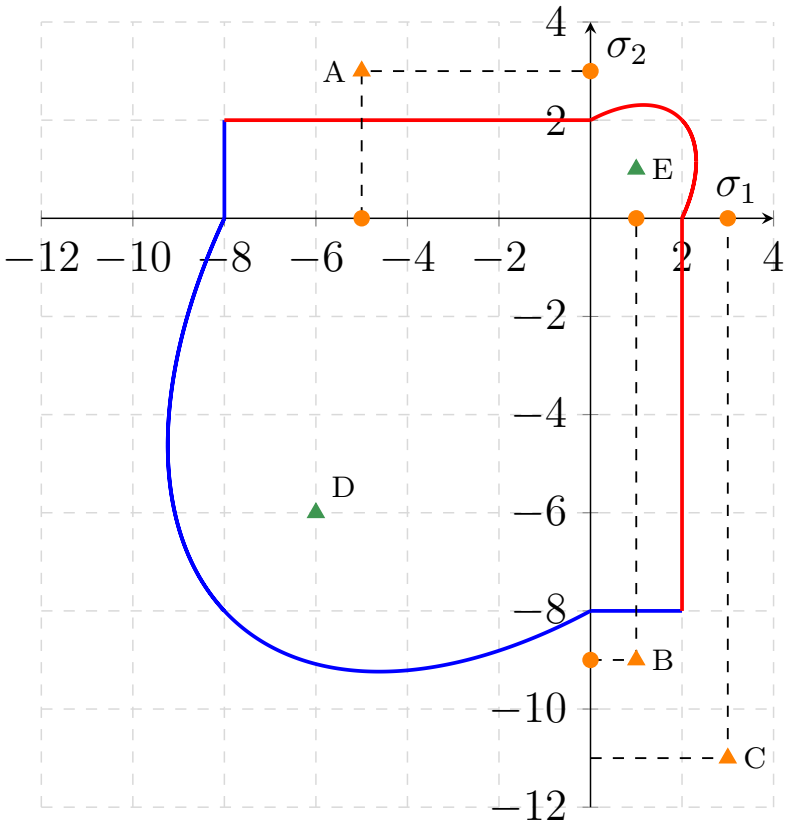

Figure I.15: Yield surface of Blond's model.

When the structure being modeled has stress states close to these singularities, difficulty in the convergence may arise. Nevertheless, this should not be a problem if the yield stress is equal to zero, i.e., the material starts to creep as soon as a load of any magnitude is imposed, which is often the case for refractories.

One of the main advantages of this model is that the material's parameters for tensile and compression creep are completely independent, therefore they can be identified separately. This gives flexibility to fit the creep flow calculations to a large range of strain rates observed in experiments.

Nevertheless, the validity of the stress split hypothesis needs to be verified, and this model presents the characteristic of making a sum between two terms (positive and negative strain rates) that depend on the equivalent stress. The consequence of this fact is that, if this model is used with identical properties in tension and in compression, the resulting viscoplastic strain rate isn't the same as the one obtained with a symmetric model. Although this isn't necessarily a limitation, in some cases it can be desirable to have a model that is an interpolation of the tension and the compression material behaviors, without this intrinsic orthotropy.

I.5 Conclusion

This chapter presented the current state of the art of the thermo-mechanical modeling and characterization of refractory materials, as well as the general framework of inverse analysis, highlighting the key points that need to be considered to design robust and noise-tolerant characterization methods.

It was shown that experiments such as the Brazilian test or the four-point bending test present a complex distribution of stresses and strains, that can help to extract more information from a single sample in comparison to uniaxial tests, at the cost of a more complicated post-processing.

A general viscoplastic theory using a thermodynamics framework was presented, highlighting creep models available in the literature which serve as a base to the development of new ones, such as the asymmetric models required to simulate refractories.

From what was exposed, it can be concluded that refractory manufacturers and end users can benefit from experimental setups that are able to obtain more information using a reduced amount of tests, given the cost and time demands of each one, but still maintaining the easy-of-use of traditional approaches. Also, it is clear that new asymmetric creep models need to be developed and tested, to improve the accuracy of the prediction of stresses and strains in refractory parts and linings.

CHAPTER II

Traditional Approach for the Identification of Creep Parameters

The goal of this chapter is to describe the currently most common methodology used to identify the parameters of creep laws applied to refractories, and to apply it to the alumina-spinel brick.

In Section II.1, the experimental protocol for tension and compression tests is described, and Section II.2 presents the raw experimental curves obtained with this protocol.

Section II.3 explains the methodology used to perform the inverse identifications of the creep parameters under tension and compression. The statistical analysis used throughout the chapter is also explained in this section.

Finally, Section II.4 presents creep curves[1] *and the identification results, as well as the strain-time curves that allow a visual assessment of the identification's error.*

[1] In the cooperative framework of the project ATHOR, an internship was made at the University of Leoben, Austria, to perform creep tests on alumina-spinel bricks. The compression creep tests were made by Dr. Soheil Samadi.

Chapter Contents

II.1 Experimental protocol 47
II.1.1 Compression tests 47
II.1.2 Tensile tests 48
II.1.3 Choice of the imposed temperatures and loads 48
II.2 Tension and compression raw curves 50
II.3 Inverse identification using one-dimensional creep laws 53
II.3.1 Primary and secondary creep laws 53
II.3.2 Transient creep law 54
II.3.3 Statistical analysis 55
II.4 Identification of the creep parameters for the alumina-spinel brick 56
II.4.1 Compression – Primary creep 56
II.4.2 Compression – Transient creep 63
II.4.3 Tension – Secondary creep 67
II.5 Conclusion 73

II.1 Experimental protocol

The experimental creep curves presented in this work were obtained using dedicated compression and tension testing machines, developed at the University of Leoben, Austria. These machines were described and successfully used in previous works, such as Jin et al. (2014), Samadi et al. (2020), Schachner et al. (2019), Sidi Mammar et al. (2016). Sections II.1.1 and II.1.2 describe the main characteristics of the testing machines.

II.1.1 Compression tests

To measure the displacements during compression creep, two extensometers are positioned at an angle of 180° in relation to each other, and the distance between their corundum rods is 35 mm. The entire sample, the upper and the lower *SiC* pistons are located inside of a tubular furnace. A picture of the compression creep experimental setup can be seen on Figure II.1.

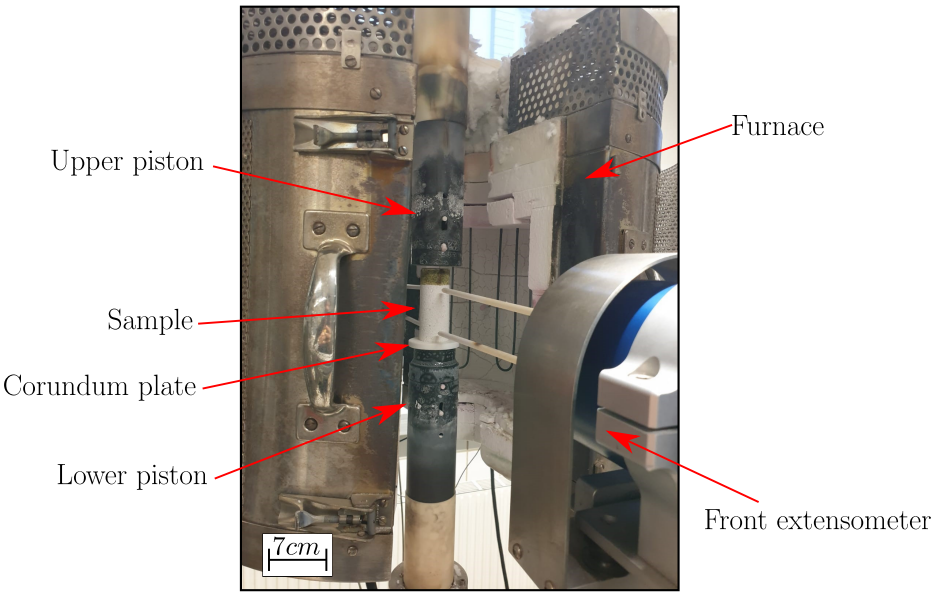

Figure II.1: Compression creep experimental setup.

The samples used in the compression tests are drilled with 35 mm diameter and 70 mm height, and a corundum plate is used at the contact between the sample and the lower piston to avoid chemical interactions. A bauxite brick is used to avoid the contact between the sample and the upper piston.

At the beginning of the test, a compression pre-load of 50 N, that corresponds to a negligible stress of 0.05 MPa, is applied to the sample to hold it in the correct position during the heating.

The heating rate for the compression tests is 10 °C/min, and a 1 h dwell is used to homogenize the temperature of the sample.

II.1.2 Tensile tests

Similar to the compression tests, two extensometers are used for the tensile creep tests, with a distance between their corundum rods of 50 mm. The main concerns during tensile creep tests of refractories are the possible damaging of the sample during the gripping and the misalignment of the load, which can result in bending stresses on the sample and cause its premature failure.

To address these two concerns, the sample is glued to two water cooled adapters using a dedicated gluing device before it is inserted in the testing machine, as shown in Figure II.2. As a second step, the sample and the adapters are positioned at the testing machine and connected to water cooled grips, that stands outside the furnace to avoid to burn the glue. In this way, only a limited part of the sample stays inside the furnace. The tensile creep experimental setup is shown in Figure II.3.

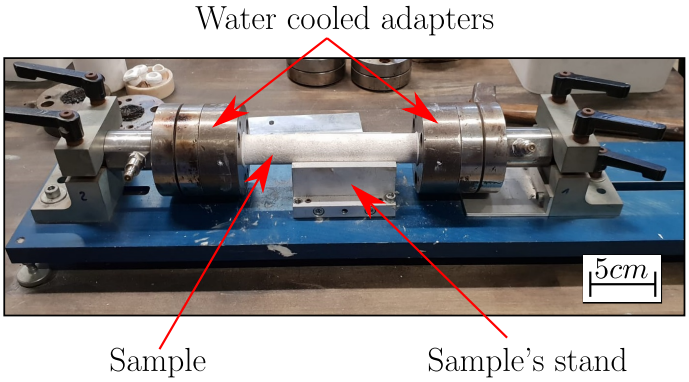

Figure II.2: Tensile creep experimental setup: Gluing device

The samples used in the tensile tests are drilled with 30 mm diameter and 230 mm height. A pre-load of 50 N is also applied in the tensile test, and the heating rate is 5 °C/min, with 1 h dwell to homogenize the temperature of the sample. Comparing with the compression case, the tensile tests use a lower heating rate because the sample is larger and can suffer undesired deformations during heating due to a thermal gradient.

II.1.3 Choice of the imposed temperatures and loads

Formally, mechanical parameters identified using experimental tests are valid only within the range of the applied test conditions, such as temperature and stress in this case. Although interpolations are expected to be sufficiently accurate, extrapolations should be made with care.

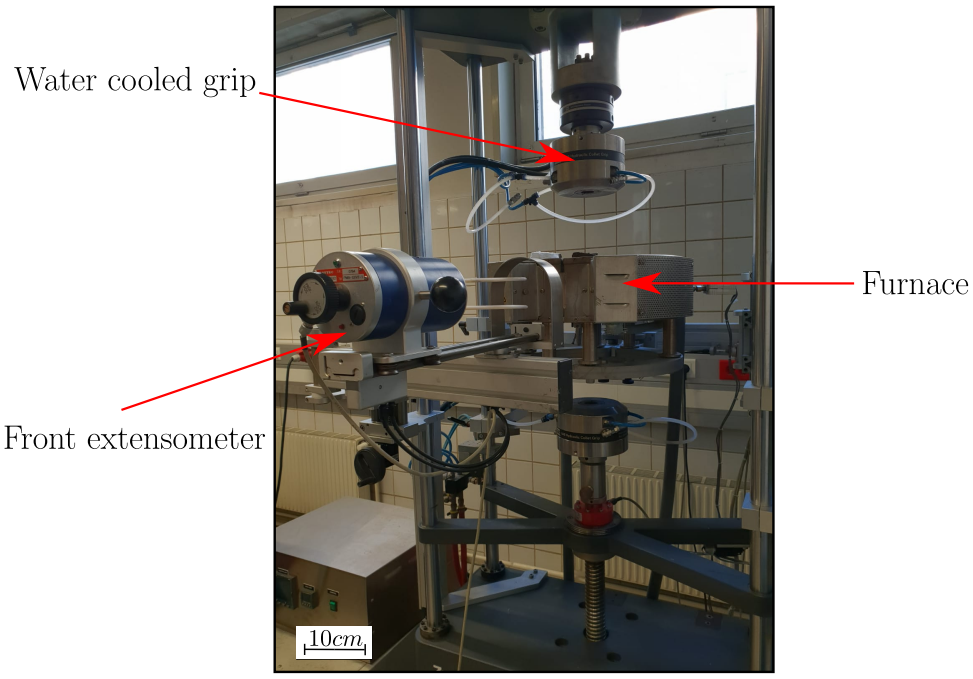

Figure II.3: Tensile creep experimental setup: Testing machine

For this reason, the selection of the imposed conditions is a critical step in an identification campaign. It should be also noticed that, sometimes, the available equipment is a limiting factor, specially in the case of high temperature tests.

In this work, no particular final application was envisioned, since the goal was to develop new identification procedures, and not to use the results of these identifications to perform further numerical simulations or calculations of other natures for real industrial cases. Nevertheless, considering the Alumina-Spinel brick is used in steel ladle linings, the range of temperatures between 1200 °C and 1500 °C was privileged.

The selection of the imposed loads was a consequence of the stability and duration of the tests. For the compression creep, a low value of imposed stress can lead the test to a prohibitive duration of several days, so load values that allowed them to be restricted to one day each were used. For the tensile creep tests, the critical factor is its stability, since the material is very sensitive to this loading conditions. For this reason, preliminary tests were made to assess the possible range that could be used, and stress values that allowed the sample not to fail too quickly were selected.

II.2 Tension and compression raw curves

Following the experimental procedures described in Section II.1, the raw curves shown in Figures II.4 and II.5 were obtained. For each pair temperature-stress three samples were tested, both under tension and under compression, in order to increase the accuracy and the robustness of the results, allowing the use of the statistical methods described in Section II.3.3.

Figure II.4 shows all the compression creep curves obtained from the tests. At 1300 °C, the samples were tested at σ = 8 MPa, σ = 9 MPa and σ = 10 MPa. At 1400 °C, the samples were tested at σ = 4 MPa, σ = 4.5 MPa and σ = 5 MPa. At 1500 °C, the samples were tested at σ = 3.5 MPa, σ = 4 MPa and σ = 4.5 MPa. The influence of the stress and of the temperature on the creep behavior is clear in this figure.

Refractories are heterogeneous materials, generally having large grains compared to the size of the samples used for mechanical test. As such, it is common to observe a considerable scatter in the data regarding their mechanical properties (Samadi et al., 2020). From Figure II.4, it is possible to observe a considerable scatter in the experimental data, specially according to the final time to failure. For example, Figure II.4a shows that one of the sample tested at 8 MPa failed after 3 hours, while the other two failed after 6 hours and 11.5 hours.

Figure II.4a also shows that the scatter is such that samples subjected to different stresses can present similar time-strain curves. For example, two tests at 8 MPa and 9 MPa present almost superposing curves, even if the sample tested at 9 MPa is expected to present more pronounced creep strains. The same behavior can be observed on Figure II.4c, where samples tested at 3.5 MPa and 4.0 MPa superpose.

The scatter in the data, that is considered to be normal for refractory materials but there is large for the alumina-spinel brick, can be explained by many factors. From the material's point of view, the heterogeneity in the bricks used to produce the samples can come from the production processes, such as the pressing and the heat treatment. From the testing procedures, micro-cracking of the sample during its production and misalignment of the load can contribute to the variations in the results. It is out of the scope of this work to precisely define the causes of this scatter, as it can come from a combination of all factors mentioned.

In a similar way, Figure II.5 presents all the tensile curves obtained experimentally. At 1200 °C, the samples were tested at σ = 0.25 MPa, σ = 0.35 MPa and σ = 0.45 MPa. At 1300 °C, the samples were tested at σ = 0.15 MPa, σ = 0.20 MPa and σ = 0.25 MPa. At 1400 °C, the samples were tested at σ = 0.12 MPa, σ = 0.15 MPa and σ = 0.18 MPa. It is important to notice that, under tension, the applied stresses are considerably lower than under compression, and the difference between stress values at a given temperature can be of the order of 0.03 MPa.

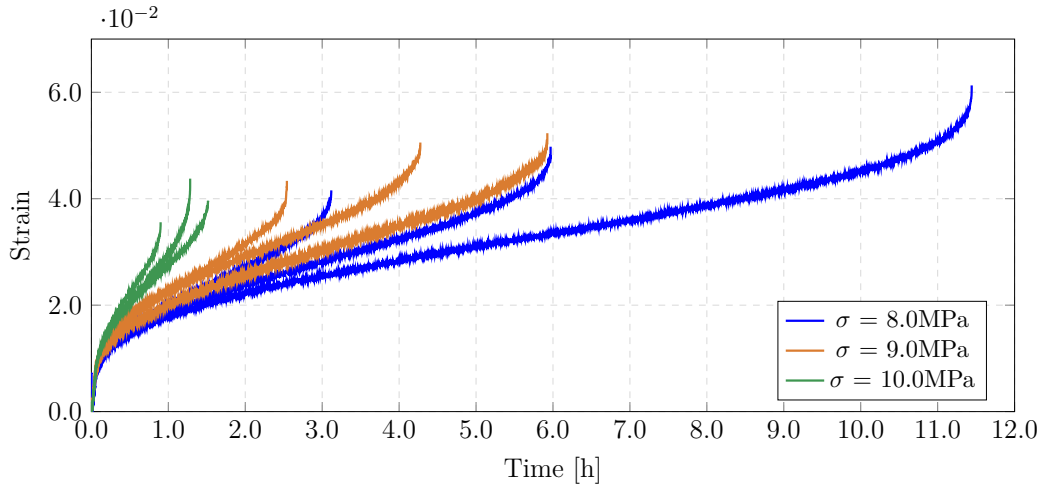

(a)

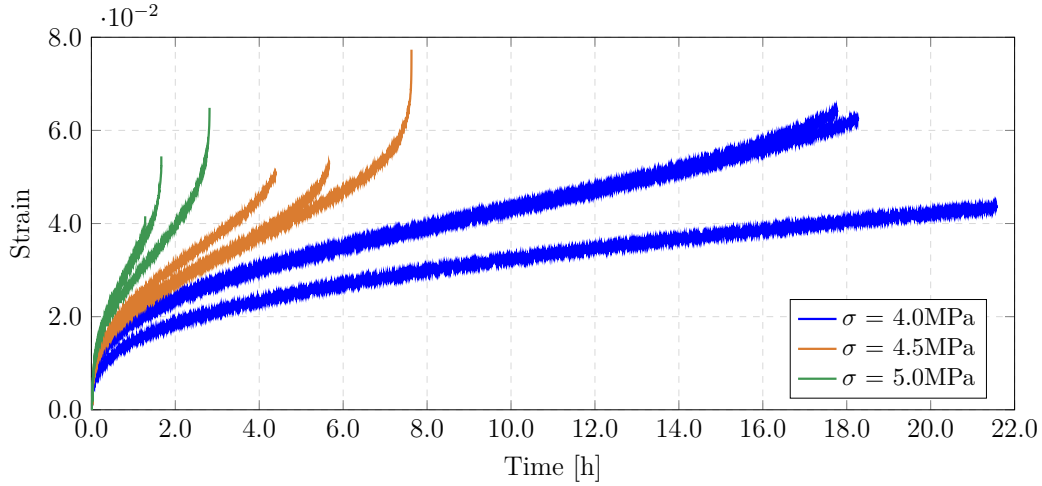

(b)

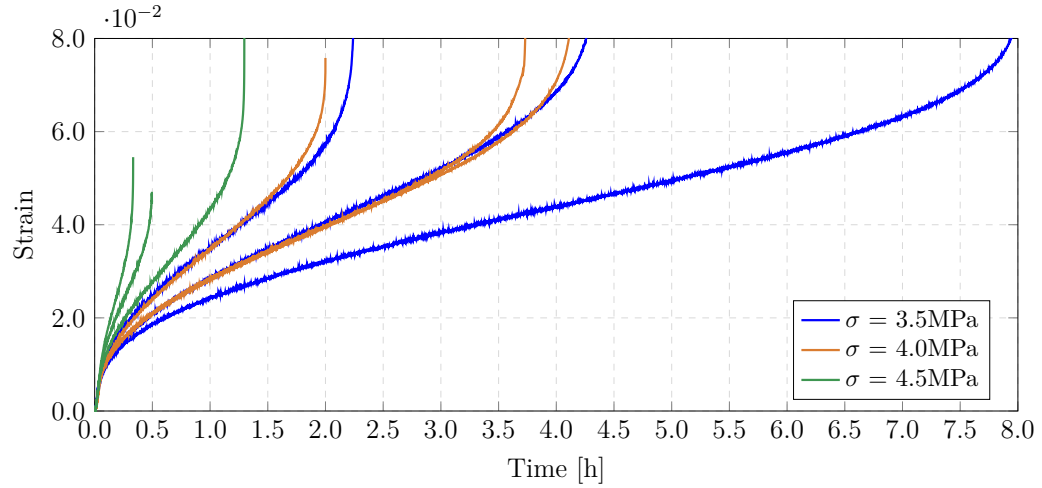

(c)

Figure II.4: Compressive creep curves. (a) 1300 °C. (b) 1400 °C. (c) 1500 °C.

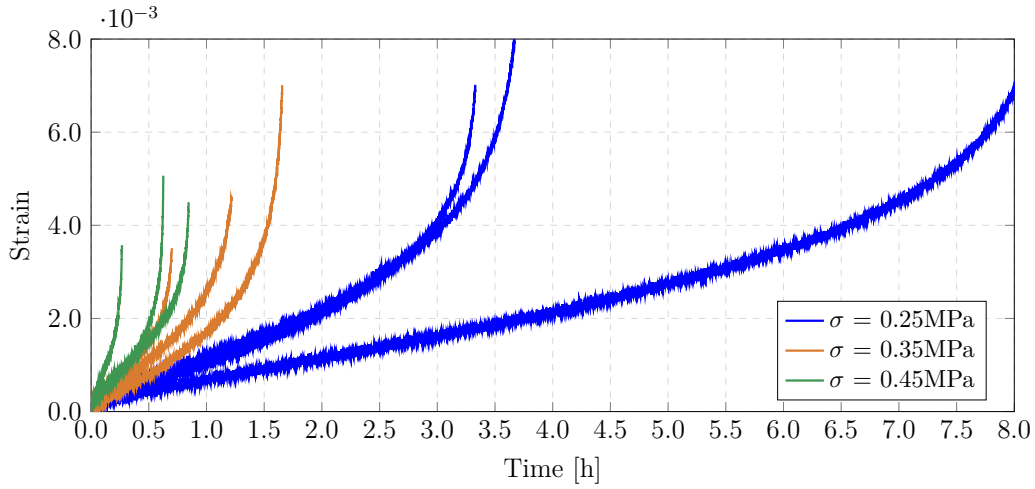

(a)

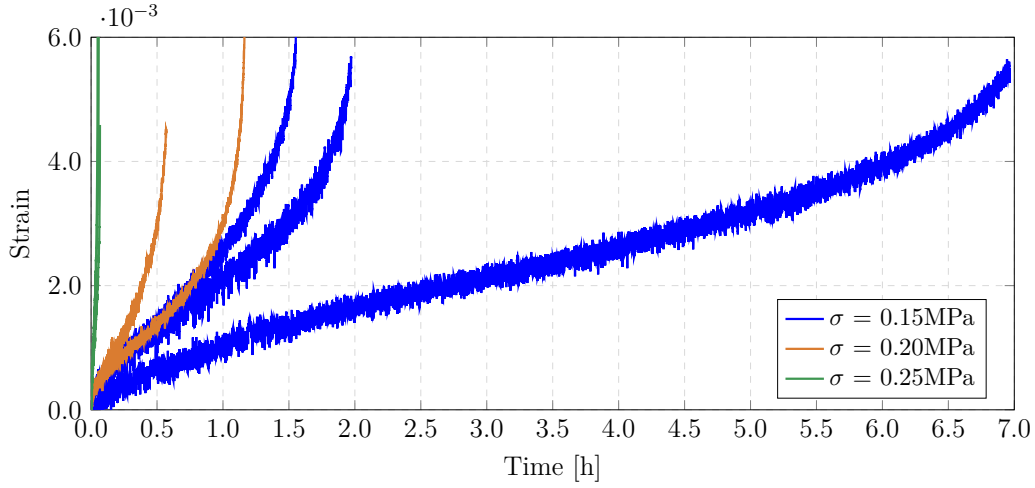

(b)

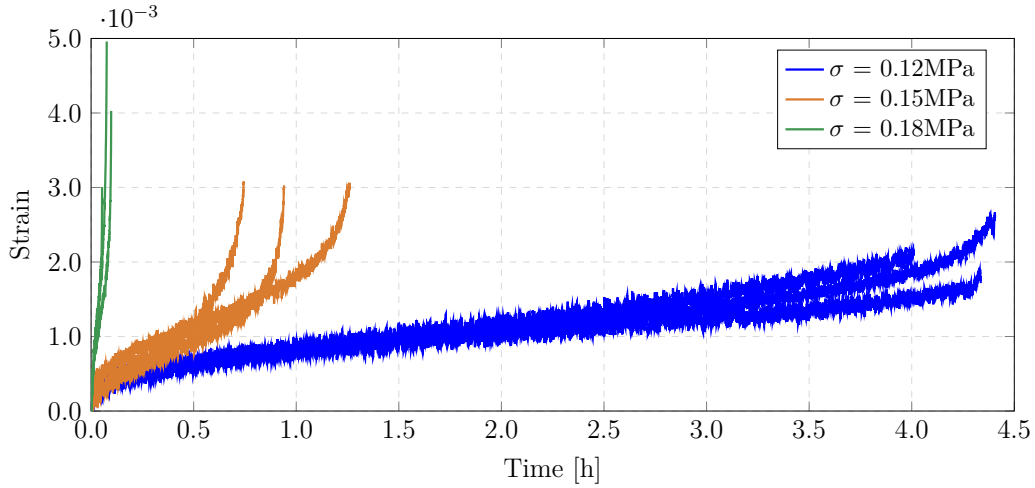

(c)

Figure II.5: Tensile creep curves. (a) 1200 °C. (b) 1300 °C. (c) 1400 °C.

As in the compression creep case, superposition of curves obtained from samples tested under different stresses is also observed, such as in Figure II.5b.

Comparing the curves for tension and compression creep, it is possible to verify a considerable asymmetry between the strains obtained with each of these loads, which corresponds to the expected behavior of refractory materials.

II.3 Inverse identification using one-dimensional creep laws

II.3.1 Primary and secondary creep laws

To identify the material parameters from tension or compression creep tests, Equation I.15 can be integrated using the trapezoidal rule (Jin et al., 2014), resulting in:

$$\varepsilon_{i+1}^{cr} \approx \left[{\varepsilon_i^{cr}}^{1-m} + \frac{(1-m)\cdot A \cdot (\sigma_{i+1}^n + \sigma_i^n)\cdot (t_{i+1} - t_i)}{2} \right]^{\frac{1}{1-m}} \tag{II.1}$$

where A, n and m are material parameters, t is the time and i is the time step index. In this way, depending on the stress variation over time and on a given set of material's parameters, it's possible to obtain an analytic calculation of the resulting time-strain curve, which can later be compared to the experimental results using a least squares approach.

It should be taken into account that the experimental creep curves comprise both the elastic and creep strains (ε^{tot}), but Equation I.15 doesn't account for the elastic part. Therefore, either the experimental data should be treated or the elastic strains should be included in the equation, following the expression for the one-dimensional case:

$$\varepsilon^{tot} = \varepsilon^{cr} + \frac{\sigma}{E} \tag{II.2}$$

where the second part of the right hand side of the equation corresponds to the elastic strain, being E the Young's modulus of the material.

The inverse identifications carried out in this work were done according to the following steps:

- **Step 1**: Definition of the input variables.

    1. Sample's diameter
    2. Young's modulus

3. Type of creep (primary or secondary)
4. Allowed range of variation for the material's properties
5. Raw data from the tests (time-force-displacement tables)

- **Step 2**: Random definition of the initial guesses, depending on the variable's range of variation and the number of initial guesses.
- **Step 3**: For each of the initial guesses and each of the stress levels, calculate the analytic time-strain curves using Equation II.1, at the same time points as the ones available from the experimental data.
- **Step 4**: For each time point, calculate the difference between the experimental and analytic values (identification error), using a least-squares approach.
- **Step 5**: Using the Levenberg-Marquardt optimization algorithm explained in Chapter I.3.3, change the material parameters in order to minimize the identification error.

II.3.2 Transient creep law

Section I.4.1.3 presented the general equations of a kinematic creep model that can be used to represent the transient creep behavior, from the primary to the secondary stages. In this section, an integration procedure is proposed in order to identify the material parameters using compression creep tests.

Equation I.28 shows that, unlike the isotropic equation used to represent primary creep, for transient creep a system of equations needs to be integrated, since the backstress is a tensorial internal variable with its own evolution law.

To simplify the integration, it is assumed that the stress is constant and higher than zero during the creep test, therefore, $\sigma(t) = \sigma_0 > 0$. Even if the force increases according to a predefined ramp during loading, this assumption is reasonable if one considers that the creep test is considerably longer that the time to reach the constant force.

At the beginning of loading it is assumed that $\alpha(0) = 0$ and $\sigma_0 - \alpha > 0$, and a new variable $H = \alpha/\sigma_0$ is introduced. Variable H is similar to what is called a damage variable in damage mechanics models, in the sense it modifies the behavior of the curve and can assume values $0 < H < H_* < 1$, where H_* is a saturation value, that becomes constant once secondary creep stage is reached (Naumenko & Altenbach, 2007).

For the one-dimensional case, the following system of equations need to be integrated:

$$\begin{cases} \dot{\varepsilon}^{cr} = a\sigma_0^n(1-H)^n \\ \dot{H} = \sigma_0^{n-1}[ba(1-H)^n - cH^n] \end{cases} \tag{II.3}$$

In its discrete form, Equation II.3 becomes:

$$\begin{cases} \varepsilon_{i+1}^{cr} - \varepsilon_i^{cr} = \Delta t[a\sigma_0^n(1-H_{i+1})^n] \\ H_{i+1} - H_i = \Delta t\{\sigma_0^{n-1}[ba(1-H_{i+1})^n - c(H_{i+1})^n]\} \end{cases} \tag{II.4}$$

and $\varepsilon^{cr}(0) = 0$ and $H(0) = 0$ are considered as initial conditions.

Similar to what was described in Section II.3.1, Equations II.4 were implemented in a scripting language to automate the identification procedure, and the Levenberg-Marquardt algorithm was used to identify the material parameters. Nevertheless, in the case of kinematic creep it is more complex to obtain an analytical expression for the integration, therefore this step also used a classic numerical integration method.

II.3.3 Statistical analysis

One of the goals of this chapter is to show how the scatter in the tests can influence the identified material parameters, in terms of their range of variation.

First, two concepts should be defined:

- Statistical population: group of all possible items in the study domain. In the present case, the population is the infinite number of creep tests that could be done.
- Statistical sample: the actual subset of the population being studied. In this study, the statistical sample is used to draw conclusions about the statistical population, since the mean and the standard deviations of the population are unknown.

Confidence intervals can be used to predict what is the confidence level that one parameter of the statistical population (for example, the average) lies in a given range, calculated using the statistical sample.

For example, if one defines a 70% confidence interval for the average of the material parameter A in Equation I.15, this means that the interval resulted from the estimation procedure is 70% reliable, not that there is 70% probability that the parameter A for the statistical population lies within this interval.

Once the inverse identifications are made using the different possible combinations of curves, the average and standard deviation can be calculated. Assuming a normal distribution for the results, confidence intervals can be calculated according to the following expression:

$$\left(\overline{x} - t^* \frac{\eta}{\sqrt{n}}, \overline{x} + t^* \frac{\eta}{\sqrt{n}}\right) \tag{II.5}$$

where $\overline{x}$ is the average, η is the standard deviation of the statistical sample, n is the number of observations and t^* is the critical value according to Student's t-distribution, that can be found in specialized tables (Box et al., 2005).

Once the confidence intervals are obtained, the time-strain curves can be plotted using their extreme values, to check the variation of the creep curves within the chosen confidence level. Due to the high heterogeneity of refractories and limited amount of experimental data available, in this work it was decided to plot 70% confidence intervals for all the following analyses.

II.4 Identification of the creep parameters for the alumina-spinel brick

In this section, the creep properties of the alumina-spinel brick are identified according to the methodology presented in Sections II.1 and II.3.

All the curves presented in this section represent the average of the two extensometers used to measure the displacements over time, as explained in Section II.1. The compression creep curves were already reported by Samadi et al. (2020), where a different statistical approach was applied for the parameter determination. The tensile curves obtained at 1300 °C were published by Teixeira et al. (2020).

II.4.1 Compression – Primary creep

The curves presented in Figure II.4 were used to identify the creep parameters related to Equation I.15. It should be noticed that frequently the main goal of creep parameters identification for a given material is to later model more complex structures under multidimensional loads. In this case, the stage of the creep needed for simulation must be defined (primary or secondary), since Equation I.15 does not provide a criteria to transit from the first to the second creep stages during the calculations. From Figure II.4, it is observed that primary creep stage has an important influence in the time-strain response under compression, and therefore it was be considered during the identification.

Table II.1 shows the inversely identified compression creep parameters. For each case, the nine experimental curves were combined in sets of 3, resulting in 27 combinations. The 70% confidence interval was calculated using a Student's t-distribution critical value of $t^* = 1.057$.

Table II.1: Identification results – Compression creep

Parameter	Average	Std. dev.	70% Conf. interval
	1300 °C		
$\log_{10} A[MPa^{-n}s^{-1}]$	−13.52	0.925	(−14.08, −12.95)
n [–]	3.56	0.554	(3.22, 3.90)
m [–]	−2.59	0.218	(−2.73, −2.46)
	1400 °C		
$\log_{10} A[MPa^{-n}s^{-1}]$	−13.53	1.732	(−14.58, −12.47)
n [–]	5.96	2.187	(4.63, 7.29)
m [–]	−2.37	0.207	(−2.5, −2.24)
	1500 °C		
$\log_{10} A[MPa^{-n}s^{-1}]$	−9.75	0.913	(−10.31, −9.19)
n [–]	2.90	0.805	(2.41, 3.39)
m [–]	−1.66	0.275	(−1.83, −1.49)

In Figure II.6 the creep curves resulting from the average of the identification parameters were plotted together with the experimental curves. It is possible to observe a good agreement between the experimental and identified results. The figure also shows the upper and lower bound creep curves resulted from the extreme values of the confidence intervals.

It can be concluded that, to be 70% confident about the identification procedure, the possibility of a large variation of the average values must be assumed. This fact is due to the limited number of tests that could be done, considering the high cost and the time demand to perform them. A similar analysis can be done considering Figures II.7 and II.8 for 1400 °C and 1500 °C, respectively.

Considering the possible effects the test procedures and the material heterogeneity can have in the results, another approach for the inverse identification is to only consider the two closer curves at each load, and to eliminate the curve that deviate considerably from them. For example, considering the compression creep curves presented in Figure II.6b at $\sigma = 9$ MPa, Samples 4 and 5 are in good agreement between each other, while Sample 6 seems to deviate.

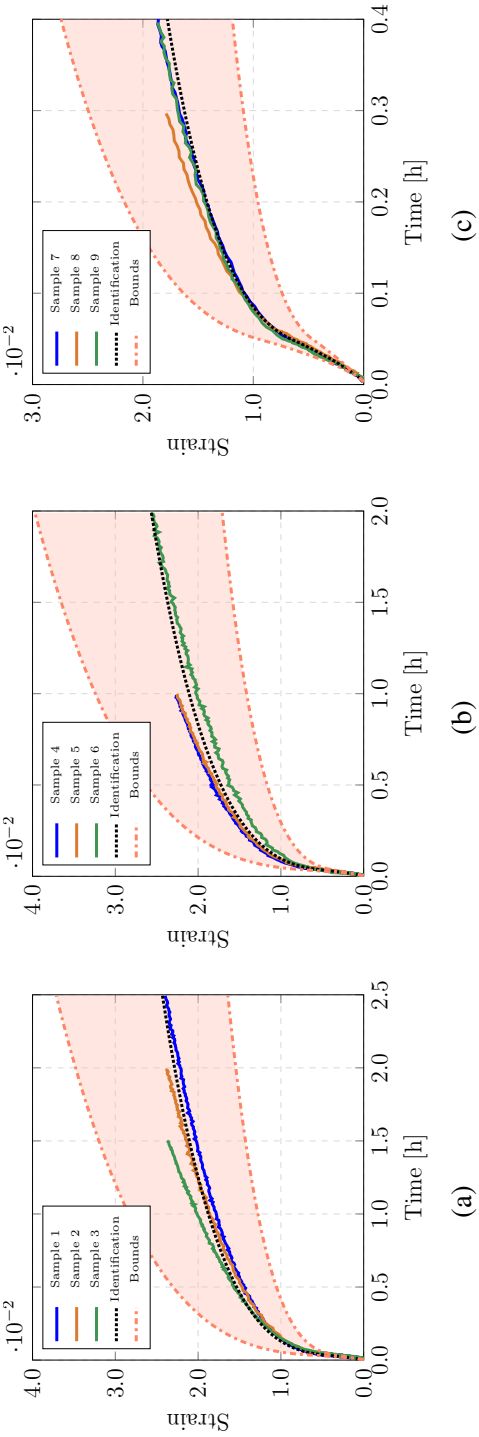

Figure II.6: Compression at $T = 1300$ °C. (a) $\sigma = 8$ MPa. (b) $\sigma = 9$ MPa. (c) $\sigma = 10$ MPa.

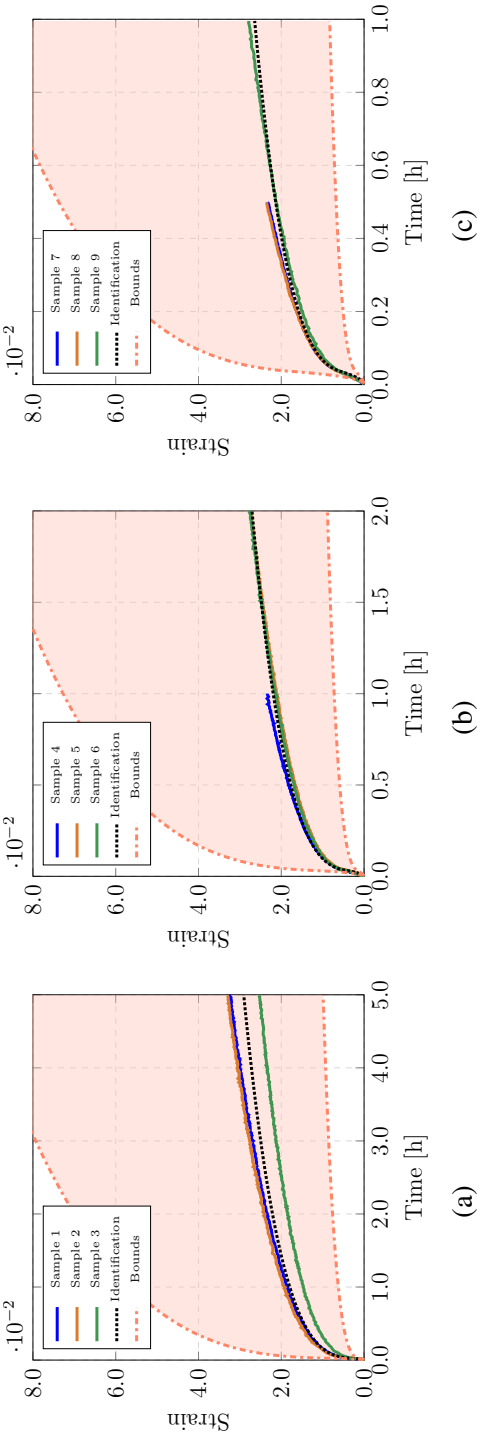

Figure II.7: Compression at $T = 1400$ °C. (a) $\sigma = 4$ MPa. (b) $\sigma = 4.5$ MPa. (c) $\sigma = 5$ MPa.

This methodology needs to be used carefully, because is not always obvious when a deviating result comes from a problem due to the testing procedure or due to an abnormal variation of the material, and when it is due to its actual normal heterogeneity. A reliable way to make this verification is to perform a higher number of tests, what presents the difficulties already mentioned.

Table II.2 shows the identification results for the compression creep tests with reduced number of samples. It can be seen that, when comparing to the case where all samples were considered, the average of the parameters changed less than 10%, but the standard deviation was reduced up to 50%.

Table II.2: Identification results – Compression creep with reduced number of samples

Parameter	**Average**	**Std. dev.**	**70% Conf. interval**
	1300 °C		
$\log_{10} A[MPa^{-n}s^{-1}]$	−14.16	1.732	(−14.49, −13.83)
n [–]	3.96	2.187	(3.80, 4.13)
m [–]	−2.74	0.207	(−2.83, −2.64)
	1400 °C		
$\log_{10} A[MPa^{-n}s^{-1}]$	−12.37	1.732	(−12.49, −12.26)
n [–]	4.21	2.187	(4.04, 4.37)
m [–]	−2.38	0.207	(−2.38, −2.37)
	1500 °C		
$\log_{10} A[MPa^{-n}s^{-1}]$	−10.09	0.477	(−10.40, −9.78)
n [–]	2.85	0.293	(2.66, 3.04)
m [–]	−1.86	0.175	(−1.97, −1.74)

It should be noticed that, since the number of experimental curves being considered decreased in the case where not all the samples were considered, the critical value of the Student's t-distribution increases, becoming $t^* = 1.134$. Nevertheless, the decrease of the standard deviation was more influential than the increase of t^*, resulting in a more restricted range of variation for the confidence interval. Figures II.9, II.10 and II.11 show the plots of the results.

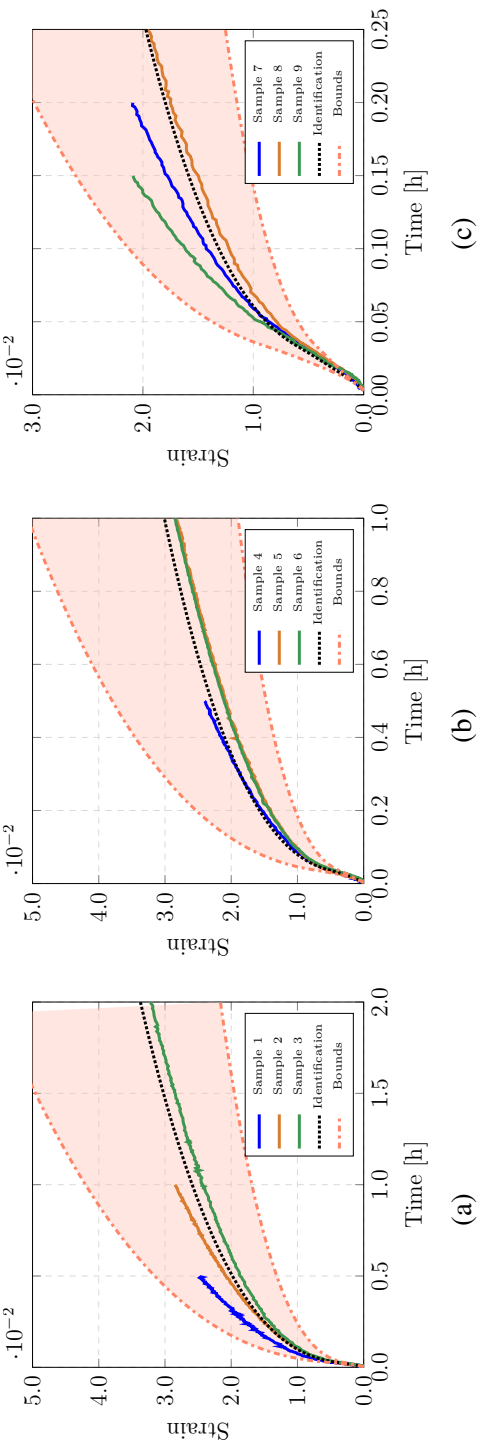

Figure II.8: Compression at T = 1500 °C. (a) σ = 3.5 MPa. (b) σ = 4.0 MPa. (c) σ = 4.5 MPa.

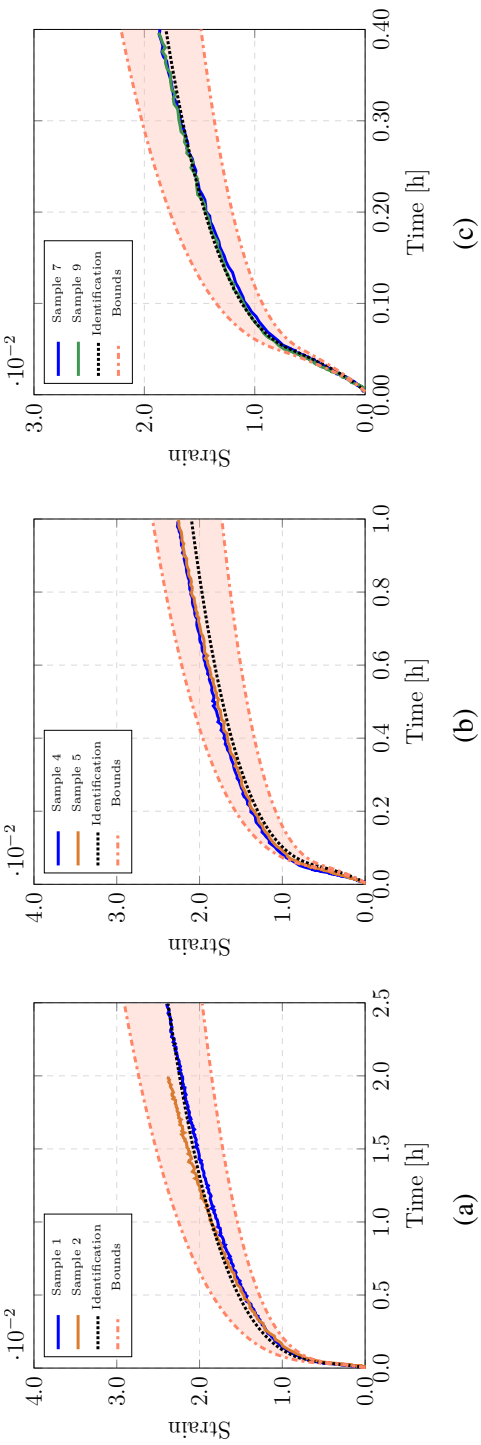

Figure II.9: Compression at T = 1300 °C – Reduced number of samples. (a) σ = 8 MPa. (b) σ = 9 MPa. (c) σ = 10 MPa.

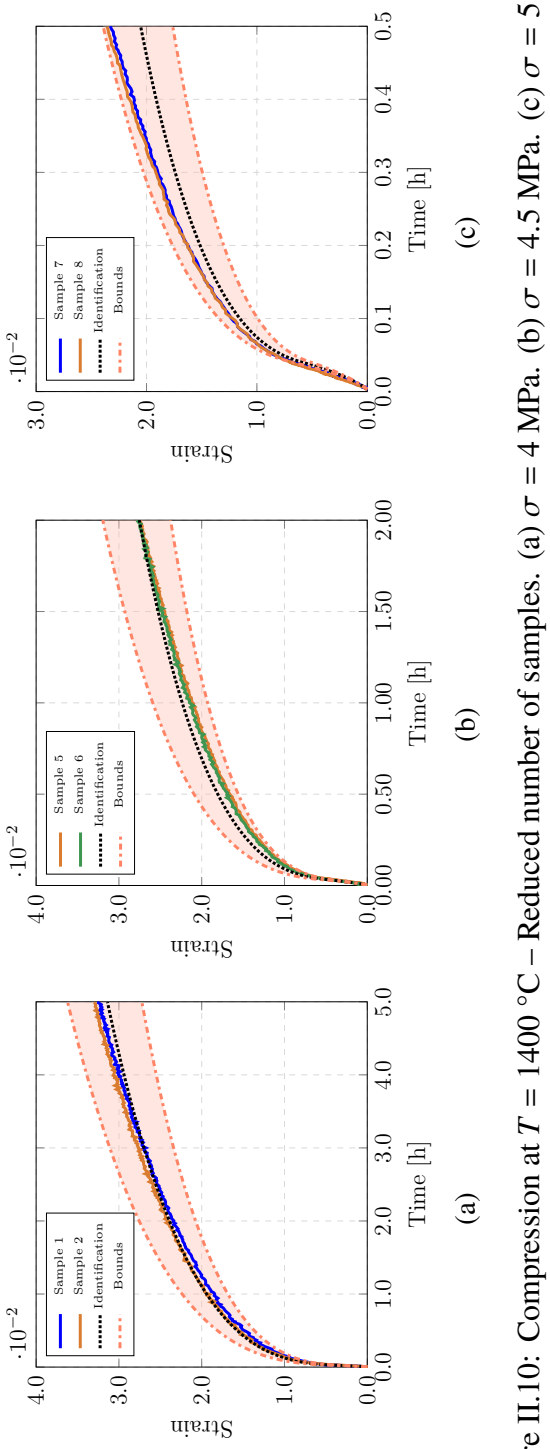

Figure II.10: Compression at T = 1400 °C – Reduced number of samples. (a) σ = 4 MPa. (b) σ = 4.5 MPa. (c) σ = 5 MPa.

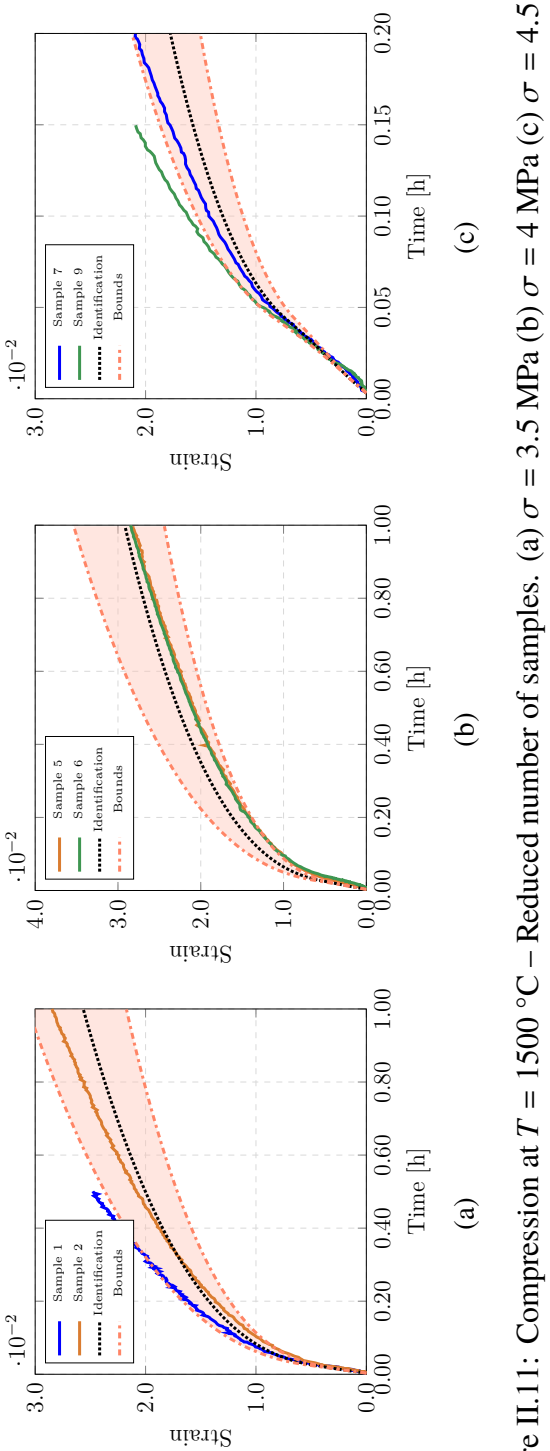

Figure II.11: Compression at T = 1500 °C – Reduced number of samples. (a) σ = 3.5 MPa (b) σ = 4 MPa (c) σ = 4.5 MPa

Figure II.12 shows the variation of the parameters for the cases with all samples and with the reduced number of samples. The error bars indicate the confidence intervals.

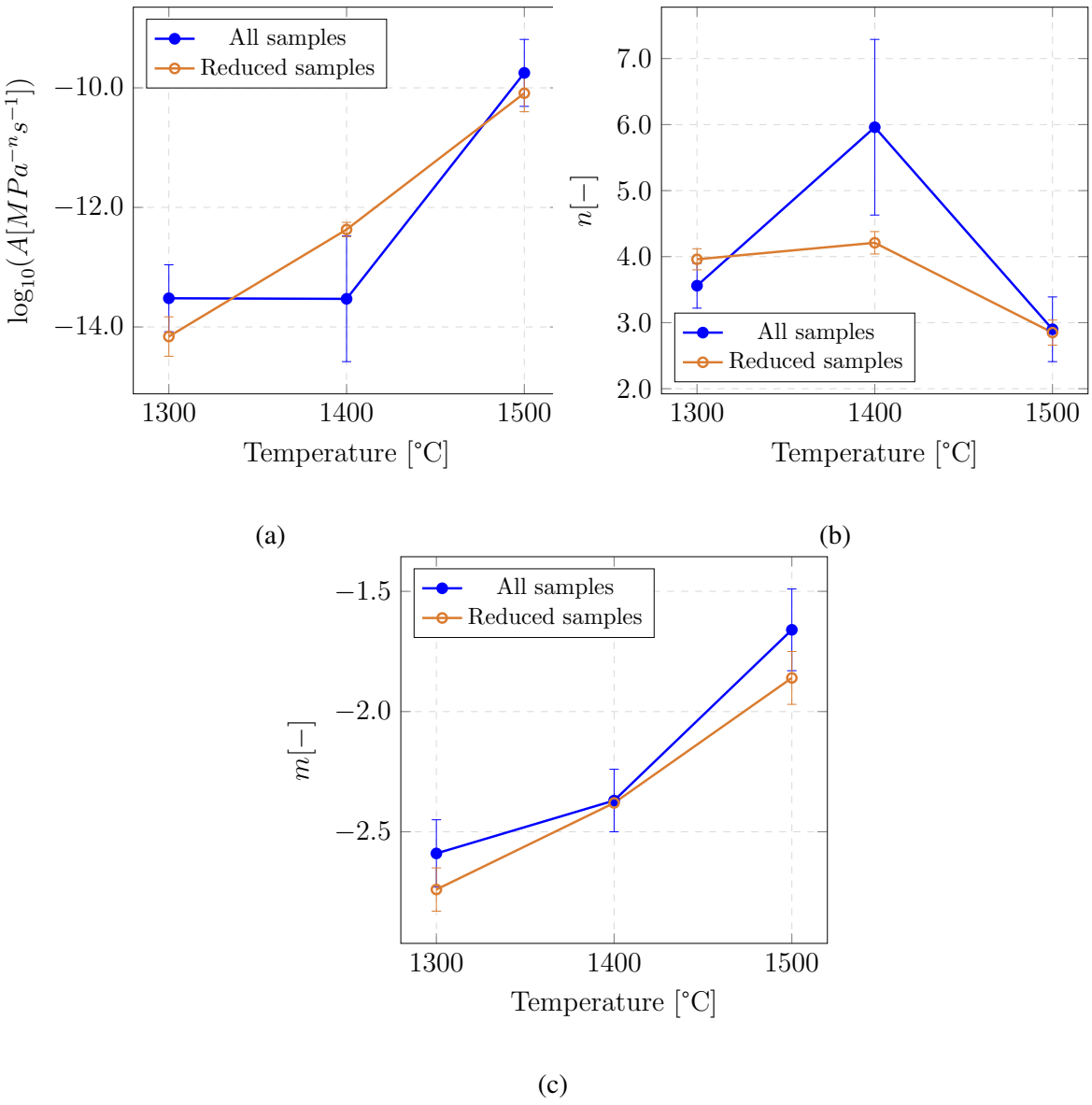

Figure II.12: Variation of the compression parameters. (a) $\log_{10}^{A}$. (b) n. (c) m.

II.4.2 Compression – Transient creep

Figure II.13 shows the primary and secondary creep curves obtained at 1300 °C, as well as the curves resulting from the identification procedure using the transient creep law, as described in Section II.3.2. It can be observed that the identification provides an accurate fit of the experimental curves. The curves identified using the primary creep law and already described in Section II.3.1 are also shown, to allow a comparison between the two assumptions.

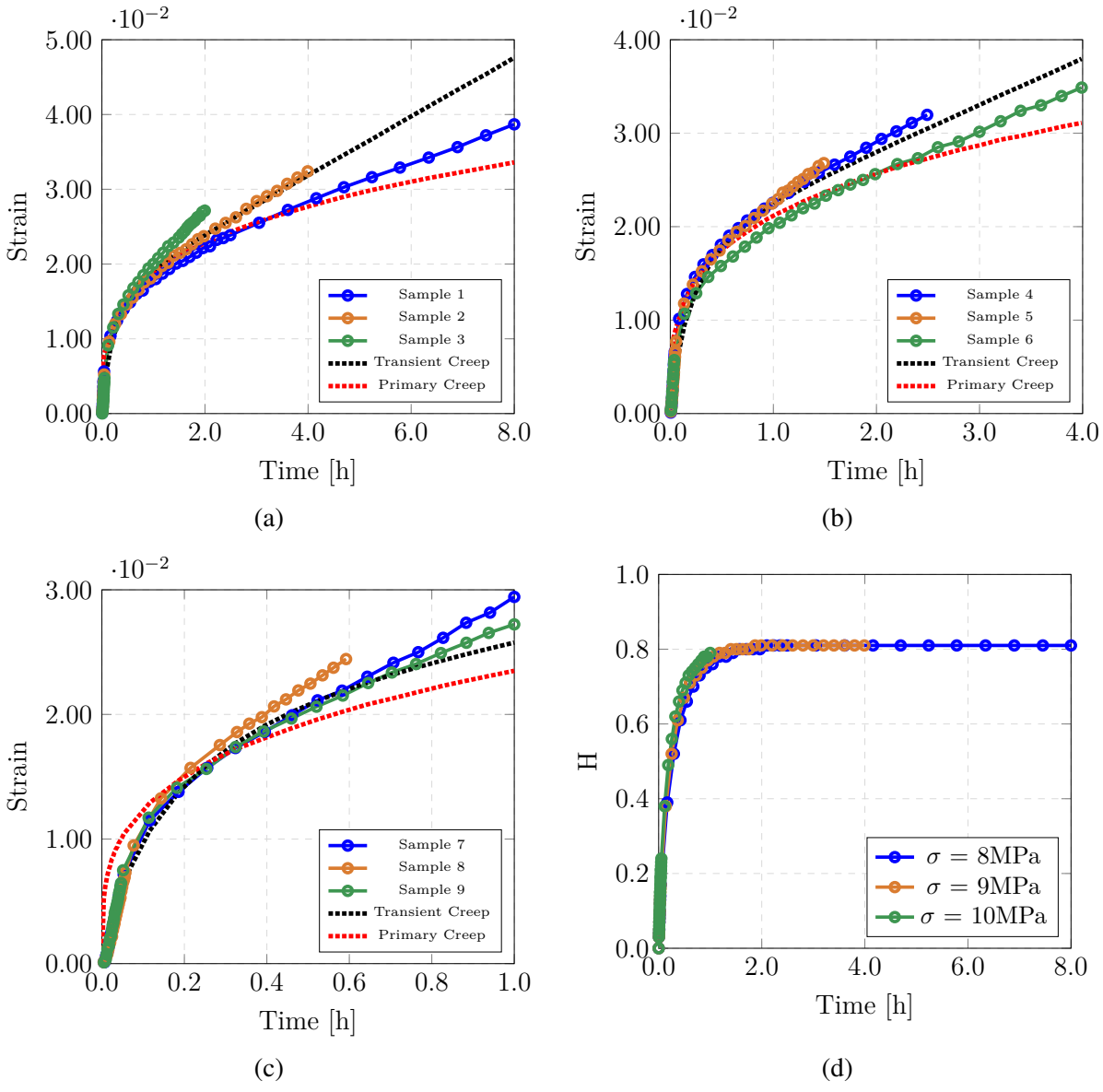

Figure II.13: Transient creep identification at $T = 1300$ °C. (a) $\sigma = 8$ MPa. (b) $\sigma = 9$ MPa. (c) $\sigma = 10$ MPa. (d) Evolution of H

Figure II.13d shows the evolution of the internal variable H. For this temperature, the stabi-

lization value for H was 0.8, and for the case where $\sigma = 10$ MPa the curve did not arrive at stabilization. This means that, at this pair temperature-stress, the secondary creep phase was negligible, according to this approximation.

It can also be observed that, at 1300 °C and 8 MPa, the identified curves considering primary and transient creep start to deviate after 2 h of testing, which corresponds to the end of primary creep. Therefore, if a model of primary creep is used to simulate a refractory lining structural behavior, after this time an additional error is included in the strains calculation. Similar results are observed in Figure II.14 for 1400 °C and Figure II.15 for 1500 °C.

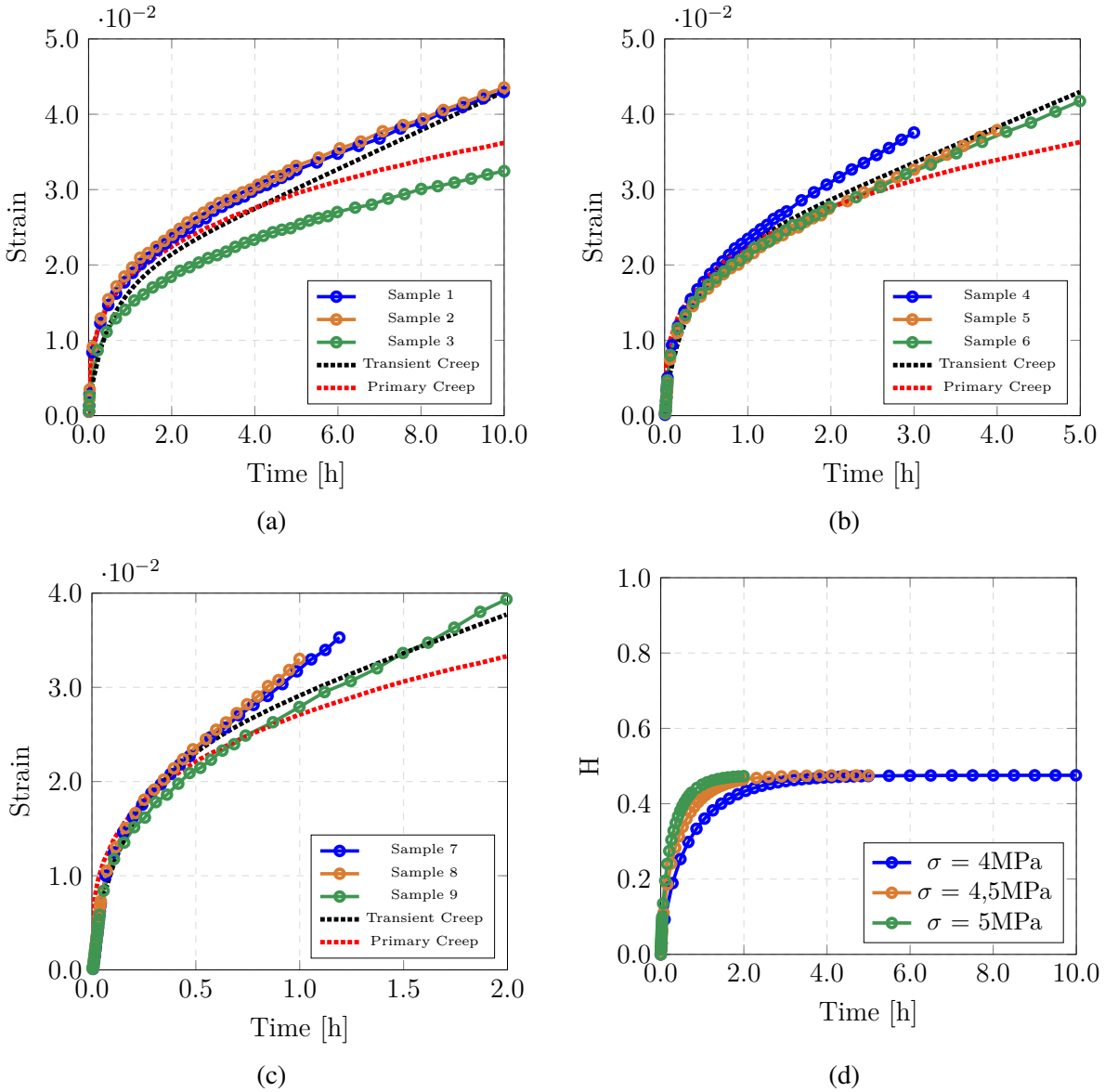

Figure II.14: Transient creep identification at $T = 1400$ °C. (a) $\sigma = 4$ MPa. (b) $\sigma = 4.5$ MPa. (c) $\sigma = 5$ MPa. (d) Evolution of H

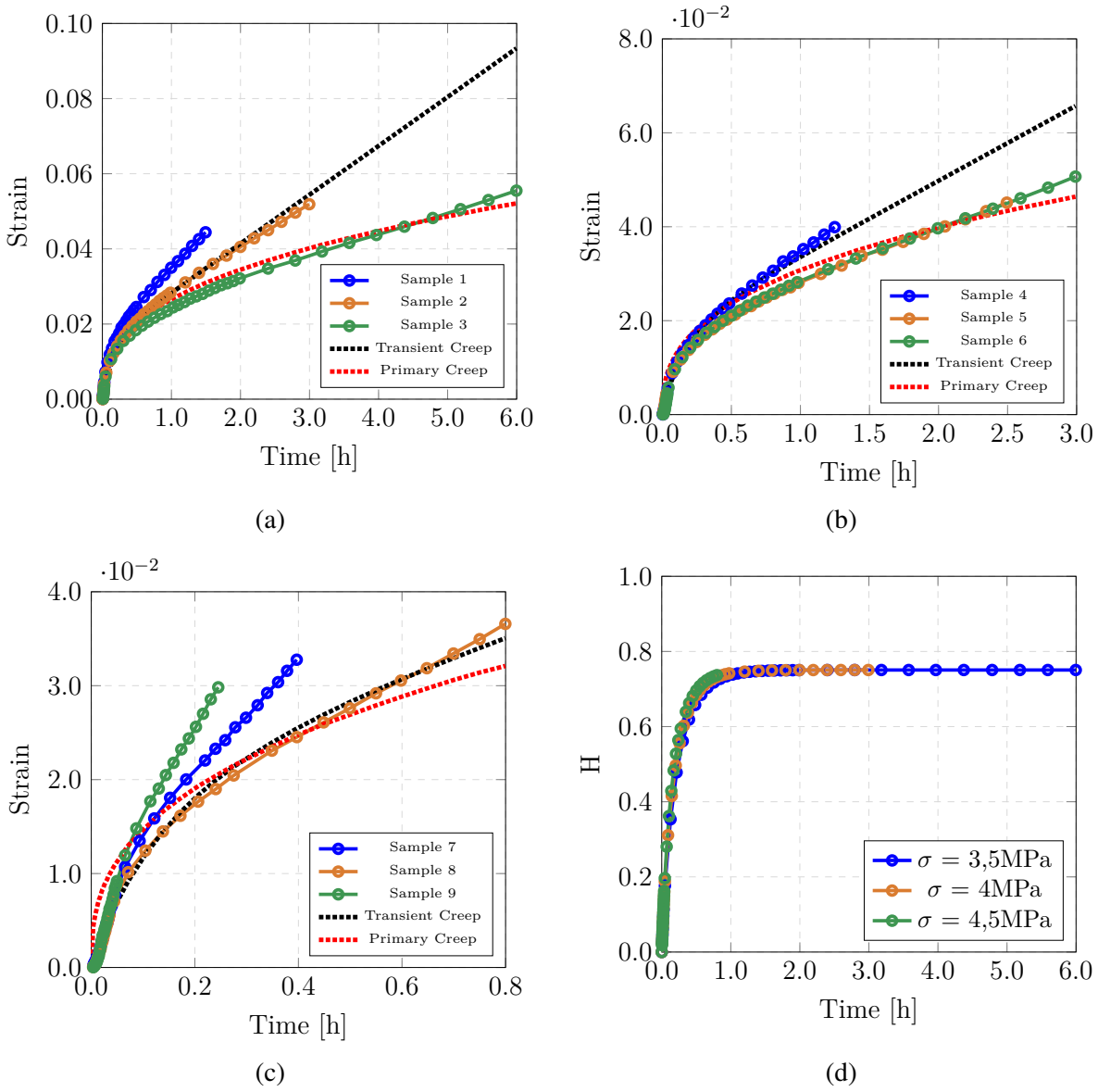

Figure II.15: Transient creep identification at $T = 1500$ °C. (a) $\sigma = 3.5$ MPa. (b) $\sigma = 4$ MPa. (c) $\sigma = 4.5$ MPa. (d) Evolution of H

Table II.3 present the values of the identified parameters for each temperature, as well as their standard deviation and 70% confidence interval, using a value of $t^* = 1.057$, and Figure II.16 shows a graphical representation of the estimated parameters varying with temperature.

Table II.3: Identification results – Transient creep

Parameter	Average	Std. dev.	70% Conf. interval
	1300 °C		
n [-]	1.981	0.689	$(1.83, 2.12)$
$\log_{10}(a[MPa^{-n}s^{-1}])$	−6.314	0.645	$(-6.44, -6.18)$
$\log_{10}(b[MPa(1+scMPa^{n-1})])$	2.562	0.092	$(2.54, 2.58)$
$\log_{10}(c[MPa^{-n}(MPa+b)/s])$	−5.010	0.681	$(-5.15, -4.86)$
	1400 °C		
n [-]	5.088	1.867	$(4.70, 5.47)$
$\log_{10}(a[MPa^{-n}s^{-1}])$	−7.784	1.258	$(-8.04, -7.52)$
$\log_{10}(b[MPa(1+scMPa^{n-1})])$	1.937	0.118	$(1.91, 1.96)$
$\log_{10}(c[MPa^{-n}(MPa+b)/s])$	−5.630	0.125	$(-5.65, -5.60)$
	1500 °C		
n [-]	1.582	1.446	$(1.28, 1.88)$
$\log_{10}(a[MPa^{-n}s^{-1}])$	−5.349	0.859	$(-5.52, -5.17)$
$\log_{10}(b[MPa(1+scMPa^{n-1})])$	2.145	0.224	$(2.10, 2.19)$
$\log_{10}(c[MPa^{-n}(MPa+b)/s])$	−3.961	0.727	$(-4.11, -3.80)$

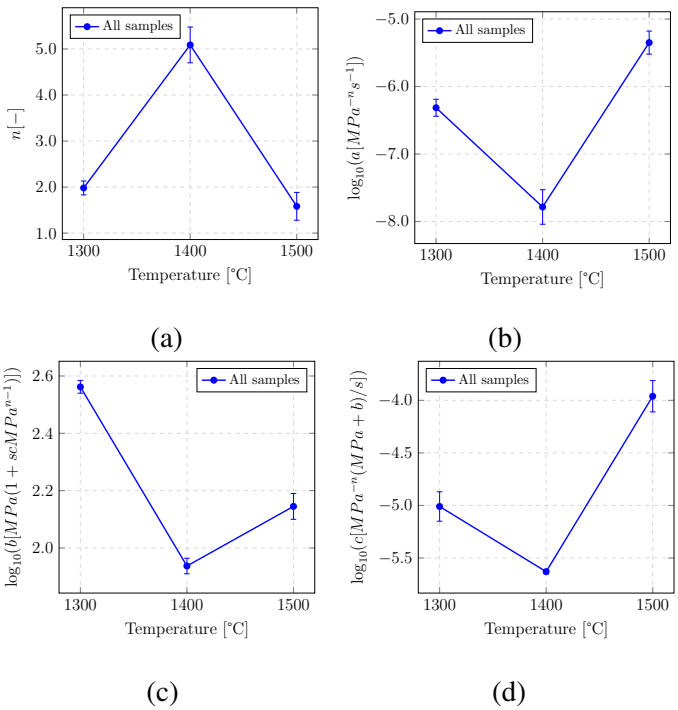

Figure II.16: Variation of material parameters – Transient creep. (a) n. (b) $\log_{10} a$. (c) $\log_{10} b$. (d) $\log_{10} c$.

II.4.3 Tension – Secondary creep

The curves presented in Figure II.5 were used to identify the creep parameters under tensile loads. From these curves, it was observed that, as the load decreases and/or the temperature increases, the behavior of the material becomes closer to primary creep. Nevertheless, the primary creep time is small and, as opposed to the compression case, the tensile creep curves presented in Figure II.5 suggest that the secondary creep stage is more pronounced under this loading condition in most of the cases. For this work, a choice was made to neglect the primary creep under tension, since a secondary creep approximation seems to be reasonable and is easier to model and to identified the material parameters.

A critical point regarding the tensile creep tests is the alignment between the sample axis and the loading, to avoid bending loads to appear. Ideally, to monitor if the testing setup is aligned, three extensometers should be used, positioned at an angle of 120° from each other, to check all possible bending directions. This configuration can cause problems related to the positioning of the extensometers for tests at high temperatures, considering that the sample is inside the furnace. If the furnace would be partitioned in three to allow the access to the sample, problems related to heat losses could start to arise.

In this work, two extensometers (called front and rear) were used, which already gives an indication about the alignment of the setup. Figure II.17 shows some examples of the tensile creep tests obtained using the front and rear extensometers, as well as the average between them. Figure II.17a corresponds to an example at 1200 °C, and shows that both extensometers have similar measurements, indicating that the sample was aligned. This is the case for all tests at this temperature.

At 1300 °C, most of the samples showed a good agreement between the front and rear extensometers. Figure II.17b shows the curves for sample 6, and samples 4 and 7 present a similar behavior. Sample 9 at 1300 °C and sample 9 at 1400 °C present a variation between both extensometers (Figure II.17c), but are still under a reasonable accuracy. The only sample presenting a considerable variation between the extensometers since the beginning of the test was sample 4 at 1400 °C (Figure II.17c).

Table II.4 presents the parameters values identified using the procedure described in Section II.3.1 considering all the samples, and Figures II.18, II.19 and II.20 show the resulting plots. For these plots, the upper and lower bounds of the creep curves were not plotted, since the parameters standard deviations were too high, and would make the visualization difficult.

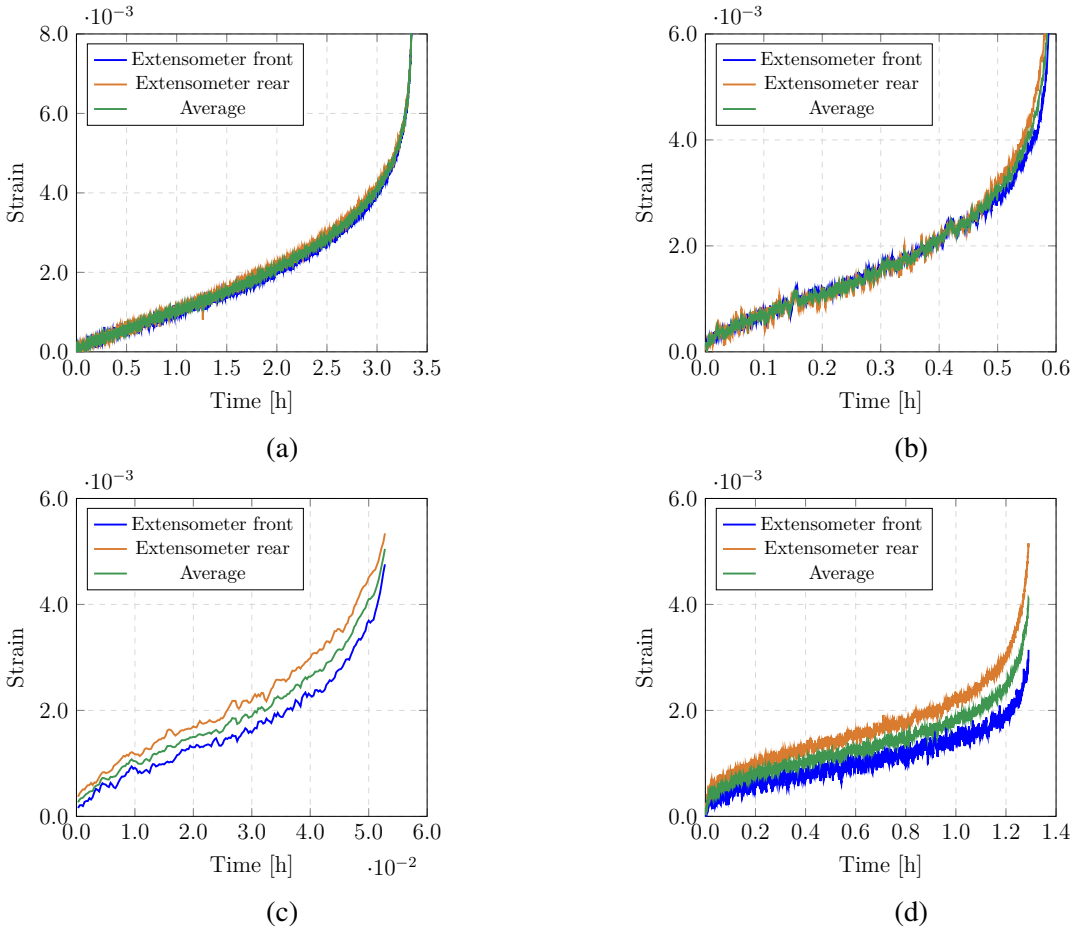

Figure II.17: Tension creep curves – Extensometer front, extensometer rear and average. (a) 1200 °C, sample 2. (b) 1300 °C, sample 6. (c) 1300 °C, sample 9. (e) 1400 °C, sample 4.

Table II.4: Identification results – Tensile creep

Parameter	Average	Std. dev.	70% Conf. interval
	1200 °C		
$\log_{10} A[MPa^{-n}s^{-1}]$	−5.04	0.438	(−5.37, −4.71)
n [–]	2.62	0.894	(1.95, 3.29)
	1300 °C		
$\log_{10} A[MPa^{-n}s^{-1}]$	2.26	1.12	(1.39, 3.14)
n [–]	11.68	1.75	(10.31, 13.06)
	1400 °C		
$\log_{10} A[MPa^{-n}s^{-1}]$	7.49	1.365	(6.42, 8.56)
n [–]	16.64	1.677	(15.33, 17.95)

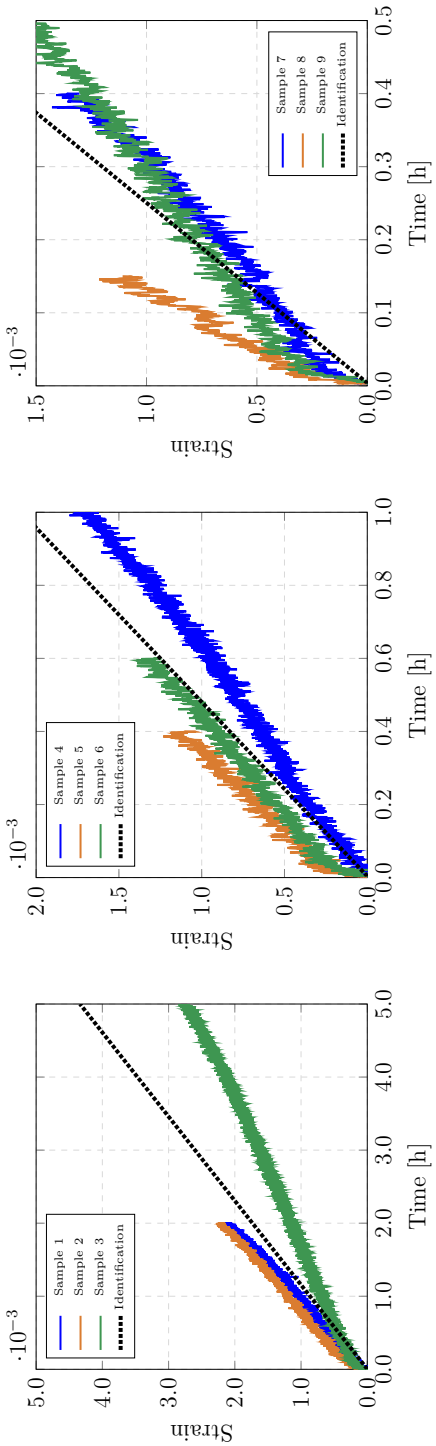

(a) (b) (c)

Figure II.18: Tension at T = 1200 °C. (a) σ = 0.25 MPa. (b) σ = 0.35 MPa. (c) σ = 0.45 MPa

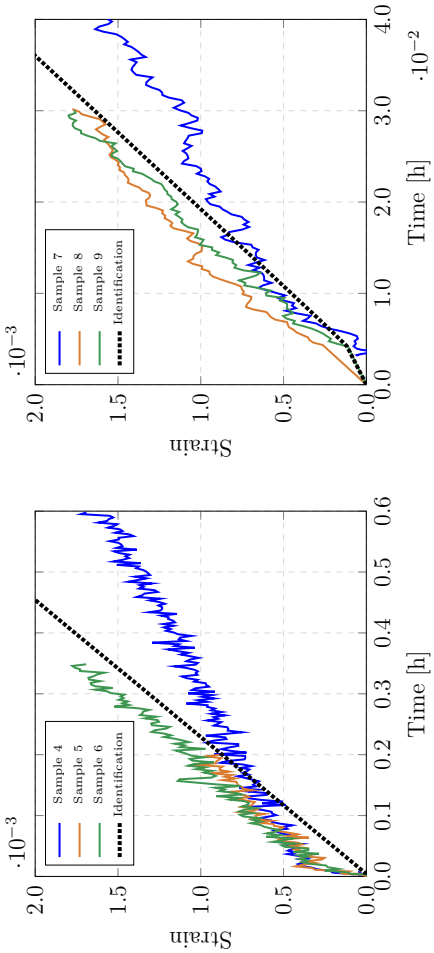

(a) (b)

Figure II.19: Tension at T = 1300 °C. (a)σ = 0.20 MPa. (b)σ = 0.25 MPa

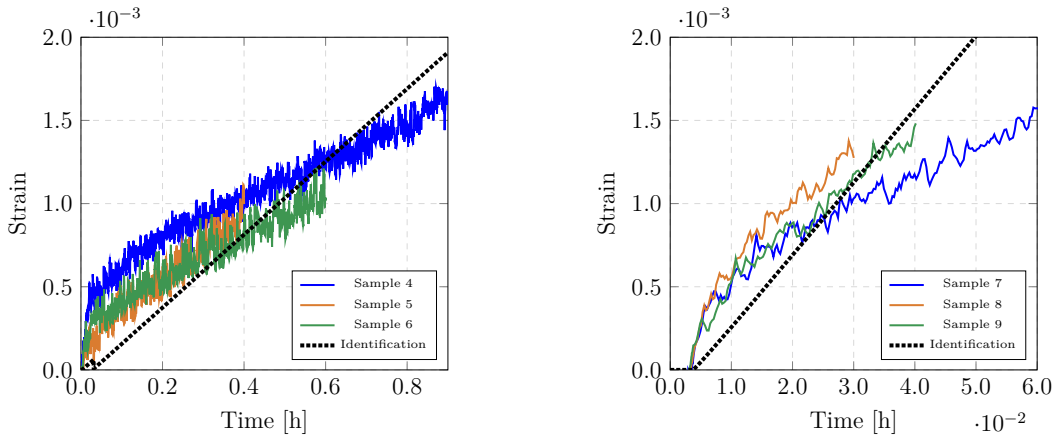

(a) (b)

Figure II.20: Tension at $T = 1400$ °C. (a) $\sigma = 0.15$ MPa. (b) $\sigma = 0.18$ MPa

For the identification at $T = 1300$ °C, the experimental curves obtained at $\sigma = 0.15$ MPa were not considered, since the three samples presented results highly different from each other. This does not cause problems for the identification, since the secondary creep law have only two parameters, and therefore can be identified using curves at two different stresses.

At 1400 °C, when a stress $\sigma = 0.12$ MPa is imposed on the sample, a remarkable primary creep behavior is observed, making the assumption of secondary creep invalid. For $\sigma = 0.15$ MPa and $\sigma = 0.18$ MPa, secondary creep is again dominant. To model this behavior, a transient creep model as the one presented in Section I.4.1.3 needs to be used. Nevertheless, in this work only secondary creep is being considered for tension, therefore the curves at $\sigma = 0.12$ MPa were ignored during the identification, so they didn't cause noise in the results.

For tensile creep, the effects of imperfections in the testing procedures and the heterogeneity of the material are even more influential in the final result. Moreover, as it can be seen in Figure II.5, the difference in the stress levels for the tests in a given temperature is small, so fluctuations on the load can cause unwanted effects.

As in the case of creep in compression, an analysis removing the outlier curves was done. Figures II.21, II.22 and II.23 show the resulting plots with the corresponding lower and upper bounds, and Table II.5 presents the identified parameters and their 70% confidence interval. For the tests at $T = 1400$ °C, even removing the outliers the standard deviation continued to be high, so the bounds were not plotted.

In general, the tensile creep curves also present a high noise in comparison to the measured value, since the strain is low and a portion of the noise is fixed. At the beginning of the test, when the strain is zero, this effect is more pronounced, leading to difficulties in the interpretations of the results, such as the differentiations between a possible primary creep behavior and the noise.

Table II.5: Identification results – Tensile creep with reduced number of samples

Parameter	Average	Std. dev.	70% Conf. interval
	1200 °C		
$\log_{10} A[MPa^{-n}s^{-1}]$	-5.33	0.045	(−5.36, −5.29)
n [−]	1.963	0.1042	(1.88, 2.04)
	1300 °C		
$\log_{10} A[MPa^{-n}s^{-1}]$	2.19	0.124	(2.08, 2.30)
n [−]	11.45	0.190	(11.28, 11.62)
	1400 °C		
$\log_{10} A[MPa^{-n}s^{-1}]$	8.15	0.963	(7.29, 9.00)
n [−]	17.42	1.21	(16.35, 18.49)

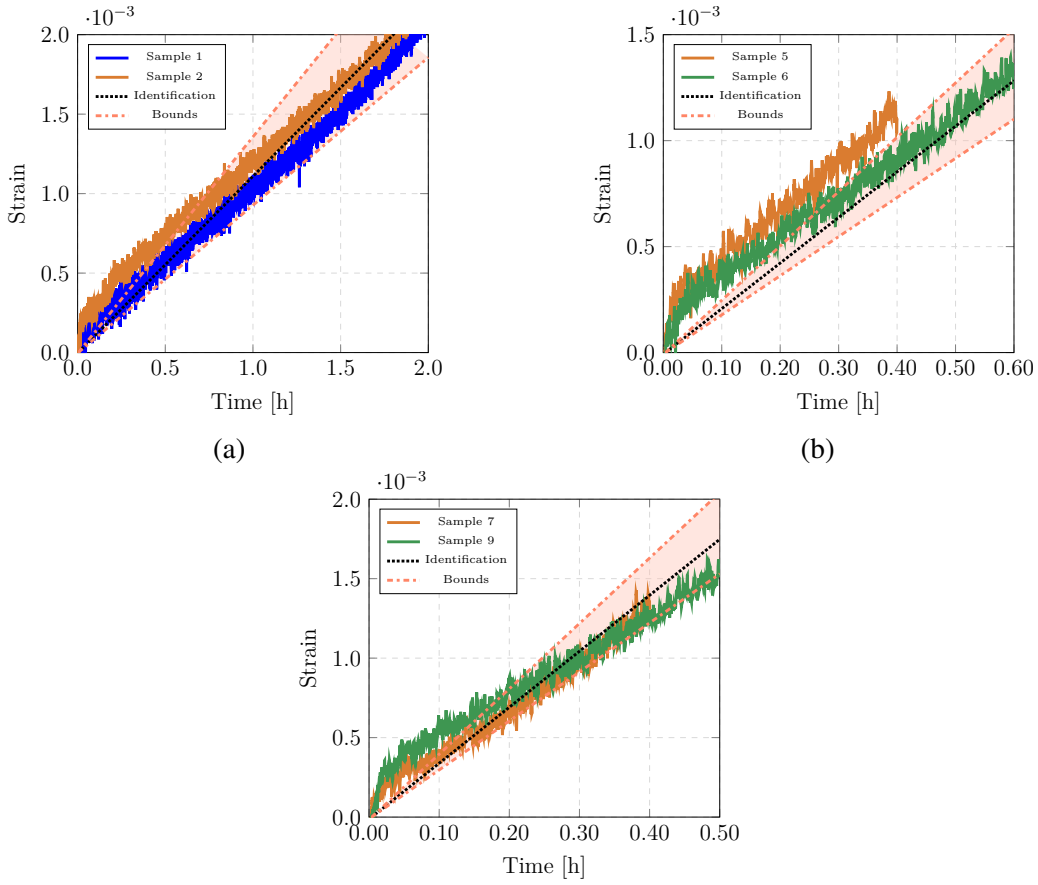

Figure II.21: Tension at T = 1200 °C – Reduced number of samples. (a) σ = 0.25 MPa. (b) σ = 0.35 MPa. (c) σ = 0.45 MPa

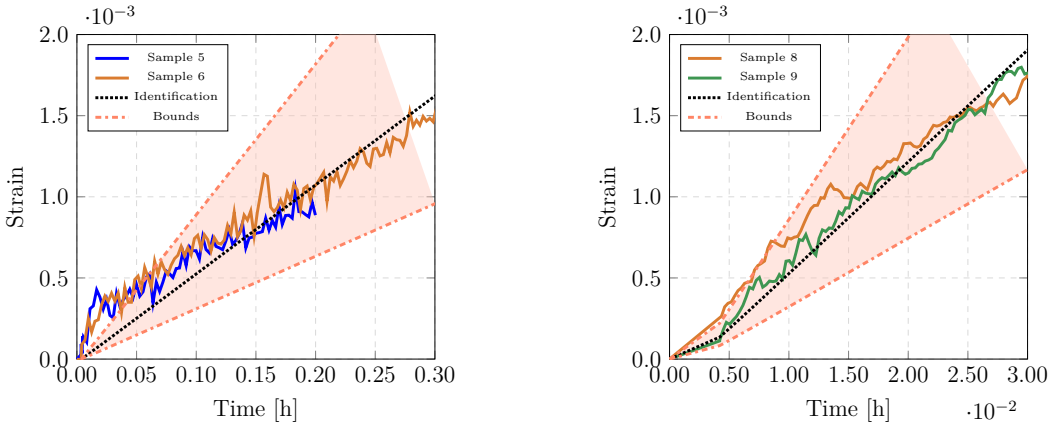

(a) (b)

Figure II.22: Tension at $T = 1300$ °C – Reduced number of samples. (a) $\sigma = 0.20$ MPa. (b) $\sigma = 0.25$ MPa

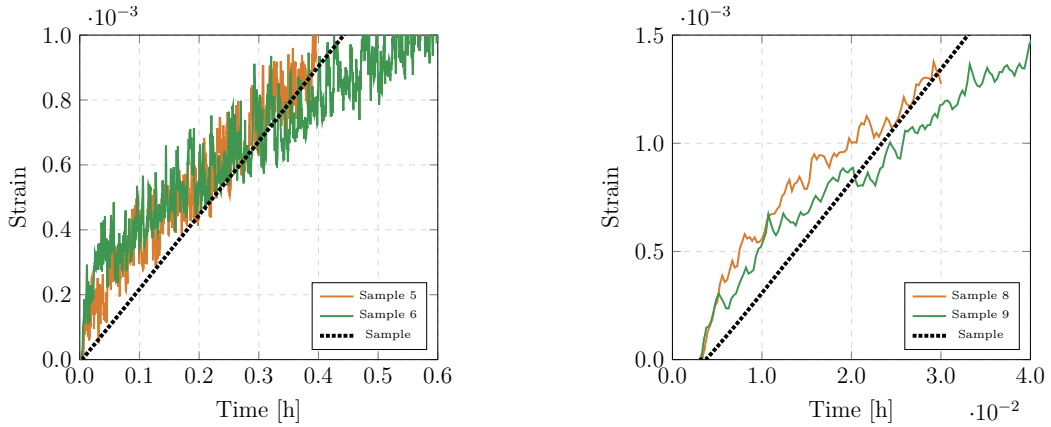

(a) (b)

Figure II.23: Tension at $T = 1400$ °C – Reduced number of samples. (a) $\sigma = 0.15$ MPa. (b) $\sigma = 0.18$ MPa

One particularity of the creep parameters identified under tension is the large difference between their values regarding the temperature variation, as it is evident from Figure II.24. For example, according to this identification procedure, the parameter A varies more than 7 orders of magnitude between 1200 °C and 1300 °C, and the parameter n is approximately 5 times larger at the higher temperature. The difference in the parameter A between 1300 °C and 1400 °C is approximately 12 orders of magnitude. These differences should be taken into account when using the identified values in numerical simulations of real structures, since usually the Finite Element software interpolate the parameters' values at intermediate temperatures other than the ones specified by the user. Therefore, the accuracy of this interpolation should be carefully verified, ideally performing more tests at intermediate temperatures.

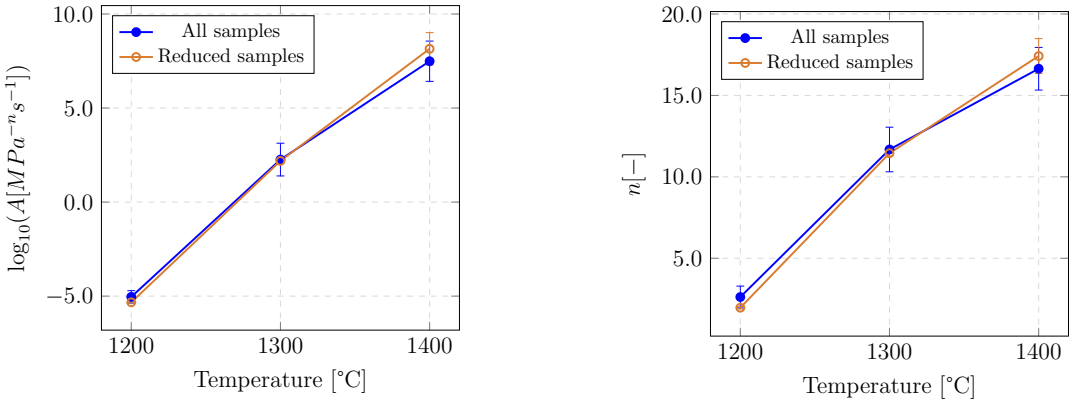

(a) (b)

Figure II.24: Variation of the tension parameters. (a) $\log_{10} A$. (b) n.

II.5 Conclusion

In this chapter, the methodology for the identification of creep parameter using uniaxial tension and compression tests was described and applied to an alumina-spinel brick. The parameters of the material were identified according to a classic Norton-Bailey type creep law, and also according to a kinematic creep law that allows the transition from primary to secondary creep, in the case of compression.

The material being studied presented a large scatter in the experimental curves obtained from the tests, resulting in large values for the parameters standard deviations and, in consequence, a broad 70% confidence interval. This situation could be mitigated by performing more tests for each pair temperature-stress, what is rarely an option for high temperature applications.

It was observed that, from the three curves generally available for each stress in a given temperature in the present study, in some situations two of them presented a good agreement, while the third one presented considerably different strain-time results. To narrow the confidence interval values, it was proposed to exclude from the analysis the curve that deviated from the others, considering that this effect can come from test imperfections and other factors other than the normal material behavior. As highlighted in this chapter, this approach is not ideal, and should be used with care.

The interpretation of the tensile creep curves is particularly challenging, since small changes in temperature and in the applied force can generate large modifications on the output time-strain curve. The heterogeneities in the refractory microstructure, associated with imperfections of the experimental procedure, result in a meaningful instability of the testing procedure, since a crack that might initiate prematurely is likely to propagate at high speed through the refractory matrix.

Although the pure tensile behavior of a material is better characterized using tensile tests, refractory materials rarely have to sustain pure tensile loads during operation, and predictions made using these curves can be excessive if not regarded carefully. In this sense, when the main goal is to model the creep behavior of complex refractory structures, identification procedures using bi-dimensional loads, such as Brazilian or four-point bending tests, may be a suitable option.

CHAPTER III

Proposed Approach for the Modeling and Identification of Creep Parameters – Theory

The goal of this chapter is to propose two new asymmetric creep models to describe the creep behavior of refractories at high temperature, as well as a new approach to identify the creep parameters of refractory materials at high temperatures, based on Digital Image Correlation (DIC) techniques and inverse analysis.

Section III.1 describes the equations of the two asymmetric creep constitutive models, and Section III.2 presents numerical simulation results using the new proposed models, to verify that they behave as expected under theoretical assumptions.

In Section III.3, a literature review of the most used DIC techniques is presented, and the experimental aspects related to mechanical tests and image acquisition is discussed. Finally, a new identification procedure based on an Integrated-DIC technique in combination with Brazilian tests is proposed in Section III.3.5.

Section III.4 presents an analysis of the error function using virtual experiments, in order to evaluate the suitability of the proposed I-DIC method in the identification of the parameters for the asymmetric creep models.

Chapter Contents

III.1 Proposition of new creep models 77
III.1.1 Asymmetric creep model considering primary and secondary creep . . 77
III.1.2 Asymmetric creep model considering transient creep under compression and secondary creep under tension 81
III.2 Numerical simulations using the proposed asymmetric creep models 82
III.2.1 Isotropic creep model 82
III.2.2 Kinematic creep model 96
III.2.3 Application of the proposed models to simulate two bricks of a steel ladle 99
III.3 Digital Image Correlation technique 109
III.3.1 DIC fundamentals 109
III.3.2 Inverse identification of material parameters using DIC techniques . . . 112
III.3.3 Experimental aspects related to mechanical tests and image acquisition . 113
III.3.4 DIC at high temperatures 115
III.3.5 Proposition of an identification procedure using an I-DIC technique combined with Brazilian tests 117
III.4 Analysis of the error function using virtual experiments 124
III.4.1 Influence of images quality 126
III.4.2 Influence of images encoding 128
III.4.3 Influence of the residual function under unstable lightening conditions . 130
III.5 Conclusion 131

III.1 Proposition of new creep models

In the following sections, two new asymmetric creep models are proposed. Both models use the split of the stress tensor described by Blond et al. (2005) to describe the material asymmetry, but they differ in the way to consider the compressive behavior. The first model considers an isotropic creep law to describe the primary creep of refractories under compression, while the second model uses a kinematic approach to consider the transient behavior from primary to secondary creep stages.

III.1.1 Asymmetric creep model considering primary and secondary creep

The compression and tension creep curves presented in Chapter II show the need to develop a constitutive model that is able to represent the asymmetric behavior of refractories, considering primary and secondary creep. To this end, Equation I.15 was adapted following the same principle of the split of the stress tensor in a positive and a negative part, as used by Blond et al. (2005).

The proposed model also differentiates from Blond's model in the way to consider the different contributions of the compression and tensile characteristics of the material. After the decomposition of the stress tensor, the deviatoric and equivalent stresses are calculated for each part (positive and negative) using Equations I.44 and I.45, respectively. Nevertheless, instead of using $\underline{\underline{s}}^{\pm}$ and $\sigma_{eq}^{\pm}$ to calculate directly the positive and negative viscoplastic strain rates (Equation I.46), these values are used to calculate relative weights that each part of the stress tensor have on the total equivalent stress, using the relation:

$$w^{\pm} = \frac{\sigma_{eq}^{\pm}}{\sigma_{eq}^{+} + \sigma_{eq}^{-}} \tag{III.1}$$

Each portion of the viscoplastic strain rate is calculated as a function of the total deviatoric and equivalent stresses (using the full stress tensor, before the decomposition into positive and negative parts) and the respective material properties:

$$\underline{\underline{\dot{\varepsilon}}}^{cr^{\pm}} = f(s, \sigma_{eq}, A^{\pm}, n^{\pm}, m^{\pm}) \tag{III.2}$$

Later, each part of the viscoplastic strain rate is weighted by the values calculated using Equation III.1. Therefore, the viscoplastic strain rate of the proposed asymmetric creep model is

given by:

$$\underline{\underline{\dot{\varepsilon}}}^{cr} = w^{+} \cdot \frac{3}{2}\frac{\underline{\underline{s}}}{\sigma_{eq}} A^{+} \left\langle \sigma_{eq} - \sigma_{y}^{+} \right\rangle^{n^{+}} p^{m^{+}} - w^{-} \cdot \frac{3}{2}\frac{\underline{\underline{s}}}{\sigma_{eq}} A^{-} \left\langle \sigma_{eq} - \sigma_{y}^{-} \right\rangle^{n^{-}} p^{m^{-}} \tag{III.3}$$

This model is also similar to the one developed by Mahnken (2003), explained in Section I.4.2.3, in the sense that it proposes a weighted calculation of the creep strain rate. Nevertheless, the model proposed here can be considered to be more straightforward, and it also requires two less parameters to characterize the creep behavior of a given material, which is an important advantage. This model was implemented in an Abaqus UMAT subroutine, and examples of calculations are shown in the next sections.

It should be noted that, when the material presents primary creep under compression and secondary creep under tension, such as in the case of the alumina-spinel brick whose tensile and compression creep curves were presented in Chapter II, $m^{-} = 0$ in Equation III.3. To summarize, Figure III.1 presents flow charts corresponding to the algorithm proposed by Blond et al. (2005) (full lines) and the algorithm proposed in this work (dashed lines).

III.1.1.1 Numerical difficulties associated with primary creep

At the beginning of a structural simulation, when the load was not yet applied, the strain in the body is assumed to be zero, unless otherwise stated. In this situation, the equivalent plastic strain is $p = 0$. Examining Equation III.5 and taking into account that the variable m can only take negative values, it is easy to deduce that:

$$\lim_{p \to 0} \underline{\underline{\dot{\varepsilon}}}^{cr} = 0 \tag{III.4}$$

Therefore, the equivalent viscoplastic strain can't be defined as zero, since this would result in the absence of creep strain, independently of the applied load. The first solution to this problem is to define a low non-zero value for p. Nevertheless, it is not always clear which value should be used, since the convergence of the simulation is highly dependent of it. In the implemented UMAT subroutine, the integration algorithm according to Benallal et al. (1988) was used. For example, consider a case where only compression creep is considered and $\sigma_y = 0$. Equation III.3 becomes:

$$\underline{\underline{\dot{\varepsilon}}}^{cr} = \frac{3}{2}\underline{\underline{s}} A^{-} \sigma_{eq}^{n^{-}-1} p^{m^{-}} \tag{III.5}$$

Supposing $\underline{\underline{s}}$ and σ_{eq} to have an order of magnitude of 10, $A \approx 1 \times 10^{-10}$, $m \approx -2$, $n \approx 2$ and an initial approximation of $p = 1 \times 10^{-15}$, the resulting creep strain rate would be $\underline{\underline{\dot{\varepsilon}}}^{cr} \approx 1 \times 10^{22}$.

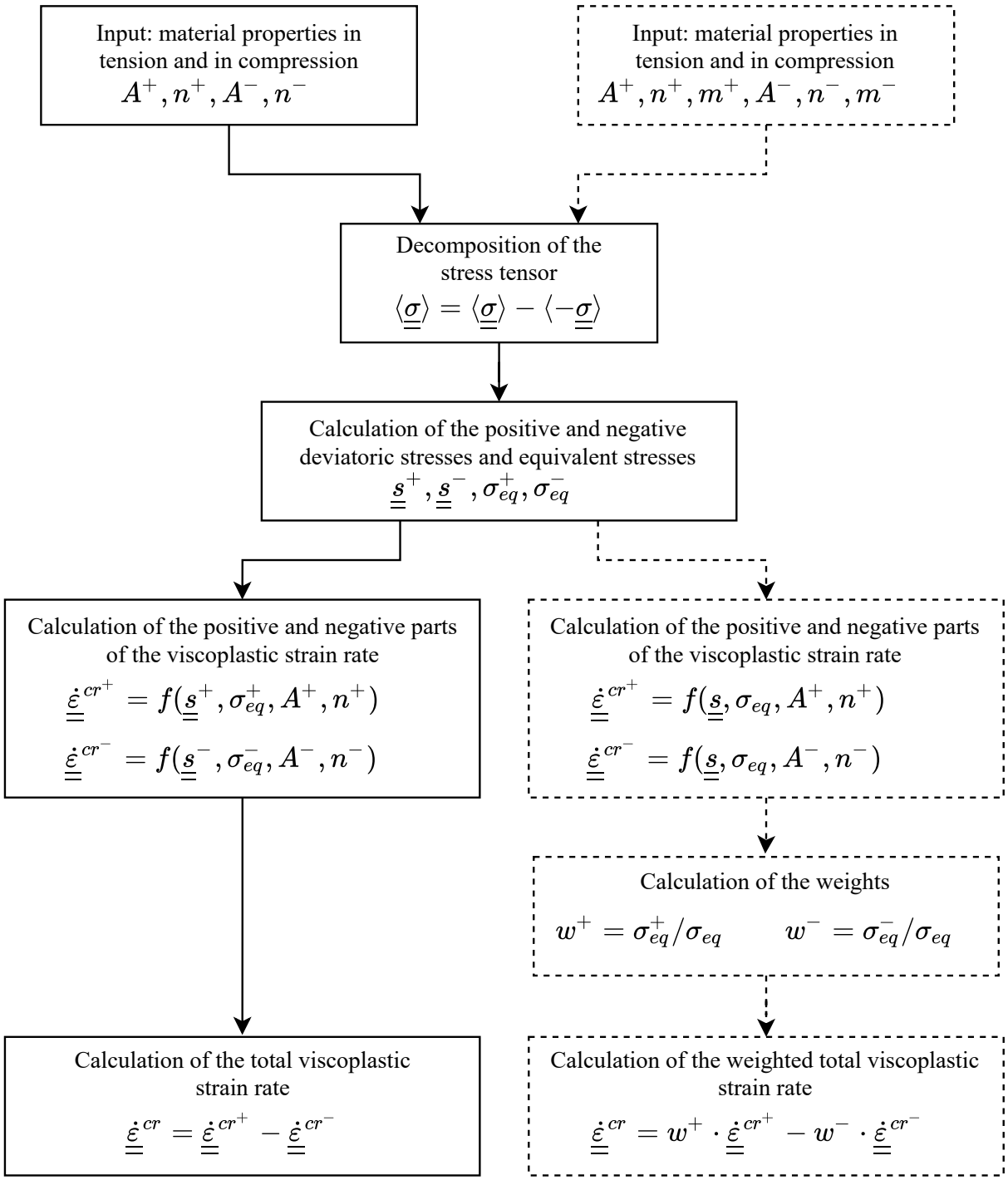

Figure III.1: Asymmetric creep model algorithms. Blond et al. (2005) (full lines) and the proposition of this work (dashed lines)

A high value of initial creep strain rate is expected from primary creep, but at this rate of strain, the integration algorithm would have to use an extremely low value for the time step in order to

converge, which is highly time consuming.

It can be concluded that an initial value of equivalent viscoplastic strain should be used so that it is small enough to don't decrease the accuracy of the solution and large enough to allow the convergence. This value depends on the material properties, the applied loads, the boundary conditions and on the time discretization used during the solution, and can be considerably difficult to estimate. To improve the convergence of the model, the following actions need to be taken:

1. Given the material properties and boundary conditions of the problem, an initial value for p needs to be determined. The convergence of the initial steps of the model is than tested, using a small time increment. If necessary, p should be increased.

2. The time step increment should be small during the first seconds of loading, since the primary creep curve can be very steep at the beginning. It can be interesting to brake the initial steps into smaller pieces, to allow a finer control of the time increment.

3. Even when the initial moments of primary creep are past, the maximum increment of time should be limited to reasonable values, since the automatic time stepping control present in most FEA software can attempt to increase it beyond the convergence limit of the integration algorithm. Even if the software is able to converge, it can take many iterations to finish a step, leading to slower computations.

Even if those measures are taken, the simulation can still diverge due to a rapid change in the creep strain rate. To limit this problem, in the UMAT subroutine used to implement the creep models developed in this work, it was implemented a variable that controls the convergence of the integration algorithm. If the algorithm doesn't converge, the subroutine automatically returns to the previous converged iteration, and tries a time step that is half the previous attempt. This action is only effective if the convergence problem is related to the integration algorithm of the constitutive equations, not to the global Newton-Raphson integration scheme.

It should be noted that, for a material that presents a high creep strain rate, the convergence becomes more difficult, therefore the steps previously enumerated should be adapted. This becomes specially critical during an inverse identification procedure, since several values of material properties are tested, and some combinations of parameters can lead to poor convergence or to divergence of the solution. Therefore, the inverse identification software should be able to handle non-convergent cases without breaking the optimization algorithm.

III.1.2 Asymmetric creep model considering transient creep under compression and secondary creep under tension

An asymmetric model is also proposed to describe the transient creep behavior of refractories under compression, and their secondary creep behavior under tension, based on the split of the stress tensor and on a weighting function dependent on the von Mises equivalent stress.

Equations I.28 become:

$$\begin{cases} \underline{\underline{\dot{\varepsilon}}}^{cr^-} = \dfrac{3}{2}\dfrac{\underline{\underline{\overline{s}}}}{\overline{\sigma}_{eq}} a^- \overline{\sigma}_{eq}^{n^-} \\ \underline{\underline{\dot{\beta}}} = \dfrac{2}{3} b^- \underline{\underline{\dot{\varepsilon}}}^{cr^-} - c^- \alpha_{eq}^{(n^- - 1)} \underline{\underline{\beta}} \\ \alpha_{eq} \equiv \sqrt{\dfrac{3}{2} \underline{\underline{\beta}} : \underline{\underline{\beta}}} \end{cases} \tag{III.6}$$

The creep strain rate associated with the tension stress is:

$$\underline{\underline{\dot{\varepsilon}}}^{cr^+} = \frac{3}{2}\frac{\underline{\underline{s}}}{\sigma_{eq}} A^+ \left\langle \sigma_{eq} - \sigma_y^+ \right\rangle^{n^+} \tag{III.7}$$

Combining Equations III.6 and III.7, the creep strain rate considering transient creep under compression and secondary creep under tension is given by:

$$\underline{\underline{\dot{\varepsilon}}}^{cr} = w^+ \cdot \underline{\underline{\dot{\varepsilon}}}^{cr^+} - w^- \cdot \underline{\underline{\dot{\varepsilon}}}^{cr^-} \tag{III.8}$$

Although the transient creep model requires one more material parameter and includes a more complex set of equations to be integrated, it does not demand the definition of an initial value for the equivalent viscoplastic strain, what is an advantage over the pure primary creep model presented in Section III.1.1.

III.2 Numerical simulations using the proposed asymmetric creep models

To evaluate the capabilities of the asymmetric models proposed in Section III.1, a set of numerical simulations is presented in the next sections, in increasing order of complexity. The goal of these simulations is to verify if the models present the expected behavior when subjected to complex load cases, such as the ones used in the inverse identification of constitutive parameters.

III.2.1 Isotropic creep model

In this section, the numerical simulations using the asymmetric model considering isotropic primary creep in compression and secondary creep in tension are presented. The material parameters used to perform these tests, related to Equation III.3, are shown in Table III.1. These parameters correspond to a simplified approximation of the alumina-spinel material properties at 1300 °C. The compression properties were taken from the uniaxial tests presented in Chapter II, and the tension properties were obtained through a hand-fitting process from the Brazilian test force-displacement curve obtained from the testing machine. Therefore, the curves used to test the models can reasonable represent the reality of refractory materials.

Table III.1: Material parameters used in the numerical simulation tests – Isotropic creep model

Parameter	**Compression (Primary Creep)**	**Tension (Secondary Creep)**
E [MPa]	30000	30000
ν [−]	0.2	0.2
$\log_{10} A[MPa^{-n}s^{-1}]$	−14.16	−5.4
n [−]	3.96	1.5
m [−]	−2.74	0

In the simulations, four situations regarding the type of model and the material parameters were considered:

1. Abaqus symmetric creep model using the compression properties of the material. This configuration is commonly seen in publications related to the creep of refractories (Chapter I).

2. Abaqus symmetric creep model using the tension properties of the material, used as a reference to compare with the asymmetric model.

3. UMAT asymmetric creep model, but using the compression properties of the material for compression and tension, to verify if the asymmetric model specializes to a symmetric one when necessary.

4. UMAT asymmetric creep model, using the corresponding properties for tension and compression.

III.2.1.1 Normal loads with stress reversal in two dimensions

The first model corresponds to a simple linear two-dimensional element with full integration (Figure III.2a) subjected to stresses in directions 1 and 2, according to Figure III.2b. The maximum tensile stress is $\sigma_t = 0.2$ MPa, and the minimum compression stress is $\sigma_c = -2.0$ MPa. Figures III.2c and III.2d show the time periods for which the stresses are kept in the sample.

Although this is a simple model, it represents a situation where, during the loading cycle, there are moments where both principal stresses are positive (Point B), both are negative (Point D), and when there is a composition of positive and negative stresses at the same integration point (Points C and E). Therefore, the model is useful to show the difference between a symmetric and an asymmetric model, as well as the effect of the loading history. For this model, an extra curve using the tension material parameters for both tension and compression material laws is also presented.

Figure III.3 shows the accumulated viscoplastic strains computed in each of the situation previously described. It is possible to observe that, when the same properties are used for tension and compression, the UMAT provides the same results as a symmetric model. More importantly, the asymmetric model presents an intermediate response between the tension and the compression symmetric models, as expected.

In Figure III.3 it is clear that, until approximately 30 min, when only tension stresses are present in the element (Points A and B in Figure III.2), the symmetric and asymmetric models give the same result. From that point further, when an asymmetry is included in the loading (Point C in Figure III.2), the model response changes, becoming an interpolation between the tension and compression behaviors.

III.2.1.2 Brazilian test

Figure III.4 shows the geometry, mesh and boundary conditions used to compare the symmetric and asymmetric models for this loading condition.

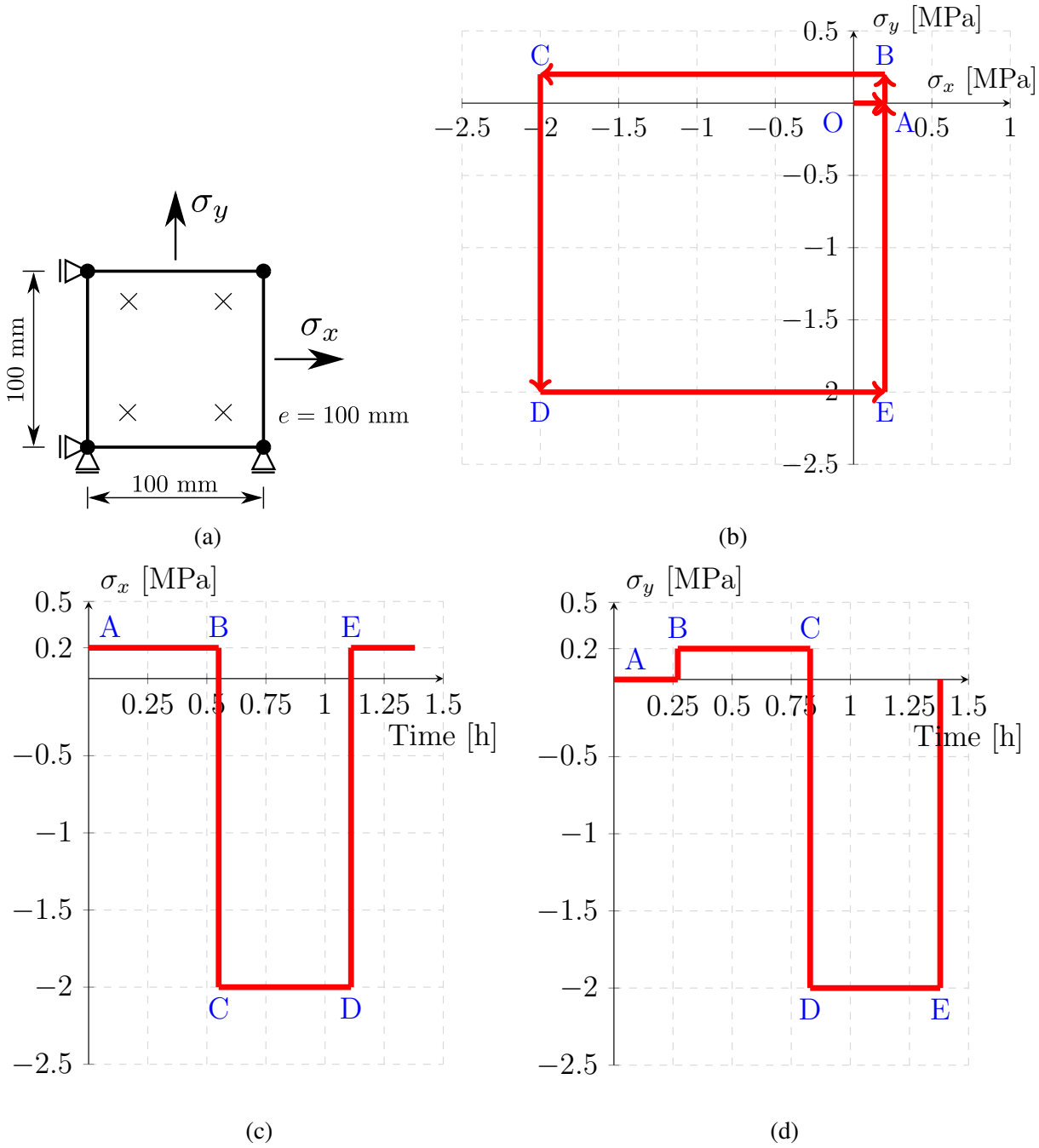

Figure III.2: Stress distribution – Normal loads. (a) Simulation model. (b) Stress path. (c) σ_x vs Time. (d) σ_y vs Time.

The sample was discretized using linear square elements with full integration, unless for a transition zone between the refined mesh in the contact region and the rest of the geometry, where linear triangular elements with full integration were used.

The sample was considered to have 50 mm diameter and 40 mm thickness. An analytic rigid surface is used to distribute the load more evenly on the sample and to avoid excessive stress

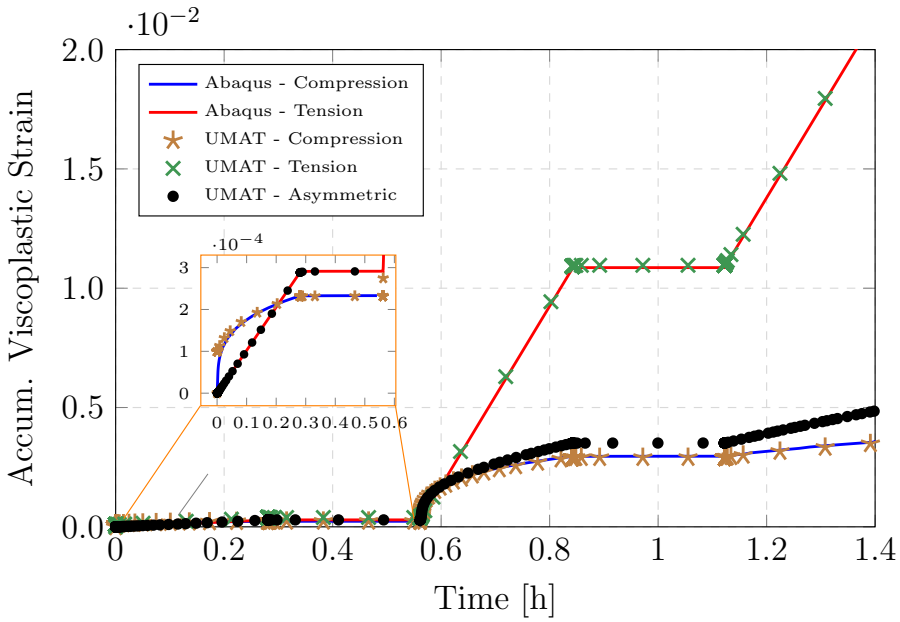

Figure III.3: Accumulated viscoplastic strain – Normal loads.

concentrations. The same strategy is used at the bottom part of the model to restrict the vertical displacement of the sample. This geometry is the same used for the mechanical tests, presented in Chapter IV. Due to the symmetry of the geometry and of the loading, only half of the sample was modeled.

A force of −400 N was applied on the model following a 30 s linear ramp and kept by two hours, resulting in a total of −800 N for the complete geometry. This load is equal to the one applied in the mechanical tests at 1300 °C.

A comparison between vertical and horizontal displacements taken at the center of the sample for the four cases is shown in Figure III.5. It is possible to observe that, when compression curves are used in the asymmetric model, the result is in high agreement with the symmetric model available on the software Abaqus.

One important aspect related to the identification of material parameters using the integrated digital image correlation method is that the experimental procedure needs to present a varied, possibly complex, stress distribution.

Figures III.6 and III.7 show the maximum principal stress and the minimum principal stress on the sample, respectively, for the cases where only tension or compression material parameters were considered (symmetric creep), and the asymmetric case. It can be observed that the maximum tensile stress value obtained on the sample was 0.35 MPa. Since refractory materials are less resistant to tension, this stress limits the amount of force that can be applied before the failure of the sample. The maximum compressive stresses observed on the sample are in

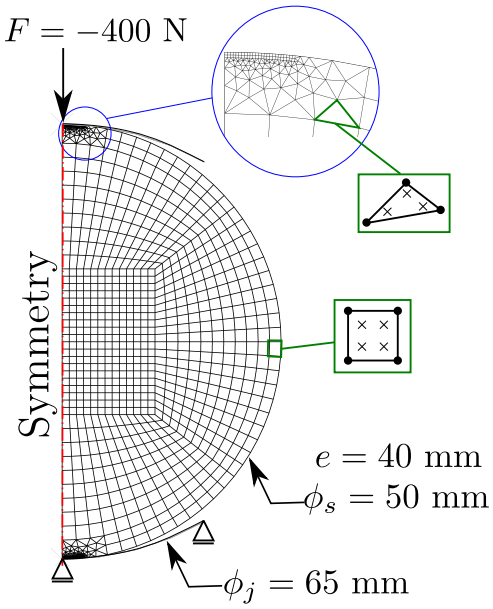

Figure III.4: Brazilian test – Geometry, mesh and boundary conditions.

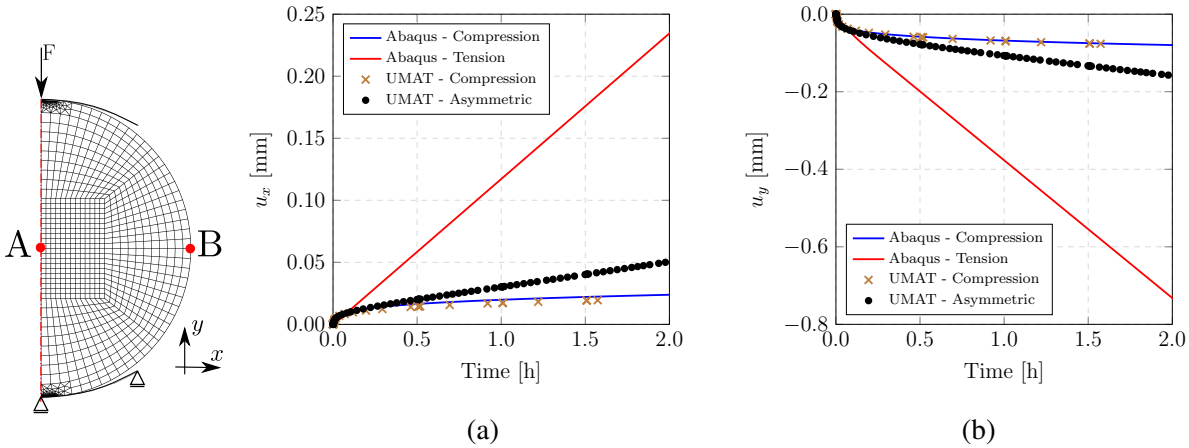

(a) (b)

Figure III.5: (a) Vertical and (b) horizontal displacements in the Brazilian test sample.

the range of −2.5 MPa to −3.8 MPa, although at the center of the sample this value does not go higher than −1.8 MPa. This can be considered as a limitation of the Brazilian test when compared to uniaxial tests, i.e., the tension and compression loads are not decoupled, therefore the material is safely characterized for a smaller stress range. Nevertheless, this only represents a problem if, during operation, the actual compression stresses withstand by the material are considerably higher than the ones during the mechanical tests.

It should be noted that, in Figures III.6 and III.7, the contact zones where excluded from the results display. This was done because, in these regions, the model can experiment stress concentrations, that makes the visualization of the plots more difficult in the other regions of the model. In a real experiment, these regions suffer from a local failure, with the crush of the

grains at the contact with the jaws. This failure can normally be neglected in the experiment, but it can influence the convergence of the numerical model. For instance, the elements with higher stresses present, as a consequence, higher strains, and the model takes longer to converge due to the need of low time steps, even if the bulk part of the sample is still under low stresses. To use the proposed asymmetric model, attention should be payed to such stresses concentration areas, and they should be removed from the model using adequate boundary conditions, if possible.

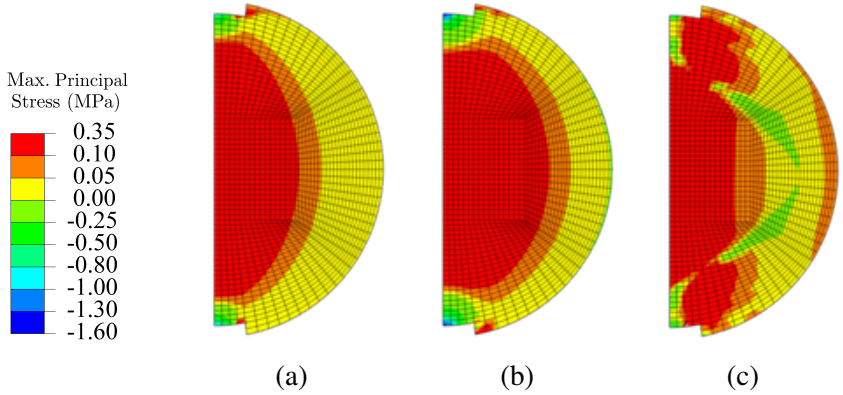

Figure III.6: Maximum principal stress distribution on a Brazilian test sample. (a) compression (b) tension and (c) asymmetric material properties.

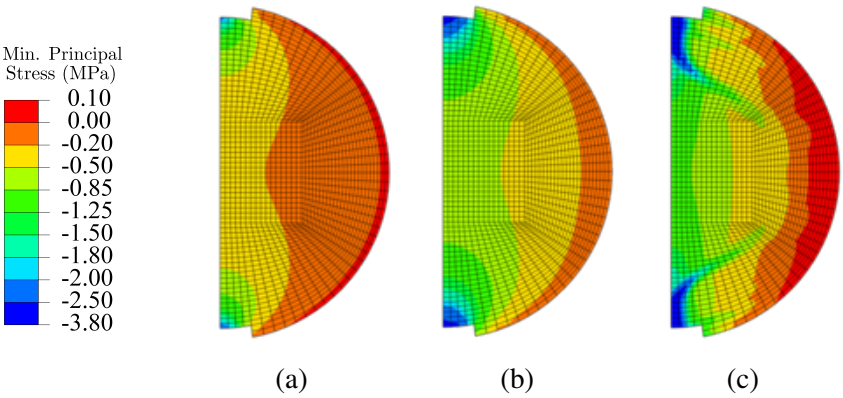

Figure III.7: Minimum principal stress distribution on a Brazilian test sample. (a) compression (b) tension and (c) asymmetric material properties.

When compared to a symmetric model using the compression creep properties, the asymmetric model has a considerably different behavior over time regarding the strains. Figure III.8 shows that, over the central line of the sample, the total strain ε_x, that is mainly positive, is the same for both models at the end of loading (30 s). Nevertheless, after one hour, the strain obtained by the asymmetric model is approximately the double of the one obtained by the symmetric model, and after two hours the ratio between them is around three. The same proportional difference is observed on Figure III.9 for the total strain ε_y, that is compressive. This fact is due

to the averaged sum of the tension and compression creep strain rates applied by the asymmetric model, where the tension part contributes to considerably increase the value of the strains.

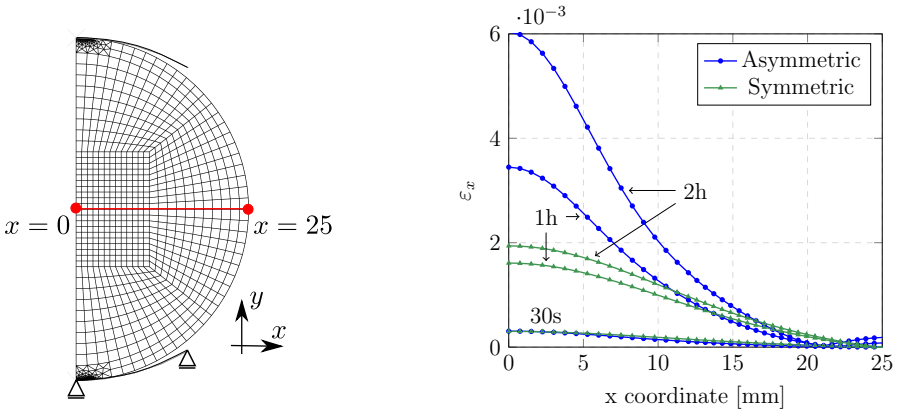

Figure III.8: Variation of the total strain in direction x with time – Symmetric and asymmetric models.

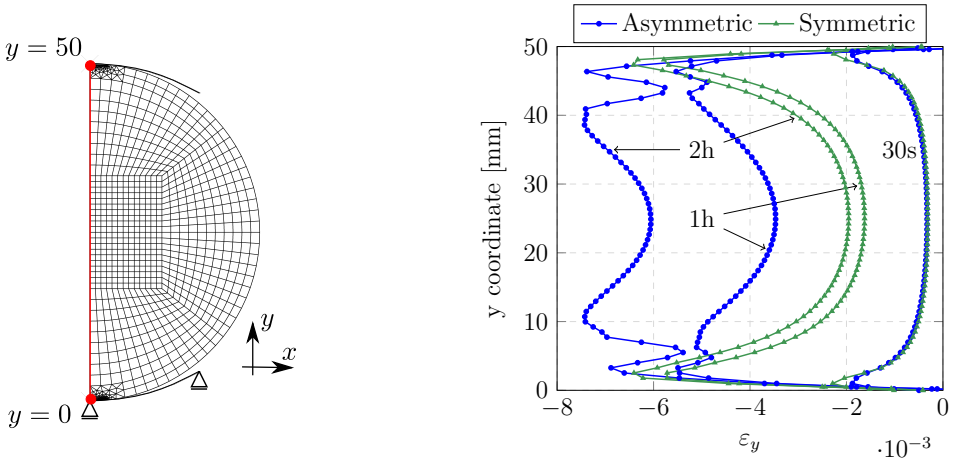

Figure III.9: Variation of the total strain in direction y with time – Symmetric and asymmetric models.

Finally, Figure III.10 shows the effect of the asymmetry in the accumulated viscoplastic strain on a Brazilian test. Once again, the proposed asymmetric model shows an intermediary behavior between the symmetric ones, and evidences the importance of the consideration of the different material properties in tension and in compression.

Influence of the constitutive model parameters To have a better idea on how each of the constitutive model parameters influences the results obtained from a Brazilian test simulation, calculations were made varying one parameter at a time around the absolute values of the nominal properties presented on Table III.1 by −10%, −20%, +10% and +20%. These values are shown in Table III.2. According to what was described in Section I.3.2.5, this is not considered an

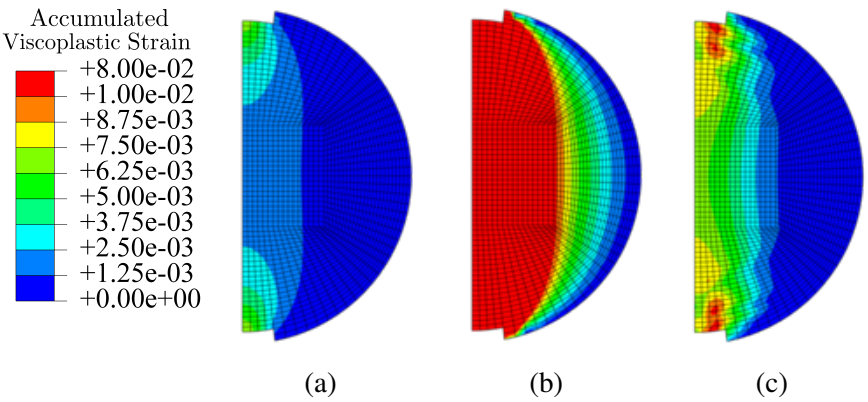

Figure III.10: Accumulated viscoplastic strain distribution on a Brazilian test sample. (a) compression (b) tension and (c) asymmetric material properties.

accurate sensitivity analysis, and the intention is to qualitatively understand how the parameters influence the shape of the time-displacement curves. Figure III.11 shows the variation of the vertical displacement u_2 of the top of the sample as a function of time.

Table III.2: Variation of the material parameters – Isotropic creep model

Parameter	+10%	+20%	−10%	−20%
$\log_{10} A^-[MPa^{-n}s^{-1}]$	−15.57	−16.99	−12.74	−11.32
$n^-[-]$	4.35	4.75	3.56	3.16
$m^-[-]$	−3.01	−3.28	−2.46	−2.19
$\log_{10} A^+[MPa^{-n}s^{-1}]$	−5.94	−6.48	−4.86	−4.32
$n^+[-]$	1.65	1.8	1.35	1.2

Figures III.11a, III.11b and III.11c shows the influence of the compression parameters A^-, n^- and m^-, respectively. The curve with the variation of −20% was not plotted, since the displacement was excessively high, due to the large influence of this parameter in the results. It is possible to observe that parameter n^-, that is an exponent of the stress, has a negligible influence on the results, due to the low values of stresses in this application. Parameters A^- and m^- influence mostly the beginning of the curve, changing its curvature radius, indicating that the compression stresses and predominant during the first hour, and the tensile stresses from this point further. This is an important conclusion, since it helps to decide in which part of the curve the identification procedure will focus, depending on the desired result.

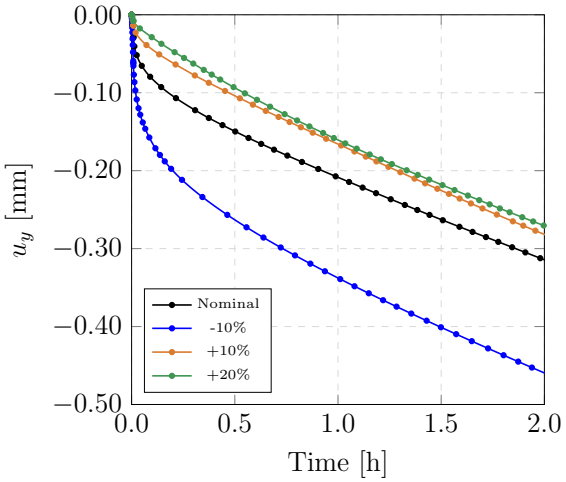

(a) $\log_{10} A^-$

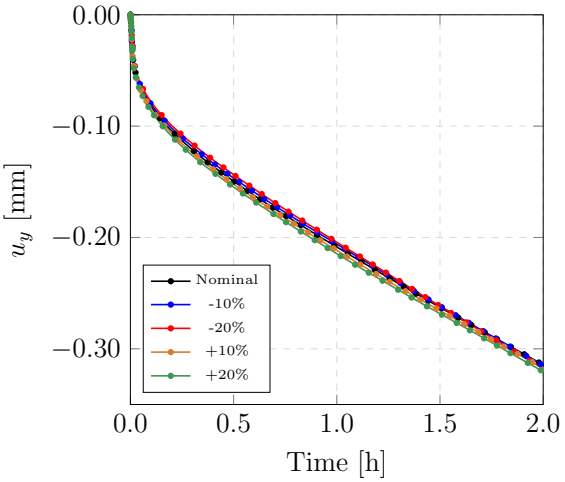

(b) n^-

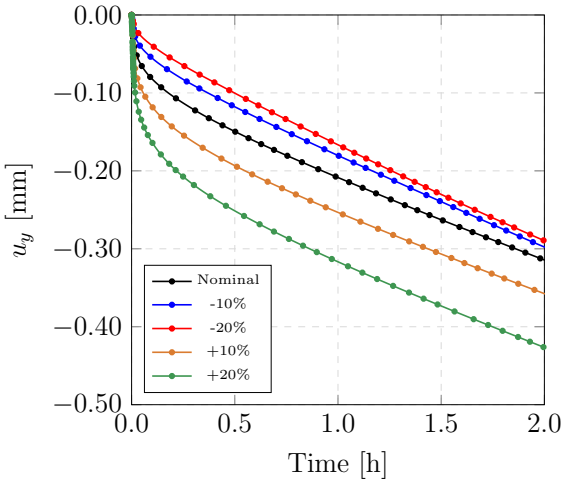

(c) m^-

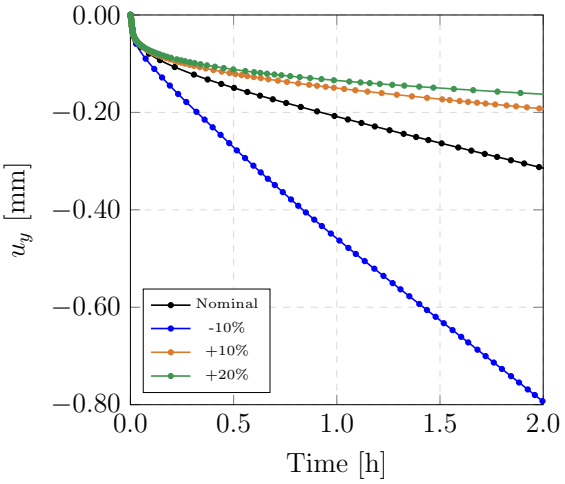

(d) $\log_{10} A^+$

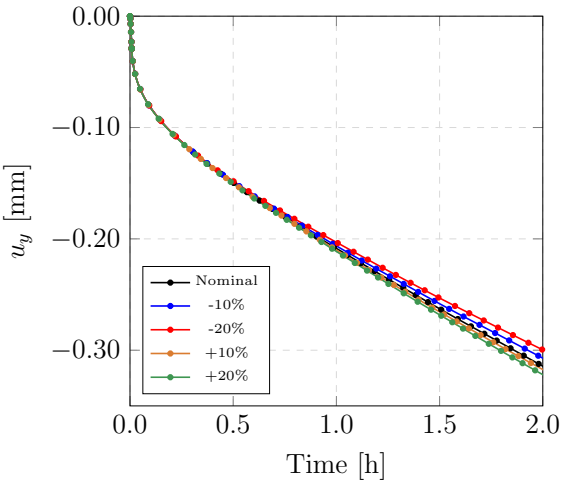

(e) n^+

Figure III.11: Change on the asymmetric creep model response due to variations of the material parameters – Brazilian test.

Similarly, A^+ has the higher influence among the tensile parameters, as can be observed in Figures III.11d and III.11e, although n^+ starts to be influent after one hour of loading and can become more meaningful for longer periods. Contrary to the compressive parameters, the tensile parameters, specially A^+, change mainly the slope of the curve after the initial curvature has passed. Again, this remarkable separation in time between the influence of the tensile and compressive parameters facilitates the inverse identifications.

III.2.1.3 Four-point bending test

Four points bending tests are part of the experimental procedures used to validate the asymmetric numerical models developed in this work, and therefore are studied in this section regarding the different response they present when compared to symmetric models, as explained in Section III.2.

The simulated model corresponds to the same geometry used for the experiments described in Section IV.2.1, and is shown in Figure III.12. The height and the thickness of the sample where considered to have 30 mm, and the length 150 mm. The upper span of the load application rolls was 40 mm, and the lower span of the supports was 120 mm. Due to the symmetry of the model, half of the geometry was modeled.

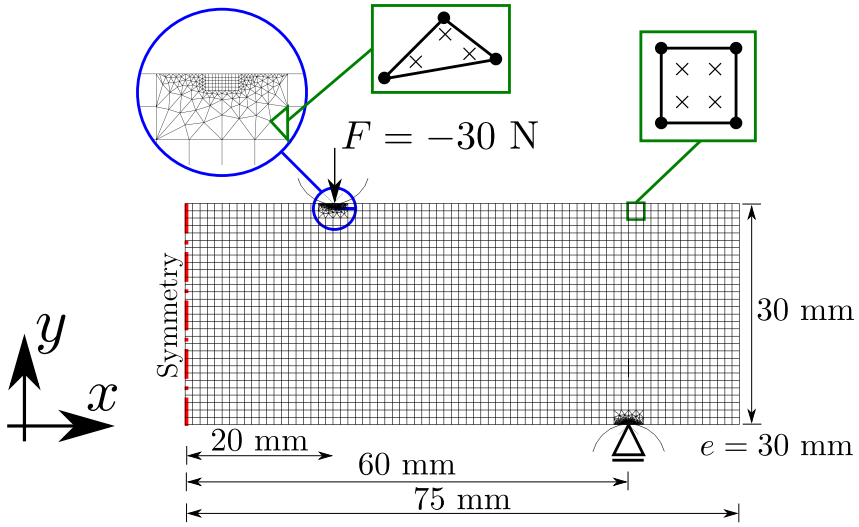

Figure III.12: Four-point bending test – Geometry, mesh and boundary conditions.

To limit the effect of stress concentrations in the contact region, circular analytic surfaces were used to apply the force, similarly to what is made in physical experiments. The force $F = -30$ N was applied as a linear ramp in 30 s, and kept for 2 hours.

The mesh was composed by squared linear finite elements with full integration, except from the transition between the refined contact region to the rest of the sample, that used triangular linear

elements with full integration. Although a quadratic mesh could be more suitable to simulate bending loads, a compromise needed to be made between accuracy and run time, since the asymmetric model can be time expensive. To compensate for the loss of accuracy due to the element order, a refined mesh was used, allowing for a satisfactory solution using a reasonable amount of degrees of freedom.

The four points bending test is an interesting example because it presents tension stresses in the direction perpendicular to the loading in the lower part of the sample, and compression stresses in the upper part of the sample. Therefore, an asymmetric model is expected to present a significantly different structural response when compared with symmetric models.

Figure III.13 shows the difference between the symmetric and asymmetric models in the vertical displacement of the lower point over the symmetry line of the sample. It is possible to notice the similar behavior between Abaqus and UMAT models when symmetric compression properties are used. As expected, the asymmetric model presents a response in between the tension and compression ones.

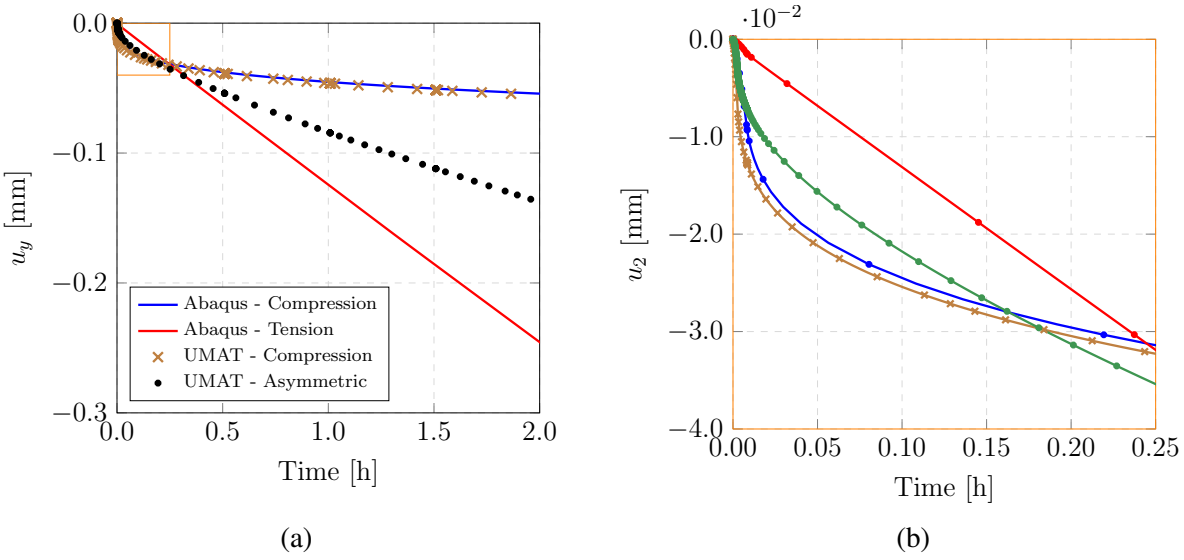

(a) (b)

Figure III.13: (a) Vertical displacement on the lower center point of the four-point bending sample. (b) Detail of the first 15 min.

Figure III.13b corresponds to a detail of the first 15 min of the simulation, showing that, at the beginning of loading, the displacement calculated using compression properties is higher than the one using tension properties, although in the overall case after 1 hour of loading this is not the situation. This comes from the fact that, in compression, a primary creep law is used, which presents a high viscoplastic strain rate at the beginning of the creep response, but that decreases rapidly over time.

Similar to what was observed on the Brazilian tests, Figures III.14 and III.15, show the influence the asymmetric nature of refractory materials have on the stresses and strains distributions when complex loading conditions are applied. It is clear that the use of compression properties largely underestimate the strains in the model, leading to erroneous assumptions about the total life of structures composed by these materials.

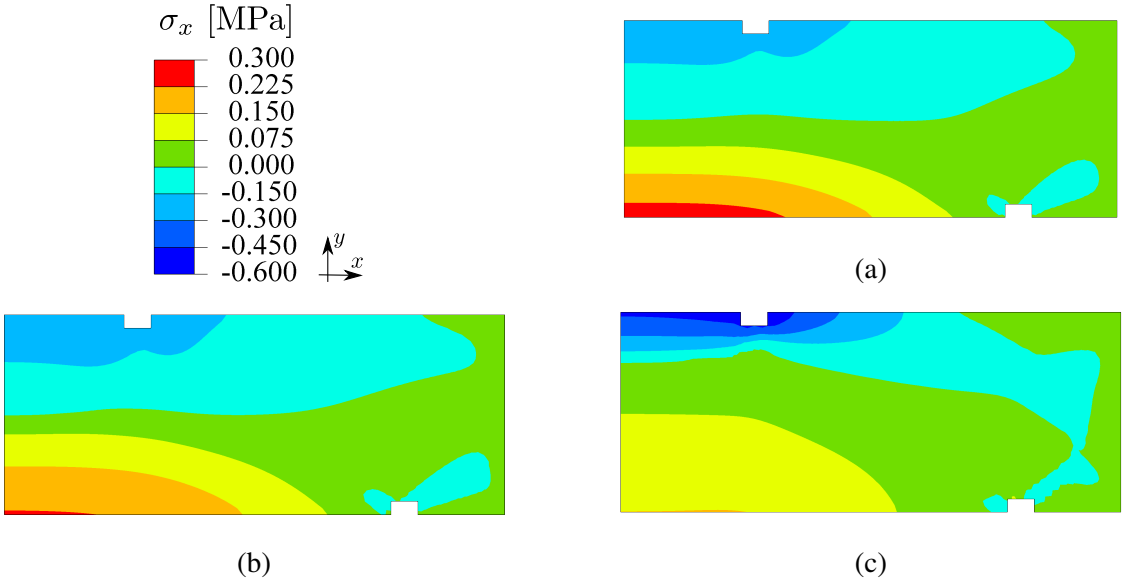

Figure III.14: Distribution of axial stresses on the four-point bending test sample. (a) Symmetric – Compression. (b) Symmetric – Tension. (c) Asymmetric.

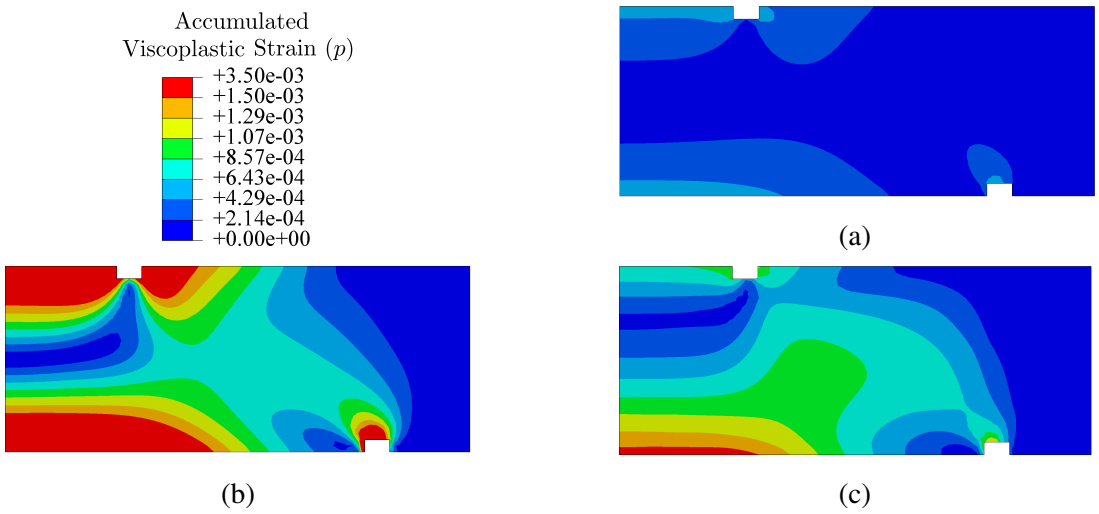

Figure III.15: Distribution of accumulated viscoplastic strain on the four-point bending test sample. (a) Symmetric – Compression. (b) Symmetric – Tension. (c) Asymmetric.

The creep model also induces a change in the position of the neutral line in the model, i.e., the vertical position where the stress $\sigma_x = 0$. Figure III.16 shows the variation of σ_x over the

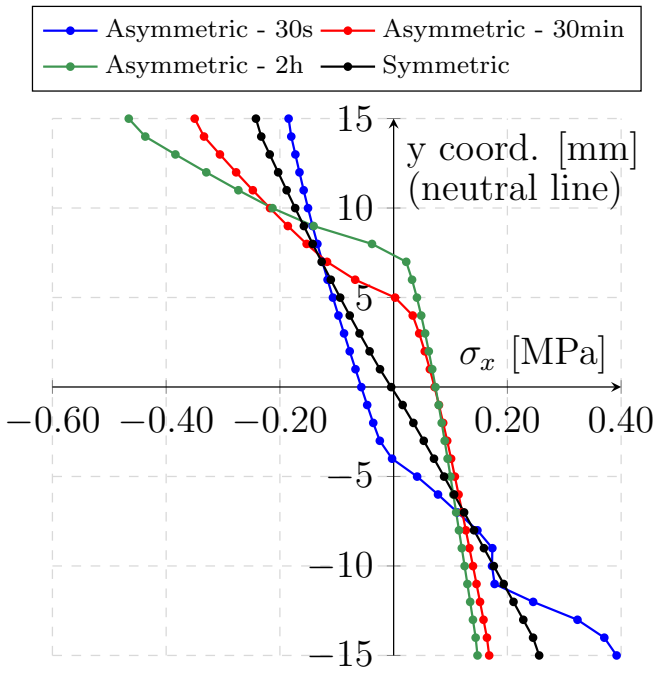

Figure III.16: Variation of the neutral line's position on the four-point bending sample over time.

coordinate y in the vertical symmetry line of the sample (Figure III.12) for the asymmetric creep model and for a symmetric model.

It is possible to observe that the initial position of the neutral line (where the plot crosses the y-axis) is locate below the center of the sample after 30 s, when the influence of the primary creep (compression properties) is higher than that of the secondary creep (tension properties). After 30 min of loading, this position is located approximately 5 mm above the center of the sample, and after 2 h it is located 7.5 mm above the center. This suggests that, during the four-point bending test, some portions of the sample experience load reversal, even if there are no loading-unloading cycles.

Influence of the constitutive model parameters Similar to what was done for the Brazilian test, the influence of the constitutive parameters was evaluated for the isotropic creep model applied to four-point bending tests, as shown in Figure III.17. The used material parameters were the same as shown in Table III.2.

Once again, the most influent parameters were A^-, m^- and A^+. In Figure III.17a, the case corresponding to −20% was not plotted, since the displacements were excessively high. As in the case of the Brazilian test, the tensile parameters showed to be more influent after the initial moments of the test have passed, and the slope of the curve from this point on is not significantly influenced by the compression parameters anymore.

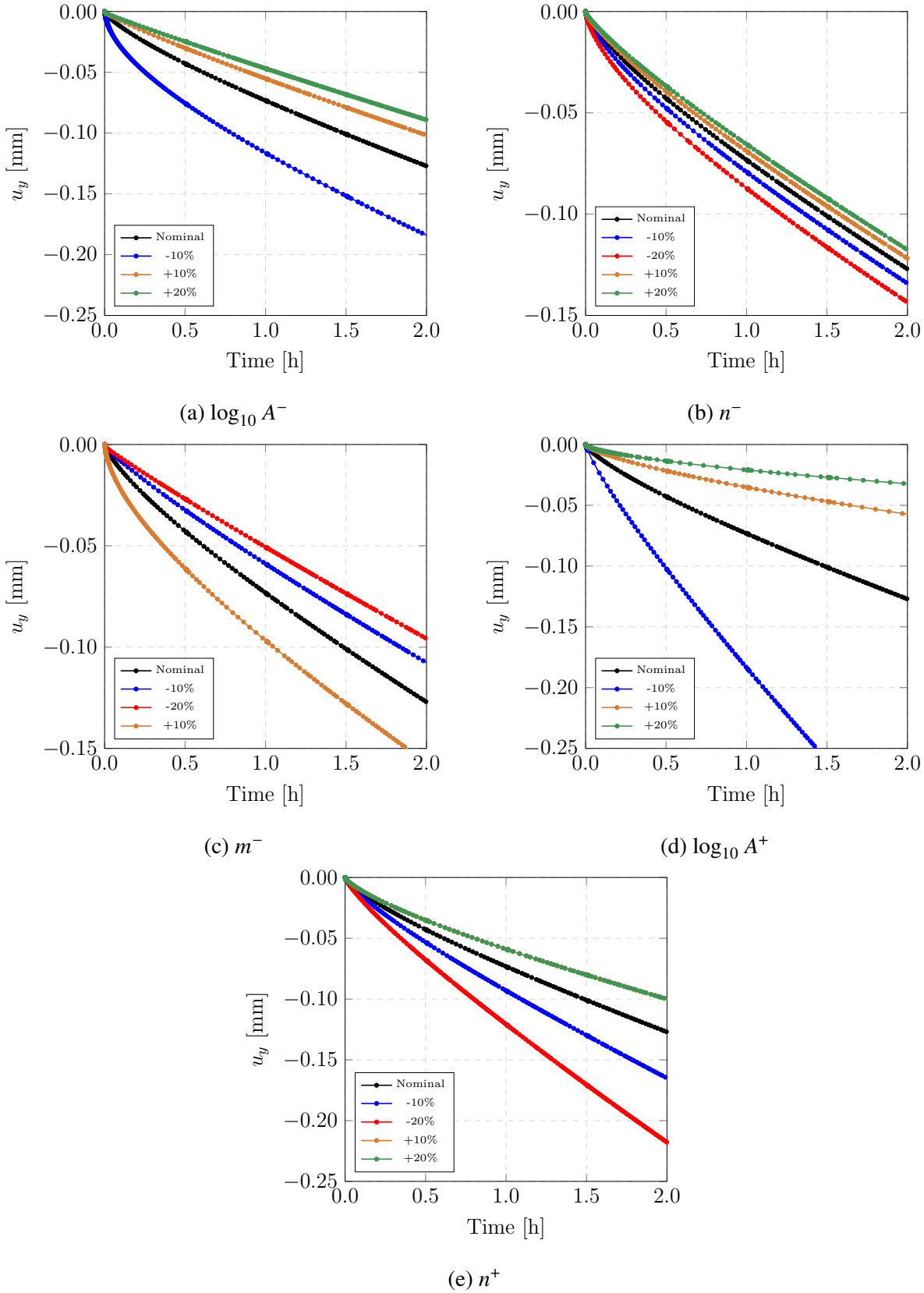

(a) $\log_{10} A^-$

(b) n^-

(c) m^-

(d) $\log_{10} A^+$

(e) n^+

Figure III.17: Change on the asymmetric creep model response due to variations of the material parameters – Four-point bending test.

III.2.2 Kinematic creep model

Similar to Section III.2.1 for the isotropic creep model, the Brazilian test and the four-point bending test were simulated using the kinematic creep model proposed in Section III.1.2. The finite element models used in these simulations were presented in Sections III.2.1.2 and III.2.1.3.

In the case of the asymmetric kinematic creep model, a comparison with a commercial FEA code is not possible, since transient creep is not implemented in the software used in this work. Therefore, the analyzes presented in this section focus on the verification of the influence of each parameter of the constitutive model on the simulation results. Table III.3 shows the nominal constitutive parameters used for the reference simulations, and Table III.4 shows ther variations.

Table III.3: Material parameters used in the numerical simulation tests – Kinematic creep model

Parameter	**Compression (Transient Creep)**	**Tension (Secondary Creep)**
E [MPa]	30000	30000
ν [−]	0.2	0.2
$\log_{10} a[MPa^{-n}s^{-1}]$	−6.314	–
$\log_{10} b[MPa(1+scMPa^{n-1})]$	2.562	–
$\log_{10} c[MPa^{-n}(MPa+b)/s]$	−5.01	–
$\log_{10} A[MPa^{-n}s^{-1}]$	–	−7.0
n [−]	1.981	1.5

Table III.4: Variation of the material parameters – Kinematic creep model

Parameter	**+10%**	**+20%**	**−10%**	**−20%**
$\log_{10} a[MPa^{-n}s^{-1}]$	−6.94	−7.57	−5.68	−5.05
$\log_{10} b[MPa(1+scMPa^{n-1})]$	2.81	3.07	2.30	2.05
$\log_{10} c[MPa^{-n}(MPa+b)/s]$	−5.51	−6.01	−4.51	−4.00
n^- [−]	2.17	2.37	1.78	1.58
$\log_{10} A^+[MPa^{-n}s^{-1}]$	−7.7	−8.4	−6.1	−5.6
n^+ [−]	1.65	1.8	1.35	1.2

From Figures III.18a and III.19a, it is possible to observe that the parameter a^- influences the entire time x displacement curve, contrary to what was observed with the isotropic creep model, what makes the identification of material parameters more difficult.

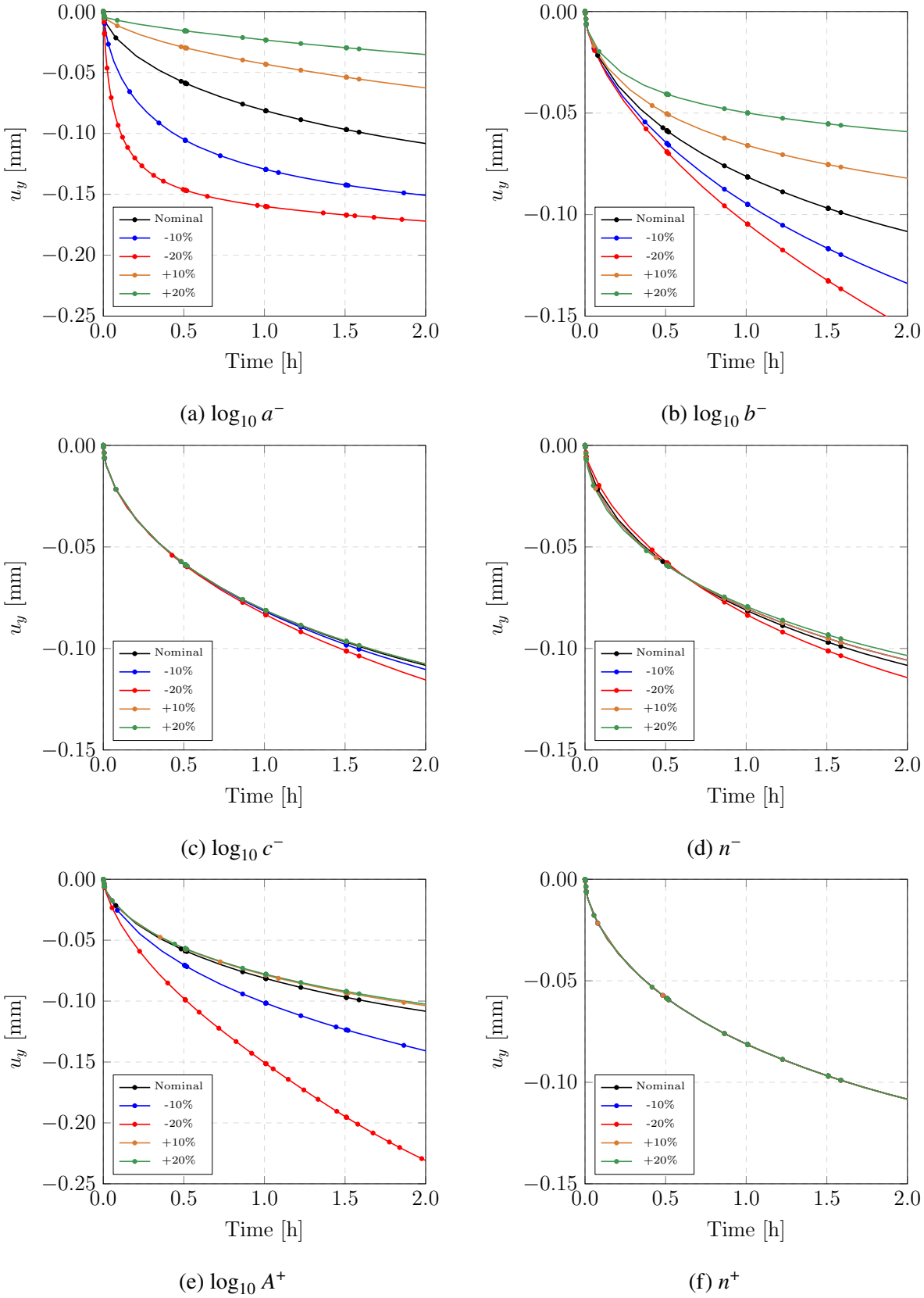

(a) $\log_{10} a^-$

(b) $\log_{10} b^-$

(c) $\log_{10} c^-$

(d) n^-

(e) $\log_{10} A^+$

(f) n^+

Figure III.18: Change on the kinematic asymmetric creep model response due to variations of the material parameters – Brazilian test.

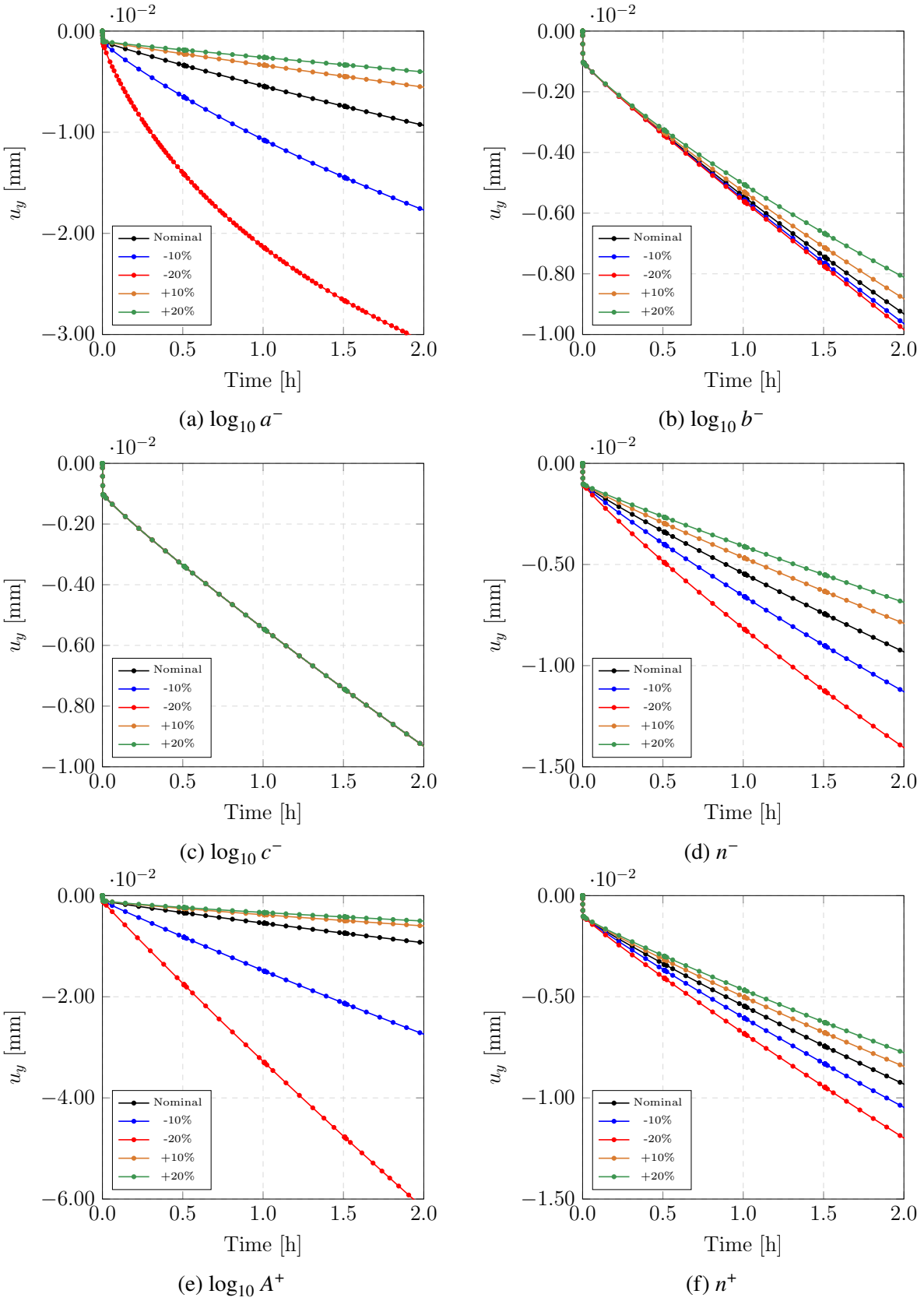

(a) $\log_{10} a^-$ (b) $\log_{10} b^-$

(c) $\log_{10} c^-$ (d) n^-

(e) $\log_{10} A^+$ (f) n^+

Figure III.19: Change on the kinematic asymmetric creep model response due to variations of the material parameters – Bending test.

Figures III.18b and III.19b show that parameter b^- has a higher influence on the Brazilian test than on the four-point bending test, and therefore would be more easily identified using the first one. Conversely, from Figures III.18f and III.19f it is observed that the parameter n^+ has a higher influence on the bending test.

To better illustrate the effect of the material parameters on the response of the kinematic creep model, Figures III.20 and III.21 show the distribution of the principal stresses in the first principal direction (direction I) for the bending and brazilian tests, respectivelly. For each test, the stress field obtained using the nominal material properties is compared to the cases for which the absolute values of the parameters a^- and A^+ are decreased by 20%.

Although Figures III.18 and III.19 show a remarkable difference on the displacements when the parameters change, the stresses do not vary in the same proportion. This illustrates the sensitivity of the creep law to the stress values, i.e., small changes in the stress values can result in a large variation of the displacements and strains.

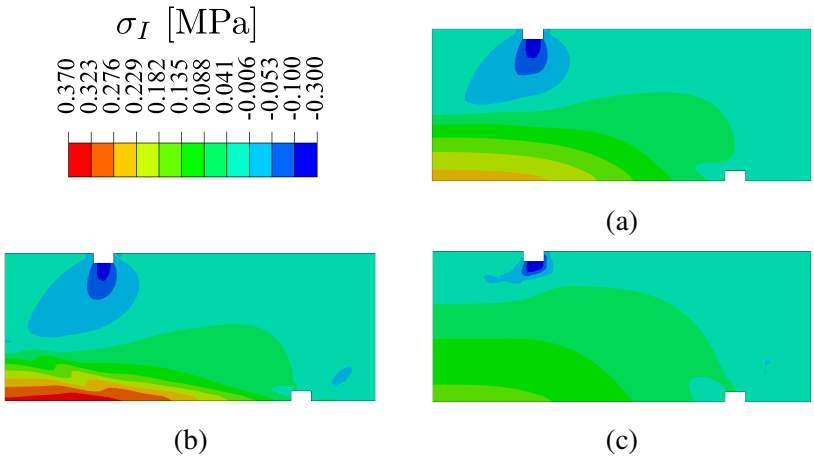

Figure III.20: Bending test: Maximum principal stress in direction I at $t = 2h$ using the kinematic creep model. (a) Nominal material parameters. (b) $a^- - 20\%$. (c) $A^+ - 20\%$.

III.2.3 Application of the proposed models to simulate two bricks of a steel ladle

To show the capabilities of the proposed models, a thermo-mechanical simulation of the interactions between two bricks in a steel ladle is presented in the next sections. Despite the relative simplicity of the model, it is able to provide a first accurate calculation during the design phase of a refractory lining, and it has been extensively used in the literature (Gruber et al., 2007; Gruber & Harmuth, 2008, 2014; Jin et al., 2020; Jin et al., 2011).

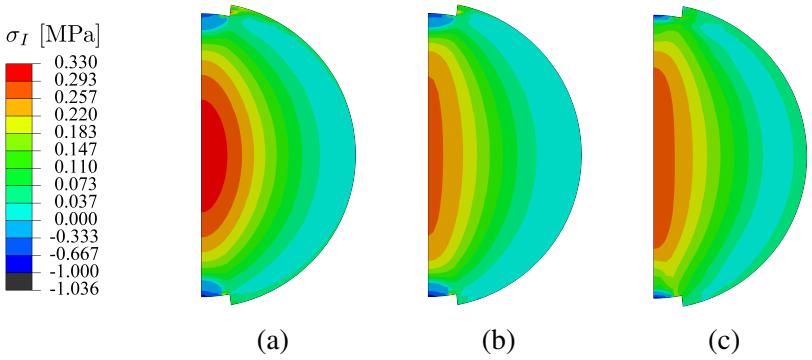

Figure III.21: Brazilian test: Maximum principal stress in direction I at $t = 2h$ using the kinematic creep model. (a) Nominal material parameters. (b) a^- – 20%. (c) A^+ – 20%.

III.2.3.1 Simulation Model

The steel ladle is a complex thermo-mechanical system, as explained in Chapter I, and the simulation of the full geometry considering the interactions between all bricks is beyond the scope of this work. The simulation model used to perform the calculations is illustrated in Figure III.22, and described in details below.

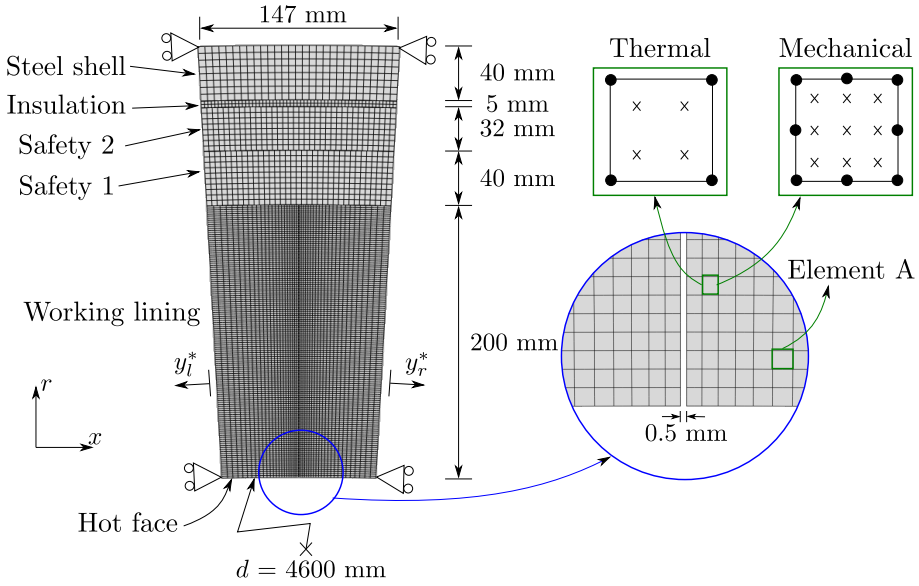

Figure III.22: Mesh and boundary conditions for the simulations of the steel ladle.

Geometry and mesh The geometric model is composed of two half-bricks at the working lining, corresponding to the alumina-spinel brick studied in this work, two safety linings, an insulation layer and the steel shell. The dimensions of each layer can be seen in Figure III.22. To account for the imperfections in the contact between the bricks, a 0.5 mm gap was considered in the undeformed configuration. The thermal problem was modelled using two-dimensional

linear square elements, with four integration points. For the mechanical problem, eight-nodes square elements under plane strain assumption and nine integration points were used.

Loads and boundary conditions A heating phase and ten thermal cycles were applied to the model. Each cycle consisted of a thermal shock (when the liquid steel starts to be in contact with the relatively cold working lining), a steel treatment phase (permanent contact of the molten steel with the hot face) and a waiting phase (when the ladle is empty and waiting for the next cycle).

Convection boundary conditions are applied at the working lining hot face, according to Table III.5, and at the steel shell outer layer, with constant values of convection coefficient and sink temperature equal, respectively, to $h_s = 10$ W/m°C and $T_s = 25$ °C. All other boundaries are considered to be adiabatic, and the initial temperature of the entire model is defined as 25 °C.

Table III.5: Convection coefficients and sink temperatures for each phase of the thermal cycle

Phase	**Convection coeff. [W/m^2 °C]**	**Sink temperature [°C]**
Heating	15	1300
Thermal shock	100	1650
Treatment	100	1650
Waiting	15	400

For the mechanical calculations, sliding conditions were defined at the left and right borders of the domain ($y_l^* = 0$ and $y_r^* = 0$), and the previously calculated temperature field was imposed following a weakly coupled scheme. The ladle was free to expand in the radial direction r, and a friction coefficient $f = 0.3$ was considered for all contacts.

Material properties The thermo-elastic material properties used for the simulations are shown in Table III.6. To identify the material's Young's modulus, two compression test were made at 1300 °C. A pre-load of 1.71 MPa was applied on the sample at room temperature, and the machine was put under force control during heating, resulting in a stress-free expansion. Figure III.23 shows the tests' results, as well as the interpolated stress-strain curve using the identified Young's modulus of $E = 2$ GPa.

To represent the compressive creep behavior considering the proposed kinematic asymmetric model, the parameters providing the best fit for the Brazilian test, presented in Table IV.2, were used. The compressive creep parameters for the isotropic creep model, as well as the tensile creep parameters used for both models, are presented in Table III.7.

Table III.6: Thermo-elastic material properties used in the numerical simulations.

	Brick	**Safety 1**	**Safety 2**	**Insulation**	**Steel**
Density [kg/m^3]	2860.0	2500.0	2400.0	1000.0	7800.0
Conductivity [W/m°C]	2.0	1.0	1.5	0.5	54.7
Specific Heat [J/kg°C]	900.0	1000.0	1300.0	1000.0	500.0
Thermal Exp. [10^{-6}/ °C]	6.9	3.0	3.6	1.0	1.5
Elastic Modulus [GPa]	2.0	20.0	20.0	10.0	190.0
Poisson ratio [−]	0.2	0.2	0.2	0.2	0.3

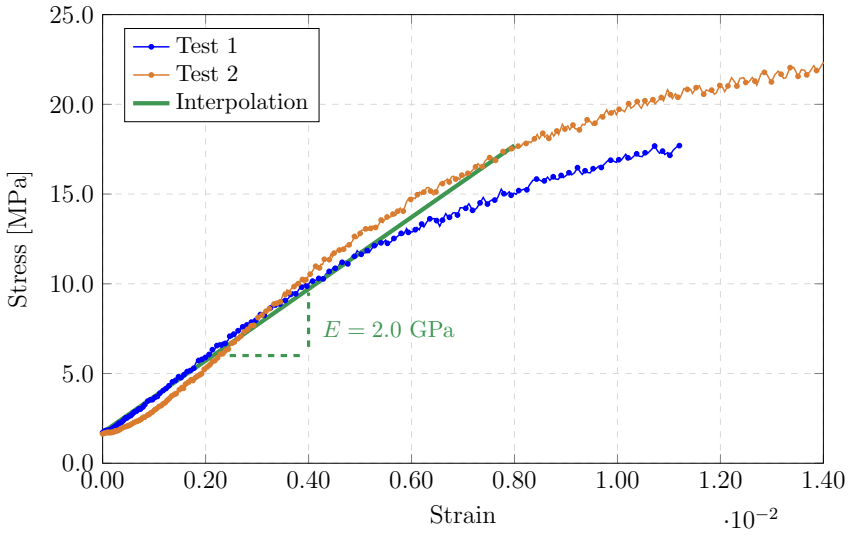

Figure III.23: Compression tests for the identification of the elastic properties.

Table III.7: Isotropic compressive creep and tensile creep parameters

Parameter	**Compression**	**Tension**
$\log_{10} A\,[\mathrm{MPa}^{-n} s^{-1}]$	−14.86	−5.55
n[−]	3.96	1.5
m[−]	−2.74	0

III.2.3.2 Simulation Results

Figure III.24 shows the temperature distribution over time at the brick's hot face, cold face and center position. During the heating phase, the maximum temperature obtained in the brick was 800 °C, which generated a temperature increase of approximately 550 °C during the first thermal shock. At the 10$^{\text{th}}$ cycle, the thermal shock was reduced to approximately 400 °C.

The dashed lines in Figure III.24 show the temperatures in each of the three positions of the

brick when steady-state conditions are obtained. As it can be observed, even after 10 thermal cycles, only the hot face achieved the maximum possible temperature for the imposed boundary conditions, which shows the importance of considering transient thermal conditions in the calculations.

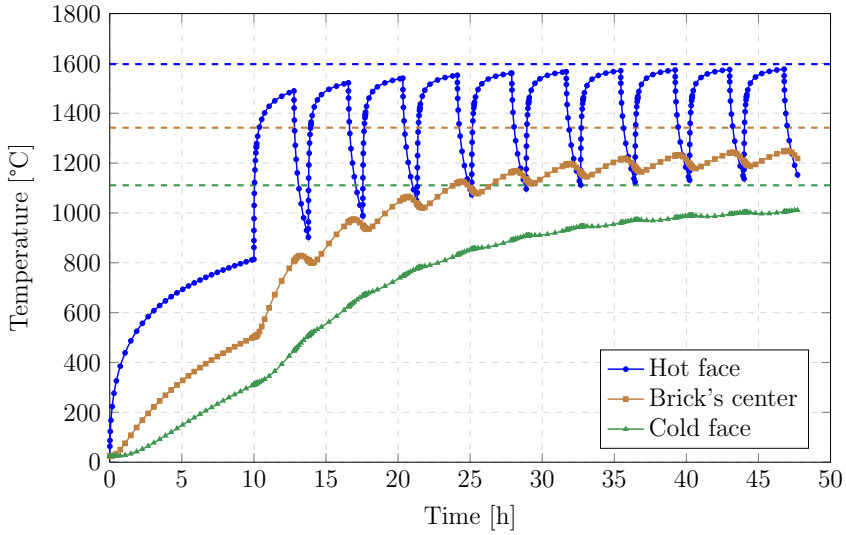

Figure III.24: Temperature distribution over time at the brick's hot face, cold face and center position.

Figure III.25 shows the spacial temperature distribution in the brick for the 5th thermal cycle. At the end of the thermal shock, the temperature varies from 1434 °C at the hot face and 856 °C at the cold face, which results into a large variation of the thermal expansion and of the mechanical properties, including zones with and without creep. At the end of the waiting period, the entire brick is at a temperature below 1200 °C.

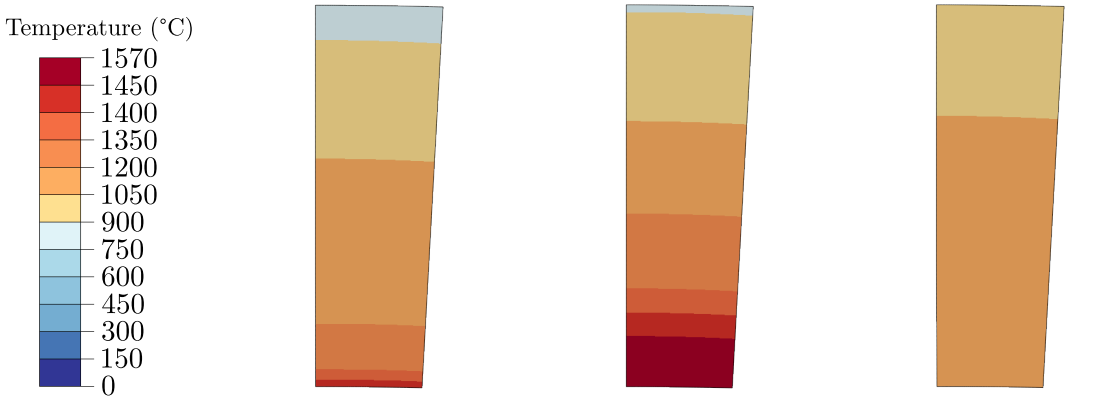

(a) End of thermal shock (b) End of treatment (c) End of waiting

Figure III.25: Spatial temperature distribution over time – 5th cycle.

Figure III.26 shows the variation of the creep strain at the integration point 1 of element A (Figure III.22), for the isotropic and kinematic models. As expected, no creep is observed before 10 h, when the ladle is being heated and did not achieved 900 °C yet.

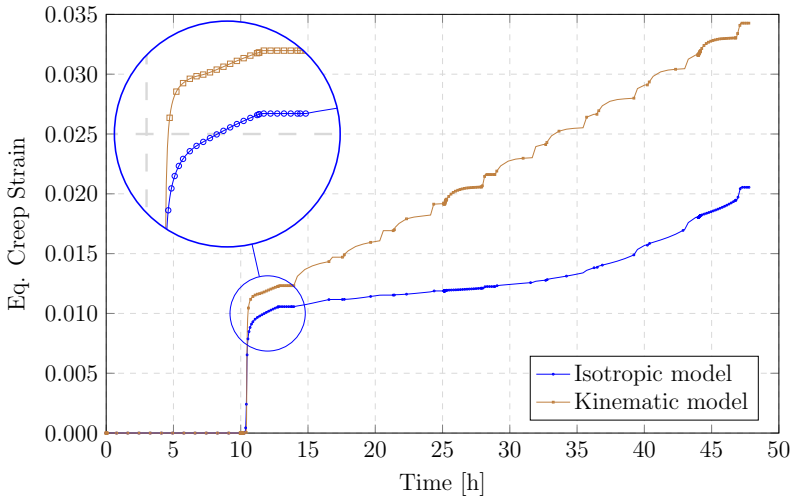

Figure III.26: Equivalent creep strain in the integration point 1 of element A. The zoomed area shows the detail of the first cycle.

As Figure III.27 shows, the minimum principal stress at the end of heating is −35 MPa, which is a reasonable value for refractories at low temperatures. At this stress level, considerable creep and relaxation are expected from the material, given that the temperature increases beyond the creep threshold.

Chapter II shows that, for the alumina-spinel brick, a considerably higher creep strain under constant stress conditions and, consequently, higher stress relaxation under constant strains are expected for the kinematic model, in comparison with the isotropic model, once secondary creep is reached. These phenomena can be observed in the simulation model of the steel ladle, where neither conditions of constant strain or stresses are observed, but both vary with time depending on the thermal expansion of the bricks and of the restrictions imposed by the closure of joints. Figures III.26 and III.27 show that both effects are more pronounced in the kinematic model, since it is able to represent the continuous increase of the creep strain once secondary creep was reached, while the isotropic model predicts a drop in the creep strain rate due to the assumption that primary creep is still active.

Figure III.28a shows the evolution of the maximum principal stresses in element A. The kinematic model presents a general decreasing trend for σ_{max}, with sudden stress drops once the thermal shock phase starts. As it can be seen in Figure III.28b, that represents the details of the 5th cycle, when T = 1100 °C, the stress is σ_{max} = 7.48 MPa. At this temperature, the relaxation of the stresses becomes more pronounced, dropping to σ_{max} = 0.1 MPa at T = 1250 °C in

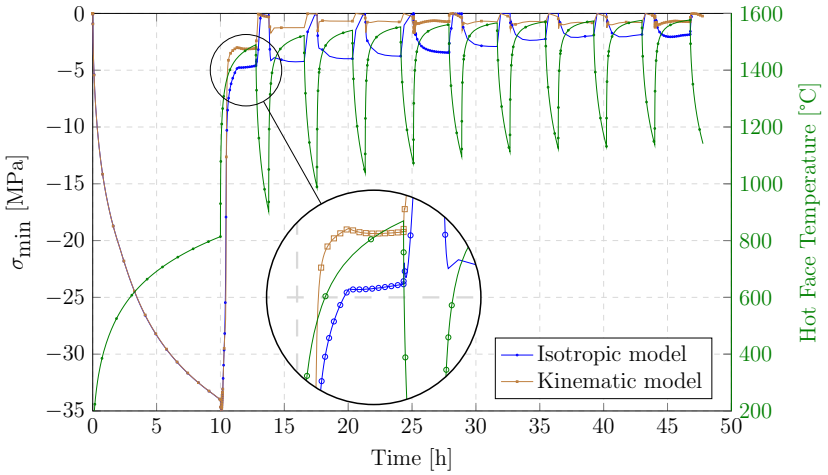

Figure III.27: Minimum principal stress in the integration point 1 of element A. The zoomed area shows the details of the first cycle.

a few seconds. The sharp decrease of the stress happens due to the fact that creep was not considered in the model at low temperatures and high stresses, due to the lack of experimental data, as explained in Section III.2.3.1. In a more realistic model, it is expected that creep starts to have a meaningful influence on the stresses and strains at an earlier stage of heating, when the temperatures are lower but the compressive stresses are high; this effect would cause a smoother decrease of the stress over time. At the end of the treatment phase, the maximum principal stress is virtually zero.

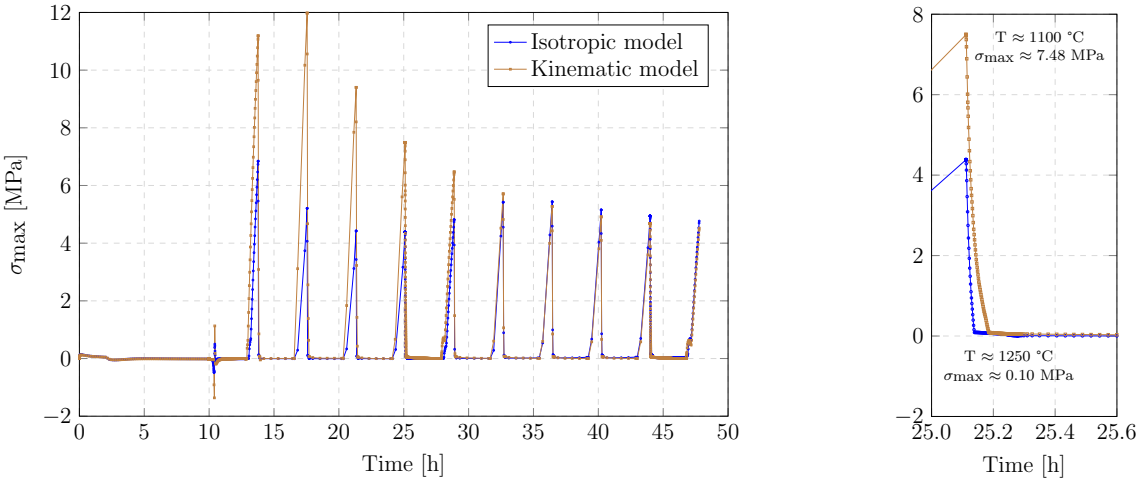

(a) (b)

Figure III.28: (a) Maximum principal stress in the integration point 1 of element A – Isotropic and kinematic models. (b) Detail of the fifth cycle.

Figures III.29 and III.30 compare the equivalent creep strain at the end of the treatment phase obtained with the isotropic and kinematic models, respectively. During the first cycle, the

models show a negligible difference in the spacial distribution of the strains, since most of the elements still did not achieve the secondary creep stage. At the tenth cycle, it is clear that the kinematic creep model predicts considerably higher strains than the isotropic creep model, with larger values concentrated at the brick's center.

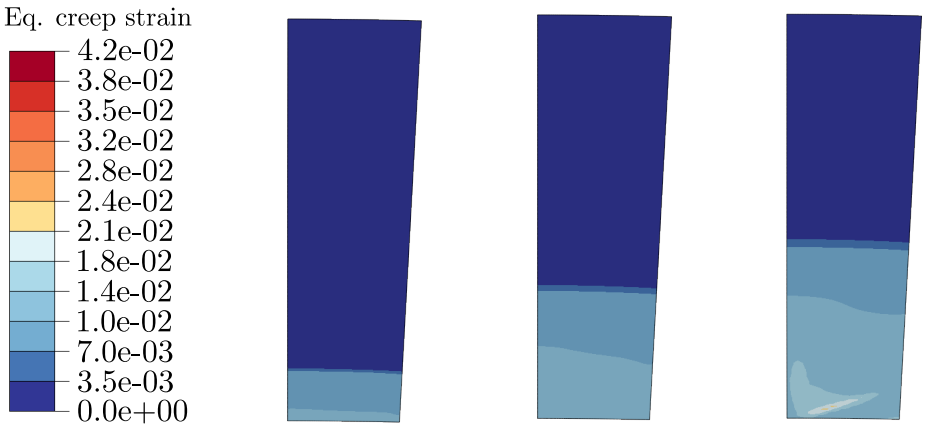

(a) 1st cycle (b) 5th cycle (c) 10th cycle

Figure III.29: Equivalent creep strain at the end of treatment – Isotropic model.

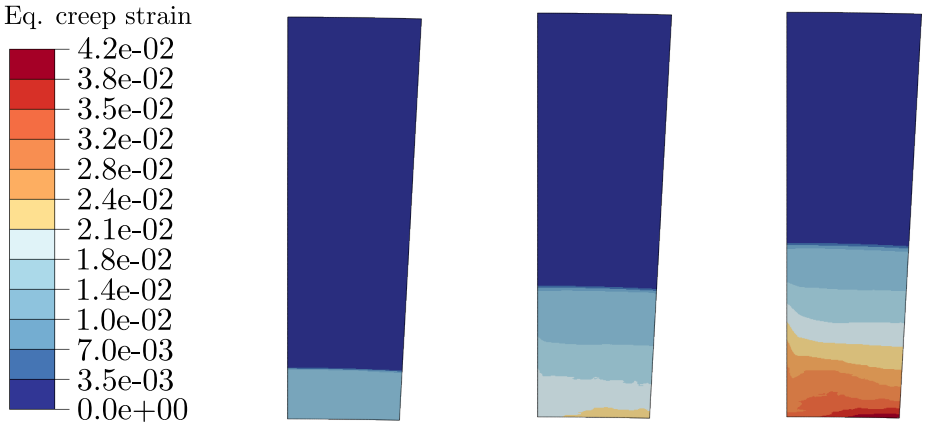

(a) 1st cycle (b) 5th cycle (c) 10th cycle

Figure III.30: Equivalent creep strain at the end of treatment – Kinematic model.

Figure III.31 highlights the zones of the right brick that present a positive minimum principal stress during the thermal shock phase, i.e., elements that are subjected exclusively to tensile stresses, in all directions. During the first cycle, no region of the brick is only under tension, due to the high compressive stresses accumulated during the heating phase with the closure of the joint. At the second cycle such zones appear, concentrated close to sides of the brick, due to the bending stresses generated at the point where the joints are closed. As the cycles proceed, there is a considerable increase in the area only affected by tension, and it moves towards the

upper center of the brick. This stress distribution can contribute to the spalling of the brick, and should be observed carefully under operational conditions.

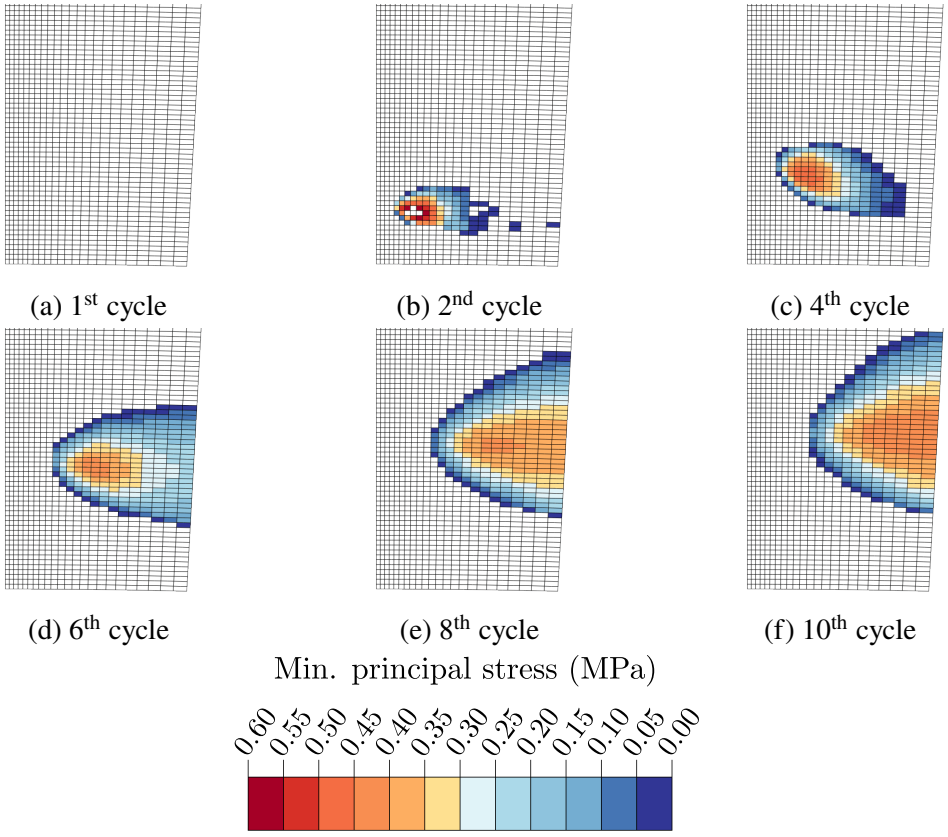

Figure III.31: Evolution of the positive values of minimum principal stress on the brick after the thermal shock.

During the operation of the steel ladle, an important safety requirement is that the joints between the bricks in the hot face are closed during the time when liquid steel is in the vessel, to avoid infiltrations and possible accidents. This is one of the factors influencing the minimum temperature allowed in the hot face during the waiting period in order to avoid joints' opening, in combination to the generation of tensile stresses that happen during cooling and the energy losses.

The creep models developed in this work present a good alternative to predict the continuous lost of pressure at the bricks' hot face, due to the relaxation induced by the high temperatures and initially high contact forces. As explained in Chapter I, the joints should be designed to allow enough expansion allowance to avoid overloading the lining, but at the same time to provide enough pressure between the bricks to avoid a loose lining.

Figure III.32 shows the distribution of the contact forces between the bricks in the hot face

during the thermal cycles, using the proposed kinematic creep model. At the end of the heating phase, the first 50 mm of the bricks present a non-zero force, with the maximum force achieving approximately 550 N, which indicates that the joints are closed in this region. At the end of the first cooling (waiting period), although the bricks can be touching each other at the hot face, there is a negligible force at the first 30 mm of the hot face, which can lead to acceleration of corrosion and erosion of the material due to infiltration of molten steel.

As the thermal cycles continue, the model shows that the zone of the brick with closed joints after cooling phases moves towards the cold face of the brick and becomes distributed over a larger area, as a combination of stress relaxation, permanent strains caused by creep and the evolution of the thermal distribution on the system.

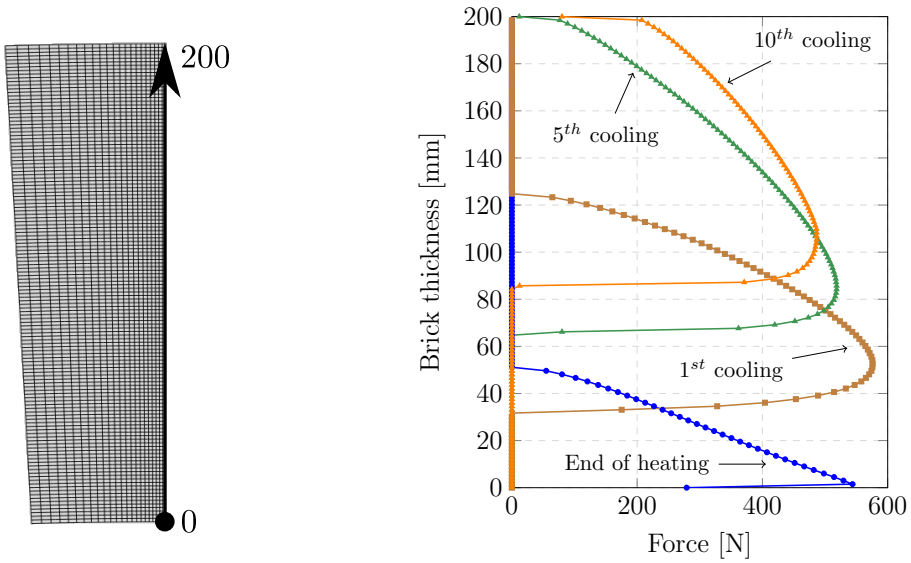

Figure III.32: Contact force distribution in the brick's length over time.

III.3 Digital Image Correlation technique

In experimental mechanics, optical full field methods for the characterization of displacements, stresses and strains are of great interest, since normally they allow to obtain a considerably higher volume of information from an experiment than classical point-wise techniques such as extensometry. Another advantage of such methods is the absence of direct contact of the measuring instrument with the sample, what is specially important in cases where this contact can result in noise on the experimental data, such as for measurements upon soft materials or in harsh conditions like high temperatures (Hild & Roux, 2006).

Several full field measuring techniques are currently available in the literature (Grédiac et al., 2013), and, among those, the Digital Image Correlation (DIC) technique has been receiving a considerable attention from various research groups, due to its versatility and to the possibility to easily compare its output to numerical simulations performed, for example, using the Finite Element Method.

Sections I.3 and I.3.3 discussed some of the most used algorithms in the context of general inverse analysis. This section presents the specific aspects related to DIC techniques, as well as the experimental concerns that normally are observed when using such techniques. Section III.3.1 describes the main features of DIC techniques, and Section III.3.2 discusses the main methods of identification of material parameters using DIC and inverse identification techniques.

III.3.1 DIC fundamentals

The fundamental assumption of the DIC technique is the conservation of optical flow, which states that the changes in the pixel values from an image obtained at instant t to the next image obtained at instant t^* during a mechanical test are due uniquely to the deformation of the sample and consequent movement of the image surface texture, which can be mathematically state as (Besnard et al., 2006):

$$g(\vec{x}) = f(\vec{x} + \vec{u}(\vec{x})) \tag{III.9}$$

where $\vec{x}$ is the set of pixel positions in the picture, $f(\vec{x})$ represents the pixel values of the image at instant t and positions $\vec{x}$, called reference image, $g(\vec{x})$ is the image at instant t^*, called deformed image, and $\vec{u}(\vec{x})$ is the imposed displacements field. The goal of the method is to find the displacements field $\vec{u}(\vec{x})$ that satisfies Equation III.9.

To evaluate the similarity between two gray image sets, a cross-correlation criterion or a sum of squared differences can be used (Pan et al., 2009). Among the various possibilities, the most simple one is a direct square difference between the images, given by:

$$C_{SSD} = \sum_{i=-M}^{M} \sum_{j=-M}^{M} [f(x_i, y_j) - g(x_i^*, y_j^*)]^2 \tag{III.10}$$

Pan et al. (2009) shows that the traditional C_{SSD} is sensitive to offset and linear scale in the image lighting, cause by variations in the light source during the experiment. The authors propose the alternative zero-normalized sum of squared differences as a way to eliminate this error:

$$C_{ZNSSD} = \sum_{i=-M}^{M} \sum_{j=-M}^{M} \left[\frac{f(x_i, y_j) - f_m}{\Delta f} - \frac{g(x_i^*, y_j^*) - g_m}{\Delta g} \right]^2 \tag{III.11}$$

where

$$f_m = \frac{1}{(2M+1)^2} \sum_{i=-M}^{M} \sum_{j=-M}^{M} f(x_i, y_i) \tag{III.12}$$

$$g_m = \frac{1}{(2M+1)^2} \sum_{i=-M}^{M} \sum_{j=-M}^{M} g(x_i^*, y_i^*) \tag{III.13}$$

$$\Delta f = \sqrt{\sum_{i=-M}^{M} \sum_{j=-M}^{M} [f(x_i, y_i) - f_m]^2} \tag{III.14}$$

$$\Delta g = \sqrt{\sum_{i=-M}^{M} \sum_{j=-M}^{M} [g(x_i^*, y_i^*) - g_m]^2} \tag{III.15}$$

The chosen measure of the difference between two images is related to the definition of the residual for inverse analysis, as discussed in Section I.3.2. The problem of finding the displacements $\vec{u}(\vec{x})$ is, therefore, that of the minimization of the functional resulting from the chosen correlation coefficient $\Gamma(\vec{u}(\vec{x}))$ with respect to $\vec{u}(\vec{x})$:

$$\min_{\vec{u}(\vec{x})} = \int \int_{\Omega} \Gamma(\vec{u}(\vec{x}))dx \tag{III.16}$$

Neggers et al. (2015) propose the so called time-resolved DIC technique, where all images from a given time period are combined to form a single objective function.

A speckle pattern can be used in order to increase the contrast of the sample's surface, facilitating the identification of the displacement of the subset, unless the original texture of the

sample is already sufficient. Different techniques can be used for the creation of the speckle pattern, depending on the test conditions of temperature, expected order of magnitude for the displacements, reactivity of the sample with the speckle, between others. Some examples of materials used to create the speckle pattern are regular low-temperature black and white paints, enamels and paints made of high temperature resistant oxides (Dong & Pan, 2017).

The problem defined by Equation III.16 is ill-posed, and one regularization strategy is to discretize the kinematic field $\vec{u}(\vec{x})$ into a linear combination of chosen basis functions (Hild & Roux, 2006). The main difference between the various DIC algorithms available rely on the choice of the discretization for $\vec{u}(\vec{x})$.

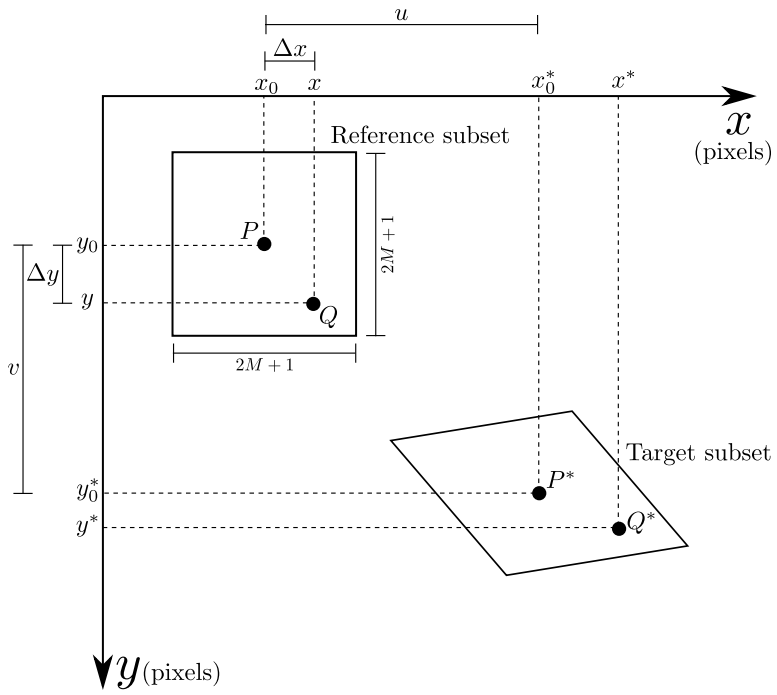

Figure III.33: Subset-based Digital Image Correlation.

One of the first and most used propositions for the discretization of the problem is the so called local subset-based method, that divides the reference image into N independent subsets with center points at $P(x_0, y_0)$ and $(2M+1)\times(2M+1)$ pixels with coordinates $Q(x, y)$ (Figure III.33). The coordinates of a point $Q(x^*, y^*)$ in the deformed subset are than given by:

$$x^* = x + u + \frac{\partial u}{\partial x}\Delta x + \frac{\partial u}{\partial y}\Delta y \tag{III.17}$$

$$y^* = y + v + \frac{\partial v}{\partial x}\Delta x + \frac{\partial v}{\partial y}\Delta y \tag{III.18}$$

Besnard et al. (2006) proposed an alternative global discretization method for the calculation of the displacements using finite elements shape functions. Instead of using independent subsets, the surface of the sample is discretized using finite elements connected by a mesh, and the unknown displacements are located at the nodes of the elements. Thus, the displacements field of an element e is given by:

$$u^e(x) = \sum_{n=1}^{n_e} \sum_{\alpha} a^e_{\alpha n} N_n(x) e_\alpha \tag{III.19}$$

where n_e is the number of nodes of the element and $a^e_{\alpha n}$ the unknown nodal displacements. Later, a global description is generated by the combination of the individual elements, similar to what is done in a traditional finite element method. This method has the advantages to automatically enforce the continuity of the displacements field, and it also offers the possibility to directly compare the results of the DIC calculations with these of numerical simulations, sufficing that the two meshes are the same.

In the literature it is possible to find several publications arguing about which of these two methods, local or global, is the more accurate and robust. It is, nevertheless, a difficult task to make a general choice, since apparently each method can be more or less adequate depending on the situation (Hild & Roux, 2012, 2013; Pan et al., 2016; Pan et al., 2015; B. Wang & Pan, 2016).

Other kinematics basis can also be used with global DIC approaches. For example, Hild et al. (2009) used Euler-Bernoulli kinematics to identify the parameters that characterize the movement of a beam, namely, two axial displacements, two vertical displacements and two rotations, resulting in a method called Beam-DIC. Similarly, Réthoré et al. (2009) studied the brittle fracture of a silicon carbide using extended finite element shape functions, and Leplay (2011) used base functions to enforce an homogeneous one-dimensional strain field in tension and compression tests (UNI-DIC). These approaches present the advantage of having considerable less degrees of freedom, since the kinematic behavior of the sample is characterized by the parameters of the kinematics base, instead of those of each subset.

III.3.2 Inverse identification of material parameters using DIC techniques

The techniques presented in Section III.3.1 can be referred to as measurement methods, in the sense they have the goal to measure displacements, strains, stresses or other physical variables. Another class of methods, related to the previous ones, has the objective to identify material parameters of certain constitutive laws based on the DIC technique. The two most popular

methods in the literature are the Finite Element Model Update (FEMU) and the Integrated Digital Image Correlation (I-DIC).

The Finite Element Model Update is a method consisting of two steps. In the first step, a DIC technique, such as the ones explained in Section III.3.1, is applied to calculate the displacements of the sample over time. The results of these measurement are then used as inputs for the second step, that consists of changing the parameters of a constitutive model until the displacements field obtained by the numerical simulation match the ones obtained from DIC (A. P. Ruybalid et al., 2016).

Figure III.34 shows a schematic representation of FEMU. It should be noted that the displacement boundary conditions are an input to the numerical simulations, to take into account the real experimental conditions, and not idealized ones (Mathieu et al., 2015).

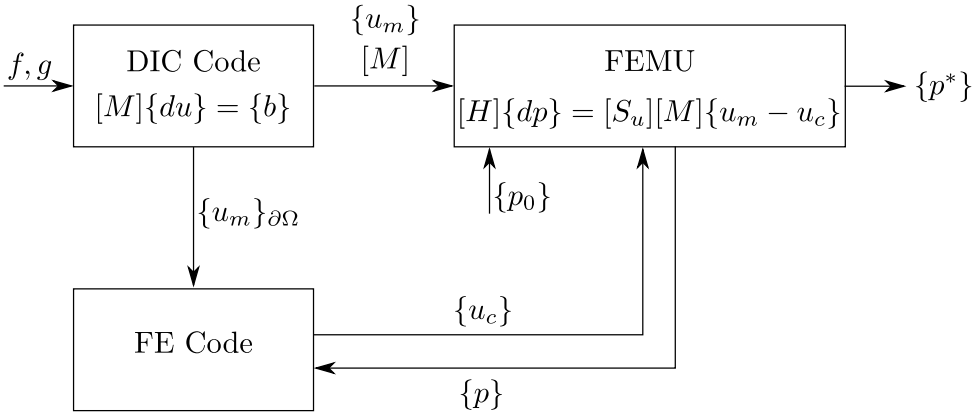

Figure III.34: FEMU – Schematic representation. Adapted from (Mathieu et al., 2015)

In the I-DIC technique, instead of the independent calculation of the displacements fields and posterior matching with simulation results, such as in the FEMU, the calculation of the displacements and the identification of the material parameters are done simultaneously (integrated), leading to a one-step process. Figure III.35 shows the usual calculation flow for I-DIC (Mathieu et al., 2015). Also, instead of displacements fields, the gray levels of the computed and experimental images are directly compared, reducing interpolation errors (A. P. Ruybalid et al., 2016).

III.3.3 Experimental aspects related to mechanical tests and image acquisition

Besides the different techniques regarding the post-processing and identifications presented in Sections III.3.1 and III.3.2, the correlation procedures can be classified according to the experimental setup, or more specifically the number of used digital cameras.

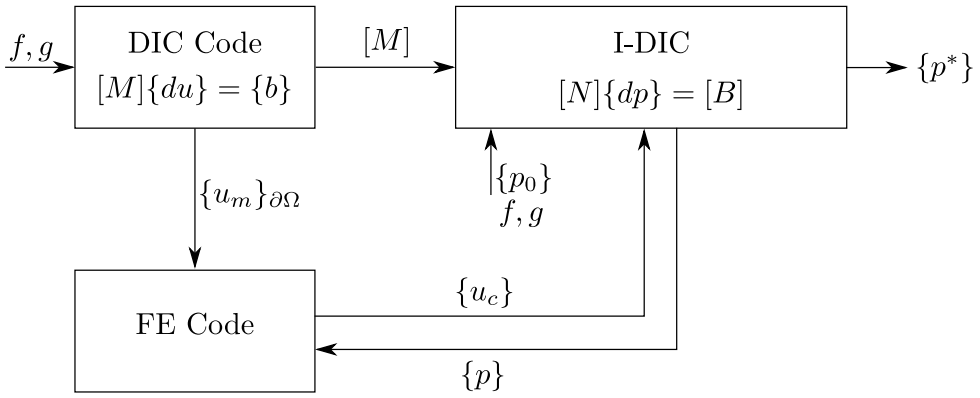

Figure III.35: I-DIC – Schematic representation. Adapted from (Mathieu et al., 2015)

The most simple technique is called 2D-DIC, and consists of using one digital camera, that is placed directly in front of the sample. This technique assumes that the sample is perfectly planar and perpendicular to the camera optical axis, what can be experimentally challenging, and therefore out-of-plane displacements are not taken into account and can introduce errors in the further calculations (Jones et al., 2018).

Stereo-DIC, also known as 3D-DIC (not to be confused with the Digital Volume Correlation technique), uses two cameras disposed at a certain angle to take pictures of the same surface of the sample and, after a calibration procedure, is able to combine images taken with both cameras at the same moment to recreate a tree-dimensional scene, therefore measuring the out-of-plane displacements (Balcaen et al., 2017). For this reason, Stereo-DIC should always be privileged over 2D-DIC, unless it is not possible to use two cameras (Jones et al., 2018).

For the majority of the DIC applications at high temperatures (Section III.3.4), where a furnace equipped with a relatively small window is used, it is difficult to use stereo techniques, since the relative angle between the cameras is considerably limited by the visibility of the sample. Therefore, for most high temperature applications seen in the literature, 2D-DIC is used.

It should be emphasized that the mechanical tests and further calculation of displacements and/or identification of constitutive parameters using DIC techniques are two separate processes, but are not completely independent. In order to obtain satisfactory results, a systematic and well defined experimental procedure should be defined, and the following issues need to be considered and addressed:

Brick and sample production: as described in Section I.1, refractories are heterogeneous materials. Although these heterogeneities may be less important during the material's operation in real applications, it can significantly impact experiments performed in a laboratory. This, of course, also affects traditional experiments, not only those instrumented using DIC techniques.

During the production of refractory bricks, uneven pressing and heterogeneous sintering can be a source of scatter in the results obtained in laboratory. Due to the high brittleness of these materials at room temperature, micro-cracks can be generated during the machining of samples. It is also possible to obtain samples with rough surfaces, which results in uneven loading and stress concentrations, and the parallelism of the surface to be photographed during the experiment may have high tolerances.

Speckle preparation: depending on the DIC technique to be used, the speckle distribution on the sample's surface plays a different role in the accuracy of the results. Problems may arise if the speckle is not homogeneously distributed over the sample, generating regions with considerably different contrast that can be favored during the identification procedure. At high temperature, it is of primary importance that the speckle remains sufficiently chemically stable and that it doesn't react with the sample, what could cause high violations of the gray level conservation principle.

Mechanical loading: during the test itself, load misalignments can lead to deviation on the assumed boundary conditions, resulting in translations and rotations of the sample both in-plane and out-of-plane. For creep tests, it should be checked that the sample and the furnace achieved temperature stability before starting the loading and the acquisition of images, to eliminate noise due to unfinished thermal expansion and light intensity variation. Besides, the constant load control is generally made using a PID controller, that should be adequately calibrated to avoid vibrations and high amplitude of load variability during the test.

Image acquisition: to take high quality pictures, it is necessary to have a stable and sufficiently powerful light source to illuminate the sample. At high temperatures this is particularly challenging, as described in Section III.3.4. In the case of 2D-DIC, it is assumed a perfect alignment between the camera and the sample, what is difficult to obtain. Lastly, the image should be adequately focused, to avoid blurred areas that may decrease the contrast.

III.3.4 DIC at high temperatures

At high temperatures, DIC techniques can be particularly interesting, since contact measurement devices can be expensive and difficult to operate, besides the other advantages of these techniques already presented. Nevertheless, such techniques also present important inconveniences, mostly related to the acquisition of high quality images. Leplay et al. (2015) highlight the three main challenges related to this topic:

1. Maintain the stability of the speckle pattern, that needs to withstand the temperature and cannot react with the sample, while keeping and acceptable contrast.

2. The excess of black body radiation, that leads to a violation of the brightness conservation.

3. The existence of a temperature gradient between the sample and the camera and the consequent variation of the refractive index of the air with the temperature, resulting in heat hazes.

To characterize the thermo-mechanical behavior a Ni-based superalloys and a C/SiC composite under temperatures up to 1500 °C, Novak and Zok (2011) used an experimental setup where the sample was heated by a CO_2 laser beam, and its deformation due to thermal expansion was measured using a stereo-DIC method. The authors illuminated the sample using an array of powerful LED assemblies, and the emitted light was filtered using blue band pass filters. An air knife system was used to reduce the effect of heat hazes, blowing the hot air away from the sample's surface. To coat the sample, speckles made of alumina and zirconia paints were applied using an air-brush.

Berny et al. (2018) used a similar experimental setup to study the effect of heat hazes on DIC calculations, proposing a temporal regularization based on the construction of a denoised reference image built from more than 200 images. Archer et al. (2020) also used a similar setup, except that only one camera was used, to propose gray level corrections at high temperatures, that might be necessary due to violations of the brightness conservation hypothesis.

In cases where it is necessary to apply a mechanical load on the sample different from the inhomogeneous temperature distribution and consequent thermal straining, such as to perform Brazilian tests and four-point bending tests, the setup proposed by Novak and Zok (2011) is not feasible. In such cases, it is expected that the temperature on the sample is homogeneous and constant through the test, and constrained expansion effects are often not desired.

In these situations, it is common to use a closed chamber furnace equipped with a glass window in order to heat the sample. Leplay et al. (2015) used an experimental setup to perform four-point bending tests, composed of a furnace with a window made of a double sapphire glazing, to avoid additional thermal heterogeneity due to excessive heat loss. To decrease the effect of heat hazes, instead of using a fan in front of the furnace or to take several images and calculate an *a posteriori* average, the authors proposed to increase the exposure time up to 30 s, in order to obtain directly from the camera an averaged image. To avoid over-saturation of the image due to the large exposure times, neutral density filters were used to block the excess of light at the camera sensors.

To improve the contrast at the image at high temperatures, some authors proposed to replace the regular LED light to blue light sources, that have their power concentrated at a narrower range of wave lengths (Pan et al., 2011; S. Wang et al., 2015; W. Wang et al., 2017). In association with blue band pass filters, this solution showed to be able to considerably increase the quality of the images.

III.3.5 Proposition of an identification procedure using an I-DIC technique combined with Brazilian tests

During the experimental investigations realized in this work, explained in details in Chapter IV, it was observed that the displacements fields obtained by applying a standard DIC calculation (Blaber et al., 2015) presented a systematic deviation from the theoretical field, i.e., instead of a symmetric displacement's field regarding the direction of the application of the load, a rotation of the sample was visible in most of the experiments.

Figure III.36 shows the example of the vertical displacements calculated for a Brazilian test's sample, at 1300 °C. It is clear, specially in Figure III.36c, that the sample is rotated in the counter-clockwise direction in relation to the vertical axis.

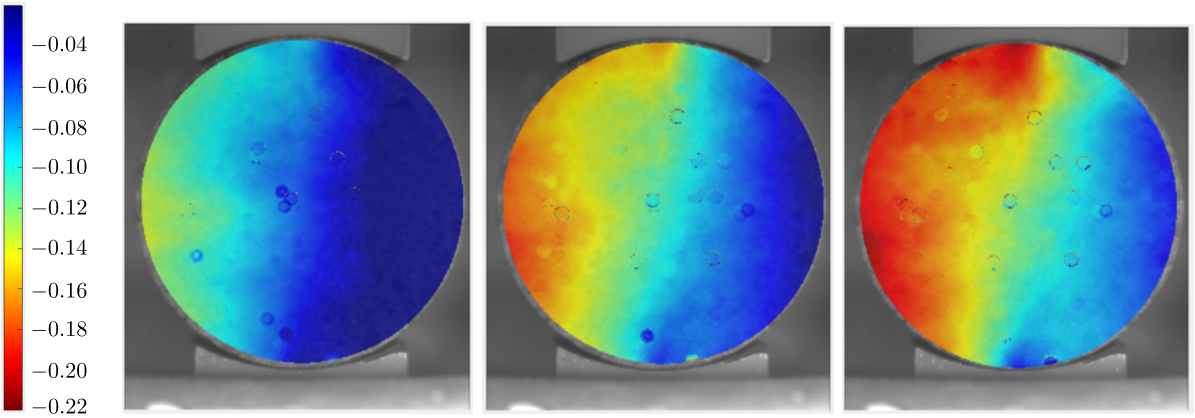

(a) (b) (c)

Figure III.36: Brazilian tests: Vertical displacement in mm at 1300 °C. (a) $t \approx 0.6$ h. (b) $t \approx 1$ h. (c) $t \approx 1.5$ h.

To analyze how the vertical displacement of the central line of the sample changes when the rotational rigid body motion is present, a numerical simulation considering an horizontal force applied at the top of the sample was made, and is shown in Figure IV.12, and it was compared with a perfectly symmetric case. When the boundary conditions are symmetric, the displacement increases monotonically in the negative y direction, and equally in both sides of the sample, as expected. Nevertheless, a horizontal force in the negative x direction causes an increase

in the magnitude of the displacements at the right side of the sample, while the left side has a positive displacement during loading. After approximately 1 h of creep deformations, the displacement of the right side becomes negative again, but always smaller than at the left. This geometrically non-symmetric behavior is frequently observed in mechanical experiments, as discussed in Chapter I, and has the potential to negatively influence the I-DIC identifications if not properly considered.

From Figure III.36, it is clear that an identification procedure that assumes a perfectly symmetric displacements field resulting from the Brazilian tests has low possibility of identifying the material parameters with acceptable accuracy, considering the large errors that are inherent to the calculation, in addition to other error sources already anticipated, both numerical and experimental (see Section III.3.3).

Considering that the error associated with rigid body movements has always the same source, i.e., the rotation of the sample, it is proposed an algorithm that, as well as the traditional I-DIC algorithm illustrated in Figure III.35, works directly using the pixel intensity levels, but instead of obtaining the real boundary conditions (as opposed to the idealized ones) from a DIC code, the error source (the horizontal force causing the rotation) is included in the finite element simulations used to obtain the theoretical displacements field. This horizontal force is, therefore, identified together with the material parameters.

This algorithm, described in details in Section III.3.5.1, can be seen as a particular case of the one presented by Mathieu et al. (2015), in the sense that is makes use of an observation relative exclusively to the Brazilian tests at high temperature made in this work (the rotation of the sample), while the traditional I-DIC algorithm is more general. The main advantage of the proposed algorithm is its simplicity, since it does not require a traditional DIC calculation, but still requiring only one calculation step and operating directly on the pixel gray levels, which reduces the interpolation errors. Considering the small displacements expected to be obtained from high temperature mechanical tests on refractories, the reduction of such interpolation errors is crucial for the success of the identification procedure.

The proposed algorithm is an extension of the work of Gazeau et al. (2015), that proposed a similar calculation, but using an analytical model to represent the theoretical displacements field and without the consideration of the test's imperfection due to the non-vertical load in the Brazilian test.

III.3.5.1 I-DIC algorithm

Step 1: The first step consists in providing the initial conditions for the identification, regarding the material parameters. If a gradient based optimization algorithm is used to perform

the inverse identification, the initial conditions generally consist of initial values for the parameters. If a genetic algorithm or other soft-computing technique is used, this condition is the allowed range of variation for the parameters. In the first calculation step, the horizontal force responsible for the geometric asymmetry of the experiment can be considered zero, and its value is included as a parameter to be identified.

Step 2: The theoretical displacements field is calculated using the current material parameters. To calculate the displacements in the Brazilian test resulting from the creep models proposed in Section III.1.1, the Finite Element Method (FEM) is a reasonable choice, and it was used in this work.

Since the horizontal force F_h is included as an unknown in the problem, it is necessary to used an adapted FEM model, since there can be convergence issues due to an initial rigid body movement, since this force is only counter-balanced by the friction between the sample and the lower jaw, and at the beginning of the simulation these parts are in contact only for a small surface (or line, since it is a 2D simulation).

The application of the load was than divided into two steps, as illustrated in Figure III.37. In the first step, only the vertical component of the force was applied, considering the real experimental ramp, and the sample's geometrical symmetry line was restricted in direction x, to avoid convergence issues related to numerical errors and consequent unbalanced residual forces. In the second step, since the contact area between the sample and the jaw had already increased and the friction force had already started to be developed, the restriction in direction x was removed, and the horizontal force was applied in a short step (t = 1 s). From that point, both forces were kept constant, and the creep strains started to increase. The procedure for the application of the forces can be seen in Figure III.38.

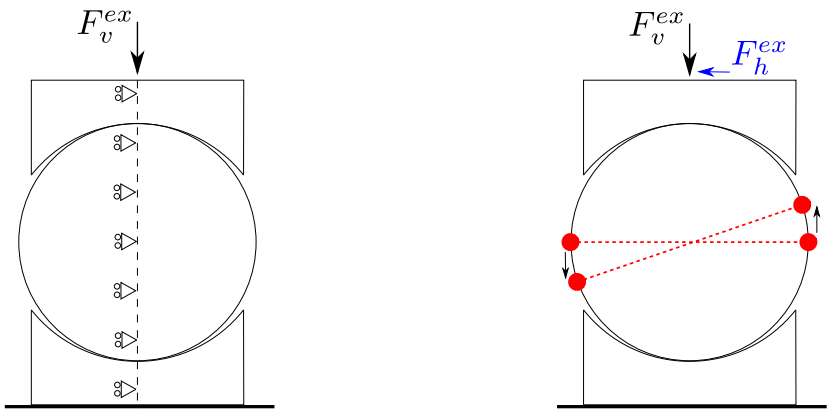

(a) Step 1 – $t \approx 30$ s (b) Step 2 – $t \approx 1$ s

Figure III.37: Proposed identification procedure – Modeling strategy

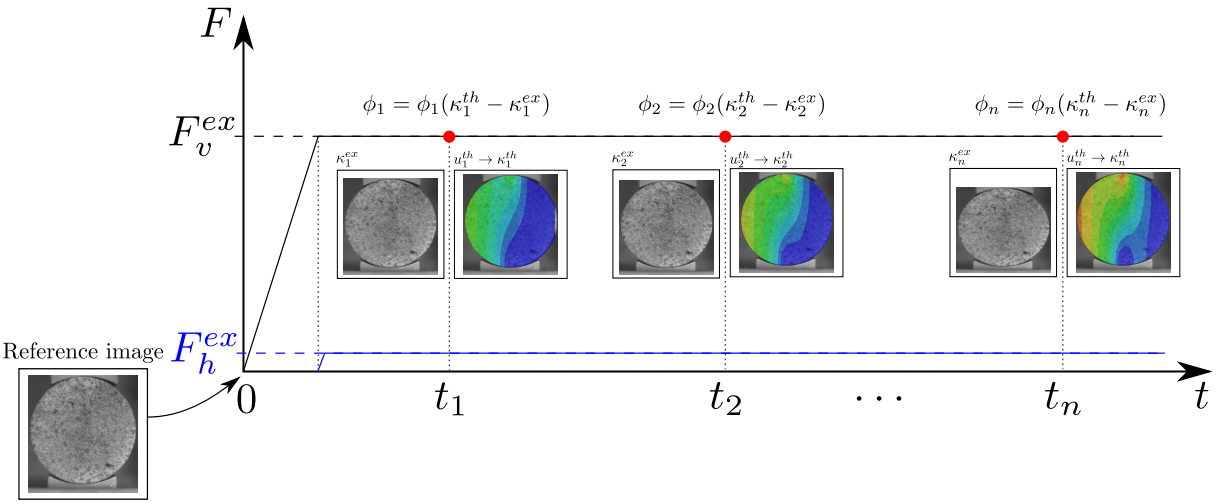

Figure III.38: Proposed identification procedure – Application of the forces and predefined time steps.

Step 3: The theoretically deformed images are formed by the imposition of the displacement's fields obtained in Step 2 on the pixel values of the reference image, through an interpolation scheme. Figure III.39 shows two examples of the interpolation procedure, where an horizontal rigid body displacement to the right is imposed on the undeformed image.

In Figure III.39a, the displacement is equal to 1 pixel, therefore the pixel values are simply shifted one position to the right.

In Figure III.39b, the displacement is equal to 0.1 pixel, and a linear interpolation is made. Since the pixel values need to be integers by definition, the resulting image needs to be rounded, which introduces a random error. In the case where the change in the pixel values caused by the imposition of the displacements is of the same order of magnitude as the interpolation errors, the identification becomes inaccurate.

One possibility to overcome the problem related to the interpolation of the pixel values is to change the image's encoding to higher values, for example from 8 to 16 bits, where the maximum pixel value would change from $2^8 - 1 = 255$ to $2^{16} - 1 = 65535$. With higher encoding, the influence of the random error is smaller for a given displacement's field, since the change in the pixels' values becomes larger.

Step 4: The differences between the theoretically deformed images and the experimentally deformed image images are calculated, for each predefined time step, as shown in Figure III.38. In this step, the definition of the appropriate error function is crucial for the success of the inverse identification, as described in Section I.3.2.4. In order to

proceed to the optimization step, the result of the difference between the theoretical and experimental images is frequently given as a scalar value.

Step 5: The convergence of the optimization algorithm is checked, according to its specific criteria. For example, if a gradient based algorithm is used, the convergence criteria can be based on the change in the identified values regarding the previous step. For genetic algorithms, it is common that no clear convergence criteria is used, but instead the calculations run until a predefined number of generations is completed.

Step 6: Finally, case the convergence was not achieved in the current step, the optimization algorithm decides what will be the next guess, and the cycle repeats.

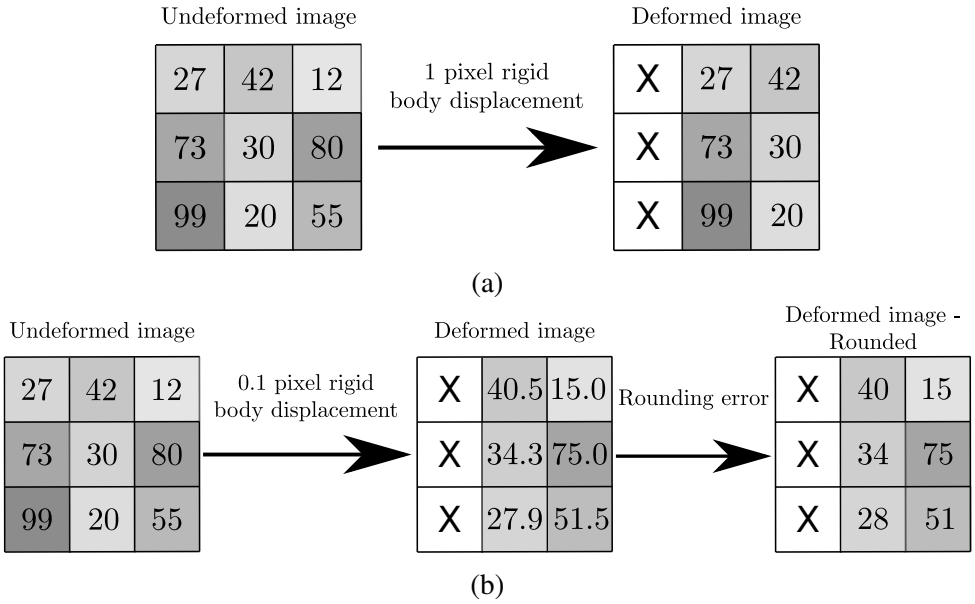

Figure III.39: Interpolation of an image's pixel values. (a) 1 pixel rigid body displacement. (b) 0.1 pixel rigid body displacement.

III.3.5.2 The error function

One of the most fundamental aspects for the success of any optimization-based algorithm is the definition of a robust error function, also called cost function or objective function, as described in Section I.3.2.4.

For the I-DIC algorithm proposed in this work, it is important that the residuals of all theoretically deformed images in relation to the corresponding real deformed images are considered at the same time. In the same sense, all pixels of the image are considered at once, as if there was only one subset, which corresponds to the entire region-of-interest (ROI). Equation III.20 shows the error function used in this work.

$$\phi(\underline{\theta}) = \frac{1}{m}\sum_{i=1}^{m}\omega_i\left(\frac{1}{n_i}\left\|\underline{r}_i(\underline{\theta})\right\|^2\right) \rightarrow \min_{\underline{\theta}\in\mathbb{R}^p} \tag{III.20}$$

where θ are the material parameters to be identified, p is the number of material parameters, m is the number of images, n is number of pixels in the ROI of an image, $\underline{r}(\underline{\theta})$ are the residuals and $\| \|^2$ is the euclidean (L2) norm.

The term ω_i acts like a weighting factor, making it possible to give more importance to certain images than to others. For example, images presenting larger deformations, obtained at time steps towards the end of the creep test, might be given more importance than the ones obtained at the beginning of the test, where the signal-to-noise ratio is smaller.

The problem to consider now is how to properly define the residuals function. It is common in the literature that a sum of squared differences (SSD) is used as a correlation criteria between two images, which, substituting in Equation III.20 results:

$$\phi(\underline{\theta}) = \frac{1}{m}\sum_{i=1}^{m}\omega_i\left(\frac{1}{n_i}\sqrt{\sum_{j=1}^{n_i}\left(I(j)^E - I(j)^T\right)^2}\right) \rightarrow \min_{\underline{\theta}\in\mathbb{R}^p} \tag{III.21}$$

where I^E is the experimental image, I^T is the theoretically deformed image, $I(j)$ is the j^{th} pixel of image I and the difference between two images implies the difference between each of their pixels.

(Pan et al., 2015) point that this methodology, although relatively simple, is only stable under perfectly constant lightening conditions, i.e., small variations in the illumination of the sample can cause large errors in the calculation of the residual. For applications at high temperature, this consideration can become important, since there is a considerable amount of light coming from the furnace where the sample is located, which is not always perfectly stable.

To mitigate this problem, Pan et al. (2015) proposes the use of a zero-normalized sum of squared differences (ZNSSD), described in Equation III.11, which results in:

$$\phi(\underline{\theta}) = \frac{1}{m}\sum_{i=1}^{m}\omega_i\left(\frac{1}{n_i}\sqrt{\sum_{j=1}^{n_i}\left(\frac{I(j)^E - I_m^E}{\Delta I^E} - \frac{I(j)^T - I_m^T}{\Delta I^T}\right)^2}\right) \rightarrow \min_{\underline{\theta}\in\mathbb{R}^p} \tag{III.22}$$

The effect of using the ZNSSD residual instead of the SSD for the proposed I-DIC algorithm is analyzed in the next section.

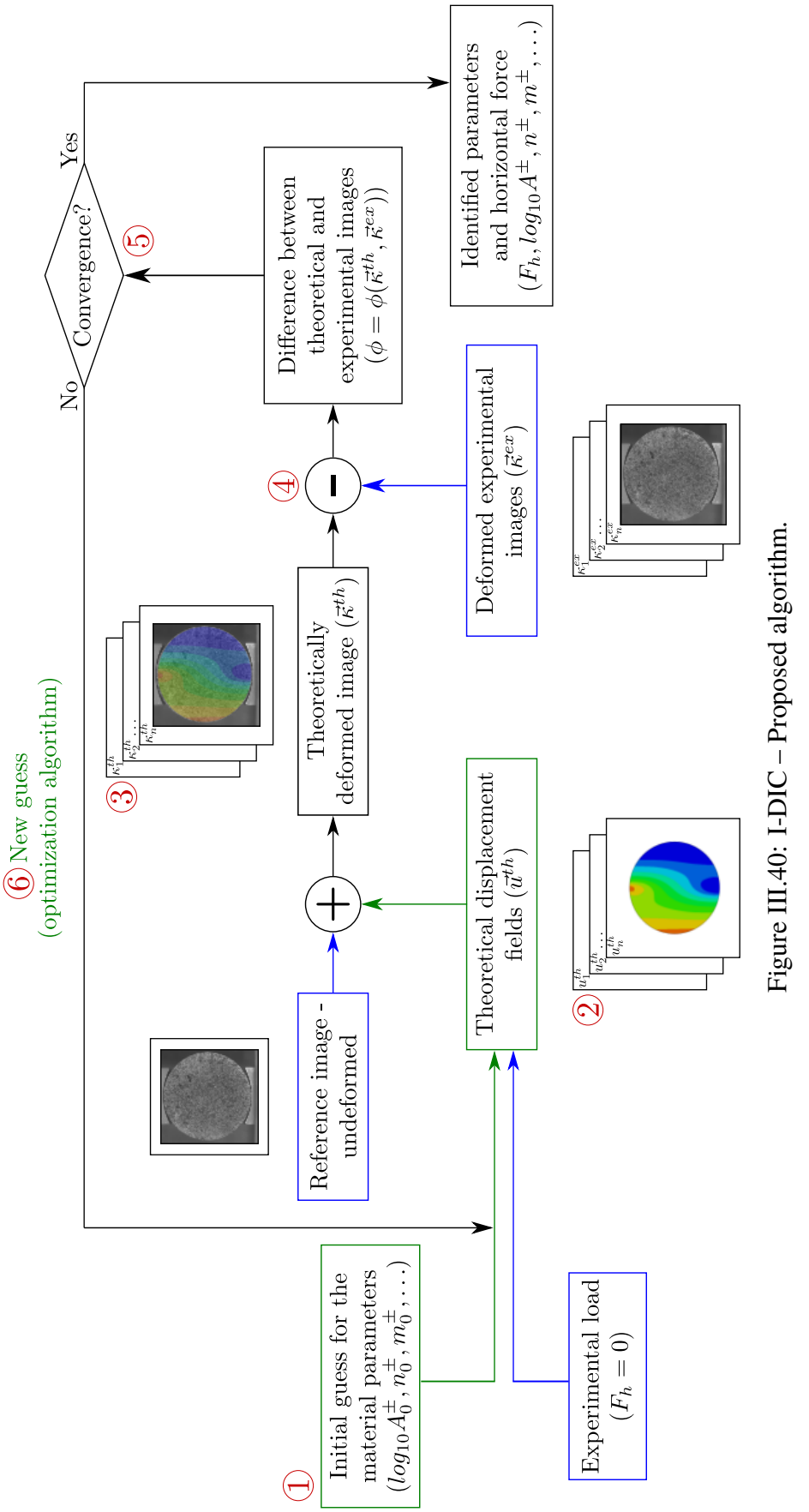

Figure III.40: I-DIC – Proposed algorithm.

III.4 Analysis of the error function using virtual experiments

In this section, the sensitivity of the I-DIC algorithm proposed in Section III.3.5.1 to experimental and numerical parameters is analyzed, to identify the limitations of the model. To do that, the variations of the objective function proposed in Equation III.20 are evaluated, by means of virtual experiments.

The use of virtual experiments to evaluate the capabilities of DIC algorithms is common practice in the literature (Rokoš et al., 2018; A. P. Ruybalid et al., 2016; A. Ruybalid et al., 2019; Vargas et al., 2018), and provides an adequate methodology to vary one parameter at a time under controlled conditions, different from real experiments, that intrinsically include some level of uncertainty and a combination of all error sources at the same time.

The I-DIC method proposed in Section III.3 is based on the variation of the material parameters for a given constitutive law until the difference between sets of virtually deformed and experimentally deformed images is minimized.

For the virtual experiments, the equivalent of the experimentally deformed images (EDI) are artificially created using the same algorithm as the I-DIC method. To create the EDI, real images of the Brazilian test, taken during the experimental campaign, were used. The use of a real image as the reference for a virtual experiment has the advantage to reproduce the same level of contrast, sharpness and speckle grain size distribution as expected in the real experiment. The virtually created experimental images will hereafter be referred to as experimental images.

In the same sense, a given set of material properties need to be considered as ground truth, in order to create the deformed images. The isotropic creep model proposed in Section III.1.1 was used during the tests, with the properties presented in Table III.8. To evaluate how each of the parameters influence the I-DIC algorithm, the material properties were varied around the ground truth, according to Table III.9, and the resulting evolution of the error function was analyzed, taking into account the ideal conditions for a stable inverse analysis, as described in Section I.3.1 and summarized in Figure I.10.

Figure III.11 shows that the parameters n^+ and n^- are the least influential in the results of a Brazilian test simulation, when considering the vertical displacement of the load application point. Therefore, in the subsequent analysis, only the parameters A^+, A^- and m^- will be considered. The numerical model described in Section III.2.1.2 was used to perform the simulations, since in the virtual experiments no load misalignments were considered.

Table III.8: Material parameters used in the virtual tests – Isotropic creep model

Parameter	**Compression (Primary Creep)**	**Tension (Secondary Creep)**
E [MPa]	30000	30000
ν [−]	0.2	0.2
$\log_{10} A[MPa^{-n}s^{-1}]$	−14.16	−5.4
n [−]	3.96	1.5
m [−]	−2.74	0

Table III.9: Variation of the material parameters for the virtual tests

	$\log_{10} A^{-}[MPa^{-n}s^{-1}]$	$\log_{10} A^{+}[MPa^{-n}s^{-1}]$	$m^{-}[-]$
−10.0‰	−15.57	−5.94	−3.01
−7.5‰	−15.22	−5.80	−2.94
−5.0‰	−14.86	−5.67	−2.87
−2.5‰	−14.51	−5.53	−2.80
−1.0‰	−14.30	−5.45	−2.76
−0.5‰	−14.23	−5.42	−2.75
0.5‰	−15.57	−5.37	−2.72
1.0‰	−15.22	−5.34	−2.71
2.5‰	−14.86	−5.26	−2.67
5.0‰	−14.51	−5.13	−2.60
7.5‰	−14.30	−4.99	−2.53
10.0‰	−14.23	−4.86	−2.46

III.4.1 Influence of images quality

To obtain accurate results using any DIC algorithm, it is fundamental to use high quality experimental images, which in general mean to have a high contrast, an homogeneous distribution of pixel intensity values on the camera's dynamic range and an appropriate focus. For applications at high temperature, this is especially difficult to obtain, because of the complications explained in Section III.3.4.

More specifically, high temperature images can present lower contrast when compared to room temperature images. As a result, the error function becomes less sensitive to changes in the imposed displacements field, and, consequently, it presents a more flat shape. This has a direct impact on the capacity of the I-DIC algorithm to find the solution of the optimization problem, since the variations in the error function with the change of the material parameters can be in the same order of magnitude as the residual of the calculation.

The images shown in Figure III.41 were used to evaluate the sensitivity of the error function to the image's quality. Figure III.41a shows a picture taken at room temperature, which has the highest sharpness compared to the other two. Figure III.41b shows a picture taken at 1300 °C, using the experimental procedure described in Chapter IV to increase its contrast. Figure III.41c was also taken at 1300 °C, but it presents a lower quality, since it is blurred at its left side and there was a considerable lost of speckle at the top right. Images taken at high temperature without using the equipment described in Chapter IV were not considered in the analysis, since they do not present enough contrast. The error function based on the SSD residuals (Equation III.21) was used in the evaluations.

Figure III.41d shows the variation of the histogram in the region of the sample for the three images, which is a criteria to evaluate their qualities. As it can be observed, the image taken at room temperature has a wider distribution of number of pixels in the camera's dynamic range, while the images at high temperature present a reduced distribution. Therefore, the error function is expected to be more sensitive to the material parameters in the first image.

Calculation of the noise floor As explained in Sections III.3.3 and III.3.4, DIC based measurements have intrinsic sources of error, related, for example, to the camera noise. At high temperatures, the main concern is related to the heat hazes. To quantify how much the I-DIC algorithm can be affected by these errors, it is necessary to calculate the noise floor, i.e., the amount of noise expected from the intrinsic error sources. In summary, the noise floor represents the values for which the changes in the error function start to be due to the changes in the material parameters, and not to the random noise present in the measurement setup.

The noise floor depends on the experimental setup, including the hardware and the temperature

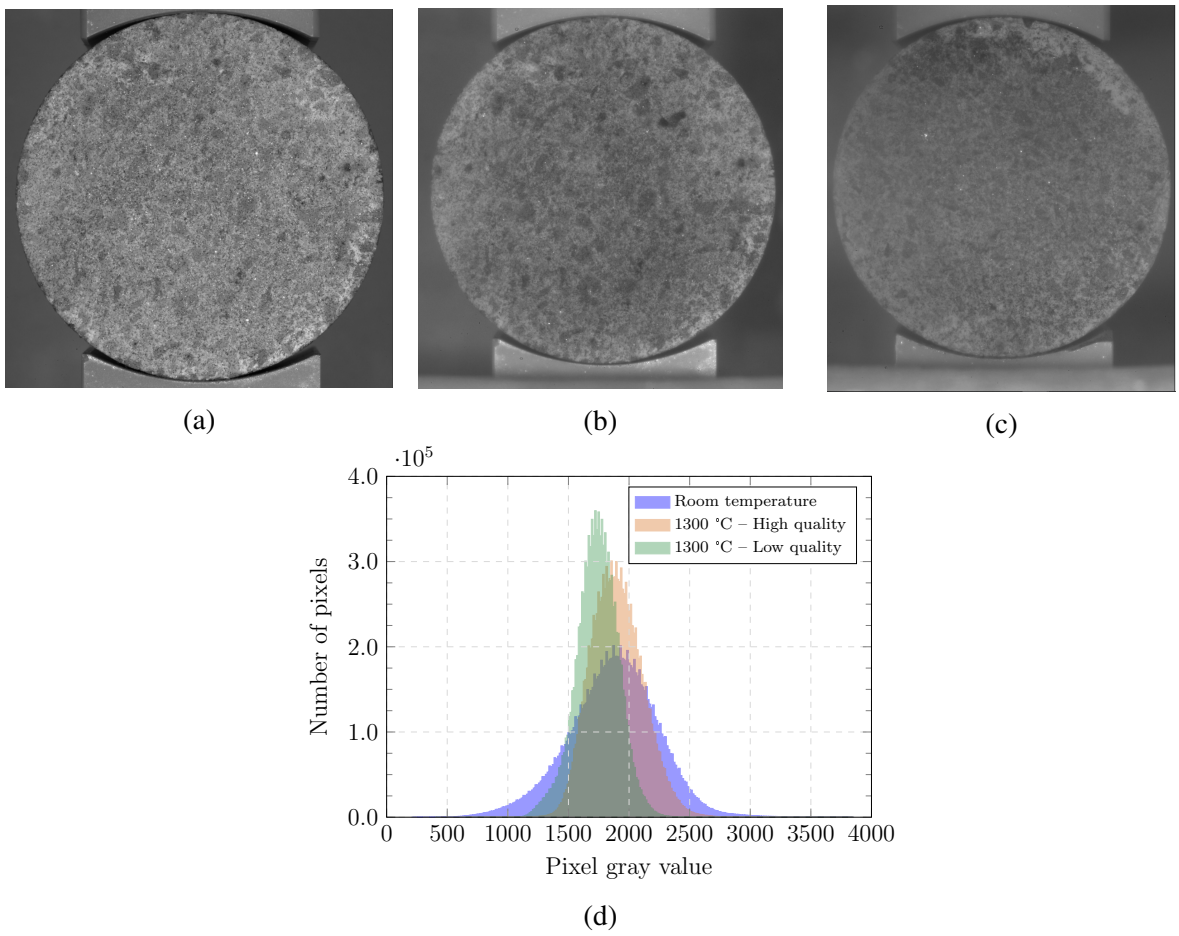

Figure III.41: Images with different qualities. (a) Room temperature image. (b) Image at 1300 °C – Higher quality. (c) Image at 1300 °C – Lower quality

in which the test is performed, since it influences the intensity of the heat hazes. The procedure to estimate the noise floor consists in taking several images in sequence, without any load applied, and calculating the error between the first image (considered the reference) and the subsequent ones. If no intrinsic error is present, the error resulting from the IDIC method is zero, which is never the case.

The noise floor at room temperature was estimated using the image shown in Figure III.41a as reference, and the average error of ten images taken under the same conditions was calculated, giving a value of $\phi = 8.957 \times 10^{-3}$. At 1300 °C, the image presented in Figure III.41b was used, also having the average error of ten images calculated, and the noise floor was $\phi = 9.289 \times 10^{-3}$.

As expected, the noise floor for the high temperature setup is higher than the one for the room temperature setup, mainly because of the heat hazes present in the first case. Nevertheless, the difference between the two values is small, showing that the experimental setup, explained in details in Chapter IV was able to minimize artifacts related to the more difficult experimental

conditions at high temperatures.

Calculation of the error variation Figure III.42 shows the variation of the error function with the material parameters, for the three images qualities described in the previous section.

Regarding the overall behavior of the error curves, it is evident that the images at room temperature are considerably more sensitive to the variation in the material parameters than the images at 1300 °C, due to their higher sharpness and contrast. It can also be observed that the high temperature images with lower quality present a flatter error function when compared to the ones with higher quality, although the difference is not large.

In accordance to what was presented in Figure III.11, that shows the variation of the vertical displacement at the point of load application of a Brazilian test according to the material parameters, the error function of the I-DIC method is more sensitive to A^- and A^+ than to m^-, since a change in those parameters causes a higher change in the error.

One important conclusion obtained from Figure III.42 is related to the expected accuracy of the identified parameters using the proposed I-DIC method, for the order of magnitude of the displacements expected for creep tests in the alumina-spinel material studied in this work. Considering the values of noise floor previously described, it is expected a minimum error of approximately 5% for the parameters A^+ and A^- and 7.5% for m^-, since the change in the error caused by variations lower than these values results in changes of the error function below the noise floor value.

III.4.2 Influence of images encoding

As explained in the description of the proposed I-DIC algorithm (Section III.3.5.1, Step 3), the encoding of the image can influence the accuracy of the results if the interpolation algorithm generate random errors of the same order of magnitude as the changes in the pixels values caused by the actual displacements. This is specially important for applications where small displacements are expected, such as in mechanical tests applied to refractories.

To verify the influence of the encoding in the identification of creep parameters for the alumina-spinel material studied in this work, an 8-bits equivalent of the image shown in Figure III.41b, taken under exactly the same conditions (1300 °C), was virtually deformed following the same procedure explained in Section III.4.1, and the evolution of the error around the reference value was calculated.

Figure III.43 shows the comparison between the error values obtained using 8-bits images and 12-bits images. The error values obtained using both encodings are not directly comparable,

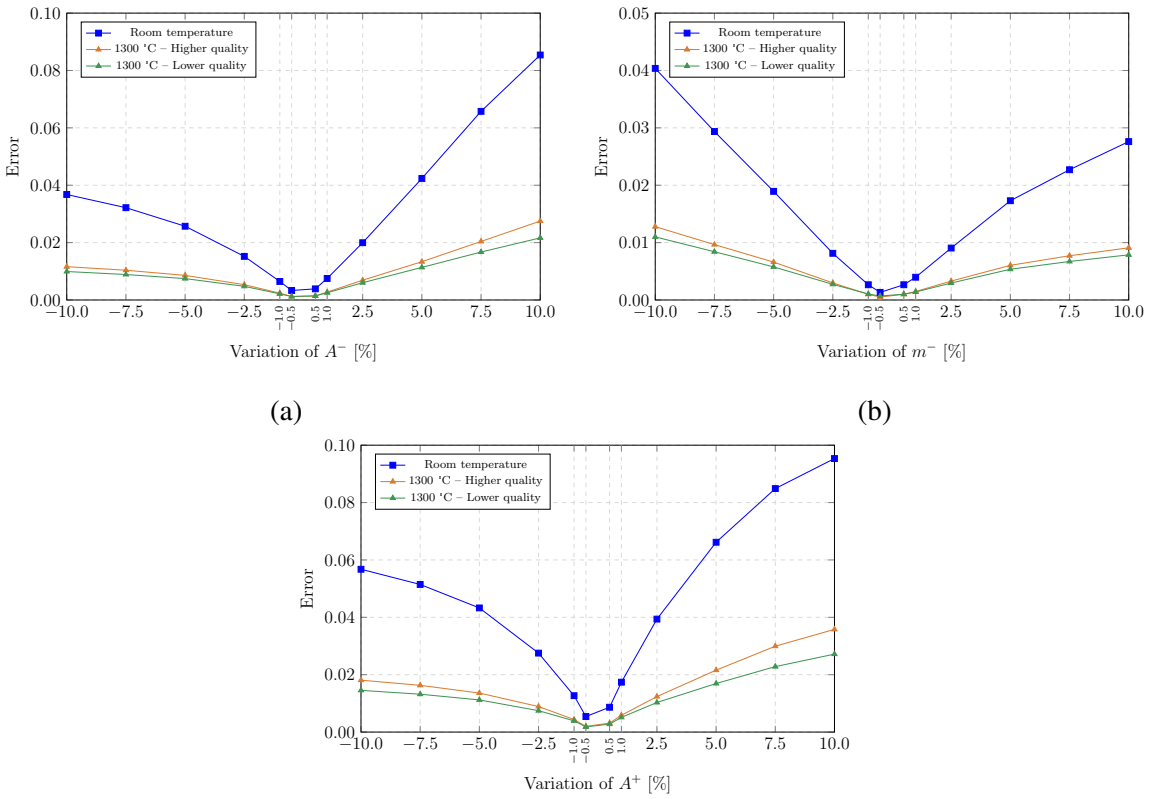

Figure III.42: Variation of the error function with the material parameters.

since 12-bits images give larger absolute values, due to the larger range of intensity values used in this case. Therefore, normalized values are presented.

Figure III.43 shows that the influence of the encoding in the variation of the error function according to the parameter A^+ is negligible, since both curves are almost overlapping in Figure III.43c. Therefore, the likelihood of an accurate identification of this parameter does not change with the encoding.

For parameter A^-, the difference between the curves starts to become more important close to the solution, and for the parameter m^- there is a considerable difference for variations below ±5%. As expected, the use of 12-bits images is more advantageous when the variation of the material parameters cause a smaller variation on the error function, since the influence of the round-off errors are larger in this case. This is confirmed by the fact that the parameter m^- is the least influential among the ones studied in this section, and also the one with the larger deviation between the 8-bits and 12-bits curves.

In general, for the I-DIC algorithm proposed in this work, which is targeted for applications involving small values of displacements, 12-bits images are recommended. When there are

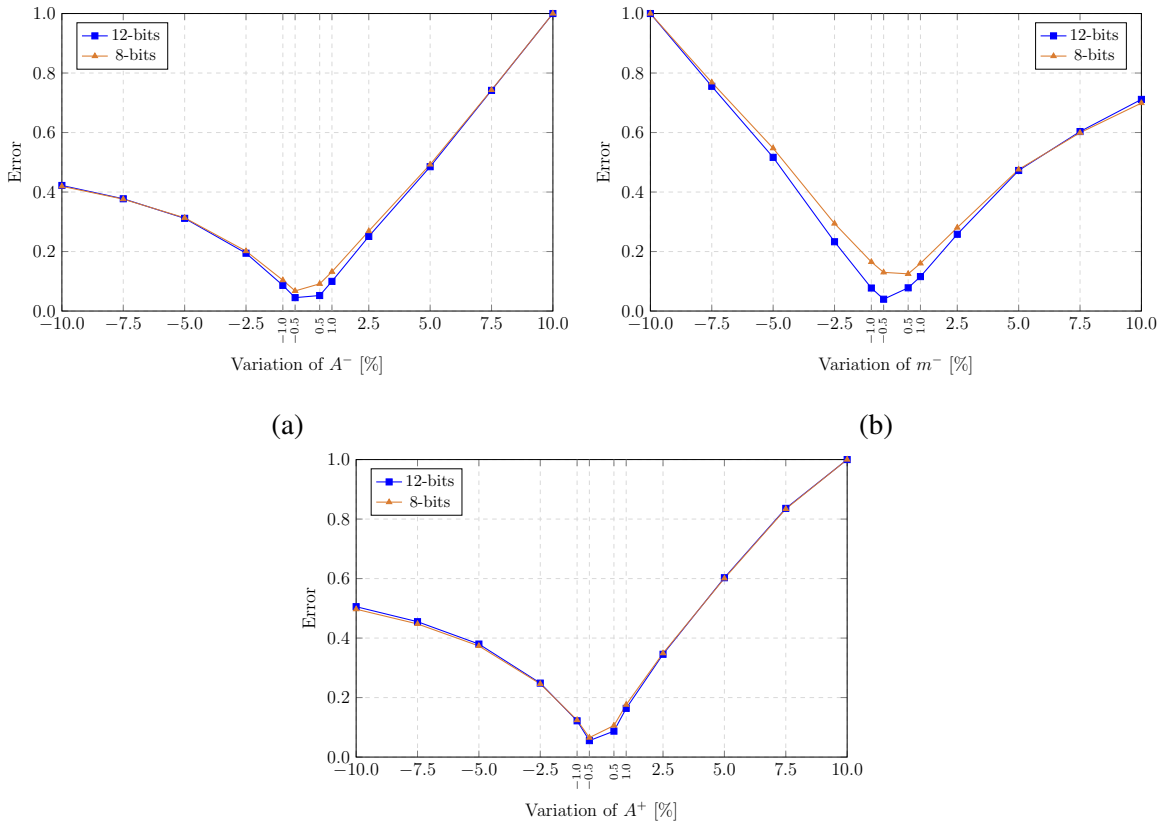

(a) (b)

(c)

Figure III.43: Variation of the error function with the material parameters – Comparison between 8-bits and 12-bits images.

limitations related to the available hardware or to the amount of storage space that the images take on the hard-drive, 8-bits images can be used, but a careful evaluation of the variation of the error function compared to the noise-floor error should be done.

III.4.3 Influence of the residual function under unstable lightening conditions

As described in Section III.3.5.2, the choice of the residuals function can have an important influence in the capacity of the algorithm to minimize the effect of changes in the lightening conditions during the experiments. To evaluate the difference in the evolution of the error function when the zero-normalized sum of squared differences (ZNSSD) for the residual function (Equation III.22) is used instead of the sum of squared differences (SSD) function (Equation III.21), the following procedure was used:

1. The image shown in Figure III.41b, which was taken at 1300 °C, was used as the reference.

2. Two levels of light variation were artificially imposed on the images:

    - Small variation: two of the five VDIs had their pixel values incremented by approximately 10% of the maximum possible intensity value, i.e., a value of 400 was summed to all pixels.
    - Large variation: four of the five VDIs had their pixel values incremented. The images had their pixel intensity values incremented by 100, 200, 400 and 800, respectively.

3. The variation of the error function with the material parameters was calculated using the SSD and the ZNSSD residual functions, and the results were compared

Figure III.44 shows the results obtained with the SSD and the ZNSSD residual functions. For all material parameters, the same behavior was observed, i.e., the ZNSSD function was insensitive to the light variations and the SSD function made the error function have a higher absolute value and to become flatter and the light variation increased. Therefore, it can be concluded that, when light variations occur during the experiment, the ZNSSD function should be used, to decrease the total error.

It should be emphasized that the ZNSSD function is not designed to mitigate errors generated by non-homogeneous light variations. Therefore, if different zones of the image experience different changes in the lightening conditions, errors will be added to the calculation.

III.5 Conclusion

This chapter presented the main contributions of this work regarding its theoretical and computational aspects. The two main topics discussed were the development of constitutive models to represent the behavior of refractories at high temperature and the proposition of a Integrated Digital Image Correlation algorithm that can be used for their characterization.

Two asymmetric creep models were proposed. Both models are based on a split of the stress tensor into positive and negative parts, and further weighting of the contributions of tensile and compressive stresses depending on a criteria based on the von Mises stress tensor.

The first model, called isotropic creep model, is able to represent primary or secondary creep under tension and compression. The material laws for each stress sign are independent from each other, which facilitates the characterization of the material.

The second model, called kinematic creep model, is able to represent the transient creep behavior from primary and secondary creep under compression. Based on experimental observations

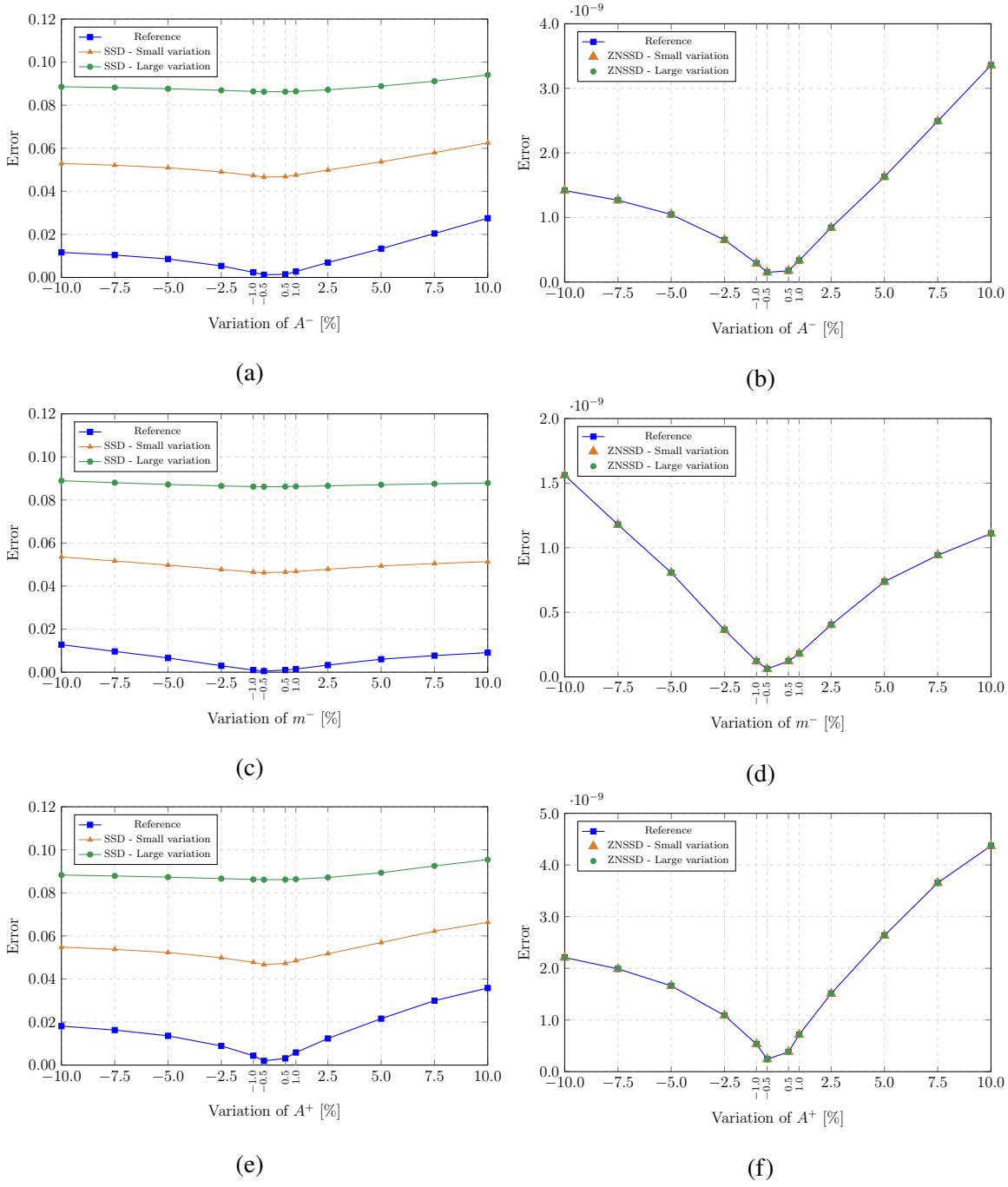

Figure III.44: Variation of the error function with the material parameters – Comparison between SSD and ZNSSD residual functions.

described in Chapter II, only secondary creep was considered under tension, in order to reduce the number of parameters to be identified.

A series of numerical simulations was presented for both models, in increasing level of complexity, including the study of the interaction between two bricks in a steel ladle under service

related thermal conditions. The goal of these simulations was to show that the models behave as expected, from a theoretical point of view.

An I-DIC method was proposed for the identification of the material properties at high temperatures, using full field measurements of a Brazilian test. This methodology has the advantage of incorporating experimental imperfections in the identification procedure, by considering the rotation of the sample on the numerical simulations that act as a digital counterpart to the mechanical tests. The Brazilian test was chosen as the main experimental technique because it results in tension and compression stresses in the sample at the same time, which is appropriate to characterize asymmetric models using a reduced number of samples.

The study of the I-DIC algorithm error function has show that the quality of the images has a large influence on the results obtained by the technique, since it influences the noise floor value and the variation of the error function with the material parameters. In general, images with high contrast, an uniform distribution of gray levels within the camera's dynamic range and high values of encoding should be used, especially when small displacements are expected, as it is the case for refractory materials. It has also been shown that a ZNSSD residual function is preferred over a simpler SSD function, since it makes the error insensitive to lightening variations during the experiment.

CHAPTER IV

Proposed Approach for the Identification of Creep Parameters – Practice

The goal of this chapter is to present the experimental aspects of the approach proposed for the identification of creep parameters of refractories at high temperature, and to show the identification results.

Section IV.1 presents the experimental setup used to perform the Brazilian tests, as well as the results obtained with each of the DIC based identification procedures proposed in this work.

Section IV.2 describes the four-point bending tests used to validate the identified material parameters, and the results of the validation.

Finally, Section IV.3 compares the advantages and disadvantages of the proposed identification procedure in relation to the traditional characterization methods described in Chapter II.

Chapter Contents

IV.1 Identification of material parameters using the Brazilian test 137
IV.1.1 Experimental methodology 137
IV.1.2 First identification approach – DIC and numerical simulations 145
IV.1.3 Second identification approach – Integrated Digital Image Correlation . 152
IV.2 Validation of the results using four-point bending tests at 1300 °C 158
IV.2.1 Experimental methodology 158
IV.2.2 Validation results 162
IV.3 Comparison between the proposed and traditional identification approaches . . 166
IV.3.1 Test design 166
IV.3.2 Sample preparation 167
IV.3.3 Experimental data post-processing and amount of retrieved information 167
IV.3.4 Availability of testing equipment and test's robustness 168
IV.3.5 Time and budget constraints 168
IV.4 Conclusion 169

IV.1 Identification of material parameters using the Brazilian test

In this chapter, Brazilian tests are used to identify the creep parameters of the alumina-spinel material, and the results are compared to what was obtained using compressive and tensile creep tests, as presented in Chapter II.

IV.1.1 Experimental methodology

IV.1.1.1 Experimental setup

Figure IV.1 shows the experimental setup used to perform the Brazilian tests and to take the pictures at high temperatures. This setup is composed of the following parts:

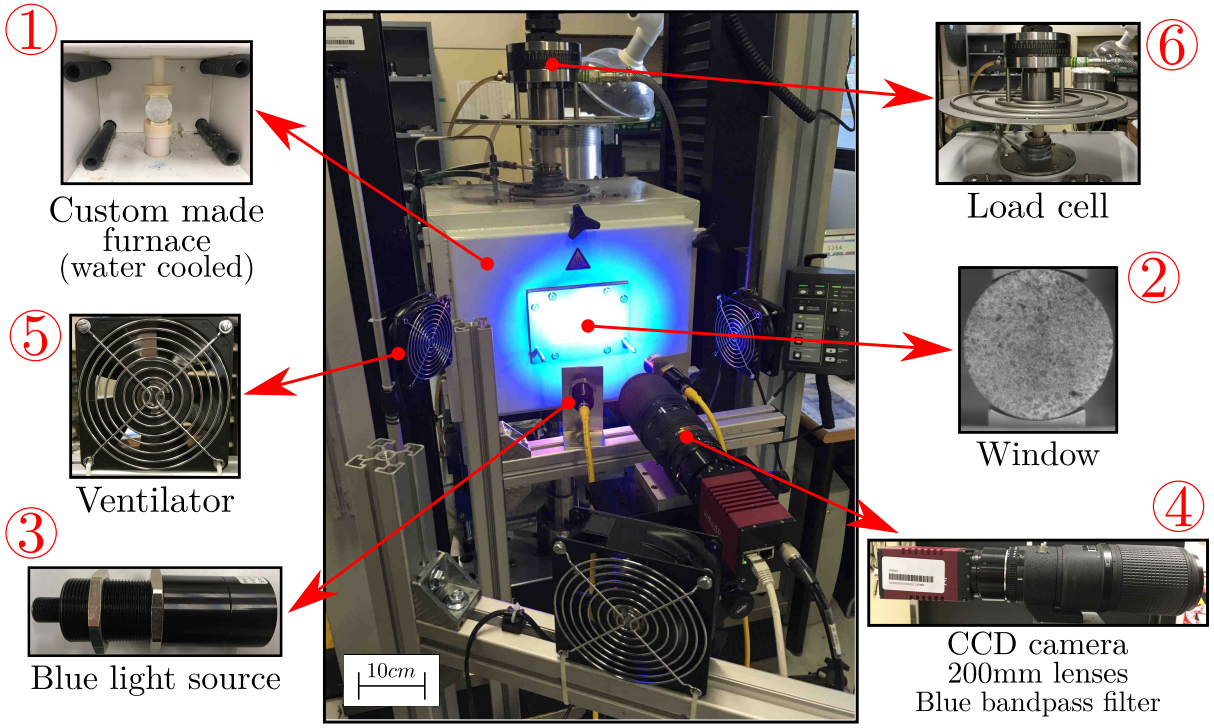

Figure IV.1: Experimental setup for the Brazilian tests at high temperature

1. A custom made furnace designed by the company AET Technologies. This furnace is water cooled, and has the capacity to heat up to 1300 °C. It has four heating elements, positioned in two rows at the internal chamber. The temperature in the furnace is controlled using a master/slave configuration, allowing the desired output temperature to be setup in one of the PID controllers and transmitted automatically to the other, that provides enough power to follow the input signal.

2. The furnace's door is equipped with a window made of a vitro ceramic material, so that the sample can be photographed. This material was chosen because of its adequate resistance to temperatures up to 1300 °C, it's near zero expansion coefficient and also due to its inexpensive price. The material is transparent enough to allow that good pictures are taken, and preliminary tests prior to the ones used to perform the inverse identifications showed that this solution is satisfactory.

3. To increase the amount of blue light available when taking the pictures, two blue light sources are used to enlighten the sample. In combination with the blue filters, it increases significantly the contrast of the pictures, to a point where the DIC analysis becomes possible. These lights are mounted in a dedicated support that was designed to offers six degrees of freedom, so they can be easily positioned to avoid glare in the pictures. Specification:

    - Product: SX30 Prox Light
    - Manufacturer: Smart Vision Lights
    - Type: Bright field
    - Minimum working distance: 500 mm
    - Maximum working distance: 4000 mm
    - Wavelength: 470 nm

4. To guarantee that the pictures start to be taken at the same moment as the test begins, an in-house software was developed to synchronize the camera and the testing machine. The pictures are taken using the following optical devices:

    - A high resolution CCD camera with capacity to transmit the output images at a fast rate using an ethernet connection, which avoids the lost of data packages. Specification:
        - Product: Prosilica GX 6600
        - Manufacturer: Allied Vision
        - Resolution: 6576 (H) x 4384 (V) pixels
        - Encoding: 12 bit
        - Interface: Two 120 MBps Gigabit Ethernet ports
    - Lenses
        - Product: AF Micro-Nikkor
        - Manufacturer: Nikon

  - Focal distance: 200 mm
  - Max-Min aperture: f/4 – f/32
  - Maximum working distance: 500 mm
- A blue band pass filter, to decrease the amount of light being captured by the camera, since it blocks all parts of the optical spectrum that are not blue, avoiding the saturation of the sensor. The variation of the transmission according to the wavelength is shown in Figure IV.2, as available on the manufacturer's website. Specification:
  - Product: BP470 blue band pass filter
  - Manufacturer: Midwest Optical Systems, Inc.
  - Useful range: 425–495 nm
  - Tolerance: ± 10 nm
  - Peak transmission: ≥ 90%

5. The camera and the lenses are cooled using two ventilators, since they stand close to the furnace and can overheat. A third ventilator is used to blow away the hot air between the window and the lenses, minimizing the generation of heat hazes.

6. A load cell with maximum capacity of 30 kN, with a full reading error of 0.25%.

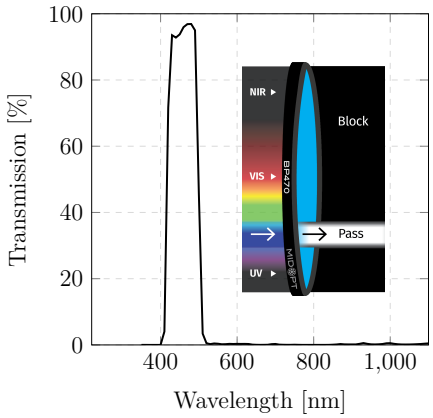

Figure IV.2: Blue band pass filter – Transmission variation according to the wavelength (Source: manufacturer's website)

IV.1.1.2 Samples preparation and speckle pattern

The samples used in the Brazilian tests were cut from parallel refractory bricks. The first step was to cut slices 40 mm thick, to guarantee the parallelism of the sample surface exposed to the

camera. Second, 50 mm cylinders were drilled from these slices. This geometry was chosen to comply with a rule of thumb that requires the minimum dimension of the sample to be at least 10 times the size of the largest grain in the material, that, in the case of the alumina-spinel brick, is 3 mm.

To improve the contrast of the samples surfaces, a SiC powder speckle pattern was used, with grain sizes varying from 50 μm to 100 μm. The surfaces of the sample were covered with a bonding agent, and the powder was deposited using a sieve, similar to what was done by Archer et al. (2020), what allowed a reasonable control over the particles dispersion. Using this method, the speckle doesn't remain strongly attached to the sample, and, even if it doesn't detach under simple gravitational action, direct contact with it should be avoided. Before the test, the sample was let at rest for 12 hours, in order to dry the excess of the bonding agent. Figure IV.4a shows an example of a sample coated with a speckle pattern, already positioned at the testing machine.

Other options for the speckle pattern were also tried, such as brown fused alumina and cobalt oxide, but none of them could be stable at high temperatures and provide enough contrast at the same time.

IV.1.1.3 Tests description

To guarantee the good quality of the pictures, a rigorous procedure was followed at each test. This procedure was composed of:

1. The sample and the jaws were positioned at the testing machine at room temperature, and an initial pre-load of approximately 10 N was applied. This pre-load was sufficient to hold the sample in place, but still allowing minor changes in its position.

2. The camera was positioned at the point it would be at the moment of the test, and the sample was visualized at the in-house software to verify if there were any misalignment. If necessary, the position of the sample and/or the jaws was changed, until the camera axis was perpendicular to the sample's surface.

3. The pre-load was increased to 50 N, to ensure the sample would not move during heating. The machine was put under force control mode, so the upper piston could move along the thermal expansion of the sample, avoiding the generation of unwanted stresses.

4. The furnace was closed, and the heating of the sample started. Figure IV.3 shows the heating curves used for the tests. Between room temperature and 600 °C, a heating rate of 10 °C/min was used. From 600 °C to the test's temperature, this rate was reduced to 5 °C, to avoid thermal damage on the sample and on the equipment. Before the beginning of the

test, the furnace was let in a dwell for 2 h, to stabilize the temperature of the testing setup. The blue curve on Figure IV.3, obtained from one of the tests made at 1300 °C, shows that the displacement of the machine piston was constant before the end of the dwell, indicating that there was no extra thermal expansion of the equipment at the beginning of the test. The camera was kept in front of the furnace and plugged to the computer during the dwell time, to allow its thermal stabilization and expansion too.

5. After the temperature homogenization time was passed, the camera lenses and the blue band pass filter were cleaned to remove any dust particles that could cause artifacts in the pictures and later mounted on the camera. To increase the images contrast, the blue lights were positioned to generate the maximum illumination of the sample as possible, avoiding glare, and the focus was manually adjusted in order to increase the sharpness. The exposure time was adjusted according to the lightning conditions to avoid too bright or too dark images.

6. Once all the parameters were properly adjusted, the image was crop to eliminate unused pixels, having only the sample on the frame.

7. Before the loading started, several reference pictures were taken.

8. The sample was loaded at a rate of 0.5 mm/min until the creep load was achieved, and the force was held constant until the end of the test.

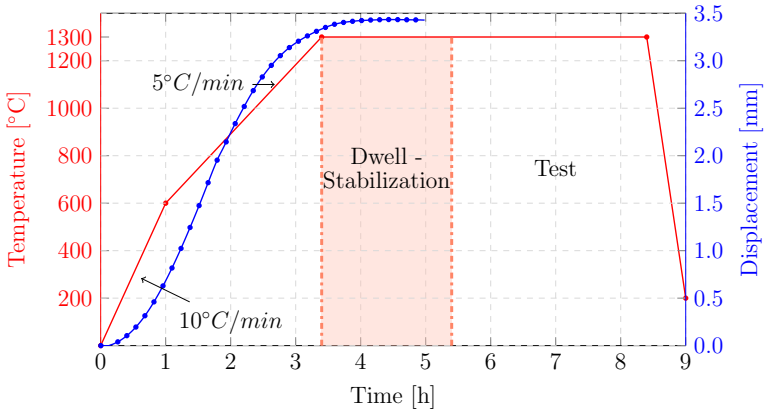

Figure IV.3: Brazilian tests: heating curve and evolution of machine displacements prior to the test.

Figure IV.4 shows the effect of the lightning and of the blue band pass filter in the quality of the images. At room temperature (Figure IV.4a), the histogram of the image, shown in Figure IV.5, is approximately normally distributed around gray values from 75 to 200, and the image presents

a high contrast. At 1200 °C, without the use of the blue lights and of the blue band pass filter (Figure IV.4b), the distribution of gray levels is restricted to the range between 105 and 115, and the images looses most of its contrast. The use only of the blue band pass filter, without the blue lights (Figure IV.4c), slightly decreases the sharpness of the histogram, but not enough to guarantee enough contrast. Finally, using the blue lights and filter (Figure IV.4d), the gray level distribution becomes closer of that of the image at room temperature, and most of the contrast is recovered.

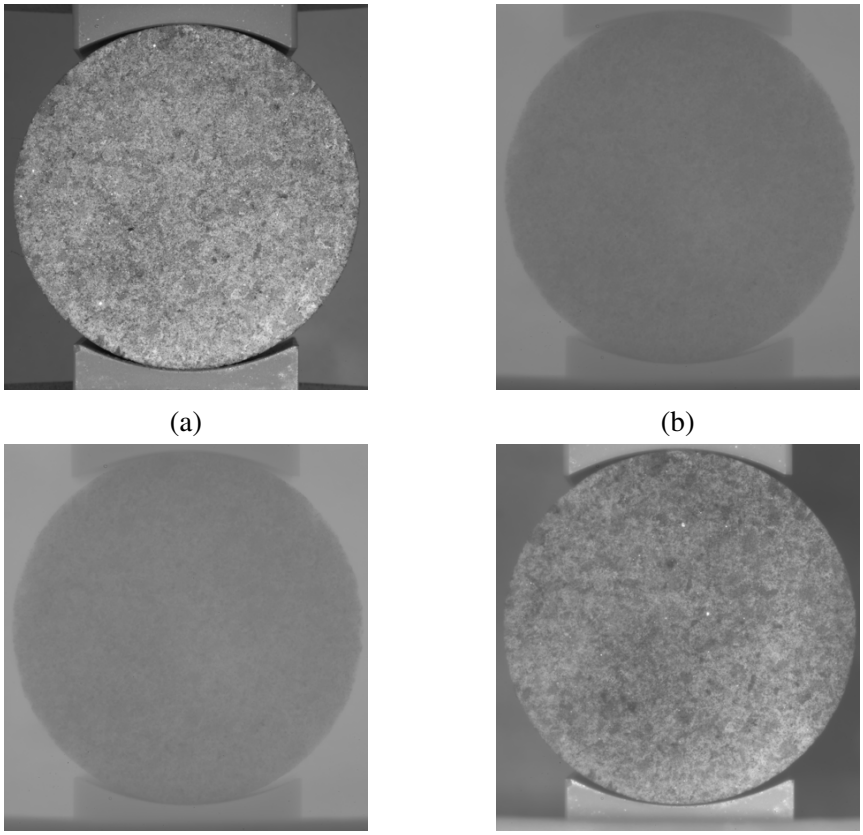

(a) (b) (c) (d)

Figure IV.4: Influence of the blue light and the blue band pass filter in the quality of the image. (a) Image at room temperature. (b) No blue light and no filter. (c) No filter. (d) Use of blue light and blue band pass filter.

IV.1.1.4 Selection of the temperatures and loads

The maximum temperature of the Brazilian tests tests was limited by the furnace capacity, that was 1300 °C. Although this value is lower than the maximum operation temperature of the alumina-spinel refractory, which is around 1600°C, it is sufficiently high to demonstrate the capabilities of the proposed creep models, identification procedure and test setup. Therefore,

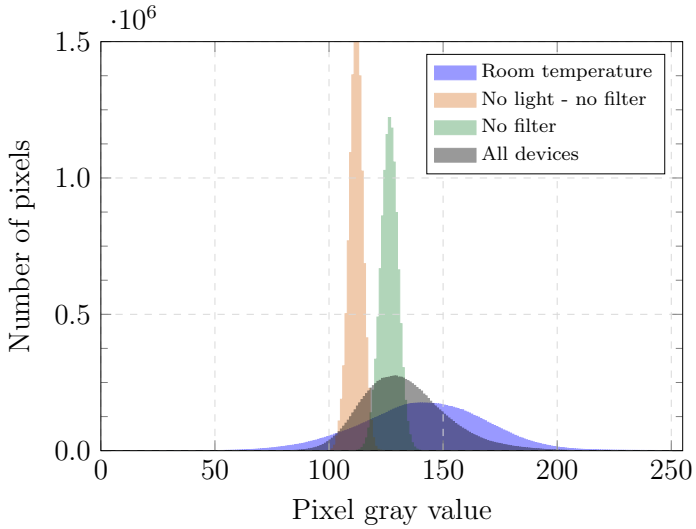

Figure IV.5: Histograms of the images at room and high temperature.

the creep tests were made at 1200 °C and 1300 °C, but only the results at 1300 °C are exploited in details.

The main goal when the selection of the load was made was to maximize the signal-to-noise ratio, i.e., the ratio between the variation of the pixel gray levels due to the loading and that due to the noise from the experiment. Considering the intrinsic low strain values associated with refractory materials, it was considered to be critical to obtain the maximum values of displacements as possible.

Using as a reference the tensile creep tests presented in Chapter II, it is possible to estimate that the maximum tensile stress that the sample can undergo before cracking at 1200 °C and 1300 °C are, respectively, 0.45 MPa and 0.25 MPa. The stress distribution for a linear elastic case, given by Equation I.3, was used to estimate maximum load that could be applied on the Brazilian sample in order to remain within this stress range. As a result, a load of 1000 N was used at 1200 °C (σ_{max} = 0.32 MPa) and a load of 800 N was used at 1300 °C (σ_{max} = 0.25 MPa).

It is important to highlight that the maximum force is only obtained at the central point of the sample, decreasing towards its edge. Figure IV.6 shows an example of stress distribution on a Brazilian test for a load of 800 N. In terms of area, 45% of the sample has maximum principal stresses between 0 and 0.05 MPa, and 20% has stresses between 0.20 MPa and 0.25 MPa (Figure IV.6a). Although the minimum principal stresses on the sample can achieve −5 MPa, disregarding the high stress concentration near the contacts with the jaws, Figure IV.6b shows that only 5% of the area of the figure is above −2 MPa, and 53% present compression stresses of less than −0.5 MPa.

It is clear that, even if only a small portion of the higher tensile and compression loads are

present at the sample during the test, they influence in the overall mechanical equilibrium, and therefore influence in the results of the identification. Nevertheless, during I-DIC identification it should be expected to have the results tending to be more accurate for a compression stress in the range between 0 and −2 MPa, since those values directly influence 96% of the pixels.

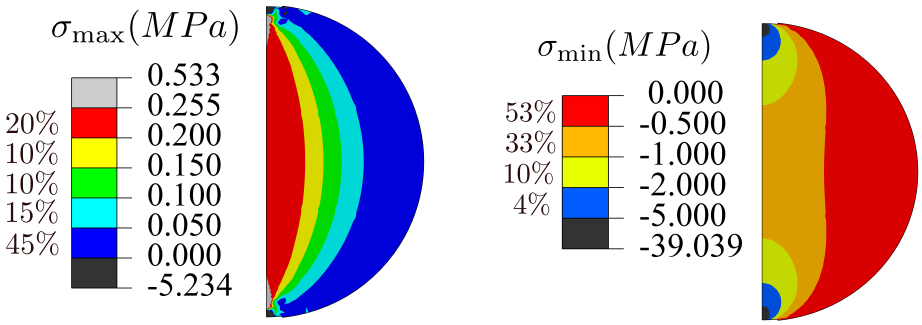

(a) (b)

Figure IV.6: Distribution of stresses in a Brazilian test considering linear elastic material properties - Distribution according to the area percentage. (a) Maximum principal stresses. (b) Minimum principal stresses.

Another constraint was the progressive oxidation of the *SiC* speckle pattern. To decrease the effect of this error source on the inverse identifications, the tests need to be designed to be as fast as possible, without major damage of the sample. This is also consistent with the need to apply a stress that is as high as possible, without excessive damage of the sample.

IV.1.2 First identification approach – DIC and numerical simulations

Before proceeding to perform an I-DIC identification, it is important to analyze the results from the experiments using simpler and faster methods. One of the goals of these pre-identification analysis is the verification of the consistency of the results among the tests, i.e., to verify if tests at the same conditions provide approximately the same results.

In this work, the open-source DIC software Ncorr (Blaber et al., 2015) was used to calculate the full field displacements of the samples. Ncorr uses the local subset-based reliability-guided DIC method according to Pan (2009). Considering the low displacements values expected for the tests on the alumina-spinel material and the relatively low contrast of the images obtained at high temperature, the DIC calculations using Ncorr are not expected to provide high accuracy results, but to a reliable first estimation of the material parameters.

All results presented in the next sections correspond to identifications performed at 1300 °C.

IV.1.2.1 Identification of the constitutive parameters for the isotropic creep model

In this section, the constitutive parameters for the isotropic creep model proposed in Chapter III.1.1, Equation III.3 are identified, and the results are compared to what was obtained using the uniaxial compressive creep tests, presented in Chapter II.4.1.

Figure IV.7 shows the vertical displacement of the upper point of the Brazilian test samples at 1300 °C, calculated using DIC. It is possible to observe that samples 1, 3, 5 and 6 are in good agreement, while samples 2 and 4 are lower and upper outliers, respectively. This presents an important result, since samples 2 and 4 can now be neglected during the more time consuming DIC analysis.

The higher repeatability of the Brazilian tests when compared to the uniaxial tests presented in Chapter II, specially in the case of the tensile tests, can be explained by the fact that, in this case, the crack initiates at the inner portion of the sample, and therefore is confined by the surrounding compressive stresses, what is closer to the reality of refractory linings.

Another important advantage of performing a standard DIC analysis prior to the more refined I-DIC calculations is to restrict the possible range of variation for the material parameters. When the solution space for the identification problem is complex, such as in the case of the asymmetric creep model, an unreasonable large range for the input parameters can result in excessive computational time and in convergence problems, so it is important to limit the input domain. Figure IV.8 shows an example of envelope for the material parameters at 1300 °C, obtained through a series of numerical simulations using the isotropic asymmetric creep model presented in Section III.1. During the I-DIC identifications, it can be expected that the material

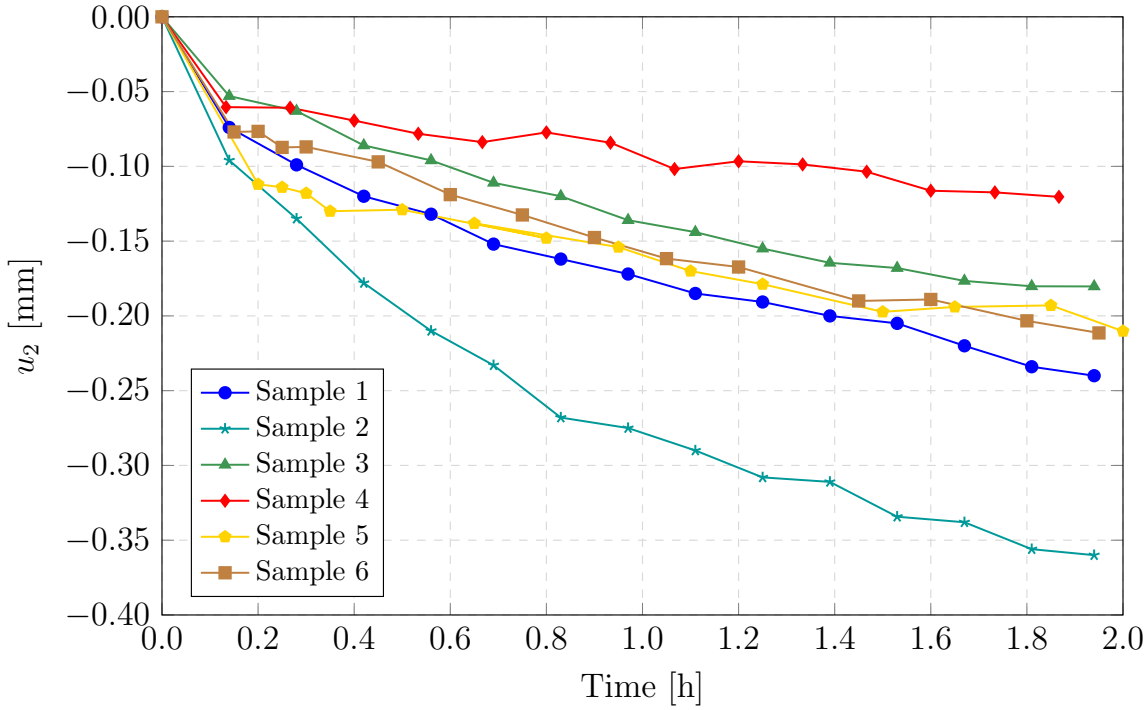

Figure IV.7: Brazilian tests time vs displacement curves obtained by DIC – 1300 °C.

parameters will not highly deviate from the ones presented in the figure, even if this analysis only considers a single displacement value, and not the full field.

Finally, taking into account the influence of the material parameters in each portion of the time vs displacement curve for Brazilian tests presented in Section III.2.1.2, the parameters for the alumina-spinel material were fitted in order to better approximate the values of the DIC calculations, and the resulting curve is presented in Figure IV.9. The identified parameters are shown in Table IV.1.

Table IV.1: Isotropic creep parameters – Identification using Brazilian creep tests

Parameter	**Value**	**Difference from uniaxial**
$\log_{10}(A^-[MPa^{-n}s^{-1}])$	−14.86	4.8%
$n^-[-]$	3.96	0.0%
$m^-[-]$	−2.74	0.0%
$\log_{10}(A^+[MPa^{-n}s^{-1}])$	−5.55	–
$n^+[-]$	1.5	–

It is important to note that the tensile creep results identified using the Brazilian tests are considerably different from what was obtained using the uniaxial tests presented in Chapter II.4.3. Once again, this deviation can be caused by factors involving the repeatability of the experiments,

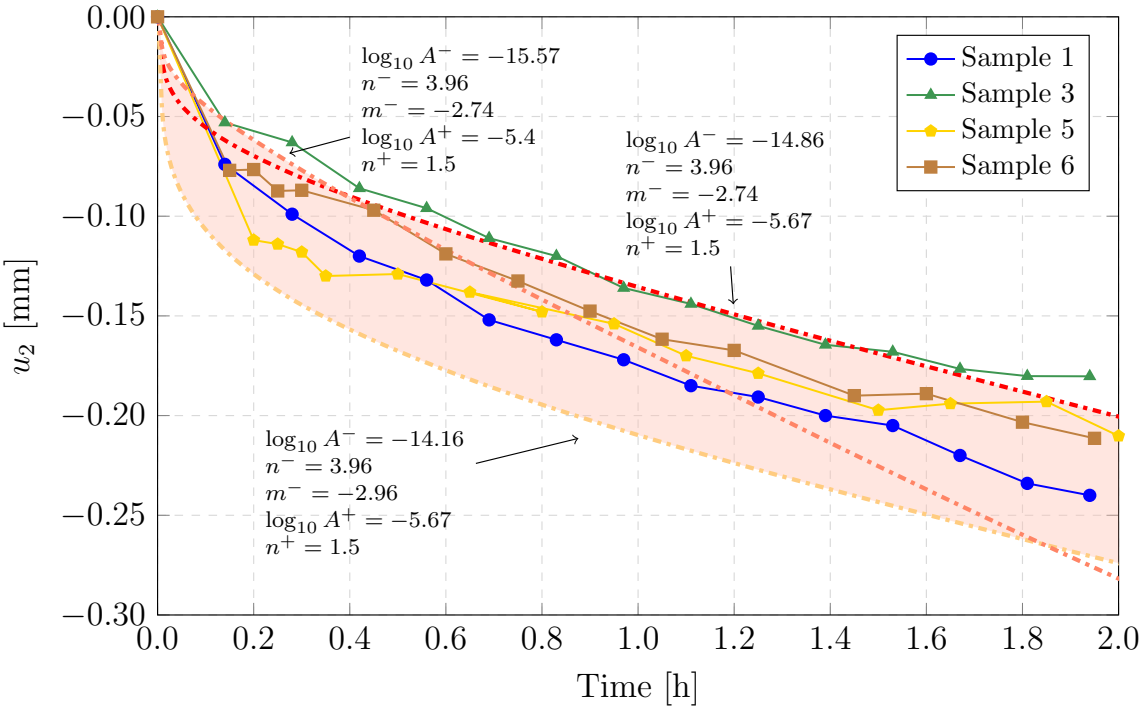

Figure IV.8: Brazilian tests time x displacement curves and parameters envelope.

but also to the way that cracks propagate fast in a pure tension test. A further investigation of the reasons of these differences are beyond the scope of this work, and are suggested for future research.

From Figure IV.9 it is possible to observe that, until 1 h of test, the identified curve is in good agreement with the data from sample 6, while being in between samples 1 and 3. From this point, it becomes closer to sample 1, presenting a deviation of approximately 20% in relation to samples 5 and 6 and approximately 45% from sample 3. Sample 5 is a particular case, that presents a higher displacement that the identified curve during the first half of the test, and a lower displacement in the second half.

A robust way to verify the accuracy of the results obtained using the hand-fit identifications is to compare the DIC displacement field with the ones resulting from the numerical simulations performed using the identified material parameters.

The vertical displacements fields of Points A, B and C represented in Figure IV.9, corresponding to t = 0.6 h, t = 1.05 h and t = 1.45 h, respectively, are shown in Figure IV.10. It is possible to see that there is a rigid body rotation of the sample, since the displacements map does not correspond to the traditional displacements field of Brazilian tests. To consider this effect, an extra identification calculation was made to determine what is the magnitude of the load that caused this deviation. An horizontal load of −7 N was identified and applied on the upper jaws in

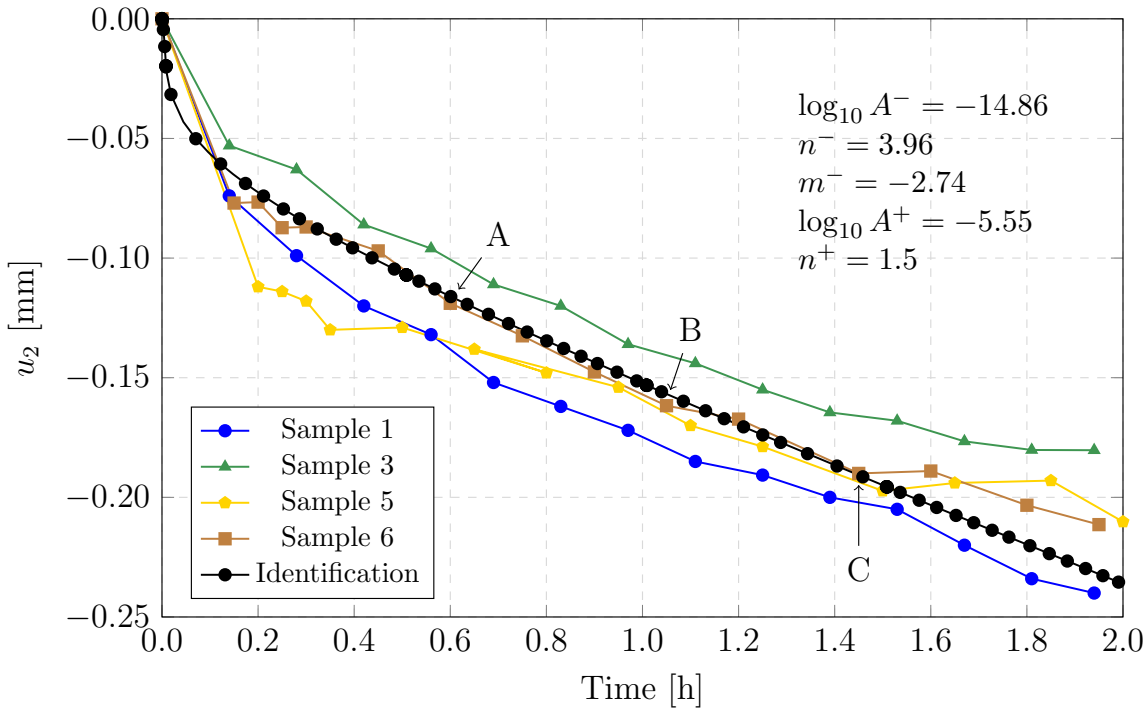

Figure IV.9: Brazilian tests time vs displacement curves and inverse identification.

the simulation model. This corresponds to an error of 0.5° in the application of the load, which shows that the experimental procedure is sensitive to small deviations from the ideal boundary conditions.

Figure IV.11 shows the results of the numerical simulations using the previously identified material parameters and the horizontal load. It is possible to observe that the displacement maps of Figures IV.10 and IV.11 have a good equivalence, despite the experimental errors and the simplicity of the identification procedure.

It is interesting to observe how the vertical displacement of the central line of the sample changes when the rigid body motions are included in the simulation, like shown in Figure IV.12. When the boundary conditions are symmetric, the displacement increases monotonically and equally in both sides of the sample, as expected. Nevertheless, a horizontal force in the negative x direction causes an increase in the right side of the sample, while the left side has a positive displacement during loading. After approximately 1 h of creep deformations, the displacement of the right side becomes negative again, but always smaller than at the left. This non-symmetric behavior is frequently observed in mechanical experiments, as discussed in Chapter I, and has the potential to negatively influence the I-DIC identifications if not properly considered.

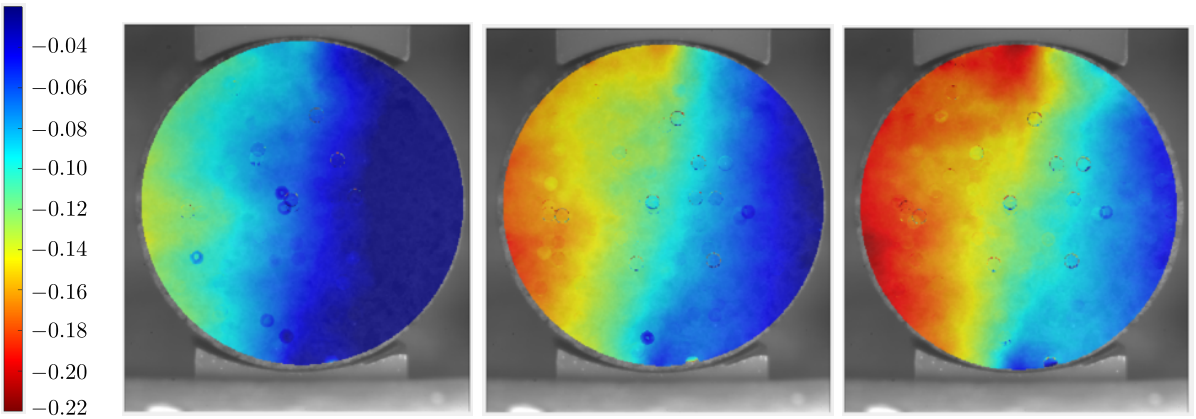

Figure IV.10: Brazilian tests: Vertical displacement in mm at 1300 °C – DIC sample 6. (a) Point A. (b) Point B. (c) Point C.

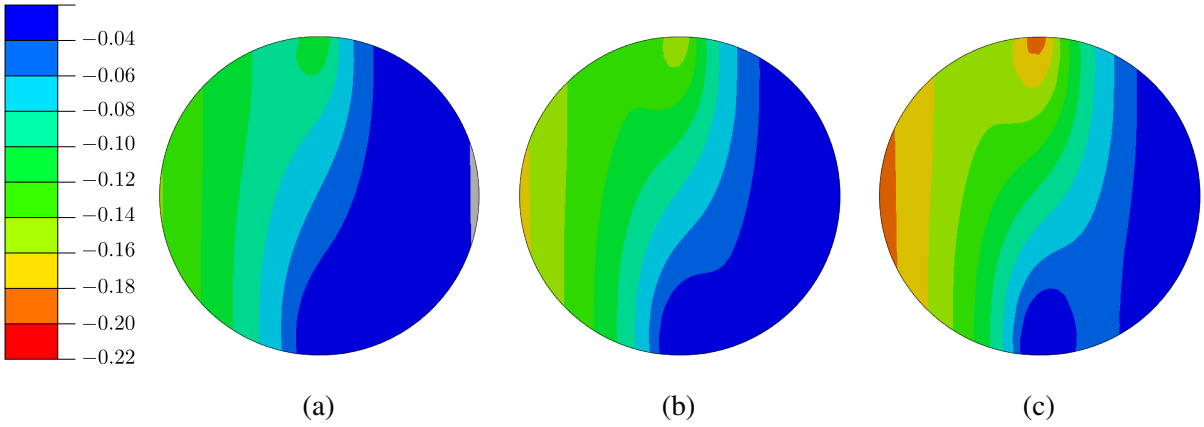

Figure IV.11: Brazilian tests: Vertical displacement in mm at 1300 °C – Simulation. (a) Point A. (b) Point B. (c) Point C.

IV.1.2.2 Identification of the constitutive parameters for the kinematic creep model

In this section, the constitutive parameters for the compressive part of the kinematic creep model proposed in Chapter III.1.2, Equation III.8 are identified, and the results are compared to what was obtained using the uniaxial compressive creep tests, presented in Chapter II.4.2. Since the tensile part of the isotropic and kinematic models is the same, the tensile parameters presented in Table IV.1 where used to obtain the following results.

Figure IV.13 shows the experimental and numerical values of vertical displacement in the Brazilian test sample at the point of application of the load. As it can be observed, the pink curve representing the simulated results using the material parameters identified using compressive tests is bounded by the experimental results, which validates the model and the identified parameters.

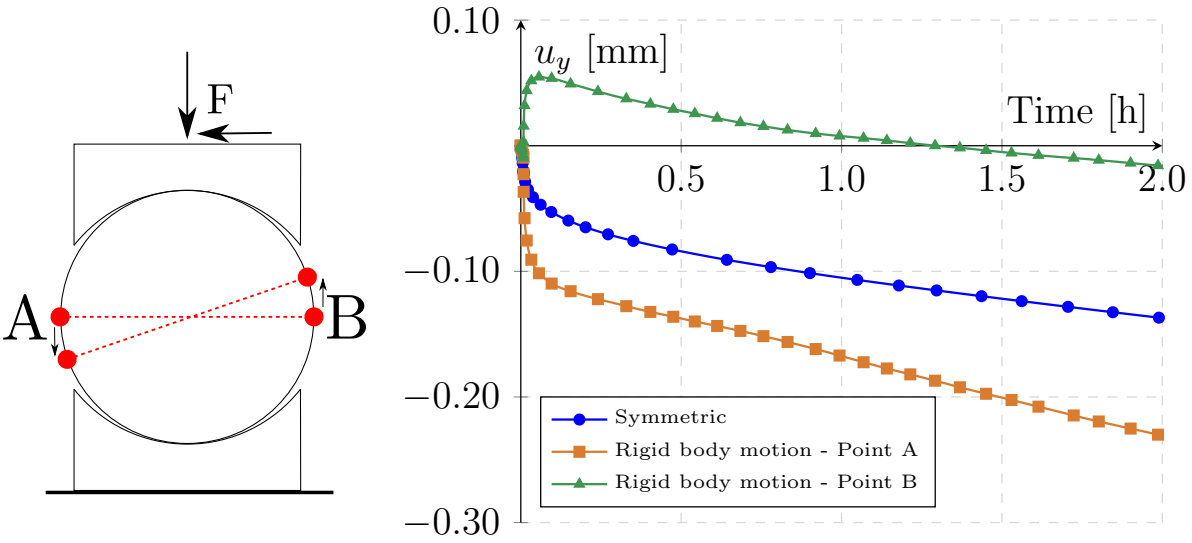

Figure IV.12: Brazilian tests: Vertical displacement in the central line of the sample.

Nevertheless, it is possible to obtain a better fit for the Brazilian tests results if small variations are made into the identified parameters, as shown by the black curve in Figure IV.13. As indicated in Table IV.2, the difference between the identified values of the variables $\log_{10} a$ and $\log_{10} b$ and those that provide the best fit for the Brazilian tests are 2.6% and 5.2%, respectively, which can be considered a small variation for highly heterogeneous materials such as refractories, where there is often a considerable scatter in experimental results.

Table IV.2: Kinematic creep parameters – Identification using Brazilian creep tests

Parameter	**Value**	**Difference from compression tests**
$\log_{10}(a[MPa^{-n}s^{-1}])$	−6.15	2.6%
$\log_{10}(b[MPa(1+scMPa^{n-1})])$	2.70	5.2%
$\log_{10}(c[MPa^{-n}(MPa+b)/s])$	−5.010	0.0%
n_k [-]	1.981	0.0%

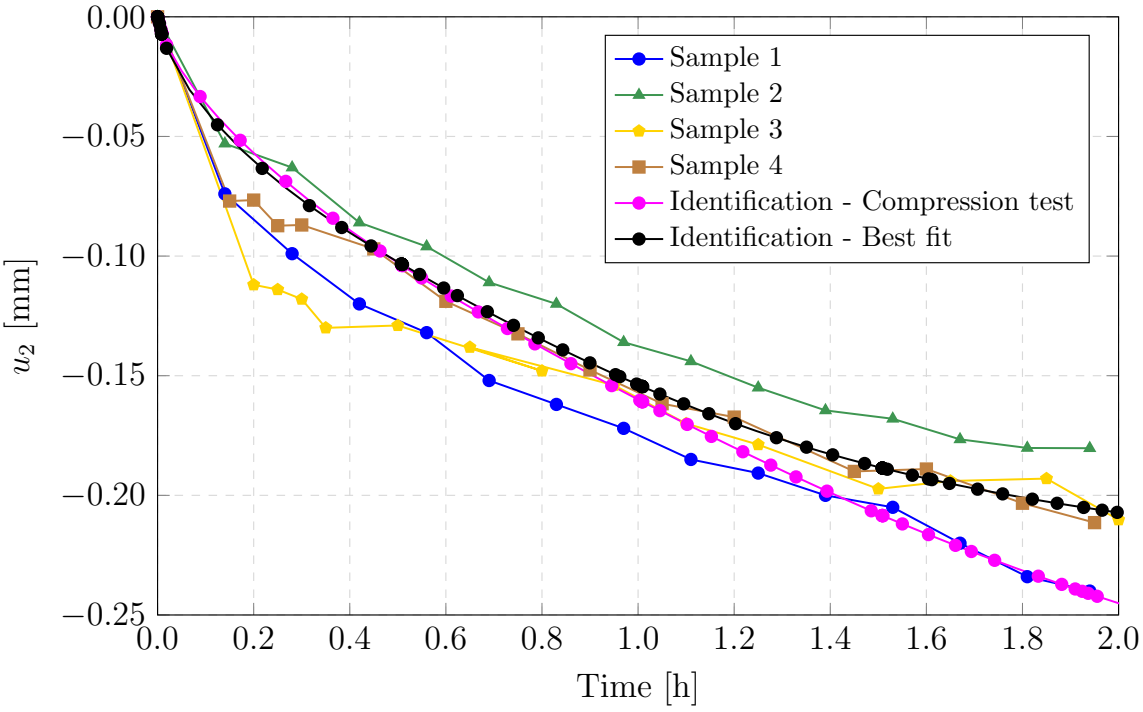

Figure IV.13: Validation of the identified kinematic creep parameters – Vertical displacement at the load application point in a Brazilian test.

IV.1.3 Second identification approach – Integrated Digital Image Correlation

In this section, the constitutive parameters for the asymmetric isotropic creep model proposed in Section III.1 are identified, using the I-DIC technique proposed in Section III.3.5.1.

As in the case of the identification using the traditional DIC techniques (Section IV.1.2), Brazilian tests at 1300 °C were used. Since Figure IV.7 showed that samples 4 and 2 presented considerably different values of vertical displacement in comparison with the remaining four samples, they were not considered in the calculations.

As in the virtual experiments (Section III.4), only the parameters $\log_{10} A^-$, m^- and $\log_{10} A^+$ were identified in the isotropic creep model, since the Brazilian test showed to have a low sensitivity to n^+ and n^-. Considering that the horizontal force causing the rotation of the sample during the mechanical test (Figure III.37) also needs to be identified, the resulting optimization problem has four unknowns for each case.

One important aspect for the success of the inverse identification is the limitation of the material parameters to a reasonable range, which depends on the specific application. For example, the parameters $\log_{10} A^-$ and $\log_{10} A^+$ have no theoretical bounds for their values, but if an excessively large range of variation is allowed during the identification, it increases the chance that local minima are identified during the optimization, since the error function becomes more complex.

Therefore, the results of the regular DIC identifications, the simulations showing the influence of each parameter in the displacement field and the virtual experiments were used to define the allowed range of variation for the material parameters, which are shown in Table IV.3. For the horizontal force, the range of variation was selected based on the observation that the testing machine had a bias to always make the sample rotate in the same counter-clockwise direction (Section IV.1.2).

Table IV.3: Range of variation for the parameters used in the I-DIC identifications.

Parameter	**Lower bound**	**Upper bound**
$\log_{10} A^-$ [MPa$^{-n}s^{-1}$]	-16.99	-12.74
m [−]	-3.28	-2.19
$\log_{10} A^+$ [MPa$^{-n}s^{-1}$]	-6.48	-4.86
F [N]	-10.0	0

Considering the results obtained using a traditional subset-based DIC technique presented in Section IV.1.2, only samples 1, 3, 5 and 6 where used in the identifications, since the remaining

ones were considered experimental outliers. As explained in details in Section IV.1.1, all samples were tested under the same conditions of temperature and stress, therefore the same identification protocol can be applied for all of them.

The numerical model used to simulate the Brazilian tests is the same as described in step 2 of the proposed I-DIC algorithm (Chapter III.3.5.1), i.e., it considers the entire sample due to the previously observed non-symmetry of the load application.

For each experiment used to perform the I-DIC identification, 11 images were selected. The first image was taken after 1000 s the beginning of the test, and the last image at 7000 s. The remaining images were taken at equally spaced times every 600 s. The reason not to use images from earlier than 1000 s is to avoid calculations when the displacements are still too low, possibly in the range of the noise-floor error.

Section IV.1.3.1 describes the optimization algorithm proposed for the inverse identifications, which is based in traditional genetic algorithms but seeks for a more efficient use of the numerical simulations used during the identification loop, given their high computational and time cost.

IV.1.3.1 A modified genetic algorithm for the identification of material properties

Chapter I.3.3.2 described conventional genetic algorithms, that have the advantage to work with a population and to be probabilistic, therefore decreasing the chance to find local minima. The main disadvantage of these methods is the high number of required function evaluations (in the current case, numerical simulations) when compared to gradient-based algorithms.

In case a traditional genetic algorithm is used for the identification of the material properties, the subsequent steps need to be followed for each experimental set of images:

1. Generate initial population using a sampling method (for example, Latin Hypercube).
2. Run the simulations for each member of the population, using the suitable creep model.
3. Calculate the I-DIC error associated with each member of the population.
4. Based on the predefined elitism, mutation and crossover parameters, defined the members of the next generation.
5. Run steps 2 to 4 until the predefined number of generations is achieved.

To partially overcome the disadvantage of having to make a high number of function evaluations, a modified version of the traditional genetic algorithm is proposed. The steps to perform the calculations are:

1. Generate a common initial population of size N for all experimental cases.

2. Run the simulations for each member of the population, using the suitable creep model.

3. Calculate the I-DIC error associated with each member of the population, for each M experimental set of images.

4. Based on the results obtained in step 3 and on the elitism, mutation and crossover parameters, calculate the next generation of N individuals for each M experimental case.

5. Repeat step 2, i.e., run all $N \times M$ simulations.

6. Repeat step 3, but now the error associated with the experiments is going to be calculated for all $N \times M$ simulations already run, independently of which experimental set of images generated that point in the function evaluation space.

7. Repeat step 4, but the elitism operator will select the E best individuals among all error calculations obtained in step 6.

8. For the following G generations, repeat steps 4 to 6.

Figure IV.14 shows an graphic representation of the algorithm applied to the Brazilian tests used in this work, where the initial population size is $N = 15$, the number of experimental cases is $M = 4$ (the samples considered for the identification) and the number of elite individuals is $E = 2$.

This algorithm is based on the fact that, for the inverse identification protocol, several experiments are performed under the same conditions of temperature and force. Therefore, function evaluations that were randomly made as a result of the application of the genetic operators of all experimental sets of images can be used to potentially find the best fit. This algorithm does not necessarily reduce the total number of simulations to be run, but it results in a better utilization of the simulations.

Another practical advantage of using genetic algorithms for the identification of material parameters is that, as a new experimental set of images are generated, the error associated with it can be easily and quickly calculated using all simulations previously ran, for all $N + N \times M \times G$, which serves as an initial exploration of the variables domain and can result in a better initial population.

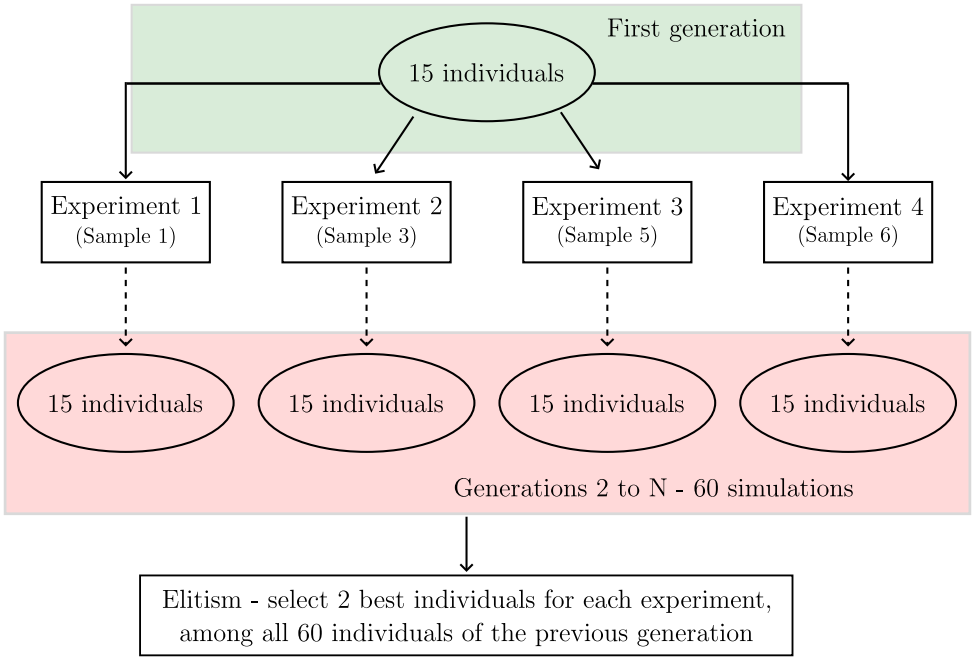

Figure IV.14: Proposed modified genetic algorithm.

IV.1.3.2 Identification results

Calculation of the noise floor As explained in Section III.4.1, one important part of the identification procedure is the calculation of the noise floor, i.e., the minimum value of noise which is obtained due to intrinsic factors, such as the errors associated with the hardware.

To estimate the noise floor associated with the images using during the identification, 10 pictures where taken prior to each experiment, at the temperature of the test, without any load application. The ZNSSD error between them (Chapter III.3.5.2) was then calculated. Under ideal conditions, this error would be zero, considering that all pictures would be exactly the same if no load was applied, but, as previously mentioned, there are intrinsic errors associated with the experimental setup.

The noise floor calculated for samples 1, 3, 5 and 6 are, respectively, 1.8176×10^{-10}, 1.7508×10^{-10}, 2.3233×10^{-10} and 2.37×10^{-10}.

First generation The first generation used in the proposed genetic algorithm was obtained using a Latin hypercube procedure, respecting the bounds described in Table IV.3. This generation had 15 individuals, to which, after running the simulation results, the I-DIC algorithm described in Chapter III.3.5.1 was applied.

Figure IV.15 shows the individuals of the population, along with the error values associated with them, for sample 1. The error was scaled between zero and one, to facilitate the visualization.

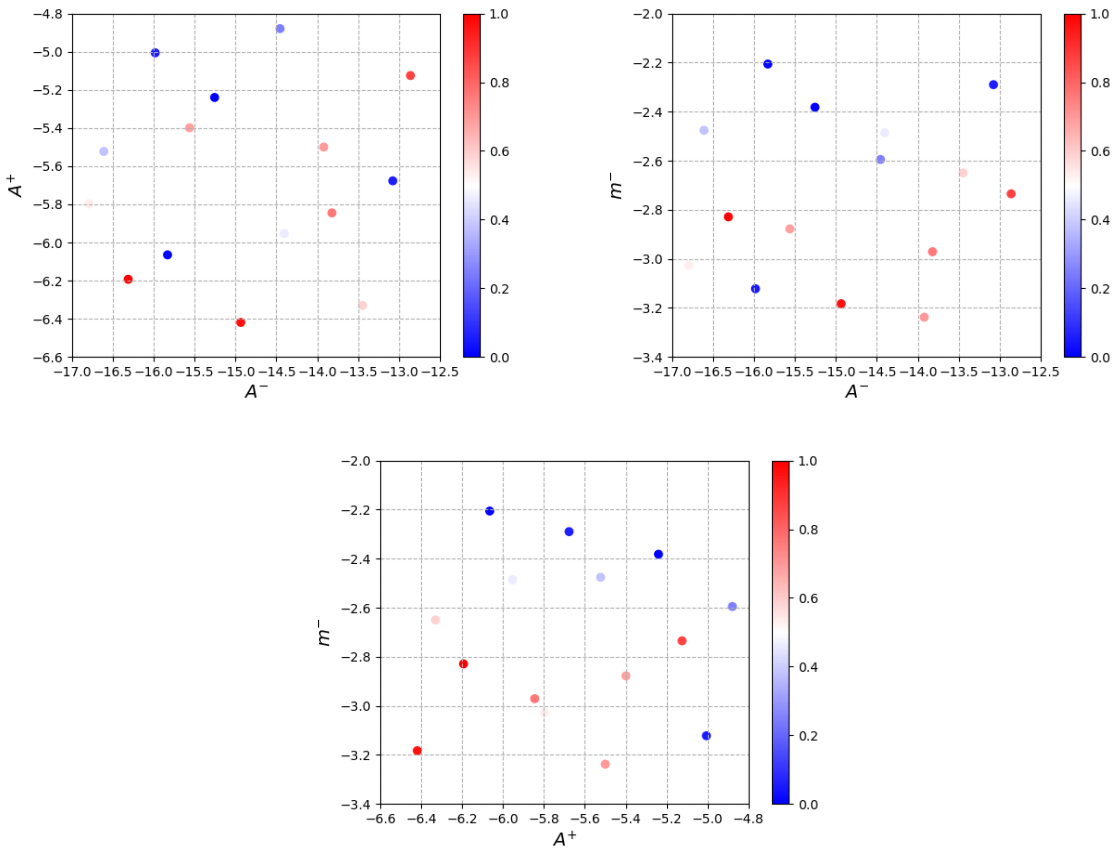

Figure IV.15: First generation of the I-DIC identification

For sample 1, the best individual had an error of 8.3048×10^{-8}, and the worst individual had an error of 8.4200×10^{-8}, which results in a error range of 1.1528×10^{-9}. This value is one order of magnitude below the noise floor error, which can be considered the acceptable limit. The same situation can be observed for sample 2, that has an error range of 1.0428×10^{-9}.

For both samples, the same set of material parameters produced the best result. These values are shown in Table IV.4 and compared to the parameters obtained in Section IV.1.2. It can be seen that the maximum difference between the two methods was 13.1%, for the value of m^-, which is in an acceptable range. The value of the horizontal force showed a relatively large deviation between the two methods, with a difference of 43%.

For samples 5 and 6, the error range provided by the I-DIC method is of 4.9629×10^{-10} and 2.4340×10^{-10}, respectively. These values are in the same order of magnitude than the noise floor error, and consequently the results of the identification would be heavily influenced by the noise. Therefore, these samples will not be considered in the further calculations.

Table IV.4: Parameters identified using the I-DIC method – first generation

Parameter	**I-DIC**	**DIC (Section IV.1.2)**	**Difference**
$\log_{10} A^{-}[\mathrm{MPa}^{-n}s^{-1}]$	-15.25	-14.86	2.7%
m [−]	-2.38	-2.74	13.1%
$\log_{10} A^{+}[\mathrm{MPa}^{-n}s^{-1}]$	-5.24	-5.55	5.58%
F [N]	-4.0	-7.0	43.0%

Further generations Following the methodology proposed in Section IV.1.3.1, three other generations were calculated, taking into account samples 1 and 2. For the given application, no further decrease of the error value could be obtained, mainly because the first generation already presented a calculation point close to the optimal solution, when compared to the identification methodology presented in Section IV.1.2.

For the sake of comparing the two identification methodologies, the material parameters obtained using the DIC technique were used to calculate the I-DIC error associated with sample 1 (Table IV.4). The resulting error was only slightly higher than the one obtained with the I-DIC identification (8.33×10^{-8}), which leads to the conclusion that the I-DIC technique is at the limit of its accuracy.

Considering the intrinsic characteristics of genetic algorithms, which do not have a clear convergence criteria, increasing the number of generations could potentially lead to the identification of a better individual. Nevertheless, this process is time consuming, since the creep simulations can take a significant time to complete.

IV.2 Validation of the results using four-point bending tests at 1300 °C

In this chapter, four-point bending tests are used to validate the results obtained with the Brazilian tests in Chapter IV.1. The four-points bending tests were done at the *Saint-Gobain Research Provence* research center, at Cavaillon, France.

IV.2.1 Experimental methodology

IV.2.1.1 Experimental setup

Figure IV.16 shows the experimental setup used to perform the four-point bending tests and to take the pictures at high temperatures. This setup was previously used by Leplay et al. (2015), and is composed of:

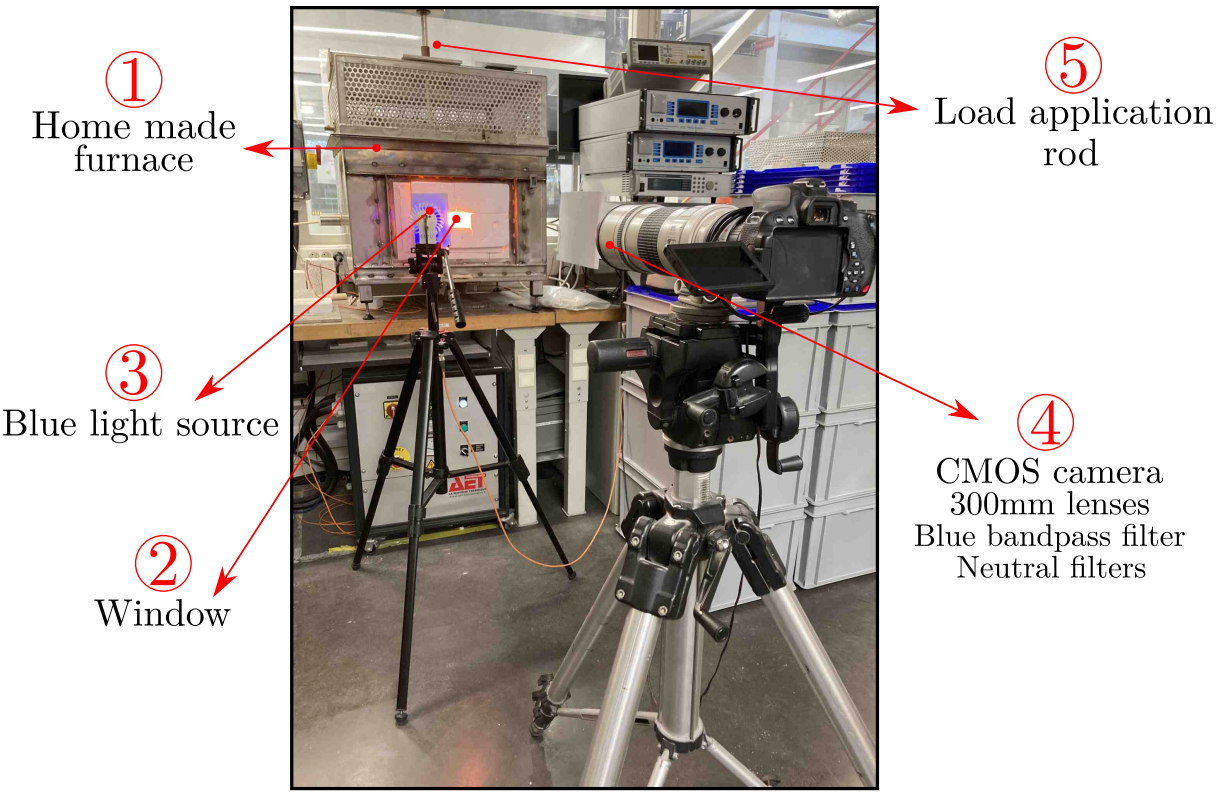

Figure IV.16: Experimental setup for four-point bending tests at high temperature.

1. A home made furnace designed at Saint-Gobain Research Provence. This furnace has the capacity to heat up to 1600 °C. It has six heating elements, positioned at the sides of the internal chamber. The temperature in the furnace is controlled using a single PID

controller. Figure IV.17 shows an internal view of the furnace, with a four-point bending sample already positioned.

In Figure IV.17 it is possible to see a small rectangular refractory positioned below the main sample. This rectangle is not loaded, and remains still during the entire test. Later, it is used as a reference to remove possible spurious movements calculated by the DIC algorithm, due to changes in the position of the camera and/or the furnace.

2. The furnace's door is made of a light-weight insulating refractory, and is equipped with a sapphire window. If necessary, a double window can be used, to better insulate the furnace.

3. One blue light source is used to enlighten the sample and increase the contrast.

4. The pictures are taken using a RGB CMOS camera and 300 mm macro telephoto lens with a 2x focal extension.

   The interior of this furnace is subjected to considerable heat hazes, what generates noise in the images. To average the effect of the noise, the pictures are taken using large exposure times (for example, 20 s). To limit the amount of light arriving at the camera's sensor, neutral density filters are used (Leplay et al., 2015). Blue band pass filters are also used, to remove UV and IR radiations.

5. The load is applied using static weights deposited under a metallic rod, which transfers the load to an alumina rod that has one end placed inside the furnace.

For these tests, no ventilator was needed, since the camera is positioned approximately 1.5 m away from the furnace, and therefore doesn't present excessive heat.

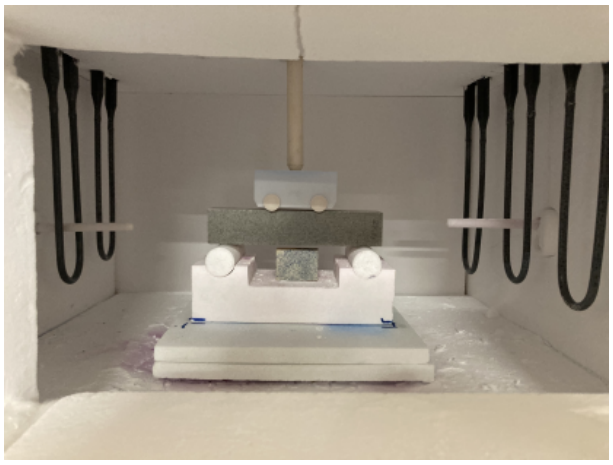

Figure IV.17: Four-point bending: Internal view of the furnace.

IV.2.1.2 Samples preparation and speckle pattern

The samples used in the four-point bending tests were cut from parallel refractory bricks, using a semi-automatic cutting machine. The cross-section of the sample had 30 mm × 30 mm, and the length was 150 mm. The lower support spam was 120 mm, and the upper spam was 40 mm. The geometries of the samples and of the testing setup are shown in Figure IV.18.

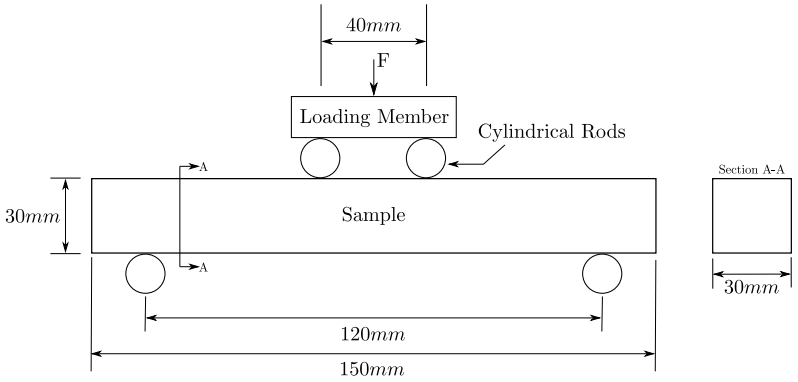

Figure IV.18: Four-point bending: Sample and testing setup geometries.

To coat the samples surfaces with the speckle pattern, the *SiC* powder was mixed with a bonding agent and applied using an airbrush. This process allows a finer control over the speckle distribution when compared to the sieving method described in Section I.2.2. Like in the case of the Brazilian test, the powder does not get strongly attached to the sample, and direct contact with it should be avoided.

Contrary to the Brazilian tests, the four-point bending tests ran until the sample's failure, causing them to take from a few hours to several days, depending on the loading conditions. For this reason, at the end of the test the speckle pattern had almost completely oxidized, as can be seen in Figure IV.19

Figure IV.19: Four-point bending: Sample before (below) and after (above) a test that took three days.

IV.2.1.3 Tests description

The four-point bending tests follow a similar procedure than the Brazilian tests, as described bellow:

1. The sample and the jaws were positioned at the testing machine at room temperature. The pre-load was applied using the weight of the metallic and alumina rods.
2. The camera was positioned at the point it would be at the moment of the test. Since the furnace can be opened without moving the camera, this position didn't change for all tests, except for fine adjustments.
3. The furnace was closed, and the heating of the sample started.
4. After the temperature homogenization time was passed, the blue lights were positioned to generate the maximum illumination of the sample as possible, avoiding glare, and the focus was manually adjusted in order to increase the sharpness. The exposure time was set to the desired value depending on the test, to average the images as described in Section IV.2.1.1, and the field of view was adjusted according to the lightning conditions to avoid too bright or too dark images.
5. Before the loading started, a reference pictures were taken.

Figure IV.20 shows an example of pictures taken at 1300 °C using the experimental setup described in this section.

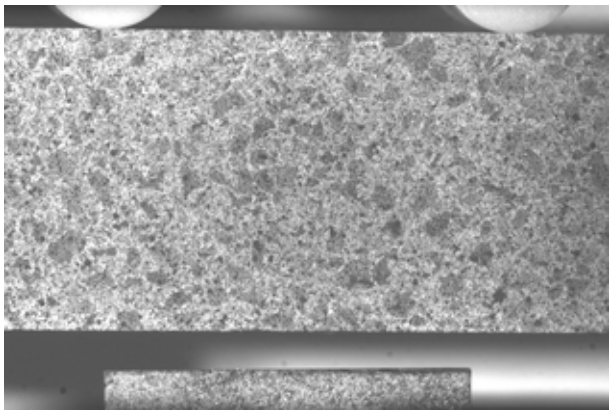

Figure IV.20: Four-point bending: Example of speckle pattern at 1300 °C.

Contrary to the Brazilian test, only the central zone of the sample was observed, due to the existence of an area where the bending is homogeneous, as described in Chapter I.2.3.

IV.2.1.4 Selection of the temperatures and loads

The four-point bending tests have the specific goal to validate the inverse identifications performed using the Brazilian tests. Therefore, the same temperatures of 1200 C and 1300 °C were used. Due to the restricted number of tests that could be made, the validation was more concentrated on the parameters obtained at 1300 °C.

For the selection of the loads, the tensile creep test results presented in Chapter II and Equation I.4, that provides the stresses in a four-point bending test considering linear elastic material properties, were used as a reference. Three values of loads were used on the tests at 1300 °C, namely, 40.2 N, 59.3 N and 85.3 N. At 1200 °C, one test using 59.3 N was made.

IV.2.2 Validation results

To validate the results obtained in Sections IV.1.2 and IV.1.3, it is important to verify if calculations using the identified parameters match the results of other experimental procedures, that have different loading conditions.

In this work, four-point bending tests were chosen to be the validation experiment due to their relative simplicity, and for the considerable amount of documentation related to them available in the literature. Nevertheless, as explained in Section IV.2.1, this test presents the inconvenient to restrict the range of stresses resisted by the sample to narrow values, since the tensile stresses generated at the lower portion of the sample can lead to the initiation and propagation of cracks.

To validate the results, time vs displacement curves of the experiments were obtained using the DIC software Ncorr (Blaber et al., 2015) and compared with simulated results using the identified material parameters. The simulation model used for the calculations was explained in Section III.2.1.3, and the experiments were done according to what was exposed in Section IV.2.1.

As explained in Section IV.2.1, the four-point bending tests used to validate the model were conducted at four different loading conditions, to verify the effect of the stress range on the model response.

Figure IV.21 shows the experimental results using a load of 59.3 N, and the corresponding simulation result. As it can be observed, both experiments presented problems at the beginning.

For sample 1, the beginning of the test presented a large rigid body movement into y direction, probably due to the manual application of the dead load, that is not always smooth. This lead to an instantaneous displacement of -0.2 mm of the experimental setup.

For sample 2, in order to try to limit the effect of speckle oxidation on the identification results, the test was initiated as soon as the furnace thermocouples indicated the test temperature was

achieved, i.e., no homogenization time was applied. For this reason, the DIC calculations indicate an upwards movement at the first 2 hours of test, there happened because the experimental setup was not in thermal equilibrium at the beginning of the test, and therefore expanded after it has already started. This effect can be better visualized in Figure IV.22.

Figure IV.22 also supports the hypothesis of rigid body movement at the beginning of test 1, since it shows a displacement of approximately 0.2 mm at the first data point, there is one order of magnitude lower than that of sample 1 and is consistent with the numerical simulations.

Due to these experimental problems, the validation of the identification results was made using the data obtained after four hours of testing. At this moment, the experimental curve is stable for both tests, and the considered validation variable was the slope of the curves.

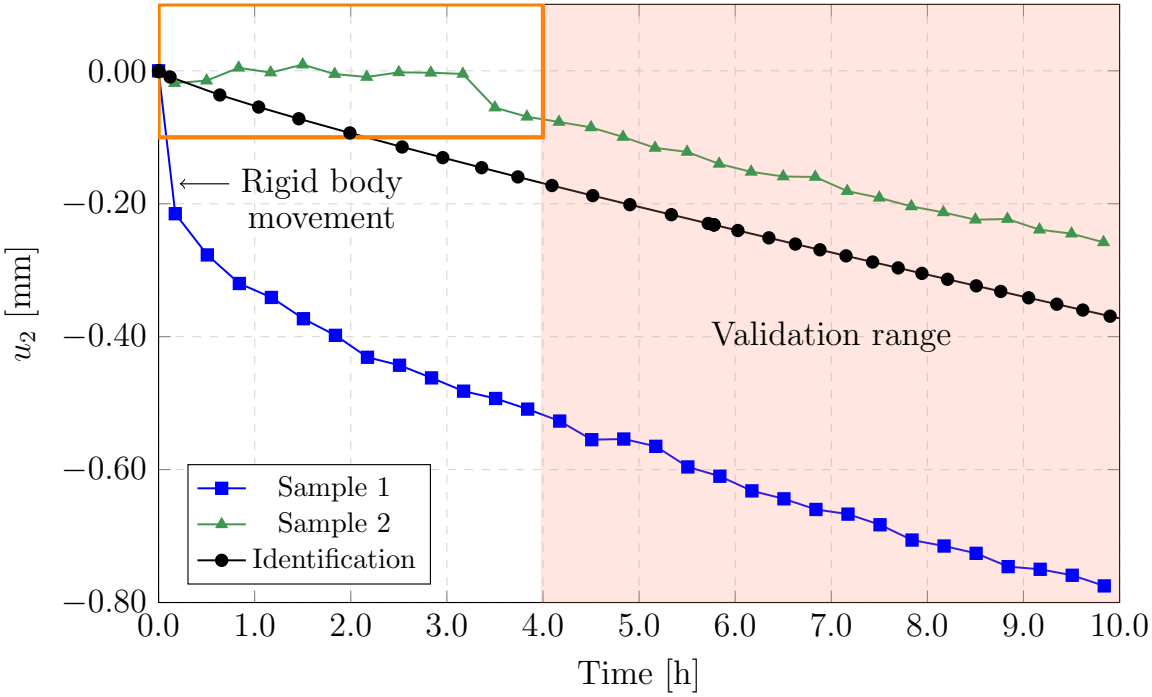

Figure IV.21: Bending tests: Vertical displacements at 1300 °C and 59.3 N.

As in the case of the Brazilian tests, the four-point bending test are not perfectly symmetric, and the boundary conditions applied on the simulations are approximated. Figure IV.23 shows the displacements of the samples as a function of the x coordinate at their vertical center line, as well as displacement fields obtained by DIC at time t =10 h. It can be seen that the maximum displacement, although close to the center of the calculated area, is not exactly at it.

Figure IV.24 shows the vertical displacements for the bending test for q load of 59.3 N, in the validation range. It is possible to verify that the slope of the simulated curve and that of sample 2 are almost identical, and differs from that of sample 1 by 20%. Considering the high

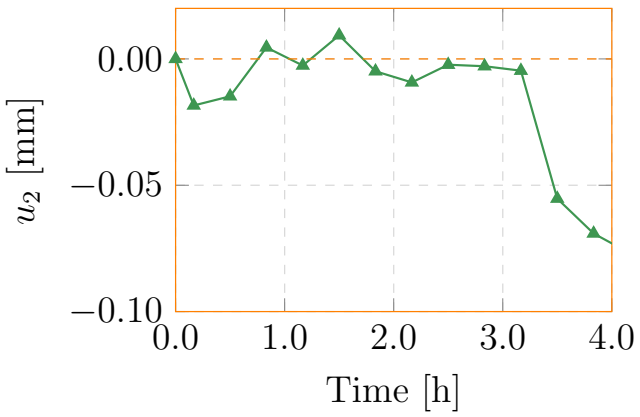

Figure IV.22: Bending tests: Vertical displacements at 1300 °C and 59.3 N – Detail of the first 4 hours.

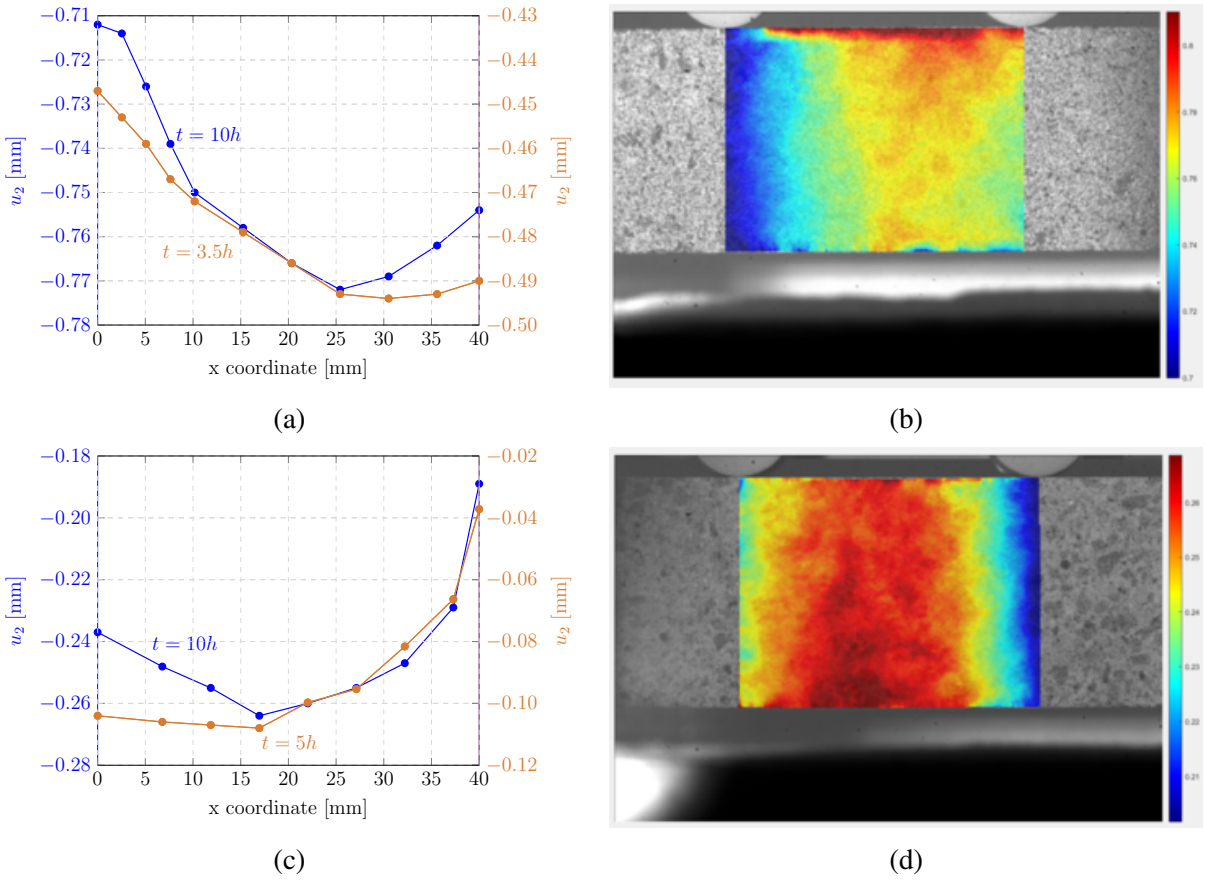

Figure IV.23: Bending tests: Vertical displacements of the samples at 1300 °C. (a) Displacements at the vertical center line of sample 1, (b) DIC results for sample 1 at t =10 h. (c) Displacements at the vertical center line of sample 2, (b) DIC results for sample 2 at t =10 h.

heterogeneity of refractory materials, explained in Chapter I, this is a result in favor of the validation of the model.

To verify that the model also works under different stress ranges, one test at 1300 °C and 40.2 N was also performed. As can be seen from Figure IV.25, the results of the experiment and of the simulation are in good agreement, despite no being exactly matching. From these results, it can be concluded that the model is able to predict the behavior of a refractory structure under complex loads, apart from the tests used to make the identifications.

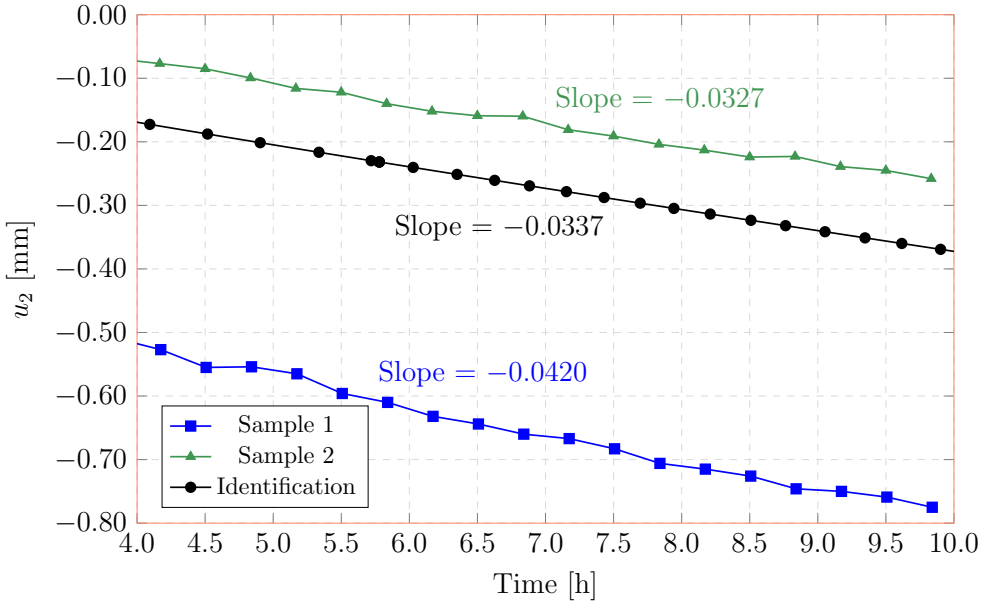

Figure IV.24: Bending tests: Vertical displacements at 1300 °C and 59.3 N – Validation range.

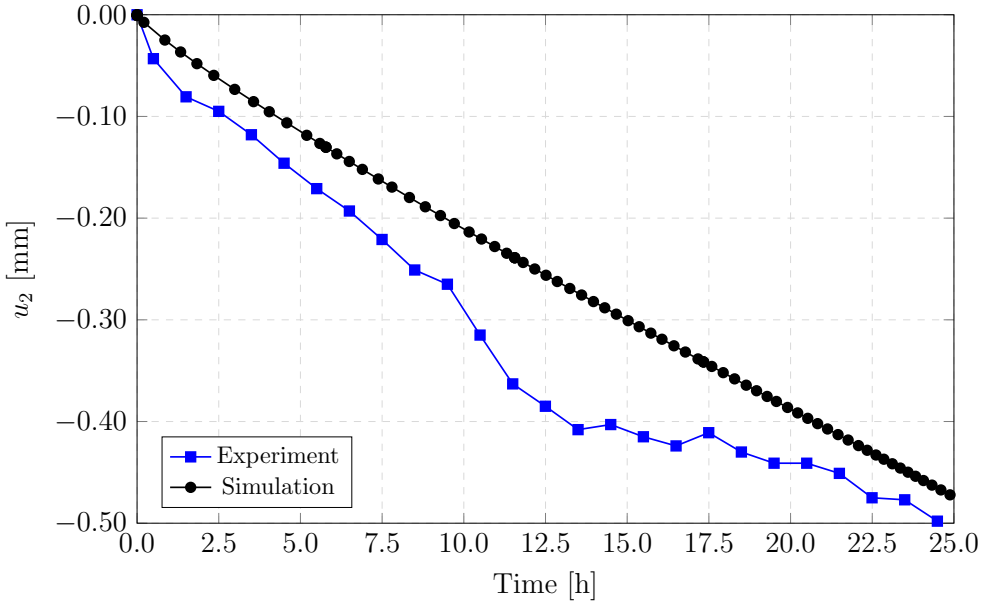

Figure IV.25: Bending tests: Vertical displacements at 1300 °C and 40.2 N.

IV.3 Comparison between the proposed and traditional identification approaches

In terms of thermo-mechanical characterization of complex material, such as refractories, it should be stated that one should conduct as many tests as possible, considering time and budget limitations, to study the material behavior under various loading conditions and to identify the optimal set of material parameters for a specific model, and even if the model is adequate for a given application. In this sense, the traditional characterization techniques presented in Chapter II and the ones proposed in this chapter are rather complimentary, instead of mutually exclusive.

In the next sections, both techniques are compared, taking into account several aspects of the characterization procedure.

IV.3.1 Test design

To successfully characterize a material, it is necessary to design the thermo-mechanical tests to cover the range of stresses and strains expected during operation, since the space of the possible parameters values can be highly non-linear (as demonstrated in Chapter III.1). Therefore, it is desired that the experimental protocol has enough flexibility to accommodate all the necessary loading conditions.

The traditional experimental techniques, i.e., one-dimensional tensile and compressive creep tests, are extremely flexible, in the sense that one is completely independent of the other. Therefore, if the material has a large asymmetry (for example, ten of fifteen times larger creep strain rate under tension than under compression), it is relatively easy to characterize it under all the desired loads.

On the contrary, the Brazilian test has a limitation imposed by the tensile strength of the material. As described in Chapter I.2.2, as the applied load increases in the Brazilian test, both the tensile and compressive stresses increase proportionally, and at a given load level the sample starts to crack in tension. Especially when the target is to perform creep tests, and not fracture tests, this load value can be rather low, depending on the material to be studied. At the load value where the sample achieves its maximum load carrying capacity in tension, it can be the case that the compression load still did not arrive at the desired value for the characterization.

This limitation described for the Brazilian test is even more accentuated for the four-point bending test, for which the maximum compression stress is equal to the maximum tensile stress in the case of a linear elastic material, and only slightly higher under creep conditions.

To overcome this difficulty, it is possible to change the geometrical design of the sample in order to obtain a stress distribution which is more compatible with the desired stress range, which in turn makes the interpretation of the results more challenging. Nevertheless, it is considerably difficult to produce refractory samples with complex shapes, due to problems associated with machining.

IV.3.2 Sample preparation

In terms of sample preparation, both methodologies have similar requirements, with the tensile creep test having the slight disadvantage of requiring a fairly long sample, as described in Chapter II.1.2.

Nevertheless, the DIC assisted measurements have the additional requirement of the preparation of the speckle pattern, that can become non-trivial at high temperatures. At such conditions, the possibility of occurring a chemical reaction between the sample and the speckle is higher than at room temperature; besides, the speckle can oxidate enough to impose a serious violation of the conservation of the optical flow (Chapter III.3), changing color during the test and producing artifacts in the measurements.

Another requirement for the speckle pattern is the color compatibility with the sample. For example, the alumina-spinel material studied in this thesis is white, and the SiC speckle pattern is black, resulting in a satisfactory contrast at the sample's surface. For materials of a color darker than white, it might be necessary to use other speckles, that should meet all the requirements previously described, which can be a topic of research on its own.

IV.3.3 Experimental data post-processing and amount of retrieved information

Since the sample in the traditional experimental methodology is subjected to a single stress value, the inverse identification of the material properties can be easily done through the optimization of a single equation, which is a considerable advantage. The DIC assisted methodology, on the contrary, requires a heavy post processing step, with sophisticated algorithms designed specifically for this end, which can take a considerable amount of time to converge.

The advantage of the DIC methodology comes from the fact that it is a full field measurement, i.e., instead of tracking only one point subjected to a single stress value, like in the case of extensometers, it maps the entire surface of the sample, providing a considerably larger amount of information about what is happening with the sample at each time step.

IV.3.4 Availability of testing equipment and test's robustness

As shown in Chapter II.1, although the compressive creep test can be made using a standard universal testing machine, with the inclusion of the high temperature extensometers, the tensile creep test requires a special setup, mainly related to the preparation of the sample and to its fixation in the testing machine using specially designed grips (gluing the sample into the metal parts), to avoid stress concentrations and premature failure. It also requires a shorter furnace than what is traditionally seen in industrial applications, otherwise the sample length would have to be further increased, to guarantee that the grips lay outside the furnace and the glue does not burn during the test.

Furthermore, it is not uncommon that, during the tensile creep test, a slight misalignment of the sample or a failure of the glue results in the lost of the experiment, requiring additional tests to be made.

The Brazilian test, however, especially when assisted by DIC measurements, can be performed using standard testing machines, as is the case for four-point bending tests and other tests that could potentially be used to characterize the asymmetric behavior of refractories. Naturally, it is still necessary to equip the furnace with a window, in order to be able to photograph the sample, but this adaptation can be made at a low cost, by using an effective insulation system and a low-cost glass.

Another aspect in favor of the Brazilian tests is its tolerance to load's misalignment. As it was demonstrated in Chapter IV.1.2, even if the load application is not perfectly vertical, which is virtually impossible to obtain, the sample accommodates in the jaws, and no premature failure is generally observed. To compensate this effect, the proposed identification protocol included this error source among the problem's unknowns, mitigating potential identification errors.

IV.3.5 Time and budget constraints

One of the main advantages of the proposed experimental procedure when compared to the traditional tensile and compressive creep tests is the number of tests required to identify the parameters of an asymmetric creep law.

Considering a creep law with six independent material parameters, three to describe the compressive behavior and three to describe the tensile behavior, it is necessary to have at least six different stress values applied to the sample to make the identification. If each test is repeated three times, for statistical reason, a total of 18 tests should be performed, per temperature.

On the other hand, on the Brazilian test there is an infinite number of different stress values applied at the sample at the same time, ranging from the maximum compressive stress to the

maximum tensile stress. Considering a finite element representation of the test, the number of different stress values is equal to the number of integration points in the mesh. Provided that the Brazilian test is well adapted to the identification, as described in the previous sections, with only one test all the parameters can be identified, resulting in a total of three tests when the minimum statistical requirements are met.

When the time to obtain the results and the budget to perform the tests are limited, as it is usually the case for industrial applications, the proposed methodology clearly presents an important advantage, which is even more meaningful when several materials are to be tested at various temperatures.

IV.4 Conclusion

In this chapter, an experimental protocol based on the Brazilian test and the Digital Image Correlation technique was proposed. It was shown that, using the adequate combination of optical devices, it is possible to obtain high quality images at high temperatures (up to 1300°C, in the present work).

Two identification procedures were proposed. In the first one, a traditional subset-based DIC technique was used to measure the displacement at the top proportion of the sample, which was compared to the corresponding values obtained by finite element calculations using the asymmetric creep models proposed in Chapter III. Using this methodology, the horizontal force responsible for the rotation of the sample during the test and caused by misalignments in the testing machine was also measured.

The second identification procedure was based on the Integrated-DIC, which aims to use the full sample's displacement field in the error function for the identification. It was observed that, despite reasonable results could be observed, the influence of the noise in the calculations is still important, due to the low values of displacements. This fact is particularly important for the Brazilian test: while the top part of the sample has a relatively high displacement during creep, the bottom part presents lower values, because it is fixed at the tsting machine's plunger. Since the error function considers the displacements of all pixels, the low values contribute for the generation of noise, which has a negative influence in the overall procedure.

In general, it was shown that the proposed asymmetric creep models are adequate to simulate the creep behavior of the alumina-spinel brick, which was further confirmed using four-point bending tests as a validation procedure.

Conclusions and Perspectives

Summary and main contributions

The goal of this thesis was to study the primary and secondary asymmetric creep behavior of refractory materials in terms of numerical constitutive models and of experimental techniques used for characterization at high temperatures.

The literature review presented in Chapter I showed the need for the development of creep models that could efficiently take into account the largely different behavior of refractory under tension and compression loads, without requiring an excessive number of experiments for the material's characterization.

Considering the elevated costs of high temperature tests, as well as the time demand due to long heat-up and cool-down cycles for the mechanical tests, it was clear that an efficient characterization procedure that minimizes the amount of necessary tests was of great interest.

In this sense, the main contributions of this thesis were:

1. Development of two new asymmetric constitutive models for creep: based on the assumption of a split of the stress tensor into positive and negative parts, the consideration of the material asymmetry could be successfully done, as demonstrated with numerical simulations and validated with experimental data. Unlike previous works present in the literature, this thesis employed a weighting strategy for the contributions of the positive and negative stresses that does not result in a intrinsic orthotropy of the creep strain rate, i.e., the symmetric behavior is recovered whenever the same material parameters are used under tension and compression. In terms of simulation features, the main differences between the models developed in this work and the ones available in the literature are:

    - Isotropic creep model: the models present in the literature were only capable of simulating the secondary creep stage of refractories. Experimental data presented in Chapter II have shown that the primary creep stage is of utmost importance

when compressive creep is to be imposed over refractory material, which is the case for most of the refractory linings under operational conditions. The isotropic creep model proposed in Chapter III.1.1 is able to consider primary or secondary creep behavior of materials under tension and compression. For the alumina-spinel material studied in this work, primary creep was assumed under compression, and secondary creep under tension, again supported by the experimental data gathered for traditional experimental techniques presented in Chapter II. Difficulties related to the integration of the creep equations were also discussed, and best practices to increase the success rate of the calculations were presented.

- Kinematic (transient) creep model: to study the life cycle of refractory linings considering all stages of its operation, including the heat-up and the inherent thermal cycles, it was clear that a model that could automatically consider the transition from primary to secondary creep stages, especially under compressive loads, was of high importance. In this work, a kinematic creep model, based on the notion of the back stress as an additional internal variable, was adapted to the use with the asymmetric creep assumption. In Chapter II.4.2, it was shown that the kinematic law allows for a good fit of the experimental curves for longer times, therefore keeping the accuracy of the calculations. In Chapter III.1.2, this law was adapted for three-dimensional loads, and the split of the stress tensor was included.

Depending on the envisaged application, one can chose which model to use. In cases where no transition from primary to secondary creep are expected, the isotropic model can be a better choice, since it has less material parameters, which can contribute for a easier identification procedure. Otherwise, the kinematic creep model presents a robust alternative.

2. Development of a characterization protocol based on the Digital Image Correlation technique and Brazilian tests: to overcome the elevated costs of high temperature characterization, this work proposed an experimental protocol that uses the Brazilian test as the main mechanical test. The main advantage of the Brazilian test is that the resulting displacements field is influenced by tension and compression loads at the same time, depending on the region of the sample. Therefore, the innovation of this work resides in the use of a single test for the characterization, instead of traditional tension and compression creep tests. The proposed experimental protocol results in a complex stress distribution on the sample and, therefore, requires more sophisticated techniques to analyse the results, for which two DIC based approaches were chosen and further developed. The first approach uses a traditional DIC technique, and takes the displacement of the contact point between

the sample and the jaws as the optimization target. The I-DIC algorithm aims to use the entire displacement field to minimize the error during the identification procedure. To simplify the I-DIC algorithm while still taking into account the intrinsic imperfections of the experimental procedure, the horizontal load that results into a rotation of the Brazilian test sample was included in the characterization, rendering the results more accurate and the experimental procedure more robust. This methodology has the additional advantage of exposing the constitutive model to bidimensional conditions directly during characterization, instead of identifying the material parameters under one-dimensional conditions and later verifying if the multidimensional hypothesis of the model are valid. Despite the advances obtained in this work, it is clear that the accuracy and the sensitivity of the I-DIC technique to noise still need to be improved.

Suggestions for future works

Despite the interesting results presented in this thesis in the fields of numerical simulations and experimental mechanics, the topic of refractories modeling and characterization is far from being completely mastered, given the complexity of the topic. Below are some suggestions for future research and engineering applications:

1. Include the third creep stage in the asymmetric models: to predict the lifetime of refractories until failure, it is important to consider the damage effects that take part after the second creep stage is over, resulting in a rapid increase of the creep strain rate. From an engineering point of view, it might be enough only to determine when the third creep stage start when the material is subjected to complex loading conditions, since any further operation after this point can be unstable. To do so, one possibility is to include a damage variable on the equations of the proposed models, be it scalar or tensorial, and to investigate what is the evolution law for this new internal variable.

2. New strategies for the integration of the creep equations: materials like refractories tend to have a considerably have creep strain rate under high temperature, as it was demonstrated in this thesis. As such, the integration of the constitutive models can require a considerable amount of time, especially when the temperature is changing fast, as in the case of thermal shocks. New integration algorithms that could use larger time steps while maintaining the stability of the solution would be important to reduce the calculation times and to allow for more calculations within a given time, making the optimization of refractory linings more feasible.

3. Optimization of the speckle pattern for high temperatures: DIC based identification procedures are highly dependent on the contrast between the sample surface and the speckle pattern. It is particularly challenging to produce a high quality speckle at high temperatures, considering the variety of refractory types available in the market, with various colors and chemical compositions. It is of great practical importance to develop better patterning techniques and materials, to increase the accuracy of the identifications.

4. Further exploration of the behavior of refractories after creep: although having an important influence on the thermo-mechanical behavior of refractories, as demonstrated throughout this thesis, creep is not the only factor when the design of refractory linings needs to be addressed. An interesting topic of research is the determination of how other types of high temperature behavior (for example, thermal shock) are influenced by previously imposed creep strains. DIC techniques, such as the ones presented in this work, can be of great use when designing experiments with non-standard loading conditions.

5. Design better tests to validate the models: although the four-point bending tests could give an indication about the validity of the models and of the identified parameters, it has the limitation of a low compressive load prior the total failure, which limits to observation of the asymmetric phenomena and focuses more on the tensile behavior. With the possibilities offered by the DIC method, it can be interesting to design more complex tests, that would provide more information as to which the models are adequate or not. Seemingly, all the limitations related to the production process of refractories and the further production of samples need to be considered, which renders this task somewhat difficult.

6. Decrease the number of tests required to characterize the material using the traditional experimental methods: currently, each creep test takes only one stress value during the entire duration of the experiment, which leads to a straightforward inverse identification. Nevertheless, this makes the characterization time consuming and more expensive. To overcome this fact, a procedure where the load is progressively increased during the test could be developed, together with a slightly more complex inverse identification algorithm, possibly supported by finite element calculations.

Bibliography

Abaqus. (2018). *Abaqus 2018 Documentation*. Providence, RI, USA, Dassault Systèmes Simulia Corp.

Abbé, F., Carin, R., & Chermant, J.-L. (1989). Tensile and compressive creep characteristics from bending tests: Application to SiC-SiC composites. *Journal of the European Ceramic Society*, *5*(3), 201–205. https://doi.org/10.1016/0955-2219(89)90036-8

Altenbach, H. (1999). Classical and Non-Classical Creep Models. In H. Altenbach & J. J. Skrzypek (Eds.), *Creep and Damage in Materials and Structures* (pp. 45–95). Vienna, Springer.

Altenbach, H. (2001). Consideration of Stress State Influences in the Material Modelling of Creep and Damage (S. Murakami & N. Ohno, Eds.). In S. Murakami & N. Ohno (Eds.), *IUTAM Symposium on Creep in Structures*, Dordrecht, Springer Netherlands. https://doi.org/10.1007/978-94-015-9628-2_15

Anderssen, R. S. (1999). The pragmatics of solving industrial (real-world) inverse problems with exemplification based on the molecular weight distribution problem. *Inverse Problems*, *15*(2), R1–R40. https://doi.org/10.1088/0266-5611/15/2/001

Archer, T., Beauchêne, P., Huchette, C., & Hild, F. (2020). Global digital image correlation up to very high temperatures with grey level corrections. *Measurement Science and Technology*, *31*(2), 024003. https://doi.org/10.1088/1361-6501/ab461e

ASTM-C1161. (2013). Standard Test Method for Flexural Strength of Advanced Ceramics at Ambient Temperature. American Society for Testing and Materials.

Balcaen, R., Wittevrongel, L., Reu, P. L., Lava, P., & Debruyne, D. (2017). Stereo-DIC Calibration and Speckle Image Generator Based on FE Formulations. *Experimental Mechanics*, *57*(5), 703–718. https://doi.org/10.1007/s11340-017-0259-1

Banerjee, S. (2004). Properties of Refractories. In *Refractories Handbook* (First, pp. 1–10). New York, NY, Marcel Dekker, Inc.

Bard, Y. (1970). Comparison of Gradient Methods for the Solution of Nonlinear Parameter Estimation Problems. *SIAM Journal on Numerical Analysis*, *7*(1), 157–186.

Baxendale, S. (2004). Testing of Refractory Materials. In *Refractories Handbook* (pp. 435–474).

Belrhiti, Y., Dupre, J., Pop, O., Germaneau, A., Doumalin, P., Huger, M., & Chotard, T. (2017). Combination of Brazilian test and digital image correlation for mechanical characterization of refractory materials. *Journal of the European Ceramic Society*, *37*(5), 2285–2293. https://doi.org/10.1016/j.jeurceramsoc.2016.12.032

Belrhiti, Y., Gallet-Doncieux, A., Germaneau, A., Doumalin, P., Dupre, J. C., Alzina, A., Michaud, P., Pop, I. O., Huger, M., & Chotard, T. (2012). Application of optical methods to investigate the non-linear asymmetric behavior of ceramics exhibiting large strain to rupture by four-points bending test. *Journal of the European Ceramic Society*, *32*(16), 4073–4081. https://doi.org/10.1016/j.jeurceramsoc.2012.06.016

Benallal, A., Billardon, R., & Doghri, I. (1988). An integration algorithm and the corresponding consistent tangent operator for fully coupled elastoplastic and damage equations. *Communications in Applied Numerical Methods*, *4*(6), 731–740. https://doi.org/10.1002/cnm.1630040606

Berny, M., Archer, T., Mavel, A., Beauchêne, P., Roux, S., & Hild, F. (2018). On the analysis of heat haze effects with spacetime DIC. *Optics and Lasers in Engineering*, *111*, 135–153. https://doi.org/10.1016/j.optlaseng.2018.06.004

Bertin, M., Hild, F., & Roux, S. (2016). Optimization of a Cruciform Specimen Geometry for the Identification of Constitutive Parameters Based Upon Full-Field Measurements. *Strain*, *52*, 307–323. https://doi.org/10.1111/str.12178

Bertin, M., Hild, F., Roux, S., Mathieu, F., Leclerc, H., & Aimedieu, P. (2016). Integrated digital image correlation applied to elastoplastic identification in a biaxial experiment. *The Journal of Strain Analysis for Engineering Design*, *51*(2), 118–131. https://doi.org/10.1177/0309324715614759

Besnard, G., Hild, F., & Roux, S. (2006). Finite-Element Displacement Fields Analysis from Digital Images: Application to Portevin–Le Châtelier Bands. *Experimental Mechanics*, *46*(6), 789–803. https://doi.org/10.1007/s11340-006-9824-8

Blaber, J., Adair, B., & Antoniou, A. (2015). Ncorr: Open-Source 2D Digital Image Correlation Matlab Software. *Experimental Mechanics*, *55*(6), 1105–1122. https://doi.org/10.1007/s11340-015-0009-1

Blond, E. (2017). Thermal, Chemical and Mechanical Couplings. In *Corrosion of Refractories: The Fundamentals* (First, pp. 337–408). Baden-Baden - Germany, Goller Verlag.

Blond, E., Schmitt, N., Hild, F., Blumenfeld, P., & Poirier, J. (2005). Modelling of high temperature asymmetric creep behavior of ceramics. *Journal of the European Ceramic Society*, *25*(11), 1819–1827. https://doi.org/10.1016/j.jeurceramsoc.2004.06.004

Boussuge, M. (2001). Some numerical approaches of creep, thermal shock, damage and delayed failure of ceramics and refractories. *Bulletin of Materials Science*, *24*(2), 97–100. https://doi.org/10.1007/BF02710082

Box, G., Hunter, J., & Hunter, W. (2005). *Statistics for Experimenters: Design, Innovation, and Discovery* (Second). Hoboken, NJ USA, Wiley.

Buljak, V. (2012). *Inverse Analyses with Model Reduction*. Berlin, Heidelberg, Springer Berlin Heidelberg. https://doi.org/10.1007/978-3-642-22703-5

Cannon, R., & Langdon, G. (1988). Creep of ceramics. *Journal of Materials Science*, *23*(1), 1–20. https://doi.org/10.1007/BF01174028

Cao, J., & Lin, J. (2008). A study on formulation of objective functions for determining material models. *International Journal of Mechanical Sciences*, *50*(2), 193–204. https://doi.org/10.1016/j.ijmecsci.2007.07.003

Chaboche, J. (2008). A review of some plasticity and viscoplasticity constitutive theories. *International Journal of Plasticity*, *24*(10), 1642–1693. https://doi.org/10.1016/j.ijplas.2008.03.009

Chaparro, B. M., Thuillier, S., Menezes, L. F., Manach, P. Y., & Fernandes, J. V. (2008). Material parameters identification: Gradient-based, genetic and hybrid optimization algorithms. *Computational Materials Science*, *44*(2), 339–346. https://doi.org/10.1016/j.commatsci.2008.03.028

Chen, R., Wang, Y., Peng, R., Jiang, S., & Hu and Ziheng Zhao, C. (2020). Identification of the Discrete Element Model Parameters forRock-Like Brittle Materials. *Computer Modeling in Engineering & Sciences*, *123*(2), 717–737. https://doi.org/10.32604/cmes.2020.07438

Coley, D. A. (1999). *An Introduction to Genetic Algorithms for Scientists and Engineers*. WORLD SCIENTIFIC. https://doi.org/10.1142/3904

Darvell, B. W. (1990). Uniaxial compression tests and the validity of indirect tensile strength. *Journal of Materials Science*, *25*(2), 757–780. https://doi.org/10.1007/BF03372161

de Melo, C. C., Furlan, M., Hild, F., Schmitt, N., & Canto, R. B. (2020). Uniaxial compression test on ceramic green compact with bending consideration using digital image correlation. *Powder Technology*, *376*, 136–148. https://doi.org/10.1016/j.powtec.2020.08.002

de Souza Neto, E. A., Peri, D., & Owen, D. R. J. (2008). *Computational Methods for Plasticity*. Chichester, UK, John Wiley & Sons, Ltd. https://doi.org/10.1002/9780470694626

Denys, K., Coppieters, S., Seefeldt, M., & Debruyne, D. (2016). Multi-DIC setup for the identification of a 3D anisotropic yield surface of thick high strength steel using a double perforated specimen. *Mechanics of Materials*, *100*, 96–108. https://doi.org/10.1016/j.mechmat.2016.06.011

Dong, Y., & Pan, B. (2017). A Review of Speckle Pattern Fabrication and Assessment for Digital Image Correlation. *Experimental Mechanics*, *57*(8), 1161–1181. https://doi.org/10.1007/s11340-017-0283-1

Dusserre, G., Nazaret, F., Robert, L., & Cutard, T. (2013). Applicability of image correlation techniques to characterise asymmetric refractory creep during bending tests. *Journal of*

the European Ceramic Society, *33*(2), 221–231. https://doi.org/10.1016/j.jeurceramsoc.2012.09.011

Dusserre, G., Valentin, O., Nazaret, F., & Cutard, T. (2016). Experimental and numerical investigation of the asymmetric primary creep of a fibre reinforced refractory concrete at 1200 °C. *Journal of the European Ceramic Society*, *36*(10), 2627–2639. https://doi.org/10.1016/j.jeurceramsoc.2016.03.007

Dutta, S. K., & Chokshi, Y. B. (2020). *Basic Concepts of Iron and Steel Making*. Singapore, Springer Singapore. https://doi.org/10.1007/978-981-15-2437-0

Esposito, L., & Bonora, N. (2011). A primary creep model for Class M materials. *Materials Science and Engineering: A*, *528*(16-17), 5496–5501. https://doi.org/10.1016/j.msea.2011.03.069

Fahad, M. K. (1996). Stresses and failure in the diametral compression test. *Journal of Materials Science*, *31*(14), 3723–3729. https://doi.org/10.1007/BF00352786

Fairhurst, C. (1964). On the validity of the 'Brazilian' test for brittle materials. *International Journal of Rock Mechanics and Mining Sciences & Geomechanics Abstracts*, *1*(4), 535–546. https://doi.org/10.1016/0148-9062(64)90060-9

Ferreira, M. D. C. (2010). Inverse analysis FOR two-dimensional structures using the boundary element method. *Advances in Engineering Software*, 12.

García, V. J., Márquez, C. O., Zúñiga-Suárez, A. R., Zuñiga-Torres, B. C., & Villalta-Granda, L. J. (2017). Brazilian Test of Concrete Specimens Subjected to Different Loading Geometries: Review and New Insights. *International Journal of Concrete Structures and Materials*, *11*(2), 343–363. https://doi.org/10.1007/s40069-017-0194-7

Gasser, A., Boisse, P., Dutheillet, Y., & Poirier, J. (2000). Experimental and numerical analyses of thermomechanical refractory lining behaviour. *Proceedings of the Institution of Mechanical Engineers, Part L: Journal of Materials Design and Applications*, *215*, 15.

Gazeau, C., Gillibert, J., Blond, E., Geffroy, P.-M., & Richet, N. (2015). Experimental set up for the mechanical characterization of plane ITM membrane at high temperature. *Journal of the European Ceramic Society*, *35*(14), 3853–3861. https://doi.org/10.1016/j.jeurceramsoc.2015.06.026

Grédiac, M., Hild, F., & Pineau, A. (Eds.). (2013). *Full-Field Measurements and Identification in Solid Mechanics: Grédiac/Full-Field Measurements and Identification in Solid Mechanics*. Hoboken, NJ USA, John Wiley & Sons, Inc. https://doi.org/10.1002/9781118578469

Groetsch, C. W. (1999). *Inverse Problems: Activities for Undergraduates*. Washington, DC, The Mathematical Association of America.

Gruber, D., Auer, T., Harmuth, H., & Rotsch, J. (2007). Finite Element Investigation of the Crack Formation in the Slag Line of a Teeming Ladle, In *Unified International Technical Conference on Refractories*, Dresden - Germany.

Gruber, D., & Harmuth, H. (2008). Durability of Brick Lined Steel Ladles from a Mechanical Point of View. *Steel Research International*, *79*(12), 913–917. https://doi.org/10.1002/srin.200806220

Gruber, D., & Harmuth, H. (2014). Thermomechanical Behavior of Steel Ladle Linings and the Influence of Insulations. *Steel Research International*, *85*(4), 512–518. https://doi.org/10.1002/srin.201300129

Guariso, G., & Sangiorgio, M. (2020). Improving the Performance of Multiobjective Genetic Algorithms: An Elitism-Based Approach. *Information*, *11*(12), 587. https://doi.org/10.3390/info11120587

Hamam, R., Hild, F., & Roux, S. (2007). Stress Intensity Factor Gauging by Digital Image Correlation: Application in Cyclic Fatigue. *Strain*, *43*(3), 181–192. https://doi.org/10.1111/j.1475-1305.2007.00345.x

Harbison-Walker. (2005). *Handbook of Refractory Practice*. Moon Township, PA, Harbison-Walker.

Harmuth, H., & Bradt, R. C. (2010). Investigation of Refractory Brittleness by Fracture Mechanical and Fractographic Methods. *Interceram Refractories*, 5.

Hein, J., & Kuna, M. (2012). Optimizing Thermal Shock Resistance of Layered Refractories. *Advanced Engineering Materials*, *14*(6), 408–415. https://doi.org/10.1002/adem.201100283

Hild, F., & Roux, S. (2006). Digital Image Correlation: From Displacement Measurement to Identification of Elastic Properties - a Review. *Strain*, *42*(2), 69–80. https://doi.org/10.1111/j.1475-1305.2006.00258.x

Hild, F., & Roux, S. (2012). Comparison of Local and Global Approaches to Digital Image Correlation. *Experimental Mechanics*, *52*(9), 1503–1519. https://doi.org/10.1007/s11340-012-9603-7

Hild, F., & Roux, S. (2013). On the Resolution of Local and Global DIC Approaches. In H. Jin, C. Sciammarella, C. Furlong, & S. Yoshida (Eds.), *Imaging Methods for Novel Materials and Challenging Applications, Volume 3* (pp. 221–225). New York, NY, Springer New York. https://doi.org/10.1007/978-1-4614-4235-6_31

Hild, F., Roux, S., Gras, R., Guerrero, N., Marante, M. E., & Flórez-López, J. (2009). Displacement measurement technique for beam kinematics. *Optics and Lasers in Engineering*, *47*(3-4), 495–503. https://doi.org/10.1016/j.optlaseng.2008.03.006

Hohage, T., Rapún, M.-L., & Sayas, F.-J. (2007). Detecting corrosion using thermal measurements. *Inverse Problems*, *23*(1), 53–72. https://doi.org/10.1088/0266-5611/23/1/003

Hynes, A., & Doremus, R. (2006). Theories of Creep in Ceramics: Critical Reviews in Solid State and Materials Sciences: Vol 21, No 2. *Critical Reviews in Solid State and Materials Sciences*, *21*(2), 129–187. https://doi.org/10.1080/10408439608241255

ISO-1893. (2007). Refractory products — Determination of refractoriness under load — Differential method with rising temperature. International Organization for Standardization.

ISO-3187. (1989). Refractory products — Determination of Creep in Compression. International Organization for Standardization.

Jin, S., Harmuth, H., & Gruber, D. (2014). Compressive creep testing of refractories at elevated loads - Device, material law and evaluation techniques. *Journal of the European Ceramic Society*, *34*(15), 4037–4042. https://doi.org/10.1016/j.jeurceramsoc.2014.05.034

Jin, S., Harmuth, H., Gruber, D., & Rössler, R. (2015). Influence Of Creep On The Thermomechanical Behavior Of a RH-Snorkel, In *Unified International Technical Conference on Refractories*, Vienna - Austria.

Jin, S., Harmuth, H., Gruber, D., Buhr, A., Sinnema, S., & Rebouillat, L. (2020). Thermomechanical modelling of a torpedo car by considering working lining spalling. *Ironmaking & Steelmaking*, *47*(2), 145–149. https://doi.org/10.1080/03019233.2018.1495797

Jin, S., Harmuth, H., Gruber, D., & Li, Y. (2011). Classification of Thermomechanical Impact Factors and Prediction Model for Ladle Preheating. *J Wuhan Univ Sci Technol*, *34*, 8.

Jones, E., Iadicola, M., Bigger, R., Blaysat, B., Boo, C., Grewer, M., Hu, J., Jones, A., Klein, M., Lava, P., Pankow, M., Raghavan, K., Reu, P., Schmidt, T., Siebert, T., Simonsen, M., Trim, A., Turner, D., Vieira, A., & Weikert, T. (2018). *A Good Practices Guide for Digital Image Correlation* (First, tech. rep.). International Digital Image Correlation Society. https://doi.org/10.32720/idics/gpg.ed1/print.format

Kirsch, A. (2011). *An Introduction to the Mathematical Theory of Inverse Problems* (Second). New York, Springer-Verlag. https://doi.org/10.1007/978-1-4419-8474-6

Lee, D.-J. (1996). Estimating tensile creep rate of ceramics from flexure data. *Journal of the European Ceramic Society*, *16*(12), 1377–1383. https://doi.org/10.1016/0955-2219(96)00060-X

Lemaître, J., & Chaboche, J. (1990). *Mechanics of solid materials*. Cambridge, Cambridge University Press.

Leplay, P. (2011). *Identification de comportements mécaniques et à rupture par corrélation d'images 2D et 3D: Application aux filtres à particules Diesel à base de titanate d'aluminium* (Doctoral dissertation). Université de Lyon. Lyon.

Leplay, P., Lafforgue, O., & Hild, F. (2015). Analysis of Asymmetrical Creep of a Ceramic at 1350°C by Digital Image Correlation. *Journal of the American Ceramic Society*, *98*(7), 2240–2247. https://doi.org/10.1111/jace.13601

Leplay, P., Réthoré, J., Meille, S., & Baietto, M.-C. (2010). Damage law identification of a quasi brittle ceramic from a bending test using Digital Image Correlation. *Journal of the European Ceramic Society*, *30*(13), 2715–2725. https://doi.org/10.1016/j.jeurceramsoc.2010.05.021

Leplay, P., Réthoré, J., Meille, S., & Baietto, M.-C. (2012). Identification of asymmetric constitutive laws at high temperature based on Digital Image Correlation. *Journal of the European Ceramic Society*, *32*(15), 3949–3958. https://doi.org/10.1016/j.jeurceramsoc.2012.03.024

Lim, H. J., Jung, J. W., Han, D. B., & Kim, K. T. (1997). A finite element model for asymmetric creep behavior of ceramics. *Materials Science and Engineering: A*, *224*(1), 125–130. https://doi.org/10.1016/S0921-5093(96)10557-8

Lin, H., Xiong, W., Xiong, Z., & Gong, F. (2015). Three-dimensional effects in a flattened Brazilian disk test. *International Journal of Rock Mechanics and Mining Sciences*, *74*, 10–14. https://doi.org/10.1016/j.ijrmms.2014.11.006

Lin, H., Xiong, W., & Yan, Q. (2016). Modified Formula for the Tensile Strength as Obtained by the Flattened Brazilian Disk Test. *Rock Mechanics and Rock Engineering*, *49*(4), 1579–1586. https://doi.org/10.1007/s00603-015-0785-z

Mahnken, R. (2003). Creep simulation of asymmetric effects by use of stress mode dependent weighting functions. *International Journal of Solids and Structures*, *40*(22), 6189–6209. https://doi.org/10.1016/S0020-7683(03)00388-3

Mahnken, R. (2017). Identification of Material Parameters for Constitutive Equations. In *Encyclopedia of Computational Mechanics* (Second, pp. 1–21). John Wiley & Sons, Ltd. https://doi.org/10.1002/9781119176817.ecm2043
_eprint: https://onlinelibrary.wiley.com/doi/pdf/10.1002/9781119176817.ecm2043

Mahnken, R., Johansson, M., & Runesson, K. (1998). Parameter estimation for a viscoplastic damage model using a gradient-based optimization algorithm. *Engineering Computations*, *15*(7), 925–955. https://doi.org/10.1108/02644409810236920

Mahnken, R., & Stein, E. (1996a). Parameter identification for viscoplastic models based on analytical derivatives of a least-squares functional and stability investigations. *International Journal of Plasticity*, *12*(4), 451–479. https://doi.org/10.1016/S0749-6419(95)00016-X

Mahnken, R., & Stein, E. (1996b). A unified approach for parameter identification of inelastic material models in the frame of the finite element method. *Computer Methods in Applied Mechanics and Engineering*, *136*(3), 225–258. https://doi.org/10.1016/0045-7825(96)00991-7

Maier, G., Bocciarelli, M., & Fedele, R. (2005). Some innovative industrial prospects centered on inverse analyses. In Z. Mróz & G. E. Stavroulakis (Eds.), *Parameter Identification of Materials and Structures* (pp. 55–93). Vienna, Springer. https://doi.org/10.1007/3-211-38134-1_3

Malinin, N. N., & Khadjinsky, G. M. (1972). Theory of creep with anisotropic hardening. *International Journal of Mechanical Sciences*, *14*(4), 235–246. https://doi.org/10.1016/0020-7403(72)90065-3

Marquardt, D. (1963). An Algorithm for Least-Squares Estimation of Nonlinear Parameters. *Journal of the Society for Industrial and Applied Mathematics*, *11*(2), 431–441.

Martinez, A. G. T., Luz, A. P., Braulio, M. A. L., & Pandolfelli, V. C. (2012). Creep behavior modeling of silica fume containing Al2O3–MgO refractory castables. *Ceramics International*, *38*(1), 327–332. https://doi.org/10.1016/j.ceramint.2011.07.010

Mathieu, F., Leclerc, H., Hild, F., & Roux, S. (2015). Estimation of Elastoplastic Parameters via Weighted FEMU and Integrated-DIC. *Experimental Mechanics*, *55*(1), 105–119. https://doi.org/10.1007/s11340-014-9888-9

Mathieu, F., Hild, F., & Roux, S. (2013). Image-based identification procedure of a crack propagation law. *Engineering Fracture Mechanics*, *103*, 48–59. https://doi.org/10.1016/j.engfracmech.2012.05.007

Maupin, M. W. (2004). Insulation of Steel Ladles, In *AISTech 2004 Proceedings*, Nashville, USA.

Merzouki, T., Blond, E., & Schmitt, N. (2016). Numerical study of the effects of refractory lining geometries on the swelling induced by oxidation. *Finite Elements in Analysis and Design*, *108*, 66–80. https://doi.org/10.1016/j.finel.2015.09.006

Mitchell, M. (1999). *An Introduction to Genetic Algorithms*. Cambridge, Massachusetts, MIT Press.

Moura Neto, F. D., & da Silva Neto, A. J. (2013). *An Introduction to Inverse Problems with Applications*. Berlin, Heidelberg, Springer Berlin Heidelberg. https://doi.org/10.1007/978-3-642-32557-1

Muskhelishvili, N. I. (1977). *Some Basic Problems of the Mathematical Theory of Elasticity*. Dordrecht, Springer Netherlands. https://doi.org/10.1007/978-94-017-3034-1

Naumenko, K., & Altenbach, H. (2007). *Modeling of Creep for Structural Analysis* (V. I. Babitsky & J. Wittenburg, Eds.). Berlin, Heidelberg, Springer Berlin Heidelberg. https://doi.org/10.1007/978-3-540-70839-1

Nazaret, F., Marzagui, H., & Cutard, T. (2006). Influence of the mechanical behaviour specificities of damaged refractory castables on the Young's modulus determination. *Journal of the European Ceramic Society*, *26*(8), 1429–1438. https://doi.org/10.1016/j.jeurceramsoc.2005.03.231

Neggers, J., Hoefnagels, J. P. M., Geers, M. G. D., Hild, F., & Roux, S. (2015). Time-resolved integrated digital image correlation. *International Journal for Numerical Methods in Engineering*, *103*(3), 157–182. https://doi.org/10.1002/nme.4882

Nguyen, T., Blond, E., Gasser, A., & Prietl, T. (2009). Mechanical homogenisation of masonry wall without mortar. *European Journal of Mechanics - A/Solids*, *28*(3), 535–544. https://doi.org/10.1016/j.euromechsol.2008.12.003

Novak, M. D., & Zok, F. W. (2011). High-temperature materials testing with full-field strain measurement: Experimental design and practice. *Review of Scientific Instruments*, *82*(11), 115101. https://doi.org/10.1063/1.3657835

NSC. (2017). An introduction to steelmaking.

Pagnacco, E., Caro-Bretelle, A.-S., & Ienny, P. (2013). Parameter Identification from Mechanical Field Measurements using Finite Element Model Updating Strategies. In *Full-Field Measurements and Identification in Solid Mechanics* (pp. 247–274). John Wiley & Sons, Ltd. https://doi.org/10.1002/9781118578469.ch9
_eprint: https://onlinelibrary.wiley.com/doi/pdf/10.1002/9781118578469.ch9

Pan, B., Wang, B., & Lubineau, G. (2016). Comparison of subset-based local and FE-based global digital image correlation: Theoretical error analysis and validation. *Optics and Lasers in Engineering*, *82*, 148–158. https://doi.org/10.1016/j.optlaseng.2016.02.019

Pan, B., Wang, B., Lubineau, G., & Moussawi, A. (2015). Comparison of Subset-Based Local and Finite Element-Based Global Digital Image Correlation. *Experimental Mechanics*, *55*(5), 887–901. https://doi.org/10.1007/s11340-015-9989-0

Pan, B. (2009). Reliability-guided digital image correlation for image deformation measurement. *Applied Optics*, *48*(8), 1535. https://doi.org/10.1364/AO.48.001535

Pan, B., Qian, K., Xie, H., & Asundi, A. (2009). Two-dimensional digital image correlation for in-plane displacement and strain measurement: A review. *Measurement Science and Technology*, *20*(6), 062001. https://doi.org/10.1088/0957-0233/20/6/062001

Pan, B., Wu, D., Wang, Z., & Xia, Y. (2011). High-temperature digital image correlation method for full-field deformation measurement at 1200 °C. *Measurement Science and Technology*, *22*(1), 015701. https://doi.org/10.1088/0957-0233/22/1/015701

Poloni, G., & Pediroda, V. (2000). GA Coupled with Computationally Expensive Simulations: Tools to Improve Efficiency. In *Genetic Algorithms and Evolution Strategy in Engineering and Computer Science: Recent Advances and Industrial Applications*. Wiley.

Prates, P. A., Oliveira, M. C., & Fernandes, J. V. (2014). A new strategy for the simultaneous identification of constitutive laws parameters of metal sheets using a single test. *Computational Materials Science*, *85*, 102–120. https://doi.org/10.1016/j.commatsci.2013.12.043

Prates, P. A., Pereira, A. F. G., Sakharova, N. A., Oliveira, M. C., & Fernandes, J. V. (2016). Inverse Strategies for Identifying the Parameters of Constitutive Laws of Metal Sheets. *Advances in Materials Science and Engineering*, *2016*, 1–18. https://doi.org/10.1155/2016/4152963

Procopio, A. T., Zavaliangos, A., & Cunningham, J. C. (2003). Analysis of the diametrical compression test and the applicability to plastically deforming materials. *Journal of Materials Science*, *38*(17), 3629–3639. https://doi.org/10.1023/A:1025681432260

Réthoré, J. (2010). A fully integrated noise robust strategy for the identification of constitutive laws from digital images. *International Journal for Numerical Methods in Engineering*, *84*(6), 631–660. https://doi.org/10.1002/nme.2908

Réthoré, J., Roux, S., & Hild, F. (2009). An extended and integrated digital image correlation technique applied to the analysis of fractured samples: The equilibrium gap method as a mechanical filter. *European Journal of Computational Mechanics*, *18*(3-4), 285–306. https://doi.org/10.3166/ejcm.18.285-306

Ribeiro, S., & Rodrigues, J. (2010). The influence of microstructure on the maximum load and fracture energy of refractory castables. *Ceramics International*, *36*(1), 263–274. https://doi.org/10.1016/j.ceramint.2009.07.033

Rokoš, O., Hoefnagels, J., Peerlings, R., & Geers, M. (2018). On micromechanical parameter identification with integrated DIC and the role of accuracy in kinematic boundary conditions. *International Journal of Solids and Structures*, *146*, 241–259. https://doi.org/10.1016/j.ijsolstr.2018.04.004

Rosenfield, A. R., Duckworth, W. H., & Shetty, D. K. (1985). Damage Analysis of Creep in Bending. *Journal of the American Ceramic Society*, *68*(9), 483–485. https://doi.org/10.1111/j.1151-2916.1985.tb15813.x

_eprint: https://ceramics.onlinelibrary.wiley.com/doi/pdf/10.1111/j.1151-2916.1985.tb15813.x

Roux, S., Réthoré, J., & Hild, F. (2009). Digital image correlation and fracture: An advanced technique for estimating stress intensity factors of 2D and 3D cracks. *Journal of Physics D: Applied Physics*, *42*(21), 214004. https://doi.org/10.1088/0022-3727/42/21/214004

Ruybalid, A. P., Hoefnagels, J. P. M., van der Sluis, O., & Geers, M. G. D. (2016). Comparison of the identification performance of conventional FEM updating and integrated DIC. *International Journal for Numerical Methods in Engineering*, *106*(4), 298–320. https://doi.org/10.1002/nme.5127

Ruybalid, A., Hoefnagels, J., van der Sluis, O., van Maris, M., & Geers, M. (2019). Mixed-mode cohesive zone parameters from integrated digital image correlation on micrographs only. *International Journal of Solids and Structures*, *156–157*, 179–193. https://doi.org/10.1016/j.ijsolstr.2018.08.010

Saltelli, A. (Ed.). (2008). *Global sensitivity analysis: The primer*. Chichester, England ; Hoboken, NJ, John Wiley

OCLC: ocn180852094.

Saltelli, A., Aleksankina, K., Becker, W., Fennell, P., Ferretti, F., Holst, N., Li, S., & Wu, Q. (2019). Why so many published sensitivity analyses are false: A systematic review of sensitivity analysis practices. *Environmental Modelling & Software*, *114*, 29–39. https://doi.org/10.1016/j.envsoft.2019.01.012

Samadi, S., Jin, S., Gruber, D., Harmuth, H., & Schachner, S. (2020). Statistical study of compressive creep parameters of an alumina spinel refractory. *Ceramics International*, *46*(10, Part A), 14662–14668. https://doi.org/10.1016/j.ceramint.2020.02.267

Schachner, S., Jin, S., Gruber, D., & Harmuth, H. (2019). Three stage creep behavior of MgO containing ordinary refractories in tension and compression. *Ceramics International*, *45*(7), 9483–9490. https://doi.org/10.1016/j.ceramint.2018.09.124

Schacht, C. A. (2004). Thermomechanical Considerations for Refractory Linings. In *Refractories Handbook* (First, pp. 369–394). New York, NY, Marcel Dekker, Inc.

Senseny, P. E., & Fossum, A. F. (1995). On Testing Requirements for Viscoplastic Constitutive Parameter Estimation. *Journal of Engineering Materials and Technology*, *117*(2), 151–156. https://doi.org/10.1115/1.2804522

Sidi Mammar, A., Gruber, D., Harmuth, H., & Jin, S. (2016). Tensile creep measurements of ordinary ceramic refractories at service related loads including setup, creep law, testing and evaluation procedures. *Ceramics International*, *42*(6), 6791–6799. https://doi.org/10.1016/j.ceramint.2016.01.056

Sivanandam, S. N., & Deepa, S. N. (2007). *Introduction to genetic algorithms*. Berlin ; New York, Springer.

Springmann, M., & Kuna, M. (2005). Identification of material parameters of the Gurson Tvergaard Needleman model by combined experimental and numerical techniques. *Computational Materials Science*, *32*(3-4), 544–552. https://doi.org/10.1016/j.commatsci.2004.09.010

Stavroulakis, G. E. (2001). *Inverse and Crack Identification Problems in Engineering Mechanics* (P. M. Pardalos & D. Hearn, Eds.; Vol. 46). Boston, MA, Springer US. https://doi.org/10.1007/978-1-4615-0019-3

Stavroulakis, G. E., Engelhardt, M., & Antes, H. (2005). Crack and Flaw Identification in Statics and Dynamics, using Filter Algorithms and Soft Computing. In Z. Mróz & G. E. Stavroulakis (Eds.), *Parameter Identification of Materials and Structures* (pp. 139–176). Vienna, Springer. https://doi.org/10.1007/3-211-38134-1_5

Stirling, R. A., Simpson, D. J., & Davie, C. T. (2013). The application of digital image correlation to Brazilian testing of sandstone. *International Journal of Rock Mechanics and Mining Sciences*, *60*, 1–11. https://doi.org/10.1016/j.ijrmms.2012.12.026

Tarantola, A. (2005). *Inverse Problem Theory and Methods for Model Parameter Estimation*. Society for Industrial and Applied Mathematics. https://doi.org/10.1137/1.9780898717921

Teixeira, L., Samadi, S., Gillibert, J., Jin, S., Sayet, T., Gruber, D., & Blond, E. (2020). Experimental Investigation of the Tension and Compression Creep Behavior of Alumina-Spinel Refractories at High Temperatures. *Ceramics*, *3*(3), 372–383. https://doi.org/10.3390/ceramics3030033

Teixeira, L., Gasser, A., & Rekik, A. (2017). Thermo-mechanical modeling of a stell ladle using the periodic linear homogenization technique, In *Unified International Technical Conference on Refractories*, Santiago - Chile.

Timoshenko, S., & Goodier, J. N. (1951). *Theory of Elasticity* (Second). New York, McGraw-Hill Book Company, Inc.

Tomba Martinez, A. G., Camerucci, M. A., & Cavalieri, A. L. (2008). Thermal stress analysis of cordierite materials subjected to thermal shock. *Journal of Materials Science*, *43*(8), 2731–2738. https://doi.org/10.1007/s10853-008-2492-6

Toropov, V., & Yoshida, F. (2005). Application of Advanced Optimization Techniques to Parameter and Damage Identification Problems. In Z. Mróz & G. E. Stavroulakis (Eds.), *Parameter Identification of Materials and Structures* (pp. 177–263). Vienna, Springer. https://doi.org/10.1007/3-211-38134-1_6

Tschegg, E., Fendt, K., Manhart, C., & Harmuth, H. (2009). Uniaxial and biaxial fracture behaviour of refractory materials. *Engineering Fracture Mechanics*, *76*(14), 2249–2259. https://doi.org/10.1016/j.engfracmech.2009.07.011

Vargas, R., Neggers, J., Canto, R., Rodrigues, J., & Hild, F. (2016). Analysis of wedge splitting test on refractory castable via integrated DIC. *Journal of the European Ceramic Society*, *36*(16), 4309–4317. https://doi.org/10.1016/j.jeurceramsoc.2016.07.007

Vargas, R., Neggers, J., Canto, R., Rodrigues, J., & Hild, F. (2018). Comparison of two full-field identification methods for the wedge splitting test on a refractory. *Journal of the European Ceramic Society*, *38*(16), 5569–5579. https://doi.org/10.1016/j.jeurceramsoc.2018.07.039

Volkova, O., & Janke, D. (2005). Influence of the Lining on the Thermal Behaviour of a Teeming Ladle. *steel research international*, *76*(4), 313–319. https://doi.org/10.1002/srin.200506014
_eprint: https://onlinelibrary.wiley.com/doi/pdf/10.1002/srin.200506014

Volkov-Husović, T., Jančić, R., Cvetković, M., Mitraković, D., & Popović, Z. (1999). Thermal shock behavior of alumina based refractories: Fracture resistance parameters and water quench test. *Materials Letters*, *38*(5), 372–378. https://doi.org/10.1016/S0167-577X(98)00192-X

Wang, B., & Pan, B. (2016). Subset-based local vs. finite element-based global digital image correlation: A comparison study. *Theoretical and Applied Mechanics Letters*, *6*(5), 200–208. https://doi.org/10.1016/j.taml.2016.08.003

Wang, Q.-Z., & Xing, L. (1999). Determination of fracture toughness KIC by using the ¯attened Brazilian disk specimen for rocks. *Engineering Fracture Mechanics*, 9.

Wang, Q., Jia, X., Kou, S., Zhang, Z., & Lindqvist, P.-A. (2004). The flattened Brazilian disc specimen used for testing elastic modulus, tensile strength and fracture toughness of

brittle rocks: Analytical and numerical results. *International Journal of Rock Mechanics and Mining Sciences*, *41*(2), 245–253. https://doi.org/10.1016/S1365-1609(03)00093-5

Wang, S., Yao, X. F., Su, Y. Q., & Ma, Y. J. (2015). High temperature image correction in DIC measurement due to thermal radiation. *Measurement Science and Technology*, *26*(9), 095006. https://doi.org/10.1088/0957-0233/26/9/095006

Wang, W., Xu, C., Jin, H., Meng, S., Zhang, Y., & Xie, W. (2017). Measurement of high temperature full-field strain up to 2000 °C using digital image correlation. *Measurement Science and Technology*, *28*(3), 035007. https://doi.org/10.1088/1361-6501/aa56d1

Zhang, Z., Pan, B., Grédiac, M., & Song, W. (2018). Accuracy-enhanced constitutive parameter identification using virtual fields method and special stereo-digital image correlation. *Optics and Lasers in Engineering*, *103*, 55–64. https://doi.org/10.1016/j.optlaseng.2017.11.016

Résumé détaillé en français

Modélisation Numérique et Caractérisation Expérimentale du Comportement de Fluage Asymétrique des Matériaux Réfractaires

Introduction

Les matériaux réfractaires sont d'une importance primordiale dans plusieurs processus de production impliquant la manipulation de matériaux à haute température, tels que l'acier, le ciment, le verre, le cuivre, entre autres. Ces matériaux sont fondamentaux pour garantir un processus sûr et économe en énergie et, en tant que tels, reçoivent une attention considérable de la part des groupes de recherche de différents pays.

Le fluage et la relaxation sont deux phénomènes majeurs liés à l'application des réfractaires à hautes températures. La caractérisation et la modélisation de ces comportements dépendant du temps sont cruciales pour prédire avec précision les contraintes et déformations thermomécaniques dans les revêtements réfractaires en conditions de fonctionnement, ainsi que dans les coques en acier qui les entourent. En particulier, les réfractaires présentent un comportement de fluage asymétrique, c'est-à-dire des propriétés de matériau différentes sous tension et compression, ce qui rend leur étude encore plus difficile.

Actuellement, il n'y a pas de modèles constitutifs de fluage disponibles dans les logiciels commerciaux qui peuvent être utilisés pour simuler avec précision le comportement de fluage asymétrique des réfractaires sous des charges thermomécaniques complexes. De plus, la caractérisation de ces matériaux à haute température est coûteuse et prend du temps, c'est pourquoi l'industrie a constamment besoin de méthodes expérimentales innovantes pouvant générer plus d'informations par échantillon.

L'application d'une instrumentation optique couplée à la technologie de corrélation d’images numériques est une option intéressante pour obtenir plus de données à partir d'essais à haute température, car elle peut mesurer le champ de déplacements complet dans l'échantillon, permettant ainsi d'appliquer des chemins de chargement plus complexes. Cette thèse vise à contribuer à l'évolution vers une modélisation et une caractérisation plus rapide, moins chères et plus robustes des réfractaires.

Méthodes traditionnelles pour l’identification des paramètres de fluage

Le comportement au fluage des matériaux céramiques peut être divisé en trois étapes, comme le montre la Figure *1*. La première étape, appelée fluage primaire, présente une vitesse de déformation qui diminue avec le temps. Dans l'étape de fluage secondaire, la vitesse de déformation est considérée comme constante et un équilibre approximatif entre les processus de durcissement et de ramollissement peut être supposé. Enfin, dans la troisième étape de fluage, la vitesse de déformation augmente avec le temps jusqu'à la rupture du matériau.

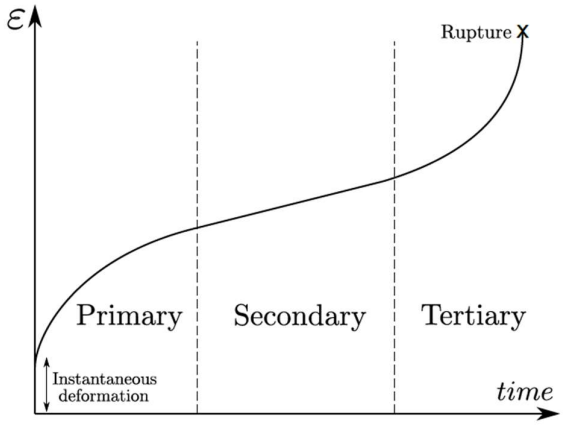

Figure 1 - Trois étapes du fluage

La caractérisation du fluage des matériaux réfractaires est traditionnellement faite avec des essaies de compression et traction unidimensionnels, avec des dispositifs expérimentaux dédiés, comme montre la Figure 2.

La loi de comportement de Norton-Bailey est la plus utilisé pour représenter le fluage des matériaux réfractaires. Dans sa forme tridimensionnelle, la vitesse de déformation en fluage est donnée pour :

$$\underline{\underline{\dot{\varepsilon}}}^{cr} = \frac{3}{2}\frac{\underline{\underline{s}}}{\sigma_{eq}} A\langle\sigma_{eq} - \sigma_y\rangle^n p^m \qquad (1)$$

ou $\underline{\underline{s}}$ est le déviateur du tenseur des contraintes, σ_{eq} est la contrainte équivalente de von Mises, σ_y est la limite d'élasticité, p est la déformation plastique accumulée. A, n et m sont des propriétés du matériau dépendantes de la température. Quand $m = 0$, l'Équation (1) représente le fluage secondaire.

Les réfractaires sont des matériaux hétérogènes, ayant généralement de gros grains par rapport à la taille des échantillons utilisés pour l'essai mécanique. Ainsi, il est courant d'observer une dispersion considérable des données concernant leurs propriétés mécaniques. A partir de la Figure *3*, il est possible d'observer une dispersion considérable des données expérimentales, notamment en fonction du temps final jusqu'à la rupture.

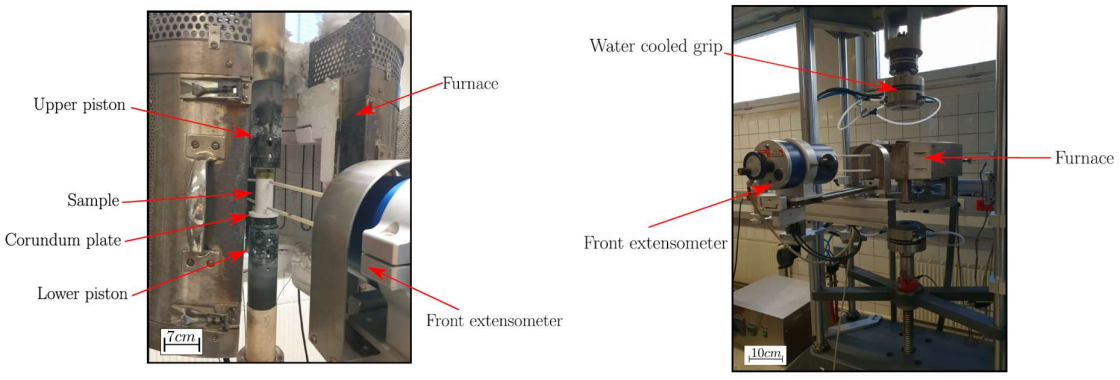

(a) (b)

Figure 2 – Dispositifs expérimentaux pour les essais de fluage en (a) compression et (b) traction.

La dispersion des données peut s'expliquer par de nombreux facteurs. Du point de vue du matériau, l'hétérogénéité des briques utilisées pour produire les échantillons peut provenir des processus de production, tels que le pressage et le traitement thermique. D'après les procédures de test, la microfissuration de l'échantillon lors de sa production et le désalignement de la charge peuvent contribuer aux variations des résultats. Il n'entre pas dans le cadre de ce travail de définir précisément les causes de cette dispersion, car elle peut provenir d'une combinaison de tous les facteurs évoqués.

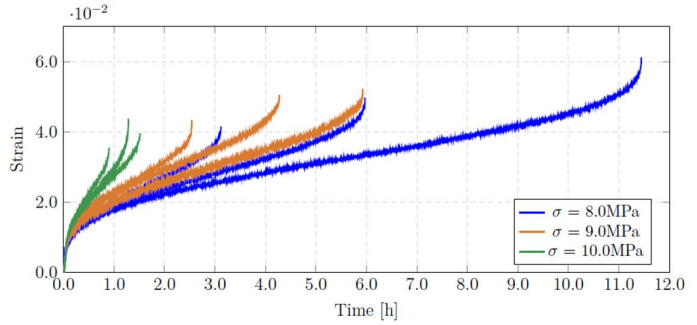

(a)

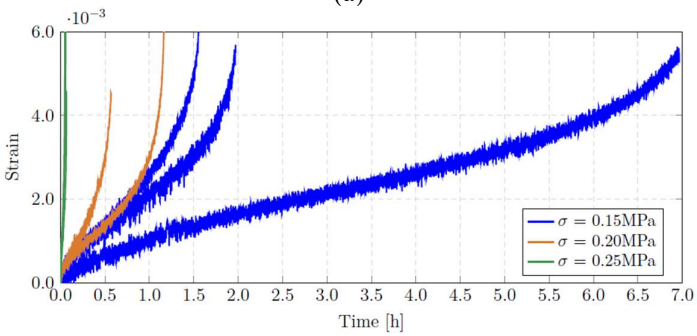

(b)

Figure 3 – Courbes de fluage pour la brique d'alumine-spinelle à 1300 °C en (a) compression et (b) traction.

En utilisant les courbes de fluage présentées sur la figure 1 pour la brique alumine-spinelle à 1300 °C, les paramètres de la loi de fluage de Norton-Bailey ont été identifiés. Le Tableau 1 montre les résultats pour les paramètres de compression en fluage primaire et le Tableau 2 montre les résultats pour les paramètres de tension en fluage secondaire.

Tableau 1 - Paramètres identifiés - compression

Paramètre	**Valeur**	**Écart-type**	**Intervalle de confiance à 70 %**
$\log_{10}(A[\mathrm{MPa}^{-n}\mathrm{s}^{-1}])$	$-14{,}16$	$1{,}732$	$(-14{,}19, -13{,}83)$
$n[-]$	$-3{,}96$	$2{,}187$	$(3{,}80, 4{,}13)$
$m[-]$	$-2{,}74$	$0{,}207$	$(-2{,}83, -2{,}64)$

Tableau 2 - Paramètres identifiés - compression

Paramètre	**Valeur**	**Écart-type**	**Intervalle de confiance à 70 %**
$\log_{10}(A[\mathrm{MPa}^{-n}\mathrm{s}^{-1}])$	$2{,}26$	$1{,}12$	$(1{,}39, 3{,}14)$
$n[-]$	$-3{,}96$	$2{,}187$	$(10{,}31, 13{,}06)$

Proposition d'une loi de comportement asymétrique pour le fluage des réfractaires

Pour tenir compte du fluage asymétrique bien connu des réfractaires, Blond et al[1] ont étendu le modèle de Norton-Bailey en utilisant la division des tenseurs de contraintes principales en une partie positive et une partie négative pour proposer un modèle de fluage secondaire, résultant en :

$$\underline{\underline{\sigma}} = \langle \underline{\underline{\sigma}} \rangle - \langle -\underline{\underline{\sigma}} \rangle \qquad (2)$$

Cette division aboutit à la définition du modèle en termes de paramètres indépendants de traction et de compression. En ce sens, les deux parties du déviateur du tenseur des contraintes sont données par :

$$\underline{\underline{s}}^{\pm} = \langle \pm \underline{\underline{\sigma}} \rangle - \frac{1}{3} \mathrm{Tr}\left(\langle \pm \underline{\underline{\sigma}} \rangle \right) \underline{\underline{I}} \qquad (3)$$

où les indices $\pm$ indiquent les parties positives et négatives des variables, respectivement. Les contraintes équivalentes de von Mises sont donc :

$$\sigma_{eq}^{\pm} = \sqrt{\frac{3}{2} \underline{\underline{s}}^{\pm} : \underline{\underline{s}}^{\pm}} \qquad (4)$$

Résultant en une vitesse de déformation en fluage de la forme :

$$\underline{\underline{\dot{\varepsilon}}}^{cr} = \frac{3}{2} \frac{\underline{\underline{s}}^{+}}{\sigma_{eq}^{+}} A^{+} \langle \sigma_{eq}^{+} - \sigma_{y}^{+} \rangle^{n^{+}} - \frac{3}{2} \frac{\underline{\underline{s}}^{-}}{\sigma_{eq}^{-}} A^{-} \langle \sigma_{eq}^{-} - \sigma_{y}^{-} \rangle^{n^{-}} \qquad (5)$$

Où $A^{\pm}$ et $n^{\pm}$ sont les paramètres matériau en traction $(+)$ et compression $(-)$.

Les courbes de fluage en compression et en tension présentées dans la Figure *3* montrent la nécessité de développer une loi de comportement capable de représenter le comportement asymétrique des réfractaires en considérant le fluage primaire et secondaire. A cette fin, l'Équation (5) a été adaptée suivant le même principe de séparation du tenseur des contraintes en une partie positive et une partie négative, tel qu'utilisé par Blond et al.

Le modèle proposé se différencie également du modèle de Blond dans la manière de considérer les différentes contributions des caractéristiques de compression et de traction du matériau. Après la décomposition du tenseur des contraintes, les déviateurs du tenseur des contraintes sont calculés pour chaque part (positif et négatif) en utilisant les Équations (3) et (4), respectivement. Néanmoins, au lieu d'utiliser $\underline{\underline{s}}^{\pm}$ et $\sigma_{eq}^{\pm}$ pour calculer directement les taux de déformation viscoplastique positive et négative (Équation I.46), ces valeurs sont utilisées pour calculer les poids relatifs que chaque partie du tenseur de contrainte a sur la contrainte équivalente totale, en utilisant la relation :

[1] Blond, E., Schmitt, N., Hild, F., Blumenfeld, P., & Poirier, J. (2005). Modelling of high temperature asymmetric creep behavior of ceramics. *Journal of the European Ceramic Society*, *25*(11), 1819–1827. https://doi.org/10.1016/j.jeurceramsoc.2004.06.004

$$w^{\pm} = \frac{\sigma_{eq}^{\pm}}{\sigma_{eq}^{+} + \sigma_{eq}^{-}} \qquad (6)$$

Chaque portion de la vitesse de déformation viscoplastique est calculée en fonction des déviateurs du tenseur des contraintes et des contraintes équivalentes totales (en utilisant le tenseur des contraintes complètes, avant la décomposition en parties positives et négatives) et des propriétés respectives du matériau. Chaque partie du taux de déformation viscoplastique est pondérée par les valeurs calculées à l'aide de l'Équation (6). Par conséquent, le taux de déformation viscoplastique du modèle de fluage asymétrique proposé est donné par :

$$\underline{\underline{\dot{\varepsilon}}}^{cr} = w^{+}\frac{3}{2}\frac{\underline{\underline{S}}}{\sigma_{eq}}A^{+}\langle\sigma_{eq} - \sigma_{y}^{+}\rangle^{n^{+}}p^{m^{+}} - \frac{3}{2}\frac{\underline{\underline{S}}}{\sigma_{eq}}A^{-}\langle\sigma_{eq} - \sigma_{y}^{-}\rangle^{n^{-}}p^{m^{-}} \qquad (7)$$

La loi de comportement décrite par l'Équation (7) a été implémenté dans le logiciel Abaqus, à l'aide d'une sous-routine UMAT.

Des simulations numériques du test brésilien ont été utilisées pour évaluer les capacités du modèle asymétrique proposé. Quatre situations concernant le type de modèle et les paramètres matériaux ont été considérées :

1. Modèle de fluage symétrique disponible dans le logiciel Abaqus, utilisant les propriétés de compression du matériau.
2. Modèle de fluage symétrique disponible dans le logiciel Abaqus, utilisant les propriétés de traction du matériau.
3. Modèle de fluage asymétrique UMAT, mais utilisant les propriétés de compression du matériau pour la compression et la traction, pour vérifier si le modèle asymétrique se spécialise en un modèle symétrique si nécessaire.
4. Modèle de fluage asymétrique UMAT, utilisant les propriétés correspondantes pour la traction et la compression.

La Figure III.4 montre la géométrie, le maillage et les conditions aux limites utilisées pour comparer les modèles symétriques et asymétriques en utilisant un essai brésilien. Une force de -400 N a été appliquée sur le modèle suivant une rampe linéaire de 30 s et maintenue pendant deux heures.

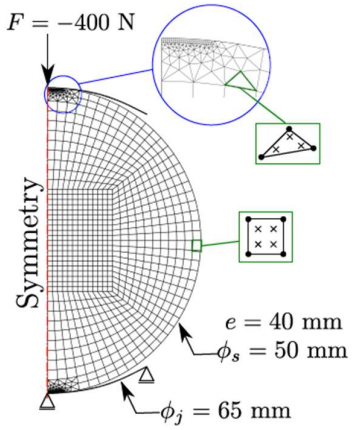

Figure 4 – Essai brésilien – Géométrie, maillage et conditions aux limites.

Une comparaison entre les déplacements verticaux et horizontaux pris au centre de l'échantillon pour les quatre cas est illustrée à la figure III.5. Il est possible d'observer que, lorsque des courbes de compression sont utilisées dans le modèle asymétrique, le résultat est en bon accord avec le modèle symétrique disponible sur le logiciel Abaqus. Lorsque le modèle asymétrique est utilisé, un résultat intermédiaire entre traction et compression est obtenu.

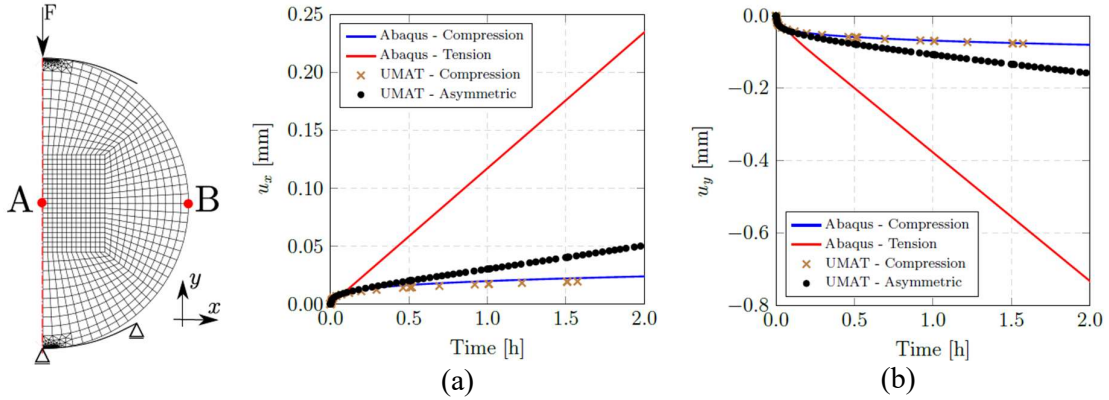

Figure 5 – (a) Déplacements verticaux et (b) horizontaux dans l'échantillon de l'essai brésilien.

La figure III.10 montre l'effet de l'asymétrie dans la déformation viscoplastique accumulée sur un essai brésilien. Encore une fois, le modèle asymétrique proposé montre un comportement intermédiaire entre les modèles symétriques, et met en évidence l'importance de la prise en compte des différentes propriétés du matériau en traction et en compression.

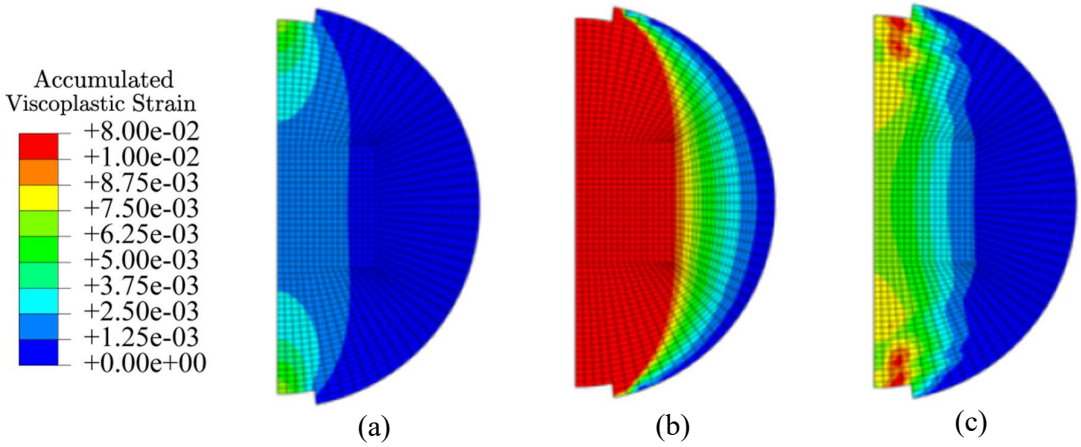

Figure 6 – Déformations viscoplastiques accumulées sur un échantillon d'essai brésilien. Propriétés matériau en (a) compression (b) tension et (c) asymétriques.

Dispositif expérimental pour les essaies brésiliens avec corrélation d'images numérique à haute température

Pour identifier les paramètres de la loi de fluage asymétrique proposée, l'essai brésilien a été utilisé, car il présente des contraintes de traction et de compression au niveau de l'échantillon lors de l'essai. Cela permet d'identifier tous les paramètres (tension et compression) en utilisant un seul essaies.

La Figure *7* montre le montage expérimental utilisé pour effectuer les tests brésiliens et pour prendre les photos à haute température. Cette configuration est composée des parties suivantes :

1. Un four sur mesure refroidi à l'eau, capable de chauffer jusqu'à 1300 °C.
2. La porte du four est équipée d'une fenêtre en vitrocéramique, de sorte que l'échantillon puisse être photographié.
3. Pour augmenter la quantité de lumière bleue disponible lors de la prise de vue, deux sources de lumière bleue sont utilisées pour éclairer l'échantillon.
4. Une caméra CCD haute résolution avec des objectifs de 200 mm et un filtre passe-bande bleu.
5. La caméra et les objectifs sont refroidis à l'aide de deux ventilateurs, car ils se trouvent à proximité du four et peuvent surchauffer.
6. Une cellule de charge d'une capacité maximale de 30 kN, avec une erreur de lecture complète de 0,25 %.

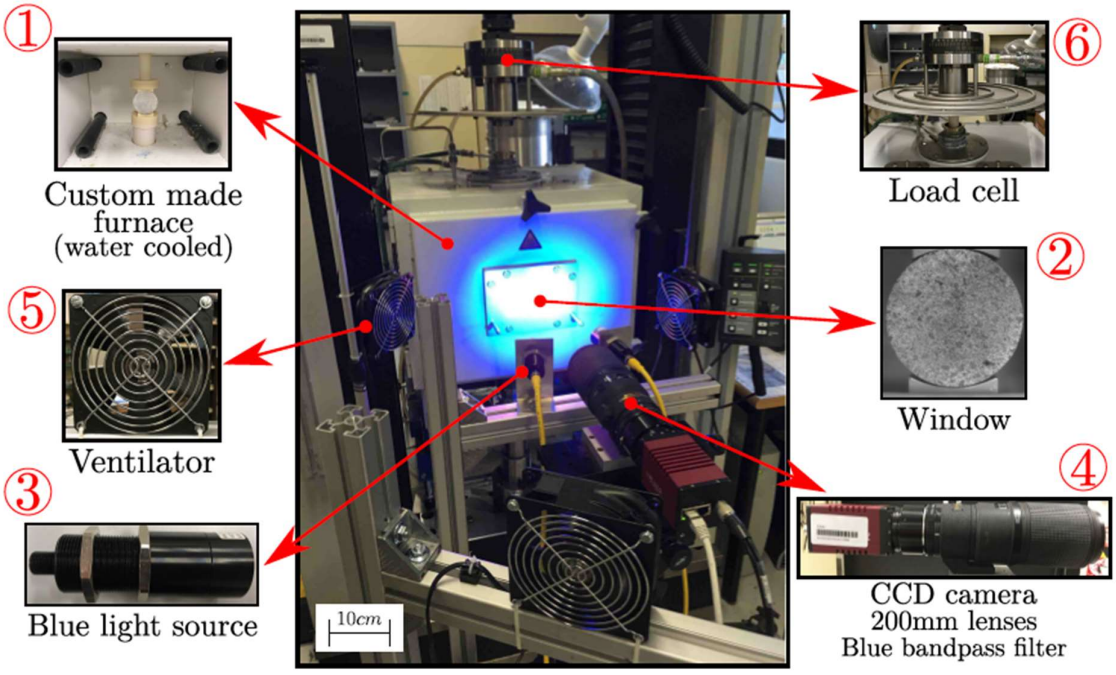

Figure 7 – Montage expérimental pour les essais brésiliens à haute température

La Figure *8* montre l'effet de la foudre et du filtre passe-bande bleu sur la qualité des images. A température ambiante (Figure *8*a), l'histogramme de l'image, représenté sur la Figure *9*, est à peu près normalement distribué autour des niveaux de gris de 75 à 200, et l'image présente un contraste élevé. A 1200 °C, sans l'utilisation des lumières bleues et du filtre passe-bande bleu (Figure *8*b), la distribution des niveaux de gris est restreinte à la plage comprise entre 105 et 115, et les images perdent la majeure partie de leur contraste. L'utilisation seule du filtre passe-bande bleu, sans les lumières bleues (Figure *8*c), diminue légèrement la netteté de l'histogramme, mais pas suffisamment pour garantir un contraste suffisant. Enfin, en utilisant les lumières bleues et le filtre (Figure *8*d), la distribution des niveaux de gris se rapproche de celle de l'image à température ambiante, et la majeure partie du contraste est récupérée.

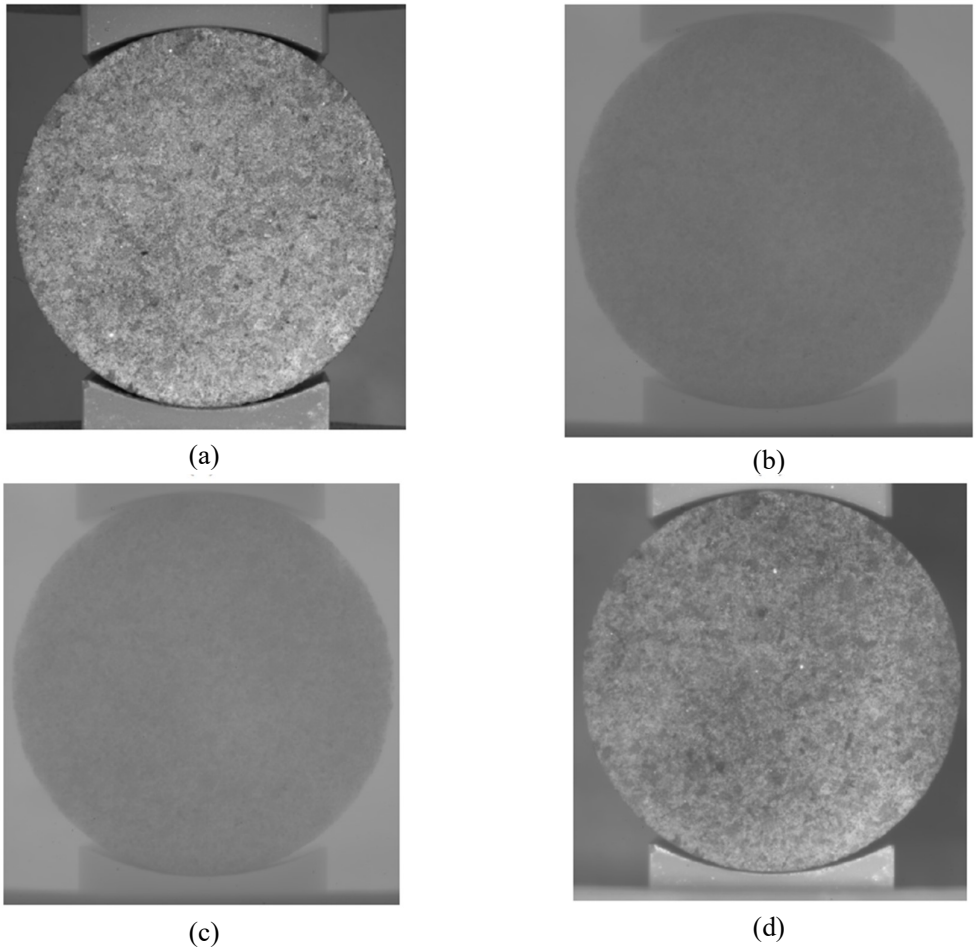

Figure 8 – Influence de la lumière bleue et du filtre passe-bande bleu sur la qualité de l'image. (a) Image à température ambiante. (b) Pas de lumière bleue et pas de filtre. (c) Pas de filtre. (d) Utilisation de la lumière bleue et du filtre passe-bande bleu.

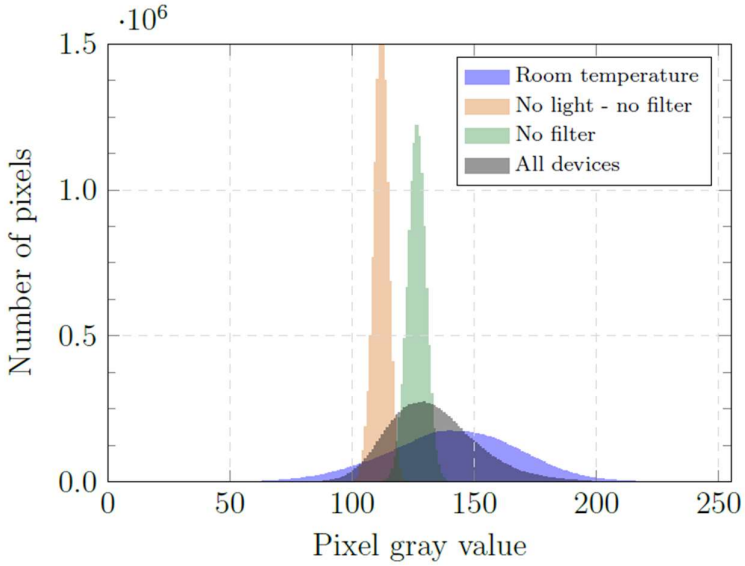

Figure 9 – Histogrammes des images à température ambiante et haute température

Proposition d'un algorithme de corrélation d'images numériques intégré (I-DIC)

Au cours des investigations expérimentales réalisées dans ce travail, il a été observé que les champs de déplacements obtenus en appliquant un calcul de corrélation d'images numériques (DIC) standard présentaient un écart systématique par rapport au champ théorique, c'est-à-dire, au lieu d'un champ de déplacement symétrique par rapport à la direction d'application de la charge, une rotation de l'échantillon était visible dans la plupart des essaies.

Considérant que l'erreur associée aux mouvements de corps rigides de l'échantillon a toujours la même source, c'est-à-dire la rotation de l'échantillon, un nouvel algorithme de corrélation d'image numérique intégré est proposé, dans lequel la force horizontale provoquant la rotation est incluse dans l'élément fini simulations utilisées pour obtenir le champ théorique des déplacements. Cette force horizontale est donc identifiée avec les paramètres du matériau.

L'algorithme proposé est illustré dans la Figure *10* et expliqué ci-dessous :

1. Étape 1 : Fournissez les valeurs initiales des paramètres de matériau et de la force horizontale.
2. Étape 2 : Le champ de déplacements théoriques est calculé à partir des paramètres courants du matériau. Pour calculer les déplacements dans l'essai brésilien résultant des modèles de fluage, la méthode des éléments finis (MEF) est un choix raisonnable, et elle a été utilisée dans ce travail.
3. Étape 3 : Les images théoriquement déformées sont formées par l'imposition des champs de déplacement obtenus à l'étape 2 sur les valeurs de pixel de l'image de référence, à travers un schéma d'interpolation.
4. Étape 4 : Les différences entre les images théoriquement déformées et les images expérimentalement déformées sont calculées, pour chaque pas de temps prédéfini.
5. Étape 5 : La convergence de l'algorithme d'optimisation est vérifiée, selon ses critères spécifiques.
6. Étape 6 : Enfin, dans le cas où la convergence n'a pas été atteinte à l'étape en cours, l'algorithme d'optimisation décide quelle sera la prochaine estimation et le cycle se répète.

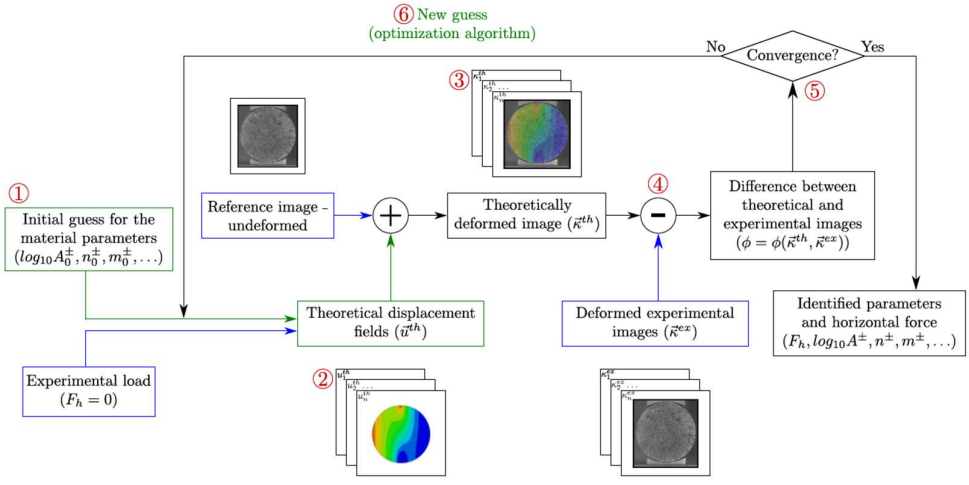

Figure 10 – I-DIC : Algorithme proposé

Afin d'éviter les minima locaux lors de la procédure d'identification, un algorithme génétique a été utilisé en combinaison avec l'algorithme I-DIC proposé.

Identification des paramètres matériaux pour la brique d'alumine-spinelle

Avant de procéder à une identification I-DIC, il est important d'analyser les résultats des essaies en utilisant des méthodes plus simples et plus rapides. L'un des objectifs de ces analyses de pré-identification est la vérification de la cohérence des résultats entre les tests, c'est-à-dire de vérifier si des tests dans les mêmes conditions donnent approximativement les mêmes résultats.

Dans ce travail, le logiciel open-source DIC Ncorr a été utilisé pour calculer les déplacements plein champ des échantillons. Tous les résultats présentés correspondent à des identifications réalisées à 1300 °C.

La Figure 11 montre le déplacement vertical du point supérieur des échantillons d'essai brésiliens à 1300 °C, calculé à l'aide de la corrélation d'images. En tenant compte de l'influence des paramètres du matériau dans chaque partie de la courbe temps vs déplacement pour les essais brésiliens, les paramètres du matériau alumine-spinelle ont été ajustés afin de mieux approximer les valeurs des calculs DIC, et la courbe résultante est présentée dans la Figure 11. Les paramètres identifiés sont indiqués dans le Tableau 3.

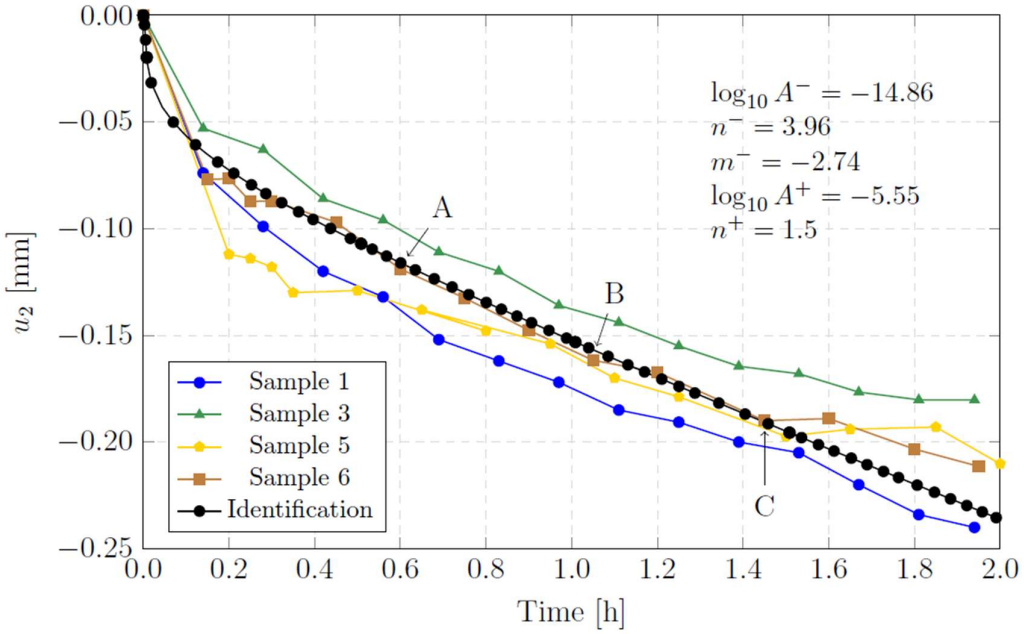

Figure 11 – Essais brésiliens : courbes temps vs déplacement et identification inverse

Tableau 3 - Paramètres identifiés à l'aide de la méthode DIC

Paramètre	Valeur	Différence avec uniaxial
$\log_{10}(A^-[\mathrm{MPa}^{-n}\mathrm{s}^{-1}])$	$-14{,}86$	4,8%
$n^-[-]$	3,6	0%
$m^-[-]$	$-2{,}74$	0%
$\log_{10}(A^+[\mathrm{MPa}^{-n}\mathrm{s}^{-1}])$	$-5{,}55$	–
$n^+[-]$	1,5	–

Les champs de déplacements verticaux des Points A, B et C représentés sur la Figure 11, correspondant respectivement à t=0,6 h, t = 1,05 h et t = 1,45 h, sont représentés sur la Figure 12. Il est possible de voir qu'il y a une rotation de corps rigide de l'échantillon, puisque la carte des déplacements ne correspond pas au champ de déplacements traditionnel d'essaies brésiliens. Pour tenir compte de cet effet, un calcul d'identification supplémentaire a été effectué pour déterminer quelle est l'ampleur de la charge qui a causé cet écart. Une charge horizontale de -7 N a été identifiée et appliquée sur les mâchoires supérieures dans le modèle de simulation

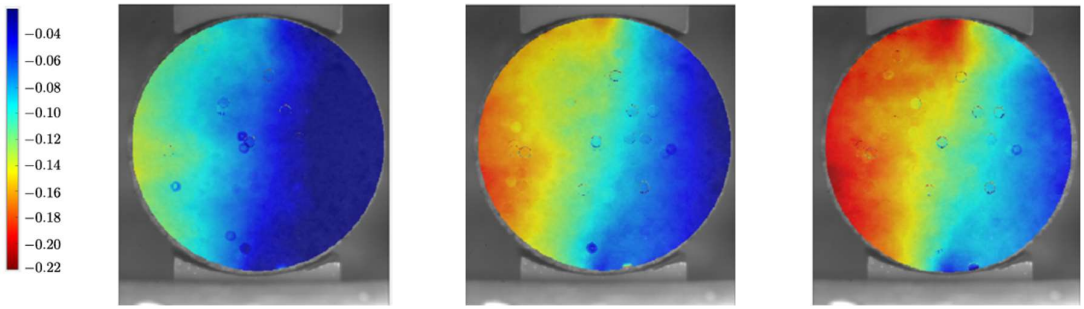

Figure 12 – Essais brésiliens : Déplacement vertical en mm à 1300 °C – Échantillon 6. (a) Point A. (b) Point B. (c) Point C.

La Figure 13 montre les résultats des simulations numériques utilisant les paramètres de matériau identifiés précédemment et la charge horizontale. Il est possible d'observer que les cartes de déplacement des Figure 12 et Figure 13 présentent une bonne équivalence, malgré les erreurs expérimentales et la simplicité de la procédure d'identification.

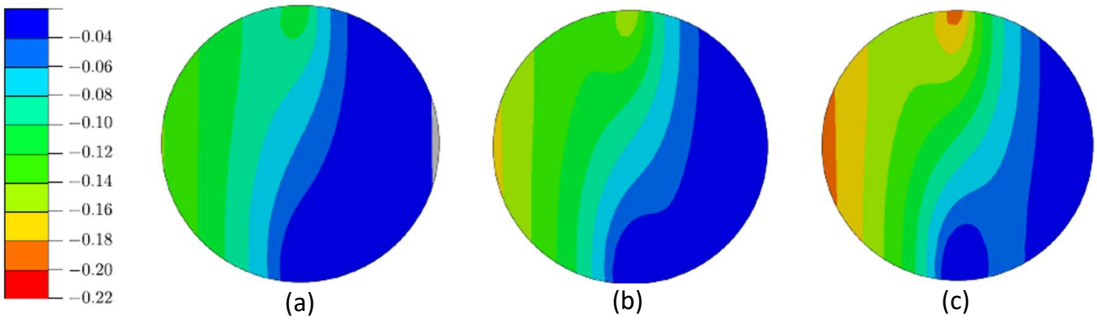

Figure 13 – Essais brésiliens : Déplacement vertical en mm à 1300 °C – Simulation. (a) Point A. (b) Point B. (c) Point C.

La Figure 14 montre les résultats obtenus pour la première génération de l'algorithme génétique, et le Tableau 4 montre les valeurs identifiées. On peut observer que les méthodes utilisant DIC et I-DIC fournissent des résultats similaires, notamment pour les paramètres les plus sensibles à la procédure d'identification.

Tableau 4 - Paramètres identifiés à l'aide de la méthode I-DIC

Paramètre	I-DIC	DIC	Différence
$\log_{10}(A^{-}[\mathrm{MPa}^{-n}\mathrm{s}^{-1}])$	$-15{,}25$	$-14{,}86$	2,7%
$m^{-}[-]$	$-2{,}38$	$-2{,}74$	13,1%
$\log_{10}(A^{+}[\mathrm{MPa}^{-n}\mathrm{s}^{-1}])$	$-5{,}24$	$-5{,}55$	5,58%
$F[\mathrm{N}]$	$-4{,}0$	$-7{,}0$	43,0%

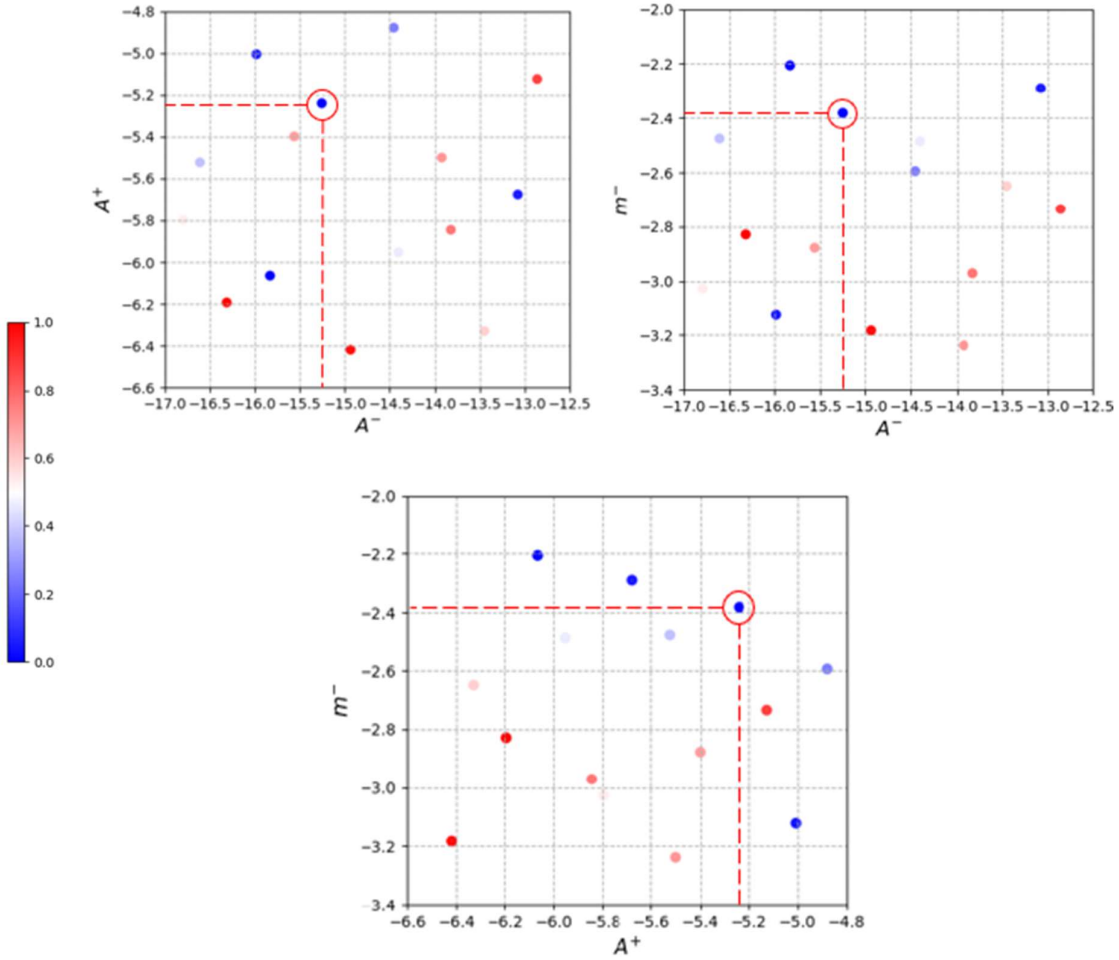

Figure 14 – Identification I-DIC

Dispositif expérimental pour les essaies de fluage quatre-point à haute température – Validation des paramètres identifiés

La Figure *15* montre le montage expérimental utilisé pour effectuer les essais de flexion quatre points et pour prendre les photos à haute température. Cette configuration est composée de :

1. Un four artisanal conçu à Saint-Gobain Research Provence. Ce four a la capacité de chauffer jusqu'à 1600 °C.
2. La porte du four est en réfractaire isolant léger et est équipée d'une fenêtre en saphir.
3. Une source de lumière bleue est utilisée pour éclairer l'échantillon et augmenter le contraste.
4. Les photos sont prises à l'aide d'une caméra CMOS RGB et d'un téléobjectif macro 300 mm avec une extension focale 2x.
5. La charge est appliquée à l'aide de poids statiques déposés sous une tige métallique, qui transfère la charge à une tige d'alumine dont une extrémité est placée à l'intérieur du four.

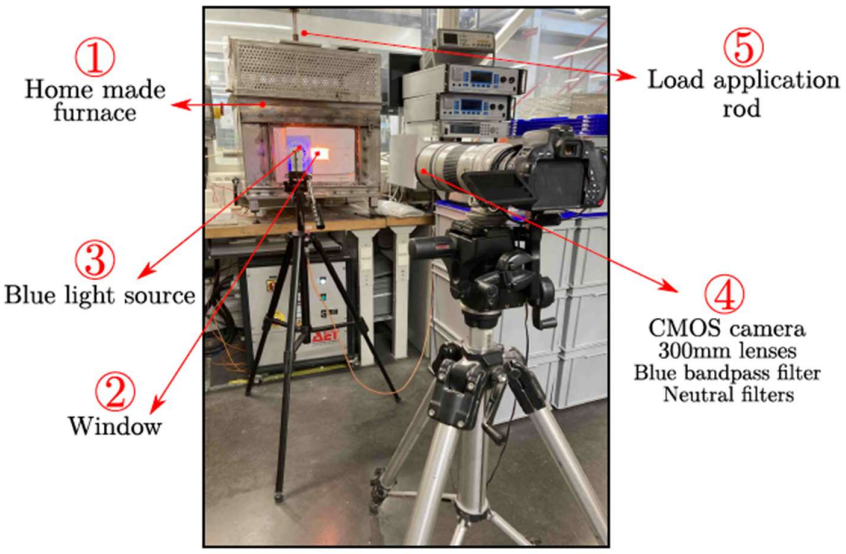

Figure 15 – Montage expérimental pour essais de flexion quatre points à haute température

La Figure *16*a montre les résultats expérimentaux en utilisant une charge de 59,3 N, et le résultat de simulation correspondant, en utilisant les paramètres de matériau identifiés. Comme on peut le constater, les deux expériences ont présenté des problèmes au début.

Pour l'échantillon 1, le début du test a présenté un mouvement important du corps rigide dans la direction y, probablement dû à l'application manuelle de la charge permanente, qui n'est pas toujours fluide. Cela a conduit à un déplacement instantané de -0,2 mm du montage expérimental.

Pour l'échantillon 2, afin d'essayer de limiter l'effet de l'oxydation du mouchetis sur les résultats d'identification, le test a été lancé dès que les thermocouples du four ont indiqué que la température de test était atteinte, c'est-à-dire qu'aucun temps d'homogénéisation n'a été appliqué. Pour cette raison, les calculs DIC indiquent un mouvement vers le haut au cours des 2 premières heures de test, cela s'est produit parce que le montage expérimental n'était pas en équilibre thermique au début du test, et donc dilaté après qu'il avait déjà commencé. Cet effet peut être mieux visualisé dans la Figure *16*b.

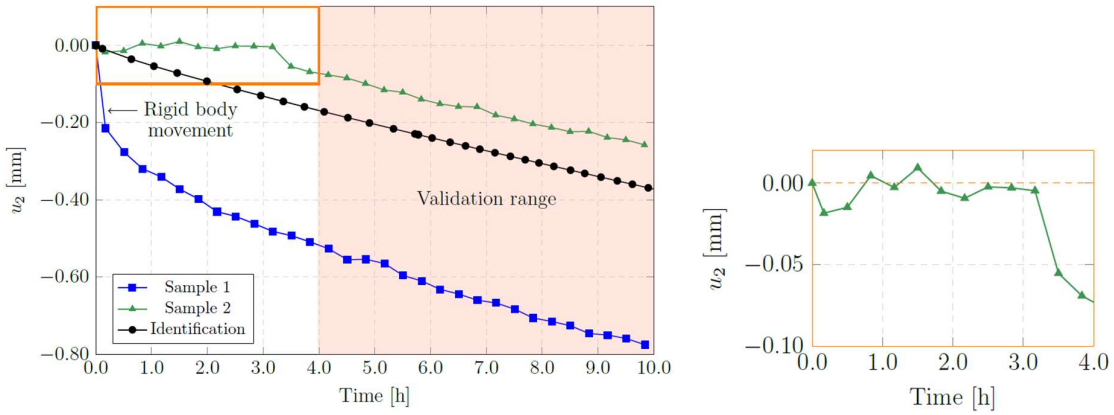

Figure 16 – Essais de flexion (a) Déplacements verticaux à 1300 °C et 59,3 N (b) Détail des 4 premières heures.

En raison de ces problèmes expérimentaux, la validation des résultats d'identification a été faite à partir des données obtenues après quatre heures de test. A ce moment, la courbe expérimentale est stable pour les deux tests, et la variable de validation considérée était la pente des courbes.

La Figure *17* montre les déplacements verticaux pour l'essai de flexion pour une charge de 59,3 N, dans la plage de validation. Il est possible de vérifier que la pente de la courbe simulée et celle de l'échantillon 2 sont quasiment identiques, et diffèrent de celle de l'échantillon 1 de 20 %. Compte tenu de la forte hétérogénéité des matériaux réfractaires, c'est un résultat en faveur de la validation du modèle.

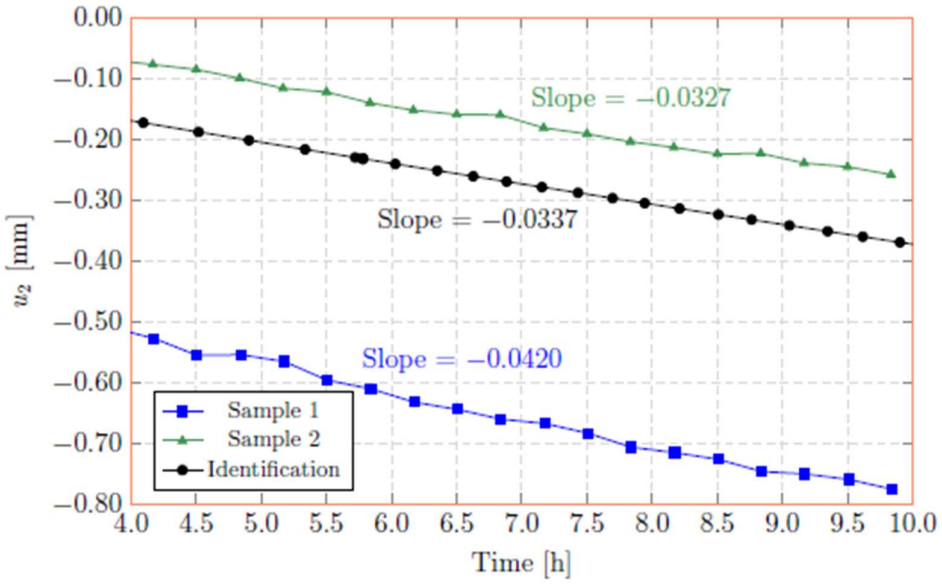

Figure 17 – Essais de flexion : Déplacements verticaux à 1300 °C et 59,3 N – Domaine de validation

Comparaison entre l'approche traditionnelle et l'approche basée sur les essaies brésiliens et la corrélation d'images numériques

Les techniques de caractérisation traditionnelles et celles proposées dans ce travail sont plutôt complémentaires, au lieu de s'exclure mutuellement. Néanmoins, ils peuvent être comparés sur certains aspects, comme discuté ci-dessous.

Conception de l'essai

Les techniques expérimentales traditionnelles, c'est-à-dire les essais de fluage en traction et en compression unidimensionnels, sont extrêmement flexibles, dans le sens où l'une est complètement indépendante de l'autre. Ainsi, si le matériau présente une asymétrie importante, il est relativement facile de le caractériser sous toutes les charges souhaitées.

Au contraire, le test brésilien a une limitation imposée par la résistance à la traction du matériau. Lorsque la charge appliquée augmente, les contraintes de traction et de compression augmentent proportionnellement et, à un niveau de charge donné, l'échantillon commence à se fissurer en tension. A la valeur de charge où l'échantillon atteint sa capacité de charge maximale

en traction, il se peut que la charge de compression n'arrive toujours pas à la valeur souhaitée pour la caractérisation.

La préparation des échantillons

En termes de préparation des échantillons, les deux méthodologies ont des exigences similaires, l'essai de fluage en traction ayant le léger inconvénient de nécessiter un échantillon assez long. Néanmoins, les mesures assistées par DIC ont l'exigence supplémentaire de la préparation du mouchetis, qui peut devenir non trivial à haute température.

Post-traitement des données expérimentales et quantité d'informations récupérées

Étant donné que l'échantillon dans la méthodologie expérimentale traditionnelle est soumis à une seule valeur de contrainte, l'identification inverse des propriétés du matériau peut être facilement réalisée grâce à l'optimisation d'une seule équation, ce qui constitue un avantage considérable. La méthodologie assistée par DIC, au contraire, nécessite une étape de post-traitement lourde, avec des algorithmes sophistiqués conçus spécifiquement à cette fin, ce qui peut prendre un temps considérable pour converger.

L'avantage de la méthodologie DIC vient du fait qu'il s'agit d'une mesure plein champ, c'est-à-dire qu'au lieu de suivre un seul point soumis à une seule valeur de contrainte, comme dans le cas des extensomètres, elle cartographie toute la surface de l'échantillon, fournissant une quantité considérablement plus importante d'informations sur ce qui se passe avec l'échantillon à chaque pas de temps.

Restrictions de temps et de budget

L'un des principaux avantages de la procédure expérimentale proposée par rapport aux essais traditionnels de fluage en traction et en compression est le nombre réduit d'essais nécessaires pour identifier les paramètres d'une loi de fluage asymétrique.

Lorsque le temps d'obtention des résultats et le budget pour réaliser les essais sont limités, comme c'est généralement le cas pour les applications industrielles, la méthodologie proposée présente clairement un avantage important, d'autant plus significatif lorsque plusieurs matériaux doivent être testés à différents températures.

Conclusions

L'objectif de cette thèse était d'étudier le comportement de fluage asymétrique primaire et secondaire des matériaux réfractaires en termes des lois de comportement et des techniques expérimentales utilisé pour la caractérisation à haute température. Les principaux apports de cette thèse ont été :

1. Développement de deux nouvelles lois de comportement asymétriques pour le fluage : basés sur l'hypothèse d'une division du tenseur de contraintes en parties positives et négatives, la prise en compte de l'asymétrie du matériau a pu être effectuée avec succès, comme démontré avec des simulations numériques et validé avec des données expérimentales. Contrairement aux travaux antérieurs présents dans la littérature, cette thèse a utilisé une stratégie de pondération des contributions des contraintes positives et négatives qui ne se traduit pas par une orthotropie intrinsèque de la vitesse de

déformation de fluage, c'est-à-dire que le comportement symétrique est récupéré chaque fois que les mêmes paramètres de matériau sont utilisés en traction et en compression.

2. Développement d'un protocole de caractérisation basé sur la technique de corrélation d'images numériques et les essais brésiliens : pour pallier les coûts élevés de la caractérisation à haute température, ce travail a proposé un protocole expérimental qui utilise l'essais brésilien comme essais mécanique principal. Le principal avantage de l'essai brésilien est que le champ de déplacements résultant est influencé à la fois par les contraintes en traction et en compression, selon la région de l'échantillon. Par conséquent, l'innovation de ce travail réside dans l'utilisation d'un seul essai pour la caractérisation, au lieu des essais traditionnels de fluage en traction et en compression. Le protocole expérimental proposé entraîne une distribution complexe des contraintes sur l'échantillon et, par conséquent, nécessite des techniques plus sophistiquées pour analyser les résultats, pour lesquels deux approches basées sur DIC ont été choisies et développées plus avant. La première approche utilise une technique DIC traditionnelle et prend le déplacement du point de contact entre l'échantillon et les mâchoires comme cible d'optimisation. L'algorithme I-DIC vise à utiliser tout le champ de déplacement pour minimiser l'erreur lors de la procédure d'identification. Pour simplifier l'algorithme I-DIC tout en tenant compte des imperfections intrinsèques de la procédure expérimentale, la charge horizontale qui se traduit par une rotation de l'échantillon de test brésilien a été incluse dans la caractérisation, rendant les résultats plus précis et la procédure expérimentale plus robuste. Cette méthodologie présente l'avantage supplémentaire d'exposer le modèle constitutif à des conditions bidimensionnelles directement lors de la caractérisation, au lieu d'identifier les paramètres du matériau dans des conditions unidimensionnelles et de vérifier ultérieurement si les hypothèses multidimensionnelles du modèle sont valides. Malgré les avancées obtenues dans ce travail, il est clair que la précision et la sensibilité de la technique I-DIC au bruit doivent encore être améliorées.